Heterogeneous Interactions of Volatile Organic Compounds with Natural Mineral Dust Samples

Mohamad Nour Zeineddine

N° d'ordre :

IMT LILLE DOUAI

UNIVERSITE DE LILLE

THESE

présentée en vue
d'obtenir le grade de

DOCTEUR

en

Discipline : Sciences de la Terre et de l'Univers
Spécialité : Optique et Lasers, Physico-Chimie, Atmosphère
par

Mohamad Nour ZEINEDDINE

**DOCTORAT DE L'UNIVERSITE DE LILLE
DELIVRE PAR IMT LILLE DOUAI**

Titre de la thèse :

Heterogeneous Interactions of Volatile Organic Compounds

with Natural Mineral Dust Samples

Yuri BEDJANIAN	*Directeur de Recherche CNRS, ICARE, CNRS/Université d'Orléans*	**Rapporteur**
Pierre DELMELLE	*Professeur, Earth and Life Institute, Environmental Sciences, Université Catholique de Louvain*	**Rapporteur**
Raluca CIURARU	*Chargée de Recherche INRA, INRA*	**Examinatrice**
Barbara D'ANNA	*Directrice de Recherche CNRS, LCE, CNRS/Université Aix-Marseille*	**Examinatrice**
Véronique RIFFAULT	*Professeure, SAGE, IMT Lille Douai*	**Directrice de thèse**
Frédéric THÉVENET	*Professeur, SAGE, IMT Lille Douai*	**Co-directeur de thèse**
Emmanouil ROMANIAS	*Maître-Assistant, SAGE, IMT Lille Douai*	**Encadrant**
Sarah STYLER	*Assistant Professor, University of Alberta*	**Membre invitée**

Laboratoire d'accueil :

Département Sciences de l'Atmosphère et Génie de l'Environnement, IMT Lille Douai
Ecole Doctorale SMRE 104 (Lille, Artois, ULCO, UVHC, Centrale Lille, IMT Lille Douai)

Acknowledgments

I would like to express my special appreciation and thanks to my directors Professor Dr. Véronique Riffault and Frédéric Thévenet, you have been a tremendous mentor for me. I would like to thank you for encouraging my research and for allowing me to grow as a research scientist. I would especially like to thank all technicians and lab members at SAGE department. All of you have been there to support me when I had technical troubles during my Ph.D. thesis.

My sincere gratitude is reserved for my supervisor Dr. Emmanouil Romanias. Your advice on both research as well as on my career have been priceless. I would also like to thank my committee members, Professor Yuri Bedjanian, Professor Pierre Delmelle, Professor Barbara D'Anna, Dr. Raluca Ciuraru, and Dr. Sarah Styler for serving as my committee members even at hardship. I want to thank you for letting my defense be an enjoyable moment, and for your brilliant comments and suggestions, thanks to you.

A special thanks to my family. Words cannot express how grateful I am to my mother, father, my sister, and brother for all of the sacrifices that you've made on my behalf. Your prayer for me was what sustained me thus far. I would also like to thank all of my friends who supported me in writing, and incented me to strive towards my goal.

Thesis Outline

Chapter IV. Heterogeneous interactions of various natural dust samples using isopropanol as a model probe VOC …………………………………………………..113

Chapter V. Heterogeneous interaction of isoprene with natural Gobi dust ……………………………………………………...141

Summary

General introduction

Environmental context

The atmosphere is a complex mixture containing a wide variety of particles and gases. The anthropogenic influence due to human expansion and industrial development has made this mixture of particles and gases even more complex. Additionally, constituents have a significant effect on processes and interactions that occur within the atmosphere. It is important to understand these processes and reactions in order to properly assess and evaluate the Earth's atmosphere in terms of its composition and climate.

Considering only homogeneous reactions to describe atmospheric physics and chemistry would be appropriate if the atmosphere was only composed of gaseous species. However, this approach does not correspond to reality. Indeed, the Earth's atmosphere contains more than 3000 million tons of solid particles creating interfaces between the gas and solid phases [1]. These solid particles can either originate from natural phenomena or anthropogenic activities. Both origins lead to the release of soil particles, colloids, and micro-crystallites of minerals or organic aerosols in the atmosphere [2].

Among the particles found in the atmosphere, mineral dust aerosol is ubiquitous. Every year around 1500 million tons of mineral dust are emitted in the atmosphere [1]. Mineral dusts can impact the Earth's radiative balance [3], human health [4], and the biogeochemical cycles [5]. Although there have been many studies performed to understand the above effects, there still remains substantial uncertainties associated with processes involved. Thus, it is difficult for current atmospheric chemistry and climate models to reconcile model results with field measurements. Therefore, it is important to have better agreement between models and observations as the accuracy of future atmospheric chemistry and climate predictions depends on it.

As a result of suspension, dust can travel thousands kilometers [6]. The combination of the large flux of mineral dust into the atmosphere and the long range global transport of these particles indicates that mineral dust will interact with many trace atmospheric species.

When considering atmospheric gases, there is a wide range of gases including inorganic and organic species. Among the organic species there are the volatile organic compounds, VOCs. VOCs are found in trace amounts compared to the gases that comprise the majority of the atmosphere, such as O_2 and N_2. Depending on their chemical structure and concentrations, VOCs can cause various effects. At human scale, they can affect wellness and health, and some of them have carcinogenic effects [7]; at atmospheric scale, they can lead to the creation of

photochemical smog and ozone layer depletion. These trace gases tend to be very reactive [8], therefore, studies that address their reactivity in the atmosphere are imperative.

The current approach used in atmospheric modeling leads to an underestimated concentrations of oxygenated volatile organic compounds when compared to field observations [9]. Large uncertainties are sometimes associated to the uptake and ageing of VOCs on mineral dusts due to a lack of understanding of these processes. Modelers have thus suggested that processes acting as sources of oxygenated compounds, and not yet taken into account in reaction schemes may exist; heterogeneous oxidation processes may be one of them and it is therefore critical to evaluate the possibility of such reactions to occur under atmospheric conditions, and form oxygenated VOCs.

In this research, a greater understanding of the role of VOC interactions with natural mineral dust sample is pursued through focused laboratory studies in order to better understand fundamental processes involved. Based on the context, this thesis focuses on the investigation of the interactions of VOCs with natural dust samples in order to evaluate their significance on the global atmospheric composition. A brief description of the content of each chapter of the manuscript is given bellow.

This work is part of the CaPPA project funded by the ANR through the PIA under contract ANR-11-LABX-0005-01, the "Hauts de France" Regional Council and the European Regional Development Fund (ERDF). This study is part of the Work Package 2 "WP2". Aerosol microphysical, chemical and optical properties from fundamental heterogeneous processes to remote sensing" of the Labex CaPPA.

Structure of this Ph.D. thesis

In Chapter 1, an overview is given about the atmosphere general composition and content. Further, a bibliography is dedicated to the fundamentals of heterogeneous interaction of gases on solid substrates. Finally the objectives of the thesis and the structure of the manuscript are defined.

In Chapter 2, the characterization and the origin of the selected natural dust samples are detailed, followed by the materials used to prepare the VOC gas mixtures. Then a detailed part is dedicated to the methods and experimental devices employed for studying different aspects of the interaction of VOCs with natural dust samples.

In Chapter 3, the impact of dust origin and chemical composition on the heterogeneous process, is investigated. In particular, experiments are performed to investigate the uptake and the adsorption efficiency of isopropanol (IPA), used here as a probe molecule, on natural dust samples collected from North and West Africa, Saudi Arabia, and Arizona desert regions. Experiments are performed under atmospheric pressure, room temperature 296 K, and in the RH range (0.01–85) %.

In Chapter 4, the interaction of IPA with a natural sample from the Gobi desert that showed the highest uptake is studied under different relevant atmospheric conditions (temperature, RH, and simulated sunlight). Experiments are performed in the temperature and RH ranges of 273 – 348 K and <0.01 – 70%, respectively.

In Chapter 5, isoprene (ISP), the highest emitted biogenic VOC in the atmosphere is selected to evaluate its interaction with natural dust from the Gobi desert. Experiments are performed in the temperature and RH ranges of 253 - 358 K and <0.01 – 10%, respectively.

In Chapter 6, the interaction of acetic acid (AcA) with natural dust from the Gobi desert is assessed under atmospheric simulated conditions. This VOC-dust system enabled to address in more details (i) the reactive sorption of a selected VOC on Gobi dust, and (ii) the relative contributions of each mineral phase of Gobi sample to the uptake and to the reactivity.

References of general introduction

1.   Satheesh, S. K.; Krishna Moorthy, K., *Radiative Effects of Natural Aerosols: A Review.* Atmospheric Environment, 2005. **39**(11): p. 2089-2110.

2.   Parmon, V.; Zakharenko, V., *Photocatalysis and photosorption in the Earth's atmosphere.* Catalysis Technology, 2001. **5**(2): p. 96-115.

3.   IPCC, *Climate change 2001: The Scientific Basis. Contribution of Working Group I to the Third Assessment Report of the Intergovernmental Panel on Climate Change.* 2001: Cambridge, U.K.

4.   Seaton, A.; Godden, D.; MacNee, W.; Donaldson, K., *Particulate air Pollution and Acute Health Effects.* The Lancet, 1995. **345**(8943): p. 176-178.

5.   Mahowald, N.; Ward, D. S.; Kloster, S.; Flanner, M. G.; Heald, C. L.; Heavens, N. G.; Hess, P. G.; Lamarque, J.-F.; Chuang, P. Y., *Aerosol Impacts on Climate and Biogeochemistry.* Annual Review of Environment and Resources, 2011. **36**(1): p. 45-74.

6.   Prospero, J. M.; Lamb, P. J., *African Droughts and Dust Transport to the Caribbean: Climate Change Implications.* Science, 2003. **302**(5647): p. 1024-1027.

7.   Ware, J. H.; Spengler, J. D.; Neas, L. M.; Samet, J. M.; Wagner, G. R.; Coultas, D.; Ozkaynak, H.; Schwab, M., *Respiratory and Irritant Health Effects of Ambient Volatile Organic CompoundsThe Kanawha County Health Study.* American Journal of Epidemiology, 1993. **137**(12): p. 1287-1301.

8.   Atkinson, R.; Arey, J., *Atmospheric Degradation of Volatile Organic Compounds.* Chemical Reviews, 2003. **103**(12): p. 4605-4638.

9.   Karl, T.; Potosnak, M.; Guenther, A.; Clark, D.; Walker, J.; Herrick, J. D.; Geron, C., *Exchange Processes of Volatile Organic Compounds Above a Tropical Rain Forest: Implications for Modeling Tropospheric Chemistry Above Dense Vegetation.* Journal of Geophysical Research: Atmospheres, 2004. **109**(D18).

Chapter I. Fundamentals of heterogeneous interactions of trace atmospheric gases with atmospheric aerosols

Chapter I. Fundamentals of heterogeneous interactions of trace atmospheric gases with atmospheric aerosols

Table of content

List of Tables

List of Figures

1   The atmosphere

The Earth's atmosphere is a complex physical and chemical reactor which exhibits wide ranges of temperature, pressure, and composition. The atmospheric chemical system is not homogeneous: although largely gaseous, air masses also contain liquid droplets and solid particles. The chemical species found in the atmosphere include noble gases, neutral molecules, reactive atoms, free radicals, and ions [1].

It is considered that the atmosphere extends up to an altitude of more than 800 km [2]. This study focuses on the lowest atmospheric layer, the troposphere that is in contact with the Earth's surface and at the same time influences and ensures life on Earth.

1.1   Variation of the temperature and relative humidity in the troposphere

In the troposphere, the actual temperature profile shows large fluctuations on short time scales and depends on season, day time, and latitude. In the troposphere, on an average scale, the temperature decreases as altitude increases. This is due to the absorption of sun radiations which causes a strong heating effect at the Earth's surface. As ground heats up, it transfers heat to the adjacent air. Indeed, the vertical mixing in the troposphere is rapid because the hot air expands, becomes less dense, and rises [3].

Humidity defines the moisture content of the atmosphere. Relative humidity (RH) is given as a percentage, and 100% correspond to saturated air. RH is calculated as shown in Equation I-1.

$$RH = 100 \ \times \ \frac{P_{water}}{P_{sat}}$$
                                                                                   (Equation I-1)

where P_{water} is the partial pressure of water and P_{sat} is the saturation vapor pressure [4].

1.2   Chemical composition of the troposphere

The Earth's troposhere is mainly composed of the following gases: N_2 (78%), O_2 (21%) and Ar (1%). The trace gases make up the remaining, they contribute to less than 1% of the total volume. The amount of oxygen in the troposphere is not constant. Its variation is due to the possible alterations in weather conditions, changes in barometric pressure, temperature, humidity, and wind strength and direction. The carbon dioxide content of air is 400 ppm.

Table I-1. Summary of trace gases with the corresponding highest concentrations or concentration ranges in the troposphere [2].

Gas species	Chemical formula	Fraction of volume of air occupied by the species
Neon	Ne	18.18 ppm_v
Helium	He	5.24 ppm_v
Methane	CH_4	1.7 ppm_v
Hydrogen	H_2	0.56 ppm_v
Nitrous oxide	N_2O	0.31 ppm_v
Carbon monoxide	CO	40-200 ppb_v
Ozone	O_3	10-100 ppb_v
Volatile organic compounds	-	5-20 ppb_v
Halocarbons	-	3.8 ppb_v
Hydrogen peroxide	H_2O_2	0.1-10 ppb_v
Nitrogen species	NO_X , N_2O_5, HNO_3	10 ppt_v - 1 ppm_v
Ammonia	NH_3	10 ppt_v - 1 ppb_v
Sulfur dioxide	SO_2	10 ppt_v - 1 ppb_v
Dimethyl sulfide (DMS)	CH_3SCH_3	10-100 ppt_v
Hydrogen sulfide	H_2S	5-500 ppt_v
Carbon disulfide	CS_2	1-300 ppt_v
Hydroxyl radical	$HO^{\cdot}$	0-0.4 ppt_v
Hydroperoxy radical	$HO_2^{\cdot}$	0-5 ppt_v
The units used are parts per million by volume ppm_v; parts per billion by volume ppb_v; parts per trillion by volume ppt_v.		

The most common unit for expressing the quantity of a gas in air is the fraction of the total volume of air the gas occupies in parts per million by volume. The volume occupied by different gases at the same temperature and pressure is proportional to the numbers of molecules of the respective gases. A summary of the trace gases with highest concentrations in the atmosphere is presented in Table I-1. As shown in this table the volatile organic compounds (VOCs) are among the trace gases in the atmosphere. Despite being found at low concentrations, VOCs are considered as the "fuel" which keeps oxidative atmospheric photochemistry running. Therefore, their sources and their impacts are the subject of much current research [5].

1.3   Volatile organic compounds (VOCs) in the atmosphere

1.3.1   Definition of VOCs

Various terms have been used in the literature to describe the subset of diverse carbon-containing gases. One of the first is non-methane hydrocarbons (NMHC), which was originally employed to distinguish alkanes, such as ethane, propane and butane, from methane. However, strictly speaking, the word hydrocarbon indicates a molecule containing only carbon and hydrogen atoms, and therefore this term excludes oxygenated species such as alcohols, carbonyls and acids as well as organic compounds containing other heteroatoms, such as nitrogen or sulfur. In an attempt to embrace all the species relevant to atmospheric chemistry, a further term "volatile organic compound", abbreviated as VOC, is employed [5].

VOCs are organic molecules presenting several definitions. On one side, the 1999/13/EC directive of the European Community [6] defines a VOC from its vapor pressure, regardless of its reactivity: "*Volatile Organic Compounds are functionally defined as organic compounds having at 293.15 K (i.e., 20 °C) a vapor pressure of 0.01 kPa or more, or having a corresponding volatility under particular conditions of use*". On the other hand, the United States Environmental Protection Agency (US-EPA) gives more importance to the reactivity of these molecules [7]: "*Volatile organic compounds means any compound of carbon, excluding carbon monoxide, carbon dioxide, carbonic acid, metallic carbides or carbonates, and ammonium carbonate, which participates in atmospheric photochemical reactions*".

According to the first definition, methane is a VOC but not according to the second one due to its low reactivity, thus leading to the common definition of non-methane volatile organic compounds.

1.3.2   Sources of VOCs

Daily human activities result in the release of organic species to the atmosphere. Car driving, house painting, cooking, making fire, cutting grass, and even breathing – all of these processes result in the emission of organic compounds such as carbonyls, alcohols, alkanes, alkenes, esters, aromatics, ethers and amides. In addition to emissions related to human activities, numerous natural sources on Earth, such as vegetation, oceans or animals, naturally release considerable amounts of organic gases in the atmosphere [5]. Table I-2 shows the sources and emission rates and their associated uncertainties for various VOCs. Such numbers have high

uncertainties because the factors controlling the emission of VOCs are complex, leading to a large variation with the time of day, season, geographical location, etc. [5].

Table I-2. Overview of sources and global annual emission rates of selected groups of VOC. Adapted from [5]

	Average emission rate (million tons)	Upper and lower limits of emission rate
Fossil fuel use		
- Alkanes	28	15-60
- Alkenes	12	5-25
- Aromatic compounds	20	10-30
Biomass burning		
- Alkanes	15	7-30
- Alkenes	20	10-30
- Aromatic compounds	5	2-10
Terrestrial plants		
- Isoprene	460	200-1800
- Sum of monoterpenes	140	50-400
- Sum of other VOCs	580	150-2400
Oceans		
- Alkanes	1	0-2
- Alkenes	6	3-12
Sum of anthropogenic and oceanic emissions		
- Alkanes	44	
- Alkenes	38	
- Aromatic compounds	25	
Sum of terrestrial plant emissionss	1180	
Total	1287	

1.3.2.1 Anthropogenic sources of VOCs

The use of fossil fuels for transport and heating, the production of consumer goods, biomass burning and various industrial processes are the main sources of anthropogenic VOCs. Recently, Huang et al. [8] published a study mapping the global anthropogenic VOC emissions for the past

4 decades showing that these emissions increased from 110 million tons in 1970 to reach around 165 million tons in 2012.

VOCs are spread all over the world. For example, propane, butane, and many other typically anthropogenic VOCs have been found in Antarctica and Greenland [9, 10], remote regions that are far from any anthropogenic sources. The observation of anthropogenic VOCs in such remote areas indicates that VOCs can be transported on a global scale [9, 11].

1.3.2.2 *Natural sources of VOCs*

Natural sources emit a wide range of organic species from vegetation, soils and oceans. It is estimated that on a worldwide scale the total amount of biogenic emissions are 10 times higher than anthropogenic ones [12]. Although on a worldwide basis VOCs from biogenic sources dominate over those from anthropogenic sources, anthropogenic VOCs often prevail in urban areas.

Isoprene is the most emitted biogenic VOC in the troposphere with emission rates exceeding 500 million tons per year; it corresponds to one-third of the annual global VOC emissions [13]. The primary sources of isoprene are natural, with deciduous trees being large emitters. After Chameides et al [14]. showed that isoprene can be the dominant VOC impacting regional tropospheric photochemistry and ozone production, the amount of research focusing on biogenic VOCs (BVOCs) dramatically increased. After a few decades the understanding of the types and quantities of these emissions has grown significantly and recently several review articles have been published that provide a scientific history on the topic (e.g. Wiedinmyer et al. 2004) [15].

1.3.3 Fate of VOCs in the troposphere

VOCs undergo a number of physical and chemical processes leading to their removal or transformation in the troposphere [16]. Figure I-1 summarizes the processes of the gas-phase fate of VOCs. These processes include photolysis, reactions with the hydroxyl radical (OH$\cdot$) typically during daytime hours, or with the nitrate radical (NO$_3\cdot$) during evening and nighttime hours, reaction with O$_3$, and reaction with Cl atoms in coastal and marine areas. Subsequently in the presence of O$_2$ and nitrogen oxides, NO$_x$, these reactions can lead to the generation of intermediate oxidants, i.e., HO$_2\cdot$, RO$_2\cdot$, RO$\cdot$ radicals, peroxides, and new VOCs [16]. These intermediates and other VOCs, for example isoprene, terpenes, and aromatics, can contribute to the formation of

secondary organic aerosol (SOA). SOA are structures produced via oxidation over several generations of parent organic molecules [2].
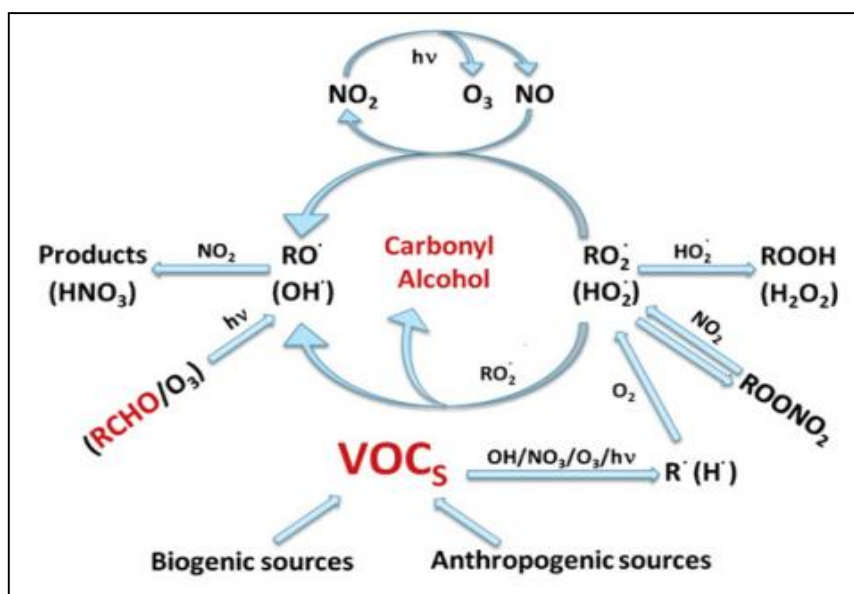
Figure I-1. Gas phase reactions of VOCs in the atmosphere. Adapted from [17]

The fate of VOCs does not solely depend on homogeneous removal since the atmosphere is highly heterogeneous. Therefore, besides the gas-phase degradation of VOCs, their interactions with liquid and/or solid particles can occur in the atmosphere [18]. In the troposphere the suspension of solid and/or liquid particles is called an aerosol. The scope of this study mainly focuses on the interaction of VOCs with solid surfaces. But what kind of surfaces present in the atmosphere could be included in such heterogeneous processes? This question is addressed in the following section.

1.4 Tropospheric aerosols: types and sources

Tropospheric aerosols range in size from a few nanometers to around 100 μm [3]. Figure I-2 shows a schematic of a typical atmospheric aerosol size distribution and the chemical processes by which they are usually produced. Although the vertical axis is not defined, it could in theory be any of the four classical distributions, that is to say, number, mass, surface, or volume concentrations. Aerosols can be produced by two distinct mechanisms: the direct injection of particles into the atmosphere (e.g. dust, sea spray) resulting in primary aerosols or the production of secondary aerosols by the conversion of gaseous precursors into liquid or solid particles through various processes such as condensation, coagulation and accumulation [19].
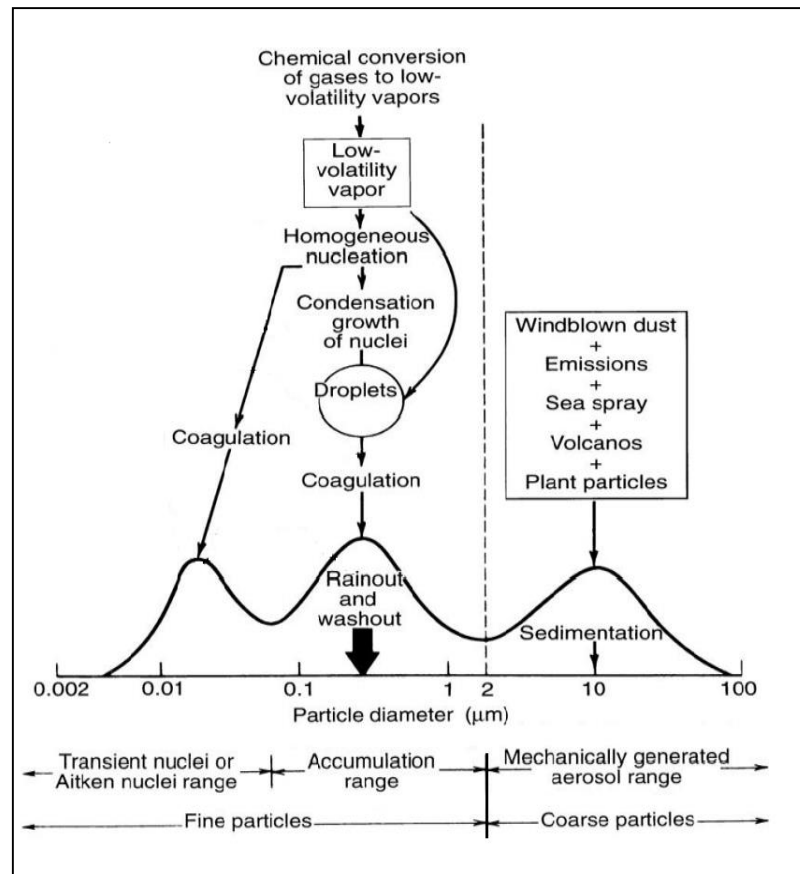
Figure I-2. Schematic diagram of an aerosol size distribution (the x-axis is in log scale) and formation mechanisms of atmospheric aerosols. Adapted from [3].

Atmospheric aerosols are usually referred to as having an aerodynamic diameter, corresponding to the diameter of a sphere of density 1 g cm^{-3} that has the same settling velocity in air as the particle under consideration. Indeed, atmospheric particles have many irregular shapes for which geometric radius and diameter are meaningless [3, 20]. Primary aerosols dominate the "coarse" fraction of the aerosol, while secondary aerosols constitute most of the "fine" particles. Table I-3 summarizes the various sources of aerosol particles and presents estimates of their flux magnitudes. Various sources of aerosols are present in the troposphere with mineral dust representing the highest emission source of aerosols with around 1,500 million tons released into the atmosphere per year. The total aerosol emissions are estimated to be around 3,500 million tons per year. Due to their high emission in the atmosphere and their role in climate change, mineral aerosols have received much attention from the scientific community in the past 40 years [21]. The second part of this chapter will be mainly focused on mineral dust, in particular, its general

chemical composition, transport phenomena, main sinks and impacts to the atmosphere will be presented.

Table I-3. Source strength of natural and anthropogenic emitted aerosols. Adapted from [22].

Source	Flux (million tons)
Natural	
Primary	
- Mineral dust	1,500
- Sea salt	1,300
- Volcanic dust	33
- Biological debris	50
Secondary	
- Sulfates from biogenic gases	90
- Sulfates from volcanic SO_2	12
- Organic matter from biogenic NMHC	55
- Nitrates from NO_x	22
Anthropogenic	
Primary	
- Industrial dust	100
- Black carbon	20
Secondary	
- Sulfates from SO_2	140
- Biomass burning	80
- Nitrates from NO_x	36
- Organics from anthropogenic NMHC	10
Total	3,450

2 Mineral dust

Mineral aerosols are soil particles that have been mobilized by strong wind currents and entrained into the atmosphere. As one of the most mass abundant types of aerosol emitted into the

atmosphere, wind-blown mineral dust aerosol accounts for about one half of the mass of the total aerosol budget [21] and mainly originate from arid and semi-arid regions.

The analysis of dust particles from different sources shows that the major minerals present in these particles are SiO_2, Al_2O_3, and calcium-rich minerals [23, 24]. Multiple studies on the elemental content of wind-blown dust originating from various locations around the world report that the exact mineralogy of mineral dust particles is variable depending on the source. For example, it has been shown that African and Asian dust particles have very different composition [25] and that the dust from Australia is enriched in iron relatively to the dust sources in the Northern Hemisphere [26].

2.1 Transport and sinks

Conventionally, "sand" describes soil particles in an approximate size range of 0.6-1 mm, while "dust" describes particles less than 0.6 mm [27]. In practice, only dust particles below 0.1 mm can be carried by suspension. Dust storms are responsible for massive transportation of soil particles by wind. For instance, a dust storm from the China desert covered the Japan islands on April 14-15, 1979 and the total dust particle mass load was estimated at least 1.63 million tons.[28]

In order to understand the physical process of a dust storm on soil, let us consider a surface made up of separate particles that are held in place by their own weight and some inter-particle bonding. At low wind speed, there will be no indication of motion, but when the wind force reaches a threshold value some particles will begin to vibrate. Increasing the wind speed will eject some particles from the surface into the airflow. When these injected particles impact back on the surface, more particles are ejected, thus starting a chain process. Once ejected, particles move in one out of three modes of transport depending on their size, shape and density. These three modes are designated as suspension, saltation and creep [27].

- The **suspension mode** involves dust particles of less than 100 μm in diameter and clay particles of 2 μm in diameter which are small in size and light in density. These fine dust particles may be transported at altitudes of up to 6 km and move over distances up to thousands kilometers.
- **Saltation particles** (i.e. those between 0.1-0.5 mm in diameter) leave the surface, but are too large to be suspended.

- The remaining particles (i.e. above 0.5 mm) are transported in the **creep mode**. These particles are too large to be ejected from the surface and are therefore rolled along by the wind and impacting particles.

As a result of suspension, dust can be transported far from its source regions. Figure I-3 shows an example of dust transportation extending over 1,600 km from the Canary Islands to the Cape Verde islands. The Saharan region is the main source of aeolian dust in the world [29] with frequent episodes reaching Europe [30], as well as Central America and southern United States [31].
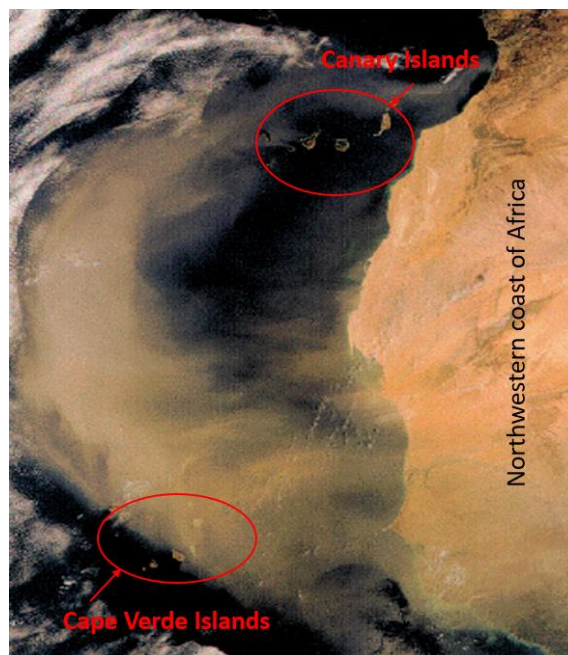
Figure I-3. Massive dust storm, extending over 1,600 km from the Canary Islands to the Cape Verde Islands, transported off the northwestern coast of Africa (right) in 2003 and detected with moderate resolution imaging spectroradiometer (MODIS) on the Terra satellite [32].

Even though dust can be transported over long distances, it is eventually removed mainly by gravitational dry deposition. The lifetime of dust in the troposphere depends on the particle size [33]. Particles with a diameter smaller than 1 μm have a lifetime around 2-3 weeks. In contrast, larger particles have a lifetime of a few hours [20, 34]. Therefore, the lifetime of mineral dust in the atmosphere is long enough to provide a surface with active site for reactions or interactions [35, 36].

2.2 Impacts of mineral dust on global atmospheric processes

The combination of the large flux of mineral dust into the atmosphere and the long range global transport of these particles implies that mineral dust can interact with many atmospheric,

terrestrial, and oceanic systems. These interactions will result in many impacts at the global atmospheric scale. Figure I-4 shows a scheme of the potential global impacts that mineral dust may have on atmospheric processes which are discussed in more details in the following paragraphs [21].
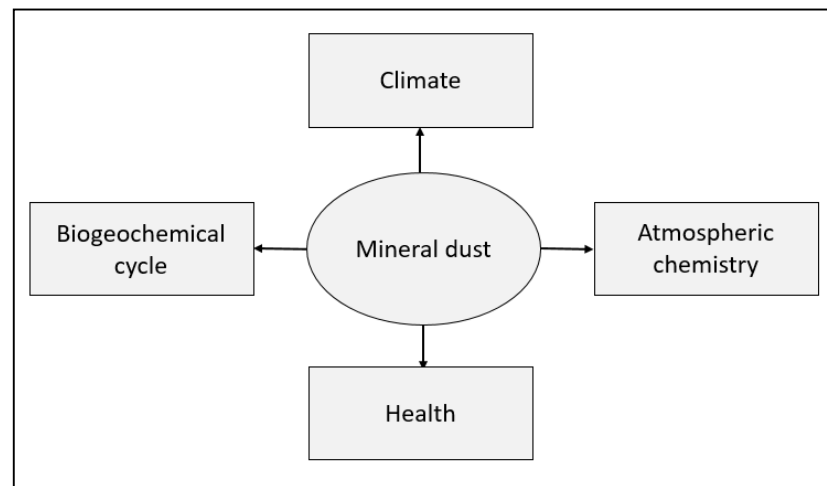
Figure I-4. Impacts of mineral dust on global atmospheric processes. Adapted from [21].

2.2.1 Effects of mineral dust aerosols on climate

Mineral dust affect the atmospheric radiative balance i.e. the difference between the incident solar radiation absorbed by the Earth and the energy radiated back to space. Hence affecting climate through three main processes: (a) scattering and absorbing solar radiation; (b) scattering, absorbing, and emitting thermal radiation; and (c) acting as cloud condensation nuclei [21, 22]. When aerosol particles absorb and scatter radiation themselves, the resulting radiative forcing is deemed to be "direct", whereas if particles influence the optical properties of clouds, then the radiative forcing is "indirect." Positive radiative forcing values, measured in W m^{-2}, result in a warming effect on the Earth's surface, and conversely, negative forcing has a cooling effect. Radiative forcing from mineral dust range from -0.06 to +0.40 W m^{-2} [37].

2.2.2 Effects of mineral dust on the biogeochemical cycle

Mineral dust can have significant direct effects on biogeochemical cycles by changing the gain and loss of nutrients through the atmosphere [38]. Due to their long range transport, mineral dust particles can be deposited far from their sources leading to soil and water enrichment with

nutrients that are not present initially [39]. For instance, it was shown that dust transported from North Africa fertilizes the Amazon rain forest [40] and the Atlantic Ocean phytoplankton [41].

2.2.3 Effect of mineral dust on human health

Mineral dust can have numerous consequences on human health, the most notable and dangerous being the effects of inhaled particles on the human respiratory system. Studies show that fine air particulate matter and traffic-related air pollution are correlated with severe health effects, including enhanced mortality, cardiovascular, respiratory, and allergic diseases [42, 43]. In 1997, the U.S. Environmental Protection Agency established the "PM (Particulate Matter) 2.5" standard [44], which recognized the importance of aerosols that have diameters of ≤ 2.5 µm in causing health problems. Long exposures to or large doses of particles below this size can cause respiratory damage because they penetrate deep into the alveoli of the human lungs, produce scarring, and potentially lead to conditions such as emphysema [42].

2.2.4 Effects of mineral dust on atmospheric trace gases

Heterogeneous and multiphase chemical interactions occurring on airborne mineral particles can influence the atmospheric gas-phase chemistry as well as the properties of atmospheric particles. Aging upon exposure to inorganic and organic chemical species or exposure to varying amounts of water vapor in the atmosphere can influence the chemical nature of mineral aerosols [21]. Heterogeneous processes that take place on mineral dust in the troposphere may provide the missing link for some reaction schemes that cannot be explained solely with gas-phase reactions [35, 45, 46].

Comparisons between field observations and model predictions suggest that taking only gas-phase reactions into account is not sufficient to simulate the atmosphere chemical composition [47]. Hence, understanding heterogeneous processes and including experimental data into models of atmospheric chemistry may greatly improve model reliability. In this thesis the focus will be the interaction of mineral dust with trace atmospheric gases. Therefore, this topic will be discussed in details in section 5 of this chapter. Before moving to that aspect, a section dedicated to the physical chemistry approach is needed to understand how to deal with heterogeneous interactions from a kinetic and thermodynamic point of view.

3   Physical chemistry approach needed to describe heterogeneous processes

Various experimental protocols can be used to address adsorption. This section presents the uptake kinetics of trace gases, the different types of adsorption of gases onto solid substrates, the various models used for processing adsorption experimental data, and finally the laboratory techniques used for studying heterogeneous processes.

The thermodynamics and kinetics of gas uptake are closely related to each other because thermodynamic properties, such as the surface coverage, are experimentally determined in kinetic experiments. Figure I-5 summarizes the different processes that may occur whenever a gas is in contact with a solid surface. These processes are explained in details in the following subsections.
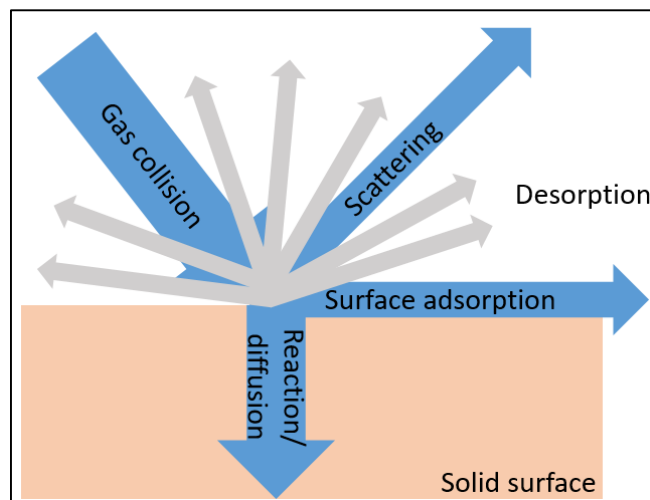
Figure I-5. Summary of the different processes that can occur whenever a gas molecule strikes a solid surface

3.1   Uptake kinetics of trace gases to mineral dust particles

Definition of the uptake coefficient

The most widely used approach to describe the kinetics of heterogeneous processes is to use the uptake coefficient γ, which is the net probability that a molecule X undergoing a gas-kinetic collision with a surface is actually taken up at the surface [48]. This approach links the processes at the interface and beyond with an apparent first-order loss of X from the gas phase as shown in Equation I-2.

$$\frac{d(X)}{dt} = -k_{het}[X] = -\omega\gamma \qquad \textbf{(Equation I-2)}$$

where [X] denotes the concentration of the gas-phase molecule (molecules cm^{-3} or ppm); k_{het} is the first-order rate coefficient of the heterogeneous degradation (s^{-1}); ω, is the VOC collision frequency (s^{-1})

The uptake coefficients are accessible only experimentally, whereas individual processes, such as adsorption or surface reaction, remain unresolved using this parameter [48]. For environmental applications, it may be tempting to consider that the measurement of an uptake coefficient is sufficient to characterize an environmental system. However, proper modeling is required not only to deduce the principal physical parameters from the measured uptake coefficient but also to take into account the often extremely different time scales (seconds to months) and surface properties in order to be able to evaluate the importance of a given heterogeneous process in the atmosphere [21].

The uptake coefficient often depends on time, as uptake may be limited by adsorption equilibrium at the surface, by a limited number of reactants at the surface or in the bulk, or by solubility. As γ can be time-dependent, more distinction is necessary, where γ_0 is the experimentally-observed initial (frequently maximum) uptake coefficient, and γ_{ss} is the experimentally-observed steady-state uptake coefficient. Figure I-6 shows qualitatively the difference between the initial and steady state uptakes.
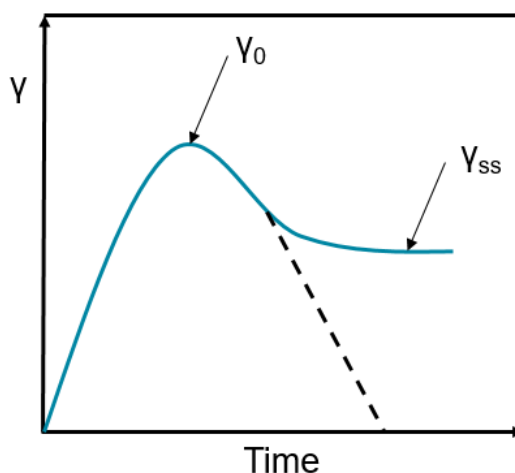
Figure I-6. Qualitative representation showing the difference between initial and steady state uptake coefficients

Initial uptakes are relevant to describe the early stages of the interaction of a gas with a surface, regardless of its nature, and are usually orders of magnitude larger than steady-state

uptakes. These values being representative of the initial time of contact between the gas and the surface, they are therefore of limited relevance for the timescales necessary to reach equilibrium in the atmosphere. Therefore other kinetic and thermodynamic parameters such as the number of molecules adsorbed and surface density should be determined.

3.2   Types of sorption

A thorough kinetic and mechanistic investigation of the heterogeneous interaction between trace gases and solid substrates requires the physicochemical description of the nature of the phenomena that govern these interactions. The aim of that section is to review the different types of interaction between a gas and a solid surface reporting their major differences.

There are two main types of interactions of molecules on surfaces: the physical and the chemical adsorptions.

- **Physical adsorption (physisorption):** The gas-phase molecules interact with the surface mainly via weak Van Der Waals forces or hydrogen bonding. Therefore, there is no significant redistribution of electrons neither in the molecule nor in the substrate surface and consequently no product formation.

- **Chemical adsorption (chemisorption):** A chemical bond is formed between the molecule and the substrate that involves substantial rearrangement of electron density and potentially atoms or chemical groups.

Given the above definitions, one can note that the distinction between both processes is the nature of bonding between the molecules and the surface sites. The major differences between physical and chemical adsorption are summarized in Table I-4 [49].

Table I-4. Differences between physisorption and chemisorption [49].

Description	Physisorption	Chemisorption
Temperature range	Between dew point and boiling point of the gas	No specific range
Adsorption enthalpy	5 to 40 kJ/mol	Wide range (40 to 800 kJ/mol)
Nature of adsorption	Non-dissociative (reversible)	Bond formation between the gas and the substrate: mostly irreversible
Kinetic of adsorption	Rapid (does not require activation energy)	Dependent on the gas/surface reaction coefficient

3.3   Classical models for sorption description

When a gas is in contact with a solid an equilibrium is established between the molecules in the gas phase, characterized by their partial pressure, i.e. concentration, and the fraction of molecules taken up by the surface of the solid. The first efforts to parameterize sorptive phenomena are reported back to 1814. However, until 1913 all proposed models were empirical. The most widespread model for reversible monolayer adsorption was proposed by Irving Langmuir, based on his work through years 1913-1918 [49]. In the following subsections, the most important adsorption models from the literature are reported chronologically.

3.3.1   The Langmuir isotherm

The Langmuir isotherm was developed by Irving Langmuir in 1918 [50] to describe the dependence of the surface coverage of a solid in contact with a gas on the gas partial pressure at a constant temperature. It relies on 5 main restrictive hypotheses which may, to some extent, induce a gap between the proposed model and the reality of adsorption:

Hypotheses of the Langmuir adsorption isotherm

1. Adsorption occurs on a single type of site.

2. Adsorption is a physical and chemical interaction without any modification of the molecule.

3. Adsorption occurs through a single layer of molecules on the surface.

4. No adsorbate - adsorbate interactions.

5. Adsorption energy does not depend on the amount of adsorbed molecules.

The model proposed by Langmuir is based on kinetic considerations. Indeed, adsorption equilibrium corresponds to the situation when the adsorption rate is equivalent to the desorption rate. The adsorption rate is related to the number of collision of gaseous molecules on the solid surface, thus it is proportional to partial pressure. The proportion factor k_{ads} (molecule s^{-1} Pa^{-1}) comprises the collision effectiveness between gas phase molecules and the solid surface. Since adsorption only occurs on the non-covered fraction of the surface, the adsorption rate (r_{ads}) is therefore proportional to the unoccupied fraction of the surface. In order to define and represent this fraction, the coverage rate θ is defined as the fraction of the surface covered by adsorbed

molecules with the unoccupied fraction being (1 - θ). The adsorption rate can be described as a function of the concentration P (in Pa) as reported in Equation I-3

$$r_{ads} = k_{ads}.P(1 - \theta)$$
(**Equation I-3**)

The desorption rate (r_{des}) is related to the thermal agitation of interacting molecules. Thus, it is proportional to the adsorbed amount, expressed by the coverage of the surface θ. In that case, the proportional coefficient is k_{des} (molecule s^{-1}), and the desorption rate can be expressed as reported in Equation I-4:

$$r_{des} = k_{des} \times \theta$$
(**Equation I-4**)

The global adsorption rate is defined as the difference between r_{ads} and r_{des}. The kinetic equation of adsorption can be rewritten converting the partial pressure into the gas concentration C (ppm or molecules cm^{-3}) and the surface coverage into N_S (molecule). The adsorbed amount can further be normalized by the quantity of sorbent (g) and/or the specific surface of the sorbent (cm^2 g^{-1}). As a result, N_S is respectively expressed in molecules cm^{-2}, and Equation I-5 is obtained. The kinetic adsorption coefficients k'$_A$ (molecules^{-1} s^{-1}) and k'$_D$ (s^{-1}) are the correspondingly modified k_{ads} and k_{des}. The constant N_{max} (molecules cm^{-2}) is introduced and represents the number of molecules needed to form a monolayer per unite surface area at the highest coverage ($\theta = 1$).

$$\frac{d(N_s)}{dt} = k'_A . C . (N_{max} - N_S) - k'_D . N_S$$
(**Equation I-5**)

When the adsorption equilibrium is reached, the adsorbed amount does not vary since adsorption and desorption rates are equal. Thus, the adsorbed amount can be expressed as a function of the concentration of the gas-phase species thus leading to Equation I-6:

$$\theta = \frac{N_S}{N_{max}} = \frac{K_{Lang} . C}{1 + K_{Lang} . C}$$
(**Equation I-6**)

where K_{Lang} is the adsorption constant of the considered gas onto the considered solid, expressed as the reverse of the concentration unit. This constant describes the partitioning between the gas and adsorbed phases. Proper rearrangement of Equation I-6 leads to Equation I-7:

$$\frac{C}{N_S} = \frac{1}{N_{max} . K_{Lang}} + \frac{1}{N_{max}} . C$$
(**Equation I-7**)

A linear fit of C/N_S as a function of C provides N_{max} and K_{Lang} values as well as K_{Lin} which is calculated as shown in Equation I-8:

$$K_{Lin} = K_{Lang} \cdot N_{max} \qquad \textbf{(Equation I-8)}$$

where K_{Lin} is an equilibrium constant (cm) introduced by the IUPAC evaluation panel in order to include the temperature dependence of surface coverage [48]. The temperature dependence of K_{Lin} is given by the Van't Hoff Equation I-9:

$$K_{Lin} = A \cdot exp[-\Delta H_{ads}/RT] \qquad \textbf{(Equation I-9)}$$

where A is the pre-exponential factor, R the ideal gas constant (kJ K^{-1} mol^{-1}), ΔH_{ads} the enthalpy of adsorption (kJ mol^{-1}) and T the temperature (K).

3.3.2 Competitive adsorption

In the atmosphere, air consists of multi-pollutant and multi-VOC mixtures. Subsequently, all these gas-phase species may interact with present solid surfaces. This aspect may be integrated as a Langmuir model evolution. The case of different gas-phase pollutant able to interact with the same kind of adsorption site leads to competitive adsorption. The subsequent determination of the non-occupied fraction of the solid shall take into account the site occupation by any VOC interacting with the considered type of site. Thus, Equation I-6 is modified as reported in Equation I-10 which describes the adsorbed quantity of one gas phase species among others interacting with the solid as a function of the adsorption constants and concentration of other gaseous species.

$$\theta = \frac{N_S}{N_{max}} = \frac{K_{Lang} \cdot C}{1 + \sum_i K_{i\,Lang} \cdot C_i} \qquad \textbf{(Equation I-10)}$$

The main limitation of the Langmuir model is based on the hypothesis of mono-layer adsorption, which considerably bounds its application to low concentrations and coverages. In order to overcome this drawback, other models can be employed such as the BET model.

3.3.3 The BET adsorption isotherm

The model proposed by Brunauer, Emmett and Teller (BET) in 1938 [51], aims at improving the Langmuir isotherm by considering the multilayer physical adsorption of gas molecules on a solid. This model is based on the following hypotheses:

1. Gaseous molecules behave as an ideal gas

2. Multiple molecules can be adsorbed on each site

3. Each adsorbed molecule provides a site for the adsorption of another molecule

4. All sites on the solid surface are equivalent.

5. No adsorbate - adsorbate interactions.

6. An adsorbed molecule is immobile.

Authors have considered that molecules may not only directly interact with the uncovered solid surface, but also with previously adsorbed molecules. As a result, the surface may be simultaneously partly uncovered and partly covered by various layers of molecules. The adsorption of molecules on uncovered solid surface as well as previously covered areas can be individually described by the Langmuir model. Based on these considerations, the variation of the adsorbed molecule quantity with their gas phase pressure is reported in Equation I-11:

$$\theta = \frac{\dfrac{P_{eq}}{P_{sat}}}{N_S\left(1 - \dfrac{P_{eq}}{P_{sat}}\right)} = \frac{c-1}{N_{max} \times c}\left(\frac{P_{eq}}{P_{sat}}\right) + \frac{1}{N_{max} \times c} \quad \textbf{(Equation I-11)}$$

where P_{eq} is the pressure of the gas at equilibrium, P_{sat} is the saturation vapor pressure, N_{max} (molecules cm^{-2}) number of molecules needed to form a monolayer per unite surface area, c is the BET constant.

3.3.4 Influence of relative humidity on adsorption isotherms

Another key parameter regarding the heterogeneous behavior of gas phase molecules on a solid surface is relative humidity. Water vapor partitions onto/into particles in the atmosphere. The amount of water associated with particles, in equilibrium with water vapor in the gas phase, depends on RH, T, and the type of particles. The partitioning of water between the gas and particle phases is called "water adsorption" in surface science and "hygroscopicity" in aerosol science. Hygroscopicity is in fact a general term which describes the ability to absorb or release water and how a substance can uptake and hold water molecules from the atmospheric environment. In aerosol science, it usually refers to a change in particle diameter, volume, or mass when exposed to water vapor [52-54]. Therefore, the impact of moisture on the heterogeneous interaction of gases on solid surfaces is far from being negligible. Apart from theoretical considerations on adsorption processes, any experimental study related to the atmosphere has to take into account the influence of relative humidity on the process characteristics.

There are different ways of considering the impact of water vapor on gas adsorption on solid surface. In a first approach, the variation of the gas adsorption enthalpy ΔH with relative humidity can be explored [55]. However, water molecules can simply be considered as another gas-phase molecule interaction with the solid surface, competing with other gas-phase molecules.

In the context of the Langmuir model, Equation I-10 can be used to model the influence of water vapor and rewritten as Equation I-12.

$$N_S = N_{max} \frac{K \cdot C}{1 + K \cdot C + K_w \cdot C_w}$$ **(Equation I-12)**

In this Equation, K (molecules^{-1}) and K$_W$ (molecules^{-1}) correspond to adsorption constants of a typical gas molecule and water, respectively, and C (molecules cm^{-3}) and C$_W$ (molecules cm^{-3}) to their corresponding gas phase concentrations.

4   Laboratory techniques for studying heterogeneous processes

In the literature, various experimental setups have been used to study the heterogeneous interactions of gases with solids [48]. A list of experimental techniques is presented in Table I-5.

Table I-5. Techniques used to study heterogeneous processes. Adapted from [48].

Type of analysis	Reactor	Analytical techniques used for detection
Gas-phase analysis	Knudsen reactor (Kn) Static reactor (SR)	Quadruple Mass Spectrometry (QMS)
		Chemical Ionization Mass Spectrometry (CIMS)
	Coated-rod flow tube (CRFT) Coated-wall flow tube (CWFT)	Fourier Transform InfraRed spectroscopy (FTIR), QMS
		Gas Chromatography / Mass Spectrometry (GC-MS)
Adsorbed-phase analysis	Optical flow reactor	Diffused Reflectance Infrared Fourier Transform Spectroscopy (DRIFTS)
		Attenuated Total Reflection infrared spectroscopy (ATR)
		UltraViolet-Visible Spectroscopy (UV-Vis)
Recently developed methods	Aerosol flow tube (AFT)	Fourier Transform InfraRed spectroscopy (FTIR)
		Gas Chromatography – Mass Spectrometry (GC+MS)
		Scanning Mobility Particle Sizer (SMPS)
		Aerosol Particle Sizer (APS)
	Atmospheric simulation chamber (ASC)	Aerosol Mass Spectrometry (AMS)
		Scanning Mobility Particle Sizer (SMPS)
		Differential Mobility Analyzer (DMA)
		Selected Ion Flow Tube Mass Spectrometry (SIFT-MS)

In general, they are classified according to two groups: (i) techniques that analyze the gas phase and ii) techniques that focus on monitoring the adsorbed phase. New methods that can be operated under simulated atmospheric conditions using real aerosol particles have been developed during the past 15 years, combined with state-of-the-art analytical equipment to monitor in real time a) the chemical composition of the gas and adsorbed phases, b) the evolution of the aerosol physical and chemical properties for instance using aerosol flow tube and atmospheric simulation chambers. These methods made it possible to study heterogeneous reactions under atmospherically-relevant conditions.

Nevertheless, a detailed description of all the techniques used to investigate heterogeneous phenomena is beyond the scope of this manuscript. Only the classically-used methods employed in the literature and which have provided the majority of the kinetic and mechanistic results are presented below.

4.1   Experimental techniques based on gas phase monitoring

4.1.1   Knudsen cells

Knudsen cells are used to study heterogeneous chemical reactions involved in atmospheric chemistry. Basically, a Knudsen cell is a low-pressure (pressures lower than 10 mTorr) flow reactor operated in the molecular flow regime and characterized by long mean free path. The advantage is that the effects of gas phase diffusion do not kinetically limit the gas uptake and therefore do not complicate the analysis of experimental data.

A Knudsen cell apparatus consists of 3 basic parts: a) the supply/storage line for the introduction of gas-phase species, b) the reactor itself and c) the detection technique, generally a direct quadrupole mass spectrometer. The schematic in Figure I-7 shows a typical version of a Knudsen cell. The surface of interest is placed on top of the sample holder. A movable lid is used to isolate the substrate from the main chamber.
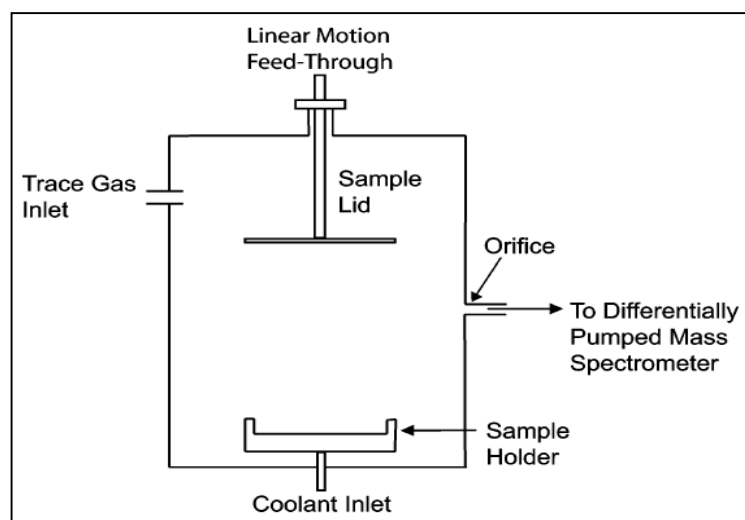
Figure I-7. Schematic of a Knudsen reactor. Adapted from [3].

The gas-phase species are introduced at the top of the reactor while they escape through an orifice of known dimension placed either at the bottom or on the side of the reactor. The residence time is controlled by the size of the orifice, the temperature and the molecular weight of the molecule, it is in the millisecond range (50-800 ms).

The Knudsen cell is an extremely useful tool that has been used extensively to investigate gas-solid interactions, providing accurate kinetic and mechanistic results. Nevertheless, one of its major limitations is its inability to mimic atmospheric conditions such as atmospheric pressure or realistic RH.

4.1.2   Low pressure coated wall/rod flow tube reactor (LP-CFTR)

Flow tubes were employed initially to obtain absolute rate coefficients for a variety of gas-phase reactions [56, 57]. Recently, the same approach has been applied to study reactions of gases with solid surfaces [48]. The schematic diagram of a flow tube reactor is shown in Figure I-8. The flow reactor itself consists of a cylindrical double-wall thermostated tube and a movable sliding injector. The thermostat helps performing experiments as a function of temperature. The wall of the flow tube is covered with the solid phase (e.g. mineral dust dust) under investigation and a movable injector supplies the gaseous reactant. At the downstream end, the reactor is connected to a gas analyzer for the detection of the gas-phase species. Initially, the injector is placed at the downstream end of the reactor to avoid premature exposure of the surface. Subsequently, the injector is moved back to expose the surface to the gas. As the gas interacts with the condensed phase the pseudo-first-order rate coefficient for the removal of the gas is measured from the change of gas concentration reaching the detector [58].
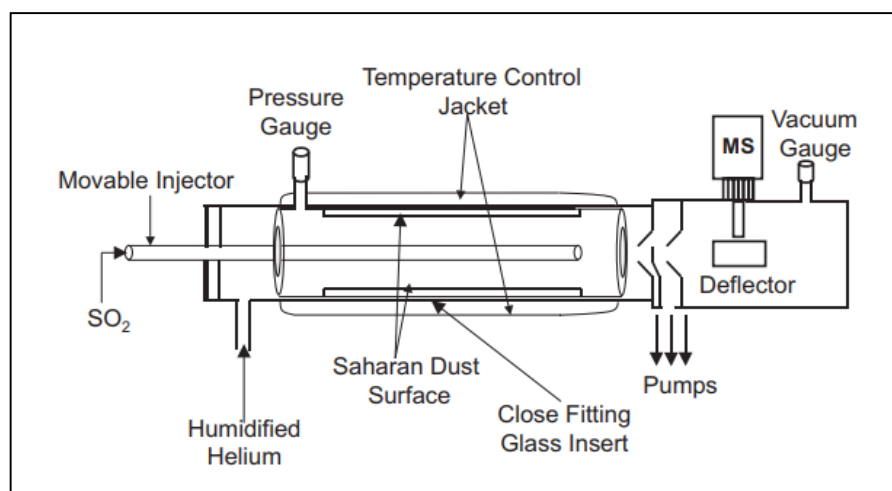
Figure I-8. Schematic of a low pressure flow tube reactor. Adapted from [58].

Due to the uptake or chemical reactions on the wall, concentration gradients can develop in the flow tube and radial diffusion can limit the observed gas uptake. Thus the evaluation of uptake coefficient is done under several assumptions, namely that the loss of the gas at the wall occurs through a first-order process and that the flow in the flow tube is a well-developed laminar flow. The second assumption implies that the flow velocity profile is parabolic and that the radial transport of the gas reactant is solely caused by molecular diffusion.

The gas diffusion limitation is the major disadvantage of the LP-CFTR technique. To overcome that issue, kinetic experiments are performed using helium as the carrier gas instead of synthetic air since diffusion corrections are lower [59]. As a consequence, the heterogeneous experiments are conducted in the absence of molecular oxygen that plays a key role in heterogeneous photochemistry. Besides diffusion phenomena, another important limitation is that it is difficult to reach realistic atmospheric RH conditions due to the low pressure range under which flow tubes are operated [3]. Nevertheless flow tubes are still a popular technique that can provide accurate kinetic and mechanistic data. With time, scientists have managed to overcome many of the limitations and develop improved versions of the LP-CFTR technique that can be operated under real atmospheric conditions studying real aerosols instead of bulk surfaces [60].

4.1.3 Aerosol Flow Tubes (AFT)

Since their introduction more than a decade ago, Aerosol Flow Tubes have been used widely to study the transformations and physical properties of aerosols under conditions typical of the troposphere and stratosphere. An aerosol, usually generated by atomization of liquid or by

homogeneous or heterogeneous condensation of vapor, is introduced to the AFT in a carrier gas flow. After conditioning at a certain temperature and relative humidity, the aerosol passes through a region where these conditions are changed to initiate the process of interest, such as deliquescence, efflorescence, or freezing. The aerosol then flows to the detection section.

4.2 Experimental techniques based on adsorbed phase monitoring

When a Knudsen cell or a flow tube is used, only the gas phase is monitored upstream and downstream the cell. Therefore, these techniques allow to measure only the uptake coefficient, γ, but cannot provide direct mechanistic information about the surface species involved (adsorption, reactivity, etc.). Thus, methods have been developed to study the adsorbed-phase composition while a trace gas is taken up by a solid substrate.

The adsorbed phase is mostly probed using *in-situ* spectroscopic techniques, notably infrared spectroscopy [61, 62]. An example of these techniques are DRIFTs, Transmission FTIR, and ATR. IR spectroscopy probes the molecular vibrations; thus it is well suited to study molecules and molecular ions, but single atoms or single atomic ions cannot be studied. *In-situ* spectroscopic techniques allow one to obtain mechanistic information on processes taking place in the first few monolayers below the surface (i.e., to a depth penetrated by the IR light). These spectroscopic techniques provide important information about the nature of the interaction process, such as the formation of hydrates or the state of dissociation, but not necessarily on the amount of uptake. *In-situ* spectroscopic techniques have proven to be very useful for studying the kinetics and interaction mechanism of aerosols in the atmosphere [63, 64]. Moreover, these techniques helped complementing proposed mechanisms. For example, Sivachandiran et al. investigated the adsorption of NO and NO_2 on TiO_2 monitoring the gas phase using FTIR [65], which allowed to propose a reaction mechanism later confirmed by investigating the same heterogeneous process using *in-situ* transmission infrared spectroscopy [66].

5 Interaction of mineral dust with atmospheric trace gases

After defining the different terms and the kinetic parameters needed to understand heterogeneous processes between gases and solid surfaces this section focuses on the interaction of mineral dust with trace atmospheric species. It attempts to cover the literature data on mineral

dust heterogeneous interactions in the troposphere. These interactions involve trace atmospheric compounds both inorganic and organic with most of the minerals.

Investigations of trace gas uptake on mineral surfaces include natural dust samples from e.g. Saharan or Asian source regions, surrogate materials such as $CaCO_3$, Al_2O_3, Fe_2O_3, MgO, and clay minerals such as kaolinite, illite etc., which are components of atmospheric dust. Mineral oxides are often used as bulk samples in laboratory experiments, which requires a careful analysis to take into account interstitial surface areas. Synthetic minerals do not necessarily mimic the interaction of natural dust. However, researchers generally assume that the bulk composition of the natural sample is the same as the surface composition to derive atmospheric implications. This is an assumption that is not yet validated.

The comparison of results from different studies is often difficult due to the use of different substrates (natural dust, or mineral phases of dust), different modes of sample presentation, and different models for surface area calculation. For example, uptakes are usually obtained from the observed loss rates of gas-phase species and calculated collision rates with the surface. For the latter the surface area available for uptake calculation is required. For solid surfaces such as dust there is a non-zero probability that the striking trace gas collides with the internal surface within the time scale of determination of the uptake coefficient. This issue may apply for aerosol particles as well. The geometric surface area represents a lower limit to the surface area, and therefore an upper limit to the uptake is obtained. The other extreme is the use of the specific surface area (e.g. the N_2-BET surface area), which is the maximum available surface area, including internal pore volume and bulk surface area of the solid material [48].

5.1   Interaction of inorganic species with mineral dust

In 2010 the IUPAC community evaluated the available literature data concerning the heterogeneous processes of mineral dust or individual mineral surfaces [48] with inorganic gases (O_3, H_2O_2, NO_2, HNO_3, N_2O_5, SO_2) and radicals ($HONO^•$, $NO_3^•$, $OH^•$, $HO_2^•$). In this evaluation the IUPAC panel chose a preferred value for each uptake of trace atmospheric species on the specified dust type. The uptake value preferred, the experimental conditions, and the methods used to determine these uptakes are summarized in Table I-6. Unless otherwise stated, all the preferred values of the IUPAC evaluation are steady-state uptakes.

As shown in Table I-6, the uptake coefficients of inorganic and radical species varies over seven orders of magnitude within the range 10^{-1} to 10^{-8}. This large variability can be explained by

the role of internal surfaces in bulk, different powder substrates, different methods, and different ways of analyzing the results i.e. the use of geometric or BET specific surface area [48].

The highest uptakes are those of radical species. For instance, γ_0 of OH at 50% RH is around 0.04. This radical is known to have a short atmospheric lifetime determined by its loss processes in the gas phase. Therefore, it is clear that even a very efficient heterogeneous loss of OH on atmospheric aerosol (up to the maximum uptake probability of unity) will be negligible compared to the gas-phase loss and will not impact the OH concentration in the atmosphere. However, heterogeneous reactions of OH are recognized to be important in the processing of atmospheric aerosol leading to modifications of its chemical composition as well as of its physical properties.

Moreover the effect of relative humidity is variable from one species to another. For instance, in the case of H_2O_2, RH enhances the interaction with dust contrary to what is observed in the case of HNO_3. Therefore it is difficult to predict a specific behavior of a species interaction towards mineral dust. The best way to evaluate the significance of a heterogeneous process is to implement the results in a chemical model.

In 1996 Dentener et al. published an article on modeling heterogeneous processes in the atmosphere [47]. Although many uncertainties were associated with the model itself due to the lack of supportive laboratory and field measurements, it predicted that mineral dust could greatly affect the nitrogen, sulfur, and photochemical oxidant cycles. Since then, laboratory and field measurements carried out in this direction have tried to develop a better understanding of the effect of heterogeneous processes in the atmosphere

Jacob et al. found that the uptake of nitrogen and hydrogen oxides is one of the most important heterogeneous reactions in the atmosphere because it affects O_3 concentrations [67, 68]. Indeed, a net impact of heterogeneous reactions on aerosols is a reduction in tropospheric ozone and related oxidants from 7% to 13.5%, resulting in a 20% to 45% reduction in ozone radiative forcing [38, 68].

Field campaigns reported a significant correlation between high dust loads and low mixing ratios for O_3 and HNO_3 [69, 70]. Besides, it has been established that dust-poor air masses originating from North Africa are characterized by significantly higher ozone concentrations than dust-rich ones [71]. Several modeling studies have investigated the potential effect of dust on O_3, inorganic nitrogen-containing species, and HO_x (OH and HO_2) [72, 73]. Bain et al. investigated the effect of reduced photolysis rates and heterogeneous chemistry on the tropospheric trace gas

mixing ratios [74]. They concluded that both processes cause a combined decrease in global mean concentrations of O_3, OH, HO_2 and HNO_3 of 0.7, 11.1, 5.2 and 3.5 %, respectively. Moreover, they evidenced that the effects of heterogeneous reactions clearly dominated over the reduced photolysis rates.

Considering the relatively well-documented impact of dust storms on the atmospheric chemistry of ozone and other inorganic trace gases [72-74], a similar effort should be undertaken to assess the impact of some organic trace gases on the global atmospheric budgets, as well as the potential changes in the oxidative capacity of the troposphere.

Table I-6. Methods and uptake values for the interaction of inorganic species and radicals on mineral dust and inorganic constituents ([48], [75-79])

Inorganic compound	Adsorbents	Temperature range (K)	IUPAC preferred uptake coefficients	Techniques used
O_3	SiO_2, α-Al_2O_3, α-Fe_2O_3, Fe_3O_4, CeO_2, PbO, TiO_2, MgO, CaO, $CaCO_3$, MgO, ZnO, ZrO_2, China loess, Saharan dust, kaolinite	Room temp.	$\gamma_{ss} = 1500 \, [O_3] \, (cm^{-3})^{-0.7}$	Knudsen cell FTIR aerosol chamber static reactor
H_2O_2	TiO_2, Gobi sand, Saharan dust	298	$\gamma_{ss} = 6.24 \times 10^{-4} - 1.87 \times 10^{-6} \, (RH) + 9.37 \times 10^{-8} \, (RH)^2$	AFT-CIMS
NO_2	SiO_2, γ-Al_2O_3, α-Al_2O_3, γ-Fe_2O_3, α-Fe_2O_3, TiO_2, MgO, CaO, $CaCO_3$, Saharan dust, kaolinite, China loess, pyrophyllite, Arizona test dust	Room temp.	For γ-Al_2O_3 and pyrophyllite: the uptake is in the order of 10^{-8} For reactive basic oxides: uptake can get up to 10^{-5} For clay minerals and Saharan dust: uptake can get up to 10^{-6}	Knudsen cell DRIFTS AFT-CLD CWFT-CLD/LOPAP
NO_3	$CaCO_3$, α-Al_2O_3, Saharan dust, kaolinite, pyrophyllite, Arizona test dust	298	$\gamma_{ss} = 1.2 \times 10^{-2}$	Knudsen cell Relative rate – CRDS
HNO_3	SiO_2, γ-Al_2O_3, α-Al_2O_3, α-Fe_2O_3, $CaCO_3$, Saharan dust, kaolinite, pyrophyllite, Arizona test dust, Chinese dust, Gobi dust, polished marble, cut marble	298	$\dfrac{1}{\gamma} = \dfrac{1}{\alpha_s} + \dfrac{1}{\Gamma_s} \qquad \dfrac{1}{\Gamma_s} = \dfrac{k_s [Y]_s \, \alpha_s \, \tau_{des}}{1 + [X]_g \, K_{lang}}$ $\alpha_s = 1 \qquad K_{lang} = 2.25 \times 10^{-15} \, cm^3/molecule$ $\tau_{des} = 0.1 \, s$ $[Y]_s = 6.5 \times 10^{13} + 4.1 \times 10^{10}(RH) + 4.0 \times 10^{11} \, (RH)^2$ in molecule/cm^2 at 298 K	Knudsen cell DRIFTS FTIR AFT
N_2O_5	$CaCO_3$, Saharan dust, Arizona test, quartz	298	For Saharan dust: $\gamma_{ss} = 1.3 \times 10^{-2}$	Knudsen cell AFT FTIR

SO$_2$	SiO$_2$, Al$_2$O$_3$, α-Al$_2$O$_3$, Fe$_2$O$_3$, CaCO$_3$, TiO$_2$, MgO Saharan dust, Chinese dust, Gobi dust, adobe clay	298	For mineral oxides: γ_0 close to 10^{-4} - 10^{-5} except for CaCO$_3$: $\gamma = 0.1$ For Saharan and Chinese dust: $\gamma_{ss} = 4 \times 10^{-5}$	Knudsen cell DRIFTS FTIR CWFT-MS
HONO	Al$_2$O$_3$ [75]	275-320	For Al$_2$O$_3$ under dark conditions: $\gamma_0 = 4.8 \times 10^{-6}$ (RH)$^{-0.61}$ For Al$_2$O$_3$ on irradiated surfaces: $\gamma_0 = 1.7 \times 10^{-5}$ (RH)$^{-0.44}$	LPFR-MBMS
	TiO$_2$ [76]	275-320	For TiO$_2$ under dark conditions: $\gamma_0 = 1.8 \times 10^{-5}$ (RH)$^{0.63}$	
OH	Arizona test dust [77]	275-320	$\gamma_0 = 0.18 / (1 + RH^{0.36})$	LPFR-MBMS
HO$_2$	Arizona test dust [78]	275-320	$\gamma_0 = 1.2 / (18.7 + RH^{1.1})$	LPFR-MBMS
	Arizona test dust [79]	Room temp.	$\gamma_0 = 0.031 \pm 0.008$ and 0.018 ± 0.006 for the lower and higher HO$_2$ concentrations, respectively	AFT-FAGE

AFT Aerosol Flow Tube, **CIMS** Chemical Ionization Mass Spectrometry, **CLD** Chemi-Luminescence Detector, **CRDS** Cavity Ring Down Spectroscopy, **CWFT** Coated Wall Flow Tube, **DRIFTs** Diffuse Reflectance Infrared Fourier Transform Spectroscopy, **FAGE** Fluorescence Assay by Gas Expansion technique, **FTIR** Fourier Transform InfraRed spectroscopy, **LOPAP** Long Path Absorption Photometer, **LPFR** Low Pressure Flow tube Reactor, **LPLPA** Long Path Liquid Phase Adsorption, **MBMS** Molecular Beam sampling Mass Spectrometry, [Ys] average surface concentration of HNO$_3$ as a function of RH

5.2 Interaction of VOCs with mineral dust

There is a lack of studies dealing with the interaction between organic species and mineral dust samples. As a matter of fact, the IUPAC community did not evaluate the heterogeneous processes of organic species on solid substrates because few studies exist [48]. But what about the impact of the heterogeneous interaction of VOC with mineral dust samples?

Table I-7 summarizes the current literature about the interaction of VOCs with mineral phases. Similar to the inorganic species, the experimental kinetic investigation of a given VOC uptake to the same substrate (ex. acetone on SiO_2) shows a great variability in the values of uptake coefficient that have been obtained, in particular due to the use of the geometric surface area for some calculations and the BET surface area for others. Although the authors tried to mimic the atmospheric conditions (temperature, relative humidity, etc.), the results are nevertheless not directly applicable to the real atmosphere because no natural dust samples were studied. Although mineral oxides are the basic components of dust, the effect of mixing the different components should probably be viewed as synergetic rather than additive. This latter effect has already been stressed out in the literature by El Zein et al. [80]. Therefore, there is a critical need to examine the interaction between VOCs and natural atmospheric samples and assess their potential impact on atmospheric chemistry.

Moreover, the current models used in atmospheric chemistry underestimate the concentrations of oxygenated volatile organic compounds (OVOCs) when compared to field observations [81]. For example, recent field observations of light OVOCs at remote locations have shown discrepancies with model calculations; concentrations of acetaldehyde and propanal measured over the Pacific Ocean troposphere were up to ten times higher than modeled concentrations [82-84]. Similarly, measurements in marine air over the Indian Ocean [85] and in the Northern Atlantic [86] also suggested higher-than-expected concentrations of light OVOCs. Modelers have thus suggested that other processes acting as sources of oxygenated compounds, and not yet taken into account in reaction schemes, may exist. Indeed, large uncertainties are associated to the uptake and ageing of VOCs on mineral dust due to a lack of understanding of these processes. The assumption that heterogeneous processes on dust can complement the missing sinks of VOCs and the missing sources of oxygenated VOCs in the atmosphere should therefore not be ruled out. It is critical to evaluate the possibility of such reactions to occur under atmospheric conditions, and form OVOCs.

Table I-7. Summary of laboratory studies on heterogeneous interactions or reactions between VOCs and mineral dust. Adapted from [17].

VOCs	Solids	Temperature range (K)	Relative humidity	Products	Initial uptake coefficients	Type of surface area used for uptake calculation	Technique
Formaldehyde	SiO_2, α-Al_2O_3, α-Fe_2O_3	Room temp.	~ 0%	Formate, methoxide (on α-Al_2O_3 and α-Fe_2O_3)	$\gamma\ SiO_2 = (2.6 \pm 0.9) \times 10^{-7}$ $\gamma\ Al_2O_3 = (7.7 \pm 0.3) \times 10^{-5}$ $\gamma\ Fe_2O_3 = (1.1 \pm 0.5) \times 10^{-4}$	BET specific surface area	Knudsen cell FTIR
	α-Al_2O_3	273-333	~ 0%	Formate, dioxymethylene, polyoxymethylene	$\gamma = (9.4 \pm 1.7) \times 10^{-9}$ at 293 K	Geometric surface area	DRIFTS
	TiO_2	163-673	~ 0%	Formate, dioxymethylene, polyoxymethylene,	$\gamma = (0.5\text{-}5) \times 10^{-8}$ at 293-295 K	BET specific surface area	DRIFTS, IC, TEM XRD
MAC, MVK	SiO_2	293-295	0 - 80%	For MAC or MVK-SiO_2-O_3: formaldehyde, propionaldehyde, MG, FA, AA, PYA, H_2O_2, HMHP, 1-HEHP, MHP, PAA only for MAC-SiO_2-O_3: PA only for MVK-SiO_2-O_3: GL	For MAC-SiO_2-O_3 γ (~0% RH) = $(2.2 \pm 0.2) \times 10^{-9}$ γ (~20% RH) = $(1.4 \pm 0.2) \times 10^{-9}$ γ (~40% RH) = $(8.2 \pm 0.7) \times 10^{-10}$ γ (~60% RH) = $(3.7 \pm 0.7) \times 10^{-10}$ γ (~80% RH) = $(3.5 \pm 0.3) \times 10^{-10}$ For MVK-SiO_2-O_3 γ (~0% RH) = $(1.1 \pm 0.2) \times 10^{-9}$ γ (~20% RH) = $(5.8 \pm 0.4) \times 10^{-9}$ γ (~40% RH) = $(4.2 \pm 0.3) \times 10^{-10}$ γ (~60% RH) = $(2.8 \pm 0.4) \times 10^{-10}$ γ (~80% RH) = $(2.7 \pm 0.2) \times 10^{-10}$	BET specific surface area	APFT, T-FTIR, HPLC, IC
	α-Al_2O_3	Room temp.	0 - 60% RH	For MAC: formaldehyde, propionaldehyde, FA, AA, PA, HMCs For MVK: crotonaldehyde, acetaldehyde, GL, AA, OA, H_2O_2, HMCs	for MAC γ (~0% RH) = $(2.0 \pm 0.5) \times 10^{-8}$ for MVK γ (~0% RH) = $(3.8 \pm 0.8) \times 10^{-8}$	BET specific surface area	APFT, T-FTIR, HPLC, IC, LC-MS

Acetone	SiO_2	Room temp.	0 - 80% RH	No species detected	γ (~0% RH) = $(2.4 \pm 0.3) \times 10^{-9}$ γ (~20% RH) = $(1.5 \pm 0.2) \times 10^{-9}$ γ (~40% RH) = $(1.3 \pm 0.3) \times 10^{-10}$ γ (~60% RH) = $(9.0 \pm 0.4) \times 10^{-10}$ γ (~80% RH) = $(8.6 \pm 0.2) \times 10^{-10}$	BET specific surface area	APFT, T-FTIR, HPLC,
Acetaldehyde, Acetone, Propionaldehyde	SiO_2, α-Al_2O_3, α-Fe_2O_3, TiO_2, CaO	Room temp.	~0% RH	Long chain unsaturated carbonyls on α-Al_2O_3, α- Fe_2O_3, TiO_2 ,CaO	For Acetaldehyde γ SiO_2 = 7.0×10^{-6} γ α-Al_2O_3 = 3.2×10^{-5} γ α-Fe_2O_3 = 2.9×10^{-6} γ TiO_2 = 9.4×10^{-5} γ CaO = 3.0×10^{-4} For Acetone γ SiO_2 = 6.2×10^{-6} γ α-Al_2O_3 = 2.0×10^{-5} γ α-Fe_2O_3 = 1.6×10^{-4} γ TiO_2 = 3.6×10^{-4} γ CaO = 1.2×10^{-4} For Propionaldehyde γ SiO_2 = 1.1×10^{-5} γ α-Al_2O_3 = 4.7×10^{-5} γ α-Fe_2O_3 = 5.1×10^{-5} γ TiO_2 = 1.5×10^{-4} γ CaO = 5.9×10^{-4}	BET specific surface area	Knudsen cell, T-FTIR, UV-vis
Acetic acid	SiO_2, α-Al_2O_3, α-Fe_2O_3	Room temp.	~ 0% RH	Acetate on α-Al_2O_3 and α- Fe_2O_3	γ SiO_2 = $(2.4 \pm 0.4) \times 10^{-4}$ γ α-Al_2O_3 = $(2 \pm 1) \times 10^{-3}$ γ α-Fe_2O_3 = $(1.9 \pm 0.3) \times 10^{-3}$	BET specific surface area	Knudsen cell, T-FTIR
Formic, Acetic, Propanoic acids	α-Al_2O_3	300K	0 - 95% RH	Carboxylate, H_2O	For Formic acid ~0% RH γ α-Al_2O_3 = $(2.4 \pm 0.3) \times 10^{-7}$ For Acetic acid ~0% RH γ α-Al_2O_3 = $(6.0 \pm 0.8) \times 10^{-7}$ For Propanoic acid ~0% RH γ α-Al_2O_3 = $(3.0 \pm 0.5) \times 10^{-7}$	BET specific surface area	DRIFTS
Formic acid	$CaCO_3$	Room temp.	0 - 94% RH	Calcium formate, carbonic acid	For Formic acid ~0% RH γ = $(3.0 \pm 1.0) \times 10^{-3}$	BET specific surface area	Knudsen cell, T-FTIR, ATR-FTIR, SEM

Acetic acid	$CaCO_3$	Room temp.	0 - 53% RH	For Acetic-$CaCO_3$: Acetate, CO_2, H_2O For Acetic-HNO_3-$CaCO_3$ CO_2, H_2O, nitrate	At ~0% RH $\gamma = 5 \times 10^{-6}$	BET specific surface area	Knudsen cell, T-FTIR, ATR-FTIR, SEM
Formic, Acetic, Propanoic, Butanoic acids	Swelling clay	212 K	0 - 45% RH	Carboxylate	For Formic acid $\gamma = (1.7 \times 10^{-5}) - (2.3 \times 10^{-5})$ For Acetic acid $\gamma = (1.3 \times 10^{-5}) - (6 \times 10^{-5})$ For Propanoic acid $\gamma = (5.4 \times 10^{-5}) - (6.2 \times 10^{-5})$ For Butanoic acid $\gamma = (2.2 \times 10^{-5}) - (2.2 \times 10^{-4})$	BET specific surface area	Knudsen cell, T-FTIR, ATR-FTIR, SEM
Oxalic acid	α-Fe_2O_3, TiO_2	Room temp.	~0% RH	CO_2	Not calculated		Knudsen cell, IC
Methanol	SiO_2, α-Al_2O_3, α-Fe_2O_3	Room temp.	~0% RH	Formate, methoxide on α-Al_2O_3, α-Fe_2O_3,	$\gamma\ SiO_2 = (4 \pm 2) \times 10^{-6}$ $\gamma\ \alpha$-$Al_2O_3 = (1 \pm 0.7) \times 10^{-4}$ $\gamma\ \alpha$-$Fe_2O_3 = (1.9 \pm 0.4) \times 10^{-4}$	Geometric surface area	Knudsen cell, T-FTIR
Ethylene glycol	SiO_2, α-Al_2O_3	Room temp.	~50% RH	No species detected	Not calculated		SFG
Isopropanol n-propanol	TiO_2, TiO_2/KNO_3	Room temp.	~0% RH	For isopropanol: acetone For n-propanol: PIA	For isopropanol dark $\gamma\ TiO_2 = 0.04$-0.12	BET specific surface area	Knudsen cell, SFG

Molecules / AA: acetic acid, **DEA:** diethylamine, **EA:** ethylamine, **FA:** formic acid, **GL:** glyoxal, **1-HEHP:** 1-hydroxyl ethyl hydroperoxide, **HMCs:** high molecular weight compounds, **HMHP:** hydroxymethylhydroperoxide, **MAC:** methacrolein, **MG:** methylglyoxal, **MHP:** methylhydroperoxide, **MVK:** methylvinylketone, **OA:** oxalic acid, **PAA:** peroxyacetic acid, **PA:** propanoic acid, **PYA:** pyruvic acid, **TEA:** triethylamine
Room temp: 293-298 K
Techniques / AMS Aerosol Mass Spectrometry, **APFT** Ambient Pressure Flow Tube, **ATR-FTIR** Attenuated Total Reflectance Fourier Transform Infrared spectroscopy, **CWFT** Coated Wall Flow Tube, **DRIFTs** Diffuse Reflectance Infrared Fourier Transform Spectroscopy, **FAGE** Fluorescence Assay by Gas Expansion technique, **HPLC** High Performance Liquid Chromatography, **IC** Ion Chromatography, **LPFR** Low Pressure Flow tube Reactor, **SFG** Sum Frequency Generation, **SEM** Scanning Electron Microscopy, **TEM** Transmission Electron Microscopy, **T-FTIR** Transmission Fourier Transform Infrared spectroscopy, **UV-vis** Ultraviolet-visible spectroscopy, **XRD** X-ray Diffraction.

6 Objectives of this thesis and structure of the manuscript

This chapter has demonstrated that information on VOC uptakes on natural atmospheric samples is limited especially when compared with that of inorganic atmospheric species. In 2016, experiments regarding the uptake of VOCs toward natural dust samples were started in our laboratory, with the interaction of limonene and toluene with natural Saharan mineral dust samples being investigated for the first time [87]. However, more detailed information regarding uptakes, products and possible mechanisms of VOC degradation on natural dust surfaces was not addressed at that time.

The main objective of the present study focuses on **investigating the interaction/reaction of VOCs with natural dust samples in order to evaluate its significance on the global atmospheric composition.** To achieve this objective, several sub-objectives have been defined:

> ➤ *Investigating the impact of dust origin and composition on VOC interaction with natural dust samples;*
> ➤ *Investigating the impact of atmospheric environmental conditions on this interaction;*
> ➤ *Investigating the reactivity of such interaction under dark and UV simulated conditions.*

A wide variety of materials and methods have been involved in the investigation of VOCs interaction on dust. The characterization and the origin of the natural dust samples used are detailed in the upcoming chapter 2, followed by the materials to prepare the VOC gas mixture. Then a detailed part is dedicated to the methods and experimental devices employed for studying different aspects of the interaction of VOCs on natural dust samples.

Chapters 3 to 6 describe and discuss the experimental results obtained during this thesis. In chapter 3, the impact of dust origin and chemical composition on the heterogeneous process, is investigated. In particular, experiments are performed to investigate the uptake and the adsorption efficiency of isopropanol (IPA), a common organic pollutant released in significant amounts in the atmosphere and used here as a probe molecule, on natural dust samples collected from North and West Africa, Saudi Arabia, and Arizona desert regions. In chapter 4, the interaction of IPA with a natural sample from the Gobi desert that showed the highest uptake is

studied under different relevant atmospheric conditions (temperature, RH, and simulated sunlight). In chapter 5, isoprene (ISP), the highest emitted biogenic VOC in the atmosphere is selected to evaluate its interaction with natural dust from the Gobi desert. In chapter 6, for reasons stated later, the interaction of acetic acid (AcA) with natural dust from the Gobi desert is assessed under atmospheric simulated conditions.

The outcome of this research and future directions are provided in the general conclusion at the end of this manuscript. The results presented herein provide insight into the impact of VOC interaction on natural dust and its effects on atmospheric trace gas concentrations.

7 References of chapter I

1. Barker, J. R., *Progress And Problems In Atmospheric Chemistry* Advanced Series in Physical Chemistry ed. Barker, J. R. Vol. 3. 1995: world scientific

2. Seinfeld, J. H., S.N. Pandis, *Atmospheric Chemistry and Physics*. Atmospheric Stability, Turbulence. 1998: Wiley, New York, .

3. Finlayson-Pitts, B. J.; pitts, J. N., *Chemistry of the Upper And Lower Atmosphere*. 2011: Acadamic Press

4. Ruzmaikin, A.; Aumann, H. H.; Manning, E. M., *Relative Humidity in the Troposphere with AIRS*. Journal of the Atmospheric Sciences, 2014. **71**(7): p. 2516-2533.

5. Koppmann, R., *Volatile Organic Compounds In The Atmosphere*. 2008: John Wiley & Sons.

6. The Official Journal of the European Union, 1999. **L 85**.

7. EPA, U. S., *Technical Overview of Volatile Organic Compounds*. 2004.

8. Huang, G.; Brook, R.; Crippa, M.; Janssens-Maenhout, G.; Schieberle, C.; Dore, C.; Guizzardi, D.; Muntean, M.; Schaaf, E.; Friedrich, R., *Speciation of Anthropogenic Emissions of Non-methane Volatile Organic Compounds: A Global Gridded Data Set for 1970–2012*. Atmospheric Chemistry and Physics, 2017. **17**(12): p. 7683-7701.

9. Beyersdorf, A. J.; Blake, D. R.; Swanson, A.; Meinardi, S.; Rowland, F. S.; Davis, D., *Abundances and Variability of Tropospheric Volatile Organic Compounds at the South Pole and other Antarctic locations*. Atmospheric Environment, 2010. **44**(36): p. 4565-4574.

10. Swanson, A. L.; Davis, D. D.; Arimoto, R.; Roberts, P.; Atlas, E. L.; Flocke, F.; Meinardi, S.; Sherwood Rowland, F.; Blake, D. R., *Organic Trace Gases of Oceanic Origin Observed at South Pole During ISCAT 2000*. Atmospheric Environment, 2004. **38**(32): p. 5463-5472.

11. Aghedo, A. M.; Schultz, M. G.; Rast, S., *The Influence of African Air Pollution on Regional and Global Tropospheric Ozone*. Atmospheric Chemistry and Physics, 2007. **7**(5): p. 1193-1212.

12. Atkinson, R.; Arey, J., *Atmospheric Chemistry of Biogenic Organic Compounds*. Accounts of Chemical Research, 1998. **31**(9): p. 574-583.

13. Guenther, A.; Karl, T.; Harley, P.; Wiedinmyer, C.; Palmer, P. I.; Geron, C., *Estimates of Global Terrestrial Isoprene Emissions Using MEGAN (Model of Emissions of Gases and Aerosols from Nature)*. Atmospheric Chemistry and Physics, 2006. **6**(11): p. 3181-3210.

14. Chameides, W.; Lindsay, R.; Richardson, J.; Kiang, C., *The Role of Biogenic Hydrocarbons in Urban Photochemical Smog: Atlanta as a Case Study*. Science, 1988. **241**(4872): p. 1473-1475.

15. Wiedinmyer, C.; Guenther, A.; Harley, P.; Hewitt, N.; Geron, C.; Artaxo, P.; Steinbrecher, R.; Rasmussen, R., *Global Organic Emissions from Vegetation*. Emissions of Atmospheric Trace Compounds, ed. Granier, C.; Artaxo, P.; Reeves, C. E. 2004, Dordrecht: Springer Netherlands. 115-170.

16. Atkinson, R.; Arey, J., *Atmospheric Degradation of Volatile Organic Compounds*. Chemical Reviews, 2003. **103**(12): p. 4605-4638.

17. Shen, X.; Zhao, Y.; Chen, Z.; Huang, D., *Heterogeneous Reactions of Volatile Organic Compounds in the Atmosphere*. Atmospheric Environment. **68**(0): p. 297-314.

18. Volkamer, R.; San Martini, F.; Molina, L. T.; Salcedo, D.; Jimenez, J. L.; Molina, M. J., *A Missing Sink for Gas-phase Glyoxal in Mexico City: Formation of Secondary Organic Aerosol*. Geophysical Research Letters, 2007. **34**(19): p. n/a-n/a.

19. Boucher, O., *Atmospheric Aerosols*. 2015, Netherlands: Springer Netherlands. XVII, 311.

20. Hobbs, J. M. W. P. V., *Atmospheric Sciences An Introductory Survey*. 2nd ed. 2006: Elsevier Inc.

21. Usher, C. R.; Michel, A. E.; Grassian, V. H., *Reactions on Mineral Dust.* Chemical Reviews, 2003. **103**(12): p. 4883-4940.

22. Satheesh, S. K.; Krishna Moorthy, K., *Radiative Effects of Natural Aerosols: A Review.* Atmospheric Environment, 2005. **39**(11): p. 2089-2110.

23. Glaccum, R. A.; Prospero, J. M., *Saharan Aerosols Over the Ttropical North Atlantic — Mineralogy.* Marine Geology, 1980. **37**(3): p. 295-321.

24. Klaver, A.; Formenti, P.; Caquineau, S.; Chevaillier, S.; Ausset, P.; Calzolai, G.; Osborne, S.; Johnson, B.; Harrison, M.; Dubovik, O., *Physico-chemical and optical properties of Sahelian and Saharan mineral dust: in situ measurements during the GERBILS campaign.* Quarterly Journal of the Royal Meteorological Society, 2011. **137**(658): p. 1193-1210.

25. Su, L.; Toon, O. B., *Saharan and Asian Dust: Similarities and Differences Determined by CALIPSO, AERONET, and a Coupled Climate-Aerosol Microphysical Model.* Atmos. Chem. Phys., 2011. **11**(7): p. 3263-3280.

26. Radhi, M.; Box, M. A.; Box, G. P.; Mitchell, R. M.; Cohen, D. D.; Stelcer, E.; Keywood, M. D., *Optical, Physical and Chemical Characteristics of Australian Continental Aerosols: Results from a Field Experiment.* Atmospheric Chemistry and Physics, 2010. **10**(13): p. 5925-5942.

27. Qian Ning, W. Z., Ni sha yun, *The Dynamics of the Sands*. 1983: Beijing: Science Press.

28. Iwasaka, Y.; Minoura, H.; Nagaya, K., *The Transport and Spacial Scale of Asian Dust-storm Clouds: A Case Study of the Dust-storm Event of April 1979.* Tellus B, 1983. **35B**(3): p. 189-196.

29. Mattsson, J. O.; Nihlén, T., *The transport of Saharan dust to southern Europe: a scenario.* Journal of Arid Environments, 1996. **32**(2): p. 111-119.

30. Alastuey, A.; Querol, X.; Aas, W.; Lucarelli, F.; Pérez, N.; Moreno, T.; Cavalli, F.; Areskoug, H.; Balan, V.; Catrambone, M.; Ceburnis, D.; Cerro, J. C.; Conil, S.; Gevorgyan, L.; Hueglin, C.; Imre, K.; Jaffrezo, J. L.; Leeson, S. R.; Mihalopoulos, N.; Mitosinkova, M.; O'Dowd, C. D.; Pey, J.; Putaud, J. P.; Riffault, V.; Ripoll, A.; Sciare, J.; Sellegri, K.; Spindler, G.; Yttri, K. E., *Geochemistry of PM10 over Europe During the EMEP Intensive Measurement Periods in Summer 2012 and Winter 2013.* Atmospheric Chemistry and Physics, 2016. **16**(10): p. 6107-6129.

31. Prospero, J. M.; Lamb, P. J., *African Droughts and Dust Transport to the Caribbean: Climate Change Implications.* Science, 2003. **302**(5647): p. 1024-1027.

32. NASA, *Gaddard Spaceflight Center: http://visibleearth.nasa.gov*. . 2003.

33. Nations, U., *Global Alarm: Dust and Sandstorms from the World's Drylands*. 2001.

34. Tegen, I.; Fung, I., *Modeling of Mineral Dust in the Atmosphere: Sources, Transport, and Optical Thickness.* Journal of Geophysical Research: Atmospheres, 1994. **99**(D11): p. 22897-22914.

35. Liu, S. C.; Trainer, M.; Carroll, M. A.; Hübler, G.; Montzka, D. D.; Norton, R. B.; Ridley, B. A.; Walega, J. G.; Atlas, E. L.; Heikes, B. G.; Huebert, B. J.; Warren, W., *A Study of the Photochemistry and Ozone Budget During the Mauna Loa Observatory Photochemistry Experiment.* Journal of Geophysical Research: Atmospheres, 1992. **97**(D10): p. 10463-10471.

36. Singh, H. B.; Herlth, D.; Kolyer, R.; Salas, L.; Bradshaw, J. D.; Sandholm, S. T.; Davis, D. D.; Crawford, J.; Kondo, Y.; Koike, M.; Talbot, R.; Gregory, G. L.; Sachse, G. W.; Browell, E.; Blake, D. R.; Rowland, F. S.; Newell, R.; Merrill, J.; Heikes, B.; Liu, S.

C.; Crutzen, P. J.; Kanakidou, M., *Reactive Nitrogen and Ozone Over the Western Pacific: Distribution, Partitioning, and Sources.* Journal of Geophysical Research: Atmospheres, 1996. **101**(D1): p. 1793-1808.

37. IPCC, *Climate change 2001: The Scientific Basis. Contribution of Working Group I to the Third Assessment Report of the Intergovernmental Panel on Climate Change.* 2001: Cambridge, U.K.

38. Mahowald, N.; Ward, D. S.; Kloster, S.; Flanner, M. G.; Heald, C. L.; Heavens, N. G.; Hess, P. G.; Lamarque, J.-F.; Chuang, P. Y., *Aerosol Impacts on Climate and Biogeochemistry.* Annual Review of Environment and Resources, 2011. **36**(1): p. 45-74.

39. Kurtz, A. C.; Derry, L. A.; Chadwick, O. A., *Accretion of Asian Dust to Hawaiian Soils: Isotopic, Elemental, and Mineral Mass Balances.* Geochimica et Cosmochimica Acta, 2001. **65**(12): p. 1971-1983.

40. Ilan, K.; Yoram, J. K.; Richard, W.; Martin, C. T.; Yinon, R.; Martins, J. V.; Daniel, R., *The Bodélé Depression: A Single Spot in the Sahara that Provides Most of the Mineral Dust to the Amazon Forest.* Environmental Research Letters, 2006. **1**(1): p. 014005.

41. Jickells, T. D.; An, Z. S.; Andersen, K. K.; Baker, A. R.; Bergametti, G.; Brooks, N.; Cao, J. J.; Boyd, P. W.; Duce, R. A.; Hunter, K. A.; Kawahata, H.; Kubilay, N.; laRoche, J.; Liss, P. S.; Mahowald, N.; Prospero, J. M.; Ridgwell, A. J.; Tegen, I.; Torres, R., *Global Iron Connections Between Desert Dust, Ocean Biogeochemistry, and Climate.* Science, 2005. **308**(5718): p. 67-71.

42. Seaton, A.; Godden, D.; MacNee, W.; Donaldson, K., *Particulate air Pollution and Acute Health Effects.* The Lancet, 1995. **345**(8943): p. 176-178.

43. Pöschl, U., *Atmospheric Aerosols: Composition, Transformation, Climate and Health Effects.* Angewandte Chemie International Edition, 2005. **44**(46): p. 7520-7540.

44. Agency, E. P., *National Ambient Air Quality Standards for Particulate Matter; Final Rule* 2006.

45. Chatfield, R. B., *Anomalous HNO₃/NOₓ Ratio of Remote Tropospheric Air: Conversion of Nitric Acid to Formic Acid and NOₓ?* Geophysical Research Letters, 1994. **21**(24): p. 2705-2708.

46. Fan, S. M.; Jacob, D. J.; Mauzerall, D. L.; Bradshaw, J. D.; Sandholm, S. T.; Blake, D. R.; Singh, H. B.; Talbot, R. W.; Gregory, G. L.; Sachse, G. W., *Origin of Tropospheric NOₓ over Subarctic Eastern Canada in Summer.* Journal of Geophysical Research: Atmospheres, 1994. **99**(D8): p. 16867-16877.

47. Dentener, F. J.; Carmichael, G. R.; Zhang, Y.; Lelieveld, J.; Crutzen, P. J., *Role of Mineral Aerosol as a Reactive Surface in the Global Troposphere.* Journal of Geophysical Research: Atmospheres, 1996. **101**(D17): p. 22869-22889.

48. Crowley, J. N.; Ammann, M.; Cox, R. A.; Hynes, R. G.; Jenkin, M. E.; Mellouki, A.; Rossi, M. J.; Troe, J.; Wallington, T. J., *Evaluated Kinetic and Photochemical Data for Atmospheric Chemistry: Volume V - Heterogeneous Reactions on Solid Substrates.* Atmospheric Chemistry and Physics, 2010. **10**(18): p. 9059-9223.

49. Ramanathan, E., *TNPCEE Chemistry New Syllabus.* 2006: sura college of competion.

50. Langmuir, I., *The Adsorption of Gases on Plane Surfaces of Glass, Mica and Platinum.* Journal of the American Chemical society, 1918. **40**(9): p. 1361-1403.

51. Brunauer, S.; Emmett, P. H.; Teller, E., *Adsorption of Gases in Multimolecular Layers.* Journal of the American Chemical Society, 1938. **60**(2): p. 309-319.

52. Joshi, N.; Romanias, M. N.; Riffault, V.; Thevenet, F., *Investigating Water Adsorption onto Natural Mineral Dust Particles: Linking DRIFTS Experiments and BET Theory.* Aeolian Research, 2017. **27**(Supplement C): p. 35-45.

53. Ibrahim, S.; Romanias, M. N.; Alleman, L. Y.; Zeineddine, M. N.; Angeli, G. K.; Trikalitis, P. N.; Thevenet, F., *Water Interaction with Mineral Dust Aerosol: Particle Size and Hygroscopic Properties of Dust.* ACS Earth and Space Chemistry, 2018. **2**(4): p. 376-386.

54. Tang, M.; Cziczo, D. J.; Grassian, V. H., *Interactions of Water with Mineral Dust Aerosol: Water Adsorption, Hygroscopicity, Cloud Condensation, and Ice Nucleation.* Chem. Rev., 2016. **116**(7): p. 4205-4259.

55. Demeestere, K.; Dewulf, J.; Van Langenhove, H.; Sercu, B., *Gas–solid Adsorption of Selected Volatile Organic Compounds on Titanium Dioxide Degussa P25.* Chemical Engineering Science, 2003. **58**(11): p. 2255-2267.

56. Howard, C. J., *Kinetic Measurements Using Flow Tubes.* The Journal of Physical Chemistry, 1979. **83**(1): p. 3-9.

57. Kaufman, F., *Kinetics of Elementary Radical Reactions in the Gas Phase.* The Journal of Physical Chemistry, 1984. **88**(21): p. 4909-4917.

58. Adams, J. W.; Rodriguez, D.; Cox, R. A., *The Uptake of SO_2 on Saharan Dust: A Flow Tube Study.* Atmospheric Chemistry and Physics, 2005. **5**(10): p. 2679-2689.

59. Li, G.; Su, H.; Kuhn, U.; Meusel, H.; Ammann, M.; Shao, M.; Pöschl, U.; Cheng, Y., *Technical note: Influence of Surface Roughness and Local Turbulence on Coated-wall Flow Tube Experiments for Gas Uptake and Kinetic Studies.* Atmospheric Chemistry and Physics, 2018. **18**(4): p. 2669-2686.

60. Knopf, D. A.; Pöschl, U.; Shiraiwa, M., *Radial Diffusion and Penetration of Gas Molecules and Aerosol Particles through Laminar Flow Reactors, Denuders, and Sampling Tubes.* Analytical Chemistry, 2015. **87**(7): p. 3746-3754.

61. Delzeit, L.; Rowland, B.; Devlin, J. P., *Infrared Spectra of Hydrogen Chloride Complexed/Ionized in Amorphous Hydrates and at Ice Surfaces in the 15-90 K Range.* The Journal of Physical Chemistry, 1993. **97**(40): p. 10312-10318.

62. Banham, S. F.; Horn, A. B.; Koch, T. G.; Sodeau, J. R., *Ionisation and Solvation of Stratospherically Relevant Molecules on Ice Films.* Faraday Discussions, 1995. **100**(0): p. 321-332.

63. Vogt, R.; Elliott, C.; Allen, H. C.; Laux, J. M.; Hemminger, J. C.; Finlayson-Pitts, B. J., *Some New Laboratory Approaches to Studying Tropospheric Heterogeneous Reactions.* Atmospheric Environment, 1996. **30**(10): p. 1729-1737.

64. Langer, S.; Pemberton, R. S.; Finlayson-Pitts, B. J., *Diffuse Reflectance Infrared Studies of the Reaction of Synthetic Sea Salt Mixtures with NO_2: A Key Role for Hydrates in the Kinetics and Mechanism.* The Journal of Physical Chemistry A, 1997. **101**(7): p. 1277-1286.

65. Sivachandiran, L.; Thevenet, F.; Gravejat, P.; Rousseau, A., *Investigation of NO and NO_2 Adsorption Mechanisms on TiO_2 at Room Temperature.* Applied Catalysis B: Environmental, 2013. **142-143**: p. 196-204.

66. Sivachandiran, L.; Thevenet, F.; Rousseau, A.; Bianchi, D., *NO_2 Adsorption Mechanism on TiO_2: An In-situ Transmission Infrared Spectroscopy Study.* Applied Catalysis B: Environmental, 2016. **198**: p. 411-419.

67. Jacob, D. J., *Heterogeneous Chemistry and Tropospheric Ozone.* Atmospheric Environment, 2000. **34**(12): p. 2131-2159.

68. Martin, R. V.; Jacob, D. J.; Yantosca, R. M.; Chin, M.; Ginoux, P., *Global and Regional Decreases in Tropospheric Oxidants from Photochemical Effects of Aerosols.* Journal of Geophysical Research: Atmospheres, 2003. **108**(D3).

69. Bory, A. J. M.; Biscaye, P. E.; Svensson, A.; Grousset, F. E., *Seasonal Variability in the Origin of Recent Atmospheric Mineral Dust at NorthGRIP, Greenland.* Earth and Planetary Science Letters, 2002. **196**(3–4): p. 123-134.

70. Hanke, M.; Umann, B.; Uecker, J.; Arnold, F.; Bunz, H., *Atmospheric Measurements of Gas-Phase HNO₃ and SO₂ Using Chemical Ionization Mass Spectrometry During the MINATROC Field Campaign 2000 on Monte Cimone.* Atmospheric Chemistry and Physics, 2003. **3**(2): p. 417-436.

71. Bonasoni, P.; Cristofanelli, P.; Calzolari, F.; Bonafè, U.; Evangelisti, F.; Stohl, A.; Zauli Sajani, S.; van Dingenen, R.; Colombo, T.; Balkanski, Y., *Aerosol-Ozone Correlations During Dust Transport Episodes.* Atmospheric Chemistry and Physics, 2004. **4**(5): p. 1201-1215.

72. Zhang, Y.; Sunwoo, Y.; Kotamarthi, V.; Carmichael, G. R., *Photochemical Oxidant Processes in the Presence of Dust: An Evaluation of the Impact of Dust on Particulate Nitrate and Ozone Formation.* Journal of Applied Meteorology, 1994. **33**(7): p. 813-824.

73. Zhang, Y.; Carmichael, G. R., *The Role of Mineral Aerosol in Tropospheric Chemistry in East Asia: A Model Study.* Journal of Applied Meteorology, 1999. **38**(3): p. 353-366.

74. Bian, H.; Zender, C. S., *Mineral Dust and Global Tropospheric Chemistry: Relative Roles of Photolysis and Heterogeneous Uptake.* Journal of Geophysical Research: Atmospheres, 2003. **108**(D21).

75. Romanias, M. N.; El Zein, A.; Bedjanian, Y., *Reactive Uptake of HONO on Aluminium Oxide Surface.* Journal of Photochemistry and Photobiology A: Chemistry, 2012. **250**: p. 50-57.

76. El Zein, A.; Bedjanian, Y., *Reactive Uptake of HONO to TiO₂ Surface: Dark Reaction.* The Journal of Physical Chemistry A. **116**(14): p. 3665-3672.

77. Bedjanian, Y.; Romanias, M. N.; El Zein, A., *Interaction of OH Radicals with Arizona Test Dust: Uptake and Products.* The Journal of Physical Chemistry A, 2013. **117**(2): p. 393-400.

78. Bedjanian, Y.; Romanias, M. N.; El Zein, A., *Uptake of HO₂ Radicals on Arizona Test Dust.* Atmospheric Chemistry and Physics, 2013. **13**(13): p. 6461-6471.

79. Matthews, P. S. J.; Baeza-Romero, M. T.; Whalley, L. K.; Heard, D. E., *Uptake of HO₂ Radicals onto Arizona Test Dust Particles using an Aerosol Flow Tube.* Atmospheric Chemistry and Physics. **14**(14): p. 7397-7408.

80. El Zein, A.; Bedjanian, Y.; Romanias, M. N., *Kinetics and Products of HONO Interaction with TiO₂ Surface Under UV Irradiation.* Atmospheric Environment, 2013. **67**: p. 203-210.

81. Karl, T.; Potosnak, M.; Guenther, A.; Clark, D.; Walker, J.; Herrick, J. D.; Geron, C., *Exchange Processes of Volatile Organic Compounds Above a Tropical Rain Forest: Implications for Modeling Tropospheric Chemistry Above Dense Vegetation.* Journal of Geophysical Research: Atmospheres, 2004. **109**(D18).

82. Singh, H.; Chen, Y.; Staudt, A.; Jacob, D.; Blake, D.; Heikes, B.; Snow, J., *Evidence From the Pacific Troposphere for Large Global Sources of Oxygenated Organic Compounds.* Nature, 2001. **410**(6832): p. 1078-1081.

83. Singh, H. B.; Tabazadeh, A.; Evans, M. J.; Field, B. D.; Jacob, D. J.; Sachse, G.; Crawford, J. H.; Shetter, R.; Brune, W. H., *Oxygenated Volatile Organic Chemicals in the Oceans: Inferences and Implications Based on Atmospheric Observations and Air-sea Exchange Models.* Geophysical Research Letters, 2003. **30**(16).

84. Singh, H. B.; Salas, L. J.; Chatfield, R. B.; Czech, E.; Fried, A.; Walega, J.; Evans, M. J.; Field, B. D.; Jacob, D. J.; Blake, D.; Heikes, B.; Talbot, R.; Sachse, G.; Crawford, J. H.; Avery, M. A.; Sandholm, S.; Fuelberg, H., *Analysis of the Atmospheric Distribution, Sources, and Sinks of Oxygenated Volatile Organic Chemicals Based on Measurements Over the Pacific During TRACE-P.* Journal of Geophysical Research: Atmospheres, 2004. **109**(D15).

85. Wisthaler, A.; Hansel, A.; Dickerson, R. R.; Crutzen, P. J., *Organic Trace Gas Measurements by PTR-MS During INDOEX 1999.* Journal of Geophysical Research: Atmospheres, 2002. **107**(D19): p. INX2 23-1-INX2 23-11.

86. Lewis, A. C.; Hopkins, J. R.; Carpenter, L. J.; Stanton, J.; Read, K. A.; Pilling, M. J., *Sources and Sinks of Acetone, Methanol, and Acetaldehyde in North Atlantic Marine Air.* Atmospheric Chemistry and Physics, 2005. **5**(7): p. 1963-1974.

87. Romanias, M. N.; Ourrad, H.; Thévenet, F.; Riffault, V., *Investigating the Heterogeneous Interaction of VOCs with Natural Atmospheric Particles: Adsorption of Limonene and Toluene on Saharan Mineral Dusts.* The Journal of Physical Chemistry A, 2016. **120**(8): p. 1197-1212.

Chapter II. Materials and methods

Table of content

List of Tables

List of Figures

This chapter includes all the necessary information regarding the materials used, the experimental setups and the analytical devices employed as well as the methods developed and applied to reach the objectives of this Thesis.

First, the origins and the characterization of the natural dust samples used are presented. This part is followed by the materials used to prepare the VOC gas mixtures. Then a section is dedicated to the experimental devices and the methods developed for studying different aspects of the interaction of VOCs with natural dust samples.

1 Materials

1.1 Origins of the samples

The natural mineral dust samples used in this study originate from various arid regions of the Earth, such as the Saharan, Sahelian and Asian deserts, and dust hot spots that contribute to more than 70% of the global emissions of mineral particles in the atmosphere. A map of the collection points of these mineral dust samples is given in Figure II-1. The natural soil samples were collected (i) close to the oasis of Nefta (Tunisia), (ii) the city of Mbour (Senegal), thus corresponding to two different regions along North and West Africa, and (iii) from Saudi Arabia (Rawdat arid region). Besides, aeolian deposits were collected in Yanchi, Ningxia province in China (Gobi arid region). After their collection, the mineral samples are mechanically sieved and the finest fraction of particles (i.e. < 100 µm), that corresponds to the particle size fraction that can be suspended in air, is used for the experiments. In addition, the commercially available ISO 12103-1 A1 ultrafine Arizona Test Dust (ATD, Powder Technology Inc.) is also used. The ATD sample was collected in June 2013 and consists of ultrafine particles with a size distribution between 3 and 22 µm, with ~ 97% below 11 µm in diameter.
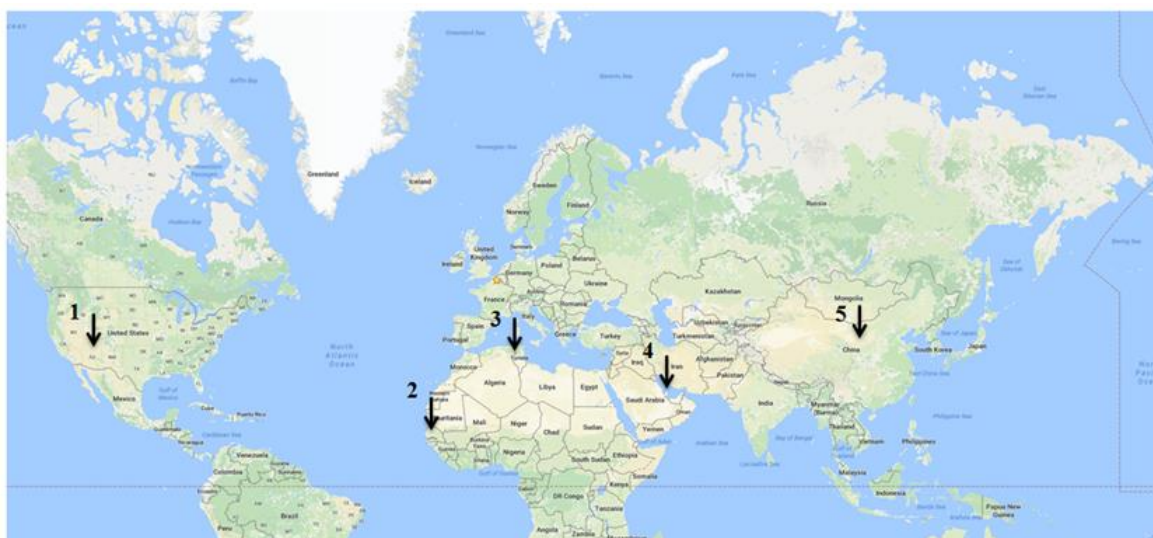
Figure II-1. Map of the collection points of mineral dust samples investigated in this work: 1: commercially available ATD, 2: Mbour, 3: Nefta, 4: Rawdat, 5: Gobi

Besides the natural samples the following commercially available synthetic minerals were also used: TiO_2 powder (Rutile/anatase, Degussa, Aeroxide-P25), Al_2O_3 powder (Aluminum oxide, Sigma-Aldrich), $CaCO_3$ powder (Calcite, Sigma-Aldrich), Fe_3O_4 powder (Magnetite, Sigma-Aldrich, 99.99% trace metal basis), and SiO_2 (Quartz, Merck). All the synthetic powders are used as purchased and their size fractions are reported in Table II-1.

1.2 Physical and chemical characterizations of the samples

Not only do the physical and chemical characterizations of the samples facilitate the understanding of VOC interactions with dusts, but it also helps quantifying this interaction.

1.2.1 BET specific surface area determination

The specific surface area (SSA) is a physical property of solids which represents the total surface area of a material per mass unit (m^2 g^{-1}) that is available to gas molecules. It is required for the determination and comparison of the kinetic and sorption parameters from one material to another. Nitrogen adsorption measurements are performed with a laboratory gas sorption analyzer. The SSA of each sample is determined employing the BET method within the 0.05 to 0.3 relative pressures range, P/P_0 [1]. At least three adsorption measurements were conducted on the different samples. The specific surface areas are reported in Table II-1. The accuracy of the BET measurements is validated by comparing the specific surface area of the commercially available TiO_2 samples with data provided by the supplier.

Table II-1. Specific surface areas (m^2 g^{-1}) for each sample determined using the 2-parameter BET method.

Sample	Specific surface area, SSA* (m^2 g^{-1})	Size fraction(μm)
ATD	6.7 ± 0.6	< 11
Rawdat	3.4 ± 0.2	< 100
Gobi	10.5 ± 2.0	< 100
Mbour	14.5 ± 1.0	< 100
Nefta	15.5 ± 1.1	< 100
SiO_2	402 ± 40	$63\text{-}200$
$CaCO_3$	0.6 ± 0.1	< 30
Al_2O_3	118 ± 22	$63\text{-}200$
Fe_3O_4	3.4 ± 0.4	< 5
TiO_2	52.0 ± 6.4	~ 0.02
*The values presented are the average of the measurements and the quoted errors correspond to the standard deviation of the measurements.		

1.2.2 Chemical characterizations of the natural dust samples

The chemical characterization of the samples is performed employing X-ray diffraction (XRD), X-ray fluorescence (XRF) and inductively coupled plasma mass spectrometry (ICP-MS) [2-4]. The chemical compositions of the different samples are reported in Tables II-2 and II-3. The X-ray measurements are performed at IMT Lille Douai, Civil Engineering department by Dr. Betrancourt. The X-ray measurements were conducted using around 1 g of sieved mineral dust and two complementary techniques:

(i)   X-ray diffraction (XRD; Bruker D2 theta analyzer) equipped with a Cobalt source (1.74 nm). XRD is primarily used for the phase identification of a crystalline material. The analyzed material is finely ground, homogenized before analyses.

(ii)   X-ray fluorescence (XRF; Bruker AXS explorer S4 pioneer). XRF is a non-destructive analytical technique used to determine the elemental composition of materials. XRF analyzers determine the chemistry of a sample by measuring the fluorescent (or secondary) X-ray emitted from a sample when it is excited by a primary X-ray source.

Regarding the ICP-MS analyses, the measurements are performed by Dr. L. Alleman at IMT Lille Douai, SAGE department. ICP-MS is capable of detecting metals and several elements at concentrations as low as the part per quadrillion, ppq [5]. From 0.5 to 5 mg of each dust sample are dissolved in an acidic solution (3 mL HCl, 1 mL HNO$_3$, 500 μL HF and 4 mL of ultrapure H$_2$O) and thermally pretreated at 220°C over 20 min before analysis [6]. Three sets of measurements were performed for each sample to evaluate the homogeneity of the dust batch; the variation coefficients of the major elements never exceeded 10 %. As reported in Table II-2 both X-ray and ICP-MS analyses provide consistent results regardless of the techniques used and the amount of dust required for each measurement, confirming the homogeneity of the samples [7].

Table II-2. Bulk compositions (in %) of the main elements (excluding O, C, H, N) of each natural mineral dust sample, combining X-ray (XRF and XRD) and ICP-MS analyses.

Element	Mbour		Nefta		Rawdat		Gobi		ATD ultrafine	
	X-ray	ICP-MS	X-ray	ICP-MS	X-ray	ICP-MS	X-ray	ICP-MS	X-ray	ICP-MS
Si	96.1	94.4	83.2	98	65.6	64	61.7	57.6	74.9	74.6
Al	1.4	1.8	0.3	0.2	6.9	6.5	10	11.0	9.8	9.5
Ca	1.3	1.3	11.3	1.0	17.4	21	15.1	16.1	3.8	4.4
Na	<0.1	0.2	<0.1	0.2	1.8	2.7	1.92	2.5	3.0	2.5
Mg	<0.1	0.1	<0.1	<0.1	<0.1	1.4	2.1	2.3	1.0	1.0
Ti	0.4	0.7	2.0	<0.1	0.2	0.2	1.3	0.8	0.4	0.5
K	<0.1	0.1	<0.1	0.1	3.4	1.9	4.0	3.5	4.2	4.0
Fe	0.8	1.3	0.3	0.1	1.8	1.2	3.83	5.5	2.9	3.1
P	<0.1	N.D[a]	2.7	N.D	<0.1	N.D	<0.1	N.D	<0.1	N.D
Zn	<0.1	<0.1	<0.1	<0.1	<0.1	<0.1	<0.1	0.2	<0.1	<0.1
Mn	<0.1	<0.1	<0.1	<0.1	<0.1	<0.1	<0.1	0.1	<0.1	<0.1
Ba	<0.1	<0.1	<0.1	<0.1	<0.1	<0.1	<0.1	<0.1	<0.1	0.1
Sum (%)	**~100**	**~100**	**~99**	**~100**	**~97**	**~99**	**~100**	**~100**	**~100**	**~99**

[a] N.D: Not determined (not in the list of 34 elements analyzed with ICP-MS).

Table II-3. Relative abundances (in %) of mineral phases identified in each natural mineral dust sample using XRD. For comparison purposes the mineralogical composition of ATD provided by the supplier is also indicated [7].

Mineral oxide		Mbour	Nefta	Rawdat	Gobi	ATD ultrafine	
						This work	Supplier
SiO_2	Quartz	95.0	82.0	61.0	55.0	76.0	68-76
$CaCO_3$	Calcite	1.5	11.0	21.0	17.8	-	-
CaO	Calcium oxide	-	-	-		2.5	2.0-5.0
$Ca(HPO_4).\ 2\ H_2O$	Brushite	-	5.0	-	-	-	-
$NaAlSi_3O_8$	Albite	-	-	10.0	10.5	-	-
Na_2O	Sodium oxide	-	-	-		1.9	2.0-4.0
TiO_2	Rutile/anatase	0.3	1.5	0.2	1.0	0.3	0.5-1.0
Al_2O_3	Aluminum oxide	1.2	0.3	4.4	6.9	8.8	10-15
Fe_2O_3	Hematite	0.5	0.2	-		2.0	2.0-5.0
Fe_3O_4	Magnetite	-	-	1.3	2.6	-	-
MgO	Magnesium oxide	-	-	-	-	0.8	1.0-2.0
K_2O	Potassium oxide	-	-	2.0	-	2.4	2.0-5.0
Unaccounted fraction		1.5	0.0	0.1	6.2	5.3	-

1.3 Gas preparations

The objective of this work is to investigate the heterogeneous interaction of several VOCs on different dust samples. In order to provide accurate kinetic parameters and mechanistic insights it is necessary to control and adjust precisely the gas phase concentrations of the VOCs of interest and ensure the stability and the quality of the carrier gas. Therefore in this section, the gas preparation i.e. generation sources, mixing process, humidification, etc., of the different VOCs and air mixtures is presented.

1.3.1 Zero air generation and quality

Zero air is used as the carrier gas and is generated by using an air compressor. This compressor is equipped with a dryer and a particle filter. The mixture gas is then sent into a catalytic zero air generator (Claind AZ-2020, Lenno, Italy) which eliminates the VOCs present in the air by oxidation on a 250 °C Platinum-Palladium catalyst to achieve a total concentration of VOCs lower than 100 ppt in the air flow at the outlet of the zero air generator. CO_2 is removed by flowing the zero air through a Parker-Balston 75-52 scrubber. This scrubber relies on a Pressure Swing Adsorption (PSA) process to extract CO_2 from the air. This separation system is based on the adsorption of CO_2 under pressure on a porous material. Two adsorbent cartridges are alternately used. While one is under a high pressure to adsorb the CO_2, the second is at atmospheric pressure in order to desorb CO_2 out of the circuit. The CO_2 concentration at the outlet of the system is lower than 10 ppb. It should be noted that the remaining impurity levels in the air stream are always lower than the analytical system detection limits, i.e. overall VOCs < 0.1 ppb, $CO_2 < 10$ ppb, $CO < 80$ ppb and $H_2O < 2$ ppm.

1.3.2 Controlling relative humidity

The relative humidity is controlled by changing the mixing ratio of dry and saturated humid air. In particular, a fraction of the initial zero air flow is moistened after passing through a H_2O bubbler and is further mixed with dry air to obtain the targeted RH level. The relative humidity in the gas flows is recorded using a temperature and relative humidity probe, (KIMO HQ 210 STD). It allows monitoring RH from 3 to 98% and the temperature from 253 to 353 K with respective accuracies of 1.5% and 0.06%.

1.3.3 Preparation of VOCs and air mixtures

The VOCs that were used in experiments with natural dust samples are isopropanol, isoprene and acetic acid. The specifications of the gas cylinders (or canisters) and concentration ranges of those VOCs used in experiments are reported in Table II-4 and Table II-5 respectively.

Isopropanol generation: Isopropanol (IPA) concentrations are obtained from calibrated gas cylinders (PRAXAIR) with 10 and 507 ppm_v nominal concentrations in N_2, which are further diluted in zero air dry or humid.

Isoprene generation: Various concentrations of isoprene (ISP) are prepared inside an 18 L stainless steel canister by injecting volumes of 1 µL to 0.1 mL of liquid ISP (Sigma-Aldrich; purity $\geq$ 99 %) and adjusting the pressure inside. First the canister is pumped until primary vacuum is reached ($P < 10^{-2}$ mbar). Then using of a 5 µL or 1 mL graduated syringe the targeted volume of ISP is injected in the canister. Thereafter, the canister is filled with zero air until a pressure of ca. 2.5 bars is reached (Table II-4). It has to be noted that the pressure of ISP in the canister is always lower than its saturation vapor pressure at room temperature i.e. 0.56 bars, in order to ensure the complete vaporization of injected ISP in the canister.

Table II-4. Characteristics of the VOC cylinder and canisters used for VOC and air mixture preparations

VOC	Type	Concentration (ppm)	Pressure (bar)
IPA	Calibrated cylinder	9.80 ± 0.48	150
		507 ± 10	150
ISP	Canister	$(13.00 \pm 0.65), (1340 \pm 41)$	2.5
AcA	Calibrated cylinder	106 ± 2	150
Formaldehyde	Calibrated cylinder	24.0 ± 1.2	150
Acetaldehyde	Calibrated cylinder	98.0 ± 4.9	150
Methanol	Canister	65 ± 6	2.5
Acetaldehyde	Canister	95 ± 9	2.5
CO_2	Calibrated cylinder	10^6	150

Acetic acid generation: Different acetic acid (AcA) concentrations are obtained from a calibrated gas cylinder (PRAXAIR) with a nominal concentration of 105 ppm in N_2, which is further diluted in zero air dry or humid air.

Since, the monitoring of other complementary VOCs, and CO_2 is required, calibrated canisters of methanol and acetone were prepared in the same manner as for ISP. CO_2, Acetaldehyde and Formaldehyde concentrations are obtained from calibrated cylinders. Their specifications are presented in Table II-4.

Table II-5 Concentration ranges used in the experiments in molecules cm^{-3} and in ppb

VOC	Concentration (10^{13} molecules cm^{-3})	Concentration (ppb)
IPA	0.15 - 615	60 – 250,000
ISP	0.3 - 615	120 – 250,000
AcA	1.2 - 39.4	500 – 16,000

2   Methods

2.1   Experimental setup

A general scheme of the experimental setups used is shown in Figure II-2. It consists of three main parts:

(i)   the gas flow generation system

(ii)   the reactor (U-shaped reactor, double-wall reactor, DRIFTs cell)

(iii)   the analytical devices (SIFT-MS, FT-IR, and DRIFTs)

The description of the different types of reactors and detectors used are presented in details in the following subsections.
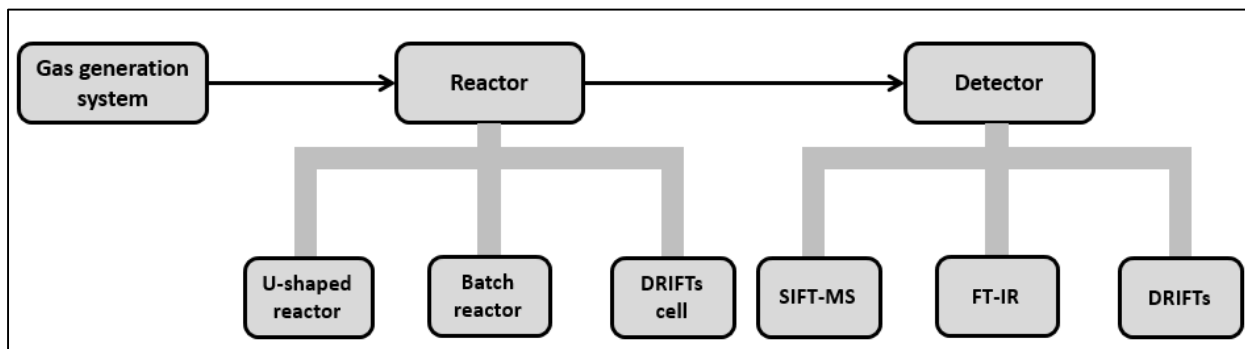
Figure II-2. General scheme of the experimental setups

2.1.1   Gas flow generation system

A scheme of the gas flow generation system is shown in Figure II-3. The gas flow generation line is made of stainless steel and Teflon. Calibrated mass flow controllers (Bronkhorst) are used to introduce the VOC that is further diluted by zero air to reach a flow rate adjusted from 250 to 1000 sccm. The relative humidity in the reactor is set by allowing part of the zero air to pass through a bubbler at room temperature, thus the air leaving the bubbler is at 100% RH. After the gas mixture is prepared it is sent to the reactor by means of a 4-way valve.
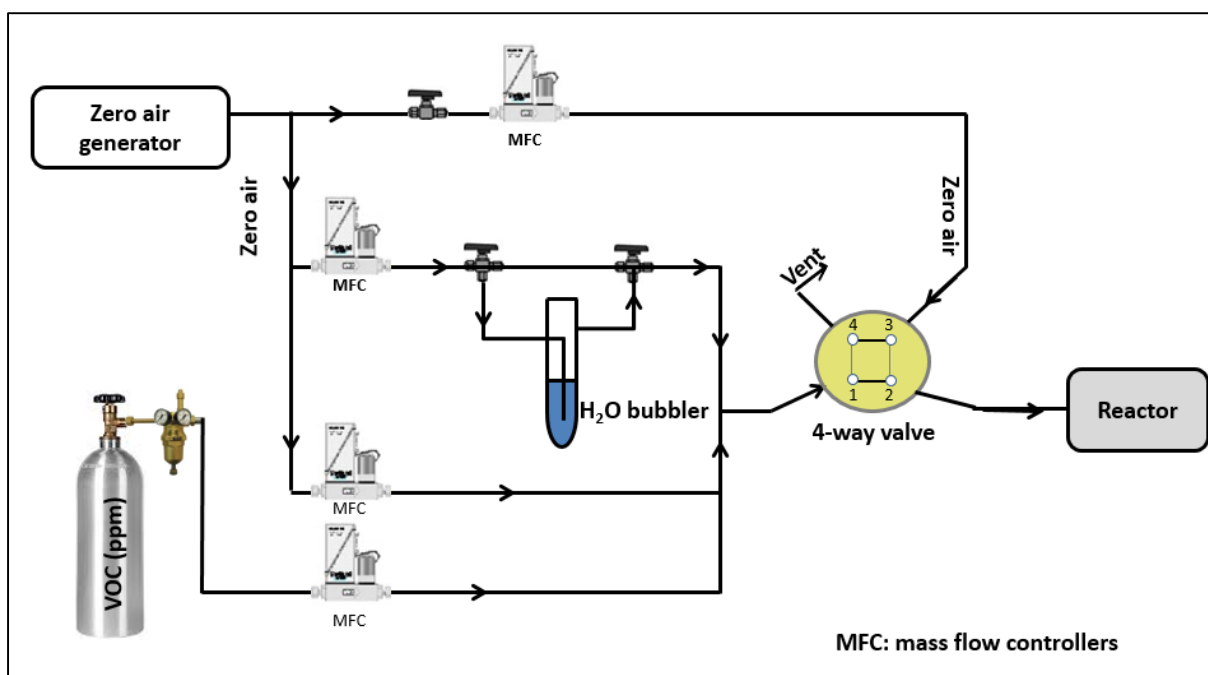
Figure II-3. Scheme of the gas flow generation system.

2.1.2   Reactors

The heterogeneous interaction of VOCs with dust is studied employing different reactors selected according to the targeted objective of each set of experiments. The U-shaped and double-wall reactors are used to study the gas phase kinetics and the possible formation of products in the gas phase under dark and UV irradiation, while the DRIFTs cell is used to monitor *in-situ* the adsorbed phase during the interaction of VOCs with dust.

The U-shaped reactor

The U-shaped reactor is employed throughout the study to determine (i) the initial uptake coefficients, (ii) the gas phase products formed, and (iii) the reversible/irreversible fractions of the heterogeneous interaction/reaction of the model VOCs with the mineral dust samples.

The schematic of the U-shaped reactor is given in Figure II-4. It consists of two parts: the upper one is a bypass line with a total volume of 15 cm^3; it is used to monitor the VOC concentration in the absence of dust. The lower part, with a similar volume of 15 cm^3, is equipped with a quartz wool sample-holder (geometric surface area 4.95 cm^2), on top of which a known amount of mineral sample is placed. The two parts are connected via two 3-way valves. The mass of the sample varies depending on the adsorption capacity of mineral dust towards the VOC studied. The inlet and outlet of the reactor are connected to the rest of the setup by Ultra Torr fittings.
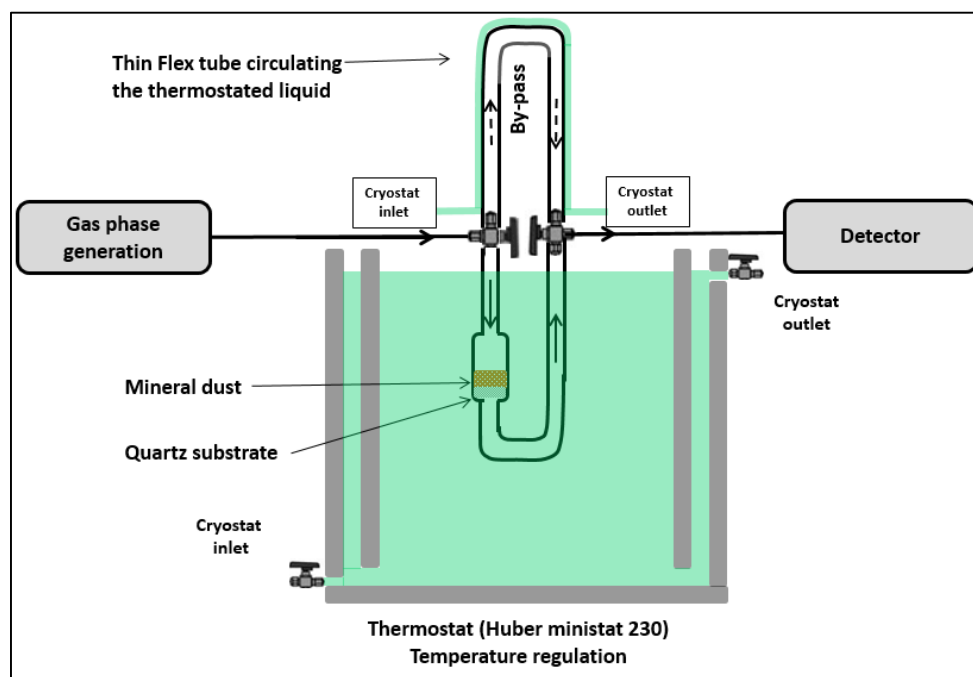
Figure II-4. Scheme of the U-shaped reactor.

In the case of temperature dependence experiments, the lower part of the reactor is immersed in a thermostated bath (Huber ministst 230) filled with ethanol or water, which allows the variation of the temperature from 253 to 358 K. The bypass line is also thermostated, by wrapping it up either with a thin flex tube circulating the thermostated liquid, or using a heating tape. The temperature of the sample is recorded using a K-type thermocouple inserted inside

the U-shaped reactor. The residence time of the VOC in the lower part of the U-shaped reactor is estimated to be around 1 second.

The double-wall reactor

A scheme of the double-wall reactor is reported in Figure II-5. It is a 600 cm^3 double-wall reactor made of Pyrex and equipped with a quartz window attached on the top with a metallic clamp and two gas connections. A glass plate supporting the mineral dust sample is placed at the bottom of the reactor. Three UV lamps (UVA, PL-L18W, Philips) are used to irradiate the dust from above, through the quartz window. The total gas flow can be varied from 300 to 700 sccm. The residence time of the VOC in the double-wall photochemical reactor is estimated to be around 2 minutes. The temperature of the sample is recorded using a K-type thermocouple placed inside the reactor.
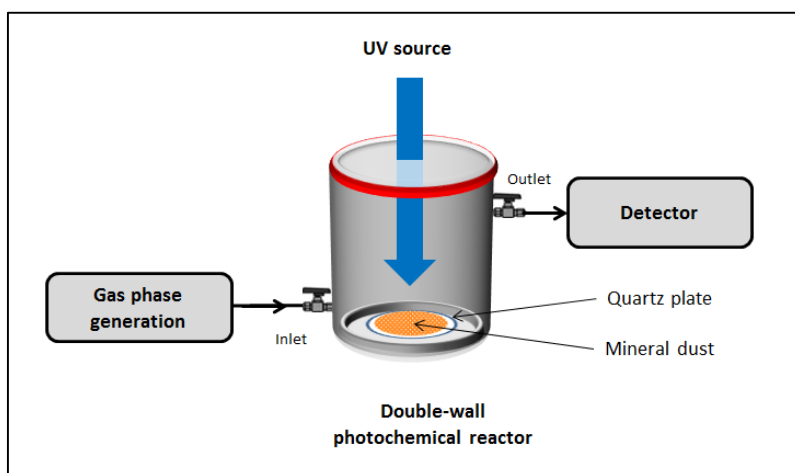
Figure II-5. Scheme of the double-wall reactor.

The DRIFTs optical cell reactor

The *in-situ* monitoring of the dust surface is performed in a DRIFTs optical cell (Harrick, Praying Mantis). A simple representation of the optical reactor is provided in Figure II-6. The dust sample is placed on the grid inside the DRIFTs cell. The diffuse reflection that is produced by the sample surface reflection of the light in all directions is collected by use of an ellipsoid mirror. The output mirror then directs this scattered energy to the MCT detector. The temperature of the sample is recorded using a K-type thermocouple placed on the top of the sample holder, which is also equipped with a heating resistor and a liquid (water/ethanol)

circulation system connected to a thermostat (Huber ministat 230) to limit possible temperature fluctuations during the experiment. The temperature can be regulated from -100°C to +100°C
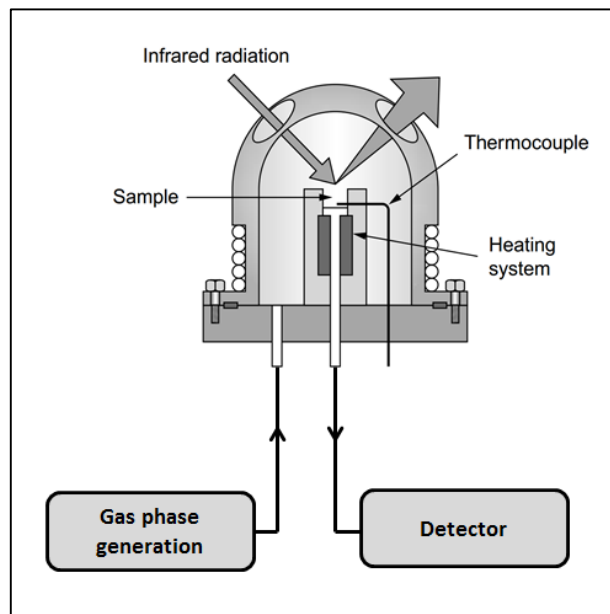
Figure II-6. Scheme of the DRIFTs cell reactor.

2.1.3 Analytical devices

Various analytical devices are employed aiming to follow the time evolution of the reactant VOCs and the potential products formed, in the gas phase and in the adsorbed phase.

2.1.3.1 Gas phase analyses

The online gas phase monitoring of primary VOCs and their potential products is achieved employing Selective Ion Flow Tube Mass Spectrometry, (SIFT-MS) and multipath Fourier Transform Infrared (FTIR) Spectroscopy.

SIFT-MS

Gas-phase VOC concentrations are monitored with a Voice 200 SIFT−MS typically in the ppb to ppm range. The SIFT mass spectrometry is based on the chemical ionization of the analytes. A microwave discharge is used for the generation of three precursor ions, H_3O^+, NO^+, and O_2^+, which are sequentially selected by a first quadrupole mass filter [8, 9]. Then, the precursor ions are injected through a Venturi-type orifice inside a flow tube reactor operated at 1 Torr total pressure using Helium as the carrier gas. The precursor ions react with the analytes along the flow tube to produce new characteristic ionized molecules [8, 9]. Subsequently, the

gas flow passes through a pinhole orifice of 0.3 mm diameter, located at the downstream end of the flow tube reactor to create a thermal molecular beam. The molecular beam enters a differentially pumped high vacuum chamber, and both the precursor and product ions are focused via electrostatic lenses into a second quadrupole mass spectrometer for mass analysis and counting for identification and quantification, respectively.

It is possible to calculate the theoretical concentrations of the analytes using the kinetics of ionization reactions in the flow tube, the ionized molecule and remaining precursor amounts, and the residence time inside the flow tube. However, this calculation is based on theoretical data and can be affected by the operating conditions. Subsequently, the mass spectrometer is experimentally calibrated, using calibrated VOC cylinders, to obtain reliable concentration measurements [8, 9]. The major advantage of SIFT-MS is that several VOCs can be monitored simultaneously eliminating the effect of mass peak overlapping. For instance, when two species are identified at the same mass peak (equal m/z ratio) but originate from different precursor ions, the MS peak intensities recorded are free of contribution. Nevertheless, in separate experiments, standards of each identified compound are introduced individually to check for any possible contribution of other products to the species mass peaks. A summary of the compounds detected employing SIFT-MS and their detection limits are presented in Table II-6.

FTIR

In some experiments, the gas phase is analyzed employing a transmission FTIR spectrometer (Thermo Scientific Antaris IGS) equipped with a 10 m path length White cell and coupled to a liquid-N_2-cooled MCT detector. Besides the monitoring of the VOCs, the analysis of the gas phase with FTIR allowed the identification of compounds that cannotbe detected by SIFT−MS, such as CO and CO_2. These compounds could be possible oxidation end products formed by the heterogeneous reaction of VOCs with dust. IR spectra are collected within the wavenumber range $600-4000$ cm^{-1} every 30 s using Result-3 software. Each IR spectrum corresponds to the average of 16 co-added scans with a resolution of 0.5 cm^{-1}. Quantification and data processing are performed using TQ-Analyst software. Calibration curves and detection limits are determined by passing standard gases supplied through the gas cell at a flow rate of 1000 sccm. Table II-6 summarizes the integration bands and the detection limits for the species of interest calibrated with the FTIR system in the laboratory.

Table II-6. Compounds detected employing SIFT mass spectroscopy and FTIR and their main specifications.

SIFT-MS [a]						
Compound	Reagent ion	Ionized species	Branching ratio (%)	Mass peak (m/z)	DLs (ppb)	
					50% RH	0% RH
IPA	H_3O^+	$C_3H_7^+$	100	43	20	5
	NO^+	$C_3H_7O^+$	100	59	1	2
ISP	H_3O^+	$C_5H_8H^+$	100	69	0	0
	NO^+	$C_5H_8^+$	100	68	0	0
AcA	H_3O^+	$CH_3COOH_2^+$	100	61	24	54
	NO^+	NO^+CH_3COOH	100	90	17	64
Formaldehyde	H_3O^+	CH_3O^+	100	31	8	8
Methanol	NO^+	CH_5O^+	100	65	3	5
Acetaldehyde	H_3O^+	$C_2H_5O^+$	100	45	3	23
	NO^+	$C_2H_3O^+$	100	43	7	9
Acetone	H_3O^+	$C_3H_7O^+$	100	59	2	2
	NO^+	$NO^+C_3H_6O$	100	88	2	2
FTIR [b]						
Compound	Wave numbers			Detection limit (ppb)		
CO_2	2300 - 2400 cm^{-1} (band integration)			20		
IPA	897 - 1000 cm^{-1} (band integration) 1307 - 1432 cm^{-1} (band integration) 2920 - 3208 cm^{-1} (band integration)			1500		
CO	2000 - 2250 cm^{-1} (band integration)			76		

(a) The precursor reagent ions used for the identification of each VOC, the ionized species formed with the corresponding branching ratio, the recorded mass peaks, and the detection limits at dry and 50% RH are given

(b) The wavelength ranges used for identification and the detection limits are given

2.1.3.2 Adsorbed phase analysis

DRIFT Spectroscopy

While the techniques stated above monitor changes in the gas-phase concentrations, the Diffused Reflectance Infrared Spectroscopy (DRIFTs) focuses on changes on the surface of solid phase. The *in-situ* monitoring of the dust surface is performed in a DRIFTs cell (Harrick, Praying Mantis) equipped with three windows the first is a zinc selenium (ZnSe) windows , the second is for collecting the diffused IR radiation and the third is for external surface irradiation. The DRIFTs optical cell is coupled to a Nicolet 6700 FTIR spectrometer. In principle, an infrared radiation directly reflected by the sample surface, gives rise to specular refraction,

which is a function of the refractive index and absorptivity of the sample. The radiation may also undergo multiple reflections occurring at the surface of the particles, without penetrating the sample. The radiation that undergoes this type of diffuse specular reflection exits the surface at any angle relative to that of the incident beam. On the contrary, true diffuse reflection is the consequence of beam penetration into one or more particles and its diffusion in the sample. This component of the radiation also exits the sample at any angle but, since it has traveled through the particles, it contains data on the absorption properties of the material [10]. Thus, this instrument can be used for the detection of products formed and accumulated on the surface of the natural dust samples. DRIFTs spectra are recorded using the Omnic 9.2 software with 16 scans per spectrum and a spectral resolution of 4 cm^{-1}.

HPLC-UV

The adsorbed phase is also investigated with offline complementary series of experiments employing the High Performance Liquid Chromatography (HPLC) instrument dedicated to the detection of aldehydes and ketones. The surface adsorbed species are extracted using 3 ml of acetonitrile as a solvent and 3 mL 2,4-dinitrophenylhydrazine (DNPH) as a derivatization agent. Thereafter the solution is analyzed with Water 2487 HPLC. Compounds are eluted at flow rate of 1.5 mL/min on C18 column (20 mm $\times$ 4.6 mm $\times$ 5 µm) thermostated at 40°C and detected by tunable wavelength UV adsorption (Water 2695). Commercially available calibrated solutions are used for the system calibration.

2.2   Experimental protocols developed and applied to the current study

This section includes the experimental procedures developed and followed to investigate the heterogeneous interactions of the selected VOCs with the mineral dust samples of interest. In order to assess the affinity of the dust sample towards the VOC, the initial uptake coefficients and the number of molecules adsorbed should be determined,[11] as well as the reactivity of the dust. In order to fulfill this objective different protocols are followed.

2.2.1 Protocol used with the U-shaped reactor

Experimental protocol

A typical experiment for VOC interaction on dust and experimental protocol followed using the U-shaped flow reactor is presented in Figure II-7.

Before each experiment the sample of interest is placed into the reactor and thermally pre-treated under dry zero air at 200°C to remove any pre-adsorbed species (e.g. H_2O, or other VOCs). Thereafter, the sample is cooled down to room temperature while still under zero air. In case of dry conditions no other pretreatment takes place. However, under RH conditions and prior to VOC exposure, the freshly prepared mineral sample is exposed for about 10 min to water vapor present in the reactor during which the background is collected in the same experimental conditions.
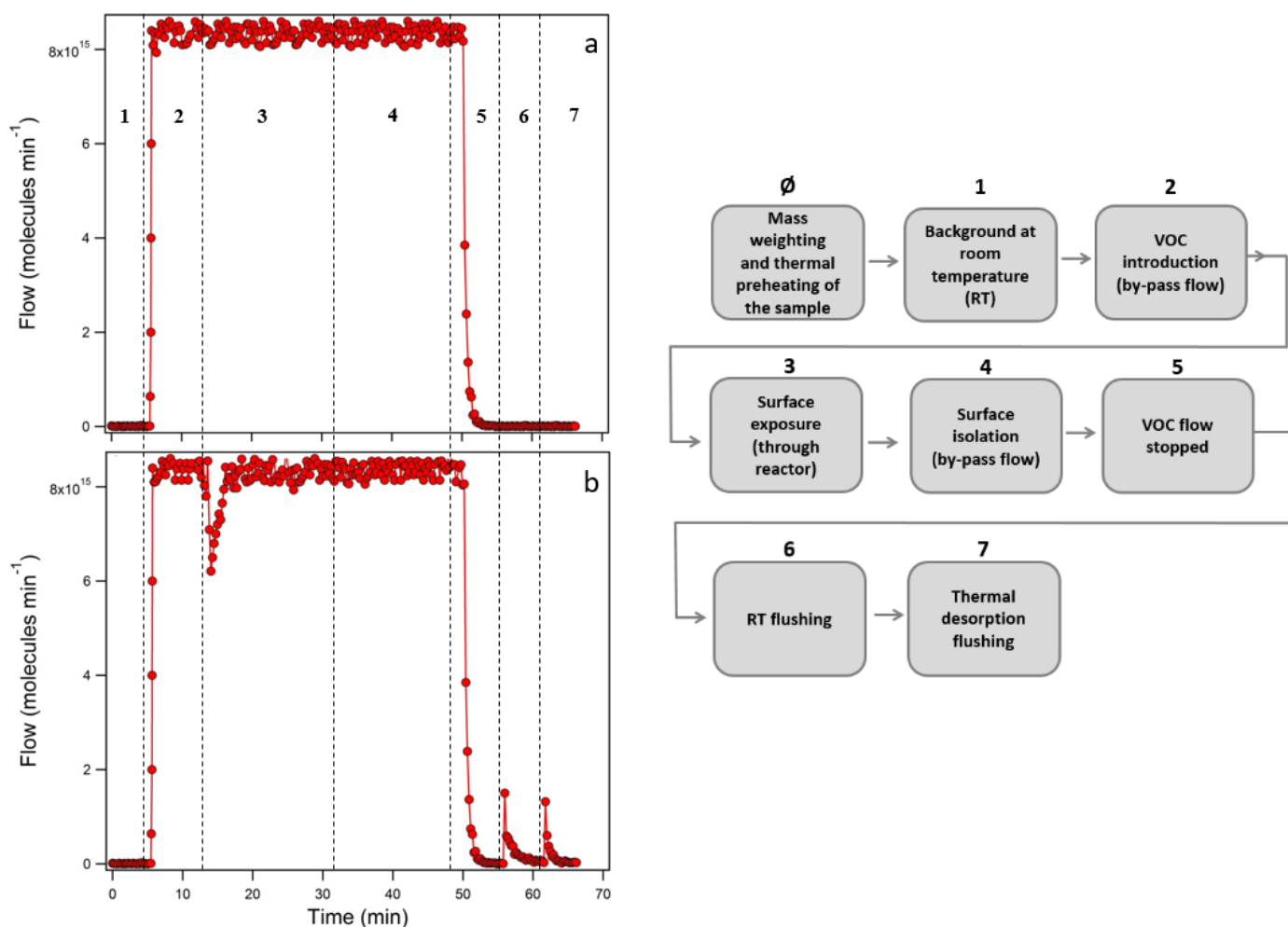
Figure II-7. Typical gas-phase profiles of VOC recorded with the SIFT-MS at 298 K and dry conditions in the absence (a) and presence (b) of dust.

Once room temperature is reached, the background level of the selected VOC is recorded, step 1. In step 2, the gas flow direction is changed to the 15 cm^3 by-pass line by means of the two 3-way valves and a known concentration of the VOC is introduced (Figure II-4). When a steady-state concentration is achieved, the flow is directed through the reactor (step 3), exposing the dust surface to the selected VOC. A rapid decrease of the VOC concentration is observed, due to the uptake of the VOC on the dust surface. It should be noted that since the by-pass and the reactor have equal volumes, the observed decrease in VOC concentration during the uptake experiment is not due to the volume difference. This point has been experimentally validated with preliminary experiments conducted in the absence of dust (Figure II-7a). Meanwhile, preliminary experiments evidenced the VOC uptake on the glass wool substrate is below the detection limit.

When the equilibrium between the adsorbed phase and the gas phase is achieved, the gas phase concentration of the selected VOC at the oulet of the reactor is equal to the inlet concentration. Then as shown in step 4 the reactor is then isolated, i.e. switched to by-pass, and the VOC flow is stopped in order to purge the lines with zero air. Consequently, the VOC concentration drops back to the background level at the outlet of the by-pass (step 5). Thereafter, step 6 takes place where the flow of zero air is directed through the reactor to purge the dust surface. Depending on the intensity of the interaction of the VOC with the natural dust sample, a transient peak of VOC can be monitored. This peak corresponds to the weakly adsorbed fraction of the selected VOC at room temperature. Lastly, the surface is heated up to 110ºC - 150 ºC depending on the VOC, in order to remove the remaining adsorbed quantity of the VOC.

The following subsections describe how the experimental data are analyzed to determine the initial uptake coefficient and the number of molecules adsorbed. A closer look at the adsorption peak and the qualitative illustration showing the method used to calculate the initial uptake coefficient and the number of molecules adsorbed is reported in Figure II-8.

Determination of initial uptake coefficients

The most widely used approach to describe the kinetics of heterogeneous processes is to determination the uptake coefficient, γ. It represents the net probability that a molecule X undergoing a gas-kinetic collision with a surface is actually taken up by the surface. [11]
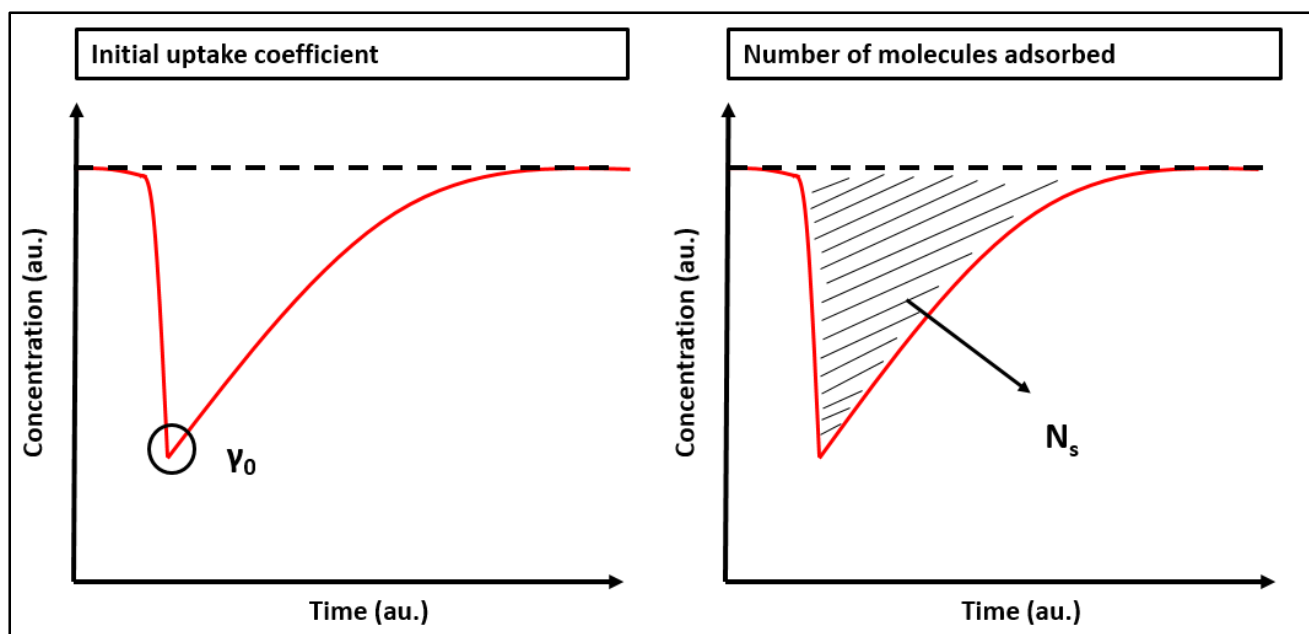
Figure II-8. Illustration of the parameters derived from the U-shaped reactor experimental data.

The initial uptake coefficient of a VOC is derived from the following equations:

$$\frac{d(VOC)/dt}{V} = k_{het}[VOC] \qquad \textbf{(Equation II-1)}$$

$$k_{het=}\frac{d(VOC)/dt}{V[VOC]} = \omega\gamma_0 \qquad \textbf{(Equation II-2)}$$

with:

$$\omega = \frac{cA_s}{4V} \qquad \textbf{(Equation II-3)}$$

and finally:

$$\gamma_0 = \frac{4\{d(VOC)/dt\}}{cA_s[VOC]} \qquad \textbf{(Equation II-4)}$$

where (VOC) denotes the number of VOC molecules taken up by the dust surface at the beginning of exposure (molecule); k_{het}, the first-order rate coefficient of the VOC heterogeneous degradation (s^{-1}); V, the volume of the reaction zone (cm^3); [VOC], the gas-phase VOC concentration (molecules cm^{-3}); ω, the VOC collision frequency (s^{-1}); c, the mean molecular speed (cm s^{-1}); A_s, the specific surface area of the dust (cm^2).

Determination of the VOC number of molecules adsorbed

The total number of molecules taken up per surface unit, N_s (molecules cm^2), is derived by integrating the area of the adsorption peak in a typical uptake experiment (Figure II-8) divided by the specific surface area of the dust, A_s, according to Equation 5: [12]

$$N_S = \int_{\tau=0}^{\tau=1} \frac{F(t)}{A_S} dt \qquad \textbf{(Equation II-5)}$$

where F is the flow rate (molecules s^{-1}) of the VOC molecules through the reactor. $\tau = 0$ is the time of exposure of VOC to the dust, $\tau = 1$ is the time when the signal returns to its initial level.

2.2.2 Protocol used with the double-wall reactor

The double-wall reactor is employed to investigate the degradation pathways of the model VOCs under dark and simulated sunlight irradiation conditions. In this type of reactor VOC breakthrough curves are determined.[13] The gas-phase VOC concentration is monitored by SIFT-MS or FTIR at the outlet of the reactor. A scheme of the protocol followed is proposed in Figure II-9.
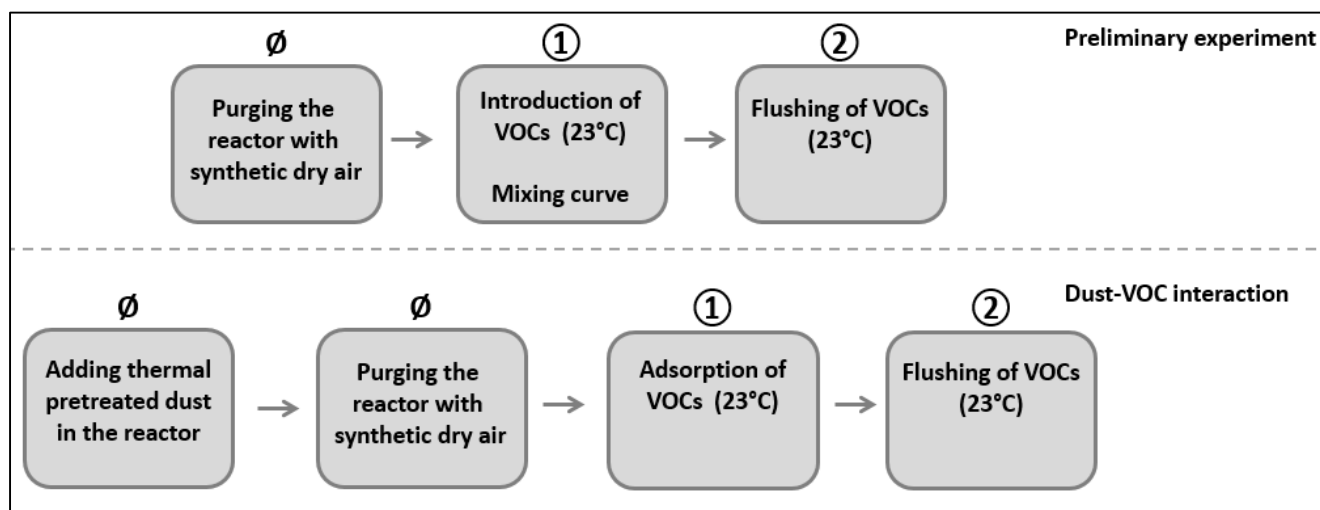
Figure II-9. Scheme of the protocol followed using the double-wall reactor.

The reactor is first purged with zero air for the collection of the background. Then a two-step procedure is followed and the temporal concentration of the VOC is recorded (i) in the absence of dust to determine the mixing curve, and (ii) in the presence of a natural dust sample to determine the VOC breakthrough curve.
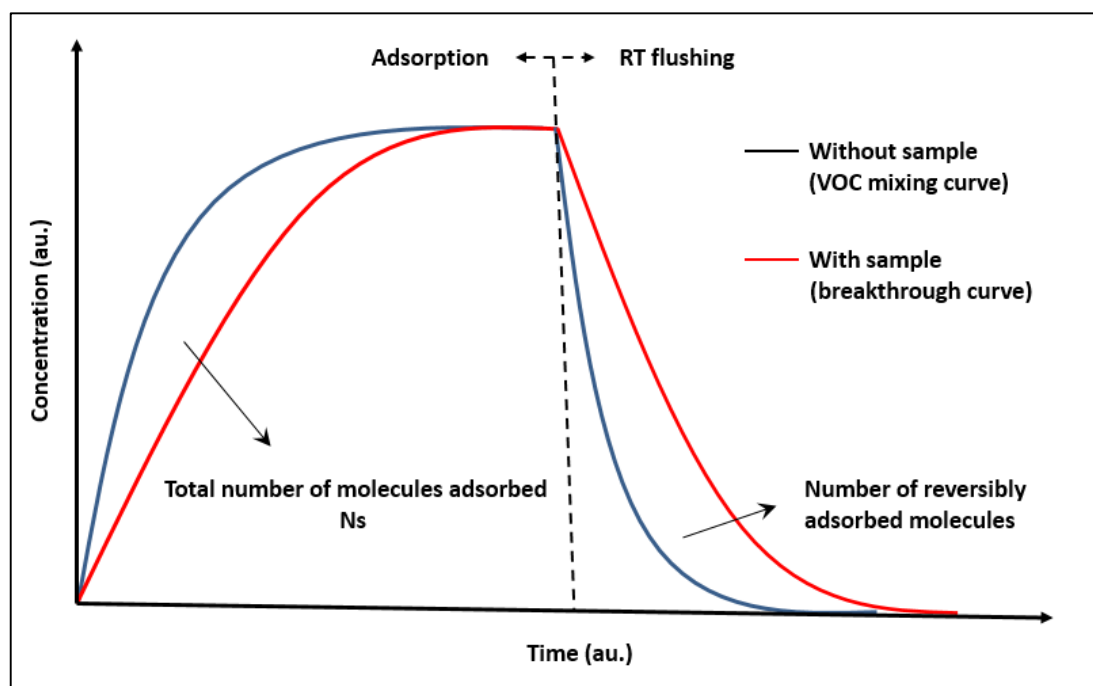
Figure II-10. VOC breakthrough curves in the absence (blue) and presence (red) of dust in the double wall photochemical reactor.

A qualitative example of a typical experiment in the double-wall reactor is shown in Figure II-10. The equilibrium is reached when the VOC outlet concentration remains constant and corresponds to the inlet concentration. Then, the VOC flow is stopped and the lines are only purged with synthetic air until the signal reaches the background level again. The integration of the area between the VOC mixing and breakthrough curves enables the calculation of the number of molecules adsorbed. The reversibly adsorbed fraction is calculated by integrating the area between both curves when flushing the lines with synthetic air. Information on the total adsorbed fraction is essential in the case of product formation since it allows determining the formation yields and the carbon mass balance.

2.2.3 Protocol used with the DRIFTs optical cell

The DRIFTs optical cell is employed to follow the adsorbed phase profiles of the VOCs and the potential products formed under dark and UV irradiation. A scheme of the protocol followed is reported in Figure II-11.
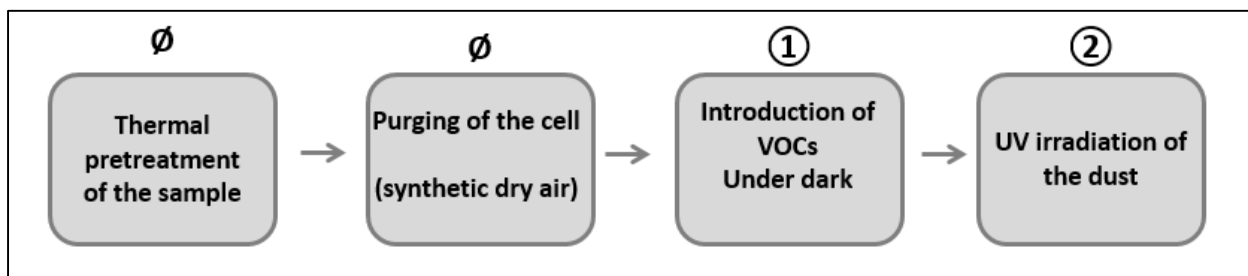
Figure II-11. Schematic of the protocol followed using the DRIFTs optical cell.

First the sample is placed in the optical cell and thermally pretreated then the cell is purged with zero air for the collection of the background. Thereafter, the gas concentration of the targeted VOC is allowed to flow through the cell and spectra are collected until surface saturation, i.e. a stable spectrum is observed. Then if required in the experiment the surface is irradiated and spectra are collected to record any reactant consumption and possible surface product formation.

2.3 Error analysis

In this section, possible systematic errors and statistical uncertainties contributing to the absolute uncertainty of γ_0 and the number of molecules adsorbed (N_s) is considered. Note that all error limits given herein are reported at 95% level of confidence. Systematic uncertainties concerning reactor temperature, VOC mixture preparation such as error on VOC injection volume or cylinder mixture, pressure of bath gas, and total flow were 1, 5, and 3 %, respectively. The overall systematic uncertainty is then calculated using the quadrature error propagation approach to derive a value of around 6% for VOC mixing ratios. Other systematic uncertainties including BET surface area determination and dust mass weight are 10 and 3 % respectively. Regarding statistical errors, the $2.\sigma$ precision, related to repeatability and reproducibility, of the signal recorder is always higher than 8 % for N_s and 13 % for γ_0. The overall uncertainty is given by Equation II-5 thus the upper limit for γ_0 uncertainty is 20 % while the N_s overall error is estimated to be up to 16 %.

(uncertainty)² = (systematic errors)² + (statistical errors)²   **(Equation II-5)**

3   Conclusion of Chapter II

In this chapter the physical and chemical characterizations and the origins of the natural dust samples followed by details on the gas preparation are presented. A subsequent part is dedicated to the methods and experimental devices used to study the interaction of VOC on natural dust samples.

The information presented in this chapter enables the reader to understand thoroughly how the experimental setups and different strategies are built in order to study the interaction of VOCs with natural dust sample. Some of them allow monitoring the gas phase; others are dedicated to the adsorbed phase. Monitoring the gas phase allows understanding the kinetics of the heterogeneous interactions of VOCs with natural dust based on the dynamic of the VOCs at the outlet of the reactor. This information is essential to improve the reliability of atmospheric models. Complementarily, the ability to monitor *in-situ* the adsorbed phase provides mechanistic information on the types of processes that are occurring at the surface of dust.

In the following chapters, the results obtained using these materials and methods are presented and interpreted in order to fulfill the scientific objectives given in chapter 1.

4 References of Chapter II

1.   Brunauer, S.; Emmett, P. H.; Teller, E., *Adsorption of Gases in Multimolecular Layers.* Journal of the American Chemical Society, 1938. **60**(2): p. 309-319.

2.   Fultz, B.; Howe, J., Diffraction and the X-Ray Powder Diffractometer. In *Transmission Electron Microscopy and Diffractometry of Materials*, Springer Berlin Heidelberg: 2013; pp 1-57.

3.   Hill, S. J.; Fisher, A.; Liezers, M., Plasma Generation, Ion Sampling and Focusing. In *Inductively Coupled Plasma Mass Spectrometry Handbook*, Blackwell Publishing Ltd.: 2009; pp 1-25.

4.   Jenkins, R., *X-ray Fluorescence Spectrometry.* Second edition. Vol. 152. 1999: John Wiley & Sons, Inc.

5.   Broekaert, J. A. C., *Inductively Coupled Plasmas in Analytical Atomic Spectrometry.* Second ed. 1993: John Wiley & Sons.

6.   Alleman, L. Y.; Lamaison, L.; Perdrix, E.; Robache, A.; Galloo, J.-C., *PM10 Metal Concentrations and Source Identification Using Positive Matrix Factorization and Wind Sectoring in a French Industrial Zone.* Atmos. Res., 2010. **96**(4): p. 612-625.

7.   Joshi, N.; Romanias, M. N.; Riffault, V.; Thevenet, F., *Investigating Water Adsorption onto Natural Mineral Dust Particles: Linking DRIFTS Experiments and BET Theory.* Aeolian Research, 2017. **27**(Supplement C): p. 35-45.

8.   Smith, D.; Spanel, P., *Selected Ion Flow Tube Mass Spectrometry (SIFT‐ MS) for Online Trace Gas Analysis.* Mass Spectrometry Reviews, 2005. **24**(5): p. 661-700.

9.   Patrik, S.; David, S., *Advances in On-line Absolute Trace Gas Analysis by SIFT-MS.* Current Analytical Chemistry, 2013. **9**(4): p. 525-539.

10.   Finlayson-Pitts, B. J.; pitts, J. N., *Chemistry of the Upper And Lower Atmosphere.* 2011: Acadamic Press

11.   Crowley, J. N.; Ammann, M.; Cox, R. A.; Hynes, R. G.; Jenkin, M. E.; Mellouki, A.; Rossi, M. J.; Troe, J.; Wallington, T. J., *Evaluated Kinetic and Photochemical Data for Atmospheric Chemistry: Volume V - Heterogeneous Reactions on Solid Substrates.* Atmospheric Chemistry and Physics, 2010. **10**(18): p. 9059-9223.

12.   Romanias, M. N.; Dagaut, P.; Bedjanian, Y.; Andrade-Eiroa, A.; Shahla, R.; Emmanouil, K. S.; Papadimitriou, V. C.; Spyros, A., *Investigation of the Photochemical Reactivity of Soot Particles Derived from Biofuels Toward NO_2. A Kinetic and Product Study.* The Journal of Physical Chemistry A, 2015. **119**(10): p. 2006-2015.

13.   Romanias, M. N.; Ourrad, H.; Thévenet, F.; Riffault, V., *Investigating the Heterogeneous Interaction of VOCs with Natural Atmospheric Particles: Adsorption of Limonene and Toluene on Saharan Mineral Dusts.* The Journal of Physical Chemistry A, 2016. **120**(8): p. 1197-1212.

Chapter III. Heterogeneous interactions of various natural dust samples using isopropanol as a model probe VOC.

82

Table of content

List of Tables

List of Figures

The adsorption properties of mineral dust toward organic molecules are poorly characterized so far. Heterogeneous processes between trace gases and mineral particles can affect the oxidative capacity of the atmosphere as well as constitute as additional sources or sinks for these species.

Therefore, in order to fullfil the objectives stated in chapter 1, in particular to investigate the impact of dust origin and chemical composition on the heterogeneous interaction of VOC with natural dust samples, experiments were performed in our laboratory and the results were published in 2018 in the **Journal of Physical Chemistry A** *as an article entitled "***Heterogeneous Interaction of Various Natural Dust Samples with Isopropanol as a Probe VOC"***.*

In this article, the adsorption efficiencies of natural dust samples collected from North and West Africa, Saudi Arabia, Gobi and Arizona desert regions toward isopropanol (IPA), a common organic pollutant released in significant amounts in the atmosphere, and used here as a probe molecule, were investigated. Experiments are performed under atmospheric pressure, room temperature, over the concentration range $(0.15 - 615) \times 10^{13}$ molecules cm^{-3}, and in the relative humidity (RH) range (0.01–85) %. Moreover, an investigation of the effect of the dust chemical composition is also carried out.

The supporting information of this chapter can be found in Annex A at the end of this manuscript. The tables and figures of the supporting information in this chapter are noted "AS" followed by their number (e.g. Table AS1).

Full citation:

M. N. ZEINEDDINE, M. N. ROMANIAS, V. RIFFAULT, F. THEVENET, *Heterogeneous interaction of various natural dust samples with isopropyl alcohol as a probe VOC*, The Journal of Physical Chemistry A 122(22), 4911–4919 (2018), DOI 10.1021/acs.jpca.8b02034

1   Introduction

It is estimated that 1600 Tg of mineral dust are released into the atmosphere on an annual basis with the ability to undergo long-range transportation [1]. The role of heterogeneous interactions of atmospheric trace gases on mineral dust particles remains an important question in tropospheric chemistry. These interactions have been a subject of great interest in the past decade, due to their momentous capability in altering the atmosphere chemical balance and modifying dust particle properties [2, 3]. Recent studies evidenced that mineral dust may significantly influence the local and regional abundances of trace gases in the troposphere [1, 4-6].

The mineralogy of dust particles is complex and diverse; it depends on the primary emission sources [7-11]. Mineral particles mostly originate from eroded soils, thus their chemical composition is similar to that of top soil material. Several studies on the elemental content of windblown dusts originating from various locations show that the primary elements are Silicon (Si) and Aluminum (Al) [12, 13]. Si is mainly present in SiO_2-based phases (e.g. quartz, cristobalite) and in various aluminosilicate minerals. Aluminosilicates such as feldspars and clays (illite, kaolinite, montmorillonite, etc.) are the major aluminum-bearing minerals [12-14]. Al is also present in the crystalline polymorphic phases of aluminum oxide Al_2O_3. Calcium (Ca) is also an important element of mineral dust mainly present in the forms of calcite, calcium oxide, aragonite, and dolomite. Besides the abovementioned elements, others such as K (K-feldspar, white mica, illite), Na (albite feldspar, smectite clay minerals), Fe (in mineral oxides e.g. hematite, magnetite), Ti (TiO_2 phases of anatase and rutile) and Mg (dolomite) are also present in mineral dust and source sediments [8, 10, 13-16]. Moreover, it should be noted that the mineralogical composition of airborne dust particles also depends on the size fractionation during emission and transport [10]. To be able to account for the fractionation effect, Journet et al. [10] specified the chemical composition of the finer textural classes of soils in the silt (2-63 µm) and clay (< 2 µm) fractions. The silt fraction contains primarily minerals such as quartz, feldspars and mica while other minerals such as clays and iron oxides are mostly found in the clay fraction [10].

Literature studies on the heterogeneous chemistry of mineral dusts mainly focused on the uptake and transformation of inorganic trace gases [17]. Nevertheless, only few studies have

been conducted on natural mineral dust samples, while even less attempted to correlate the effect of chemical composition on mineral dust reactivity [17]. Besides inorganic species, heterogeneous reactions of volatile organic compound (VOCs) are also of interest in the atmosphere since they may impact the transformation and transportation of VOC, and thus their atmospheric concentration as well as the mixing ratios of atmospheric oxidants and other related species at the local or even regional scales [18-20]. In addition, heterogeneous reactions of VOCs can produce species such as organic acids leading to secondary organic aerosol formation, [11, 18] and can alter the physicochemical properties of atmospheric particles, such as size or hygroscopic properties [21, 22]. Although the body of literature on heterogeneous reactions of VOCs has been recently expanded and reviewed [23], its impact on the Earth's atmosphere has yet to be asserted. There is still a strong lack of kinetic and product data for VOC reactions on natural mineral dusts, and particularly, how mineral dust composition can influence the uptake process. These pieces of information are of significant importance since current atmospheric models use elemental ratios as input data to simulate the impact of mineral dust reactivity to the tropospheric chemistry [24]. Therefore, the accuracy of the predictions would be significantly improved if laboratory experiments could correlate the uptake efficiency with the elemental composition.

The objective of the present work is to evaluate the effect of chemical composition on the interaction of volatile organic compounds with natural dust samples. Natural dust samples from different regions of the world are used as surrogate materials. Isopropanol (IPA) is used as a model VOC; IPA is a common anthropogenic pollutant released in the atmosphere mainly by industrial activities. It is highly reactive and may easily lead to acetone and other lighter compounds thus being a good probe to evaluate the effect of the chemical composition [25-27]. Kinetic measurements are conducted in a U-shaped flow reactor coupled with a SIFT-MS for the detection of the gas phase species. The adsorption isotherms and the uptake coefficients are determined over a wide range of concentrations $(0.15 - 615) \times 10^{13}$ molecules cm^{-3} in the relative humidity (RH) range (0.01–85)% and at room temperature (RT), 296 K. To the best of our knowledge this is the first experimental study reporting the effect of the chemical composition on VOC interaction with natural dust samples.

2   Materials and methods

2.1   Materials

2.1.1   Origins of the natural dust samples

The five natural mineral dust samples used in this study originate from various regions in order to encompass a large diversity of chemical compositions Figure II-1. The natural top soil samples used were collected (i) close to the oasis of Nefta (Tunisia) and the city of Mbour (Senegal), corresponding to two different regions along North and West Africa and (ii) from Saudi Arabia (Rawdat arid region) (iii) from the Gobi desert of china. The experiments are performed using only the smallest sieved size fraction of the natural dust samples (< 100 μm) that can be suspended in air. In particular, a mechanical sieve shaker is used to fractionate the soil samples into different classes. Then, the finest collected fraction (<100 μm) is used for the experiments. Besides, a commercially available ATD sample (Powder Technology Inc.) is also studied. The ATD sample correspond to ISO 12103-1, A1 ultrafine ATD (3-22 μm, where ~ 97% is below 11 μm), collected in June 2013.

2.1.2   Physical and chemical characterizations of the natural dust samples

The chemical characterization of the samples is performed employing widely used techniques such as X-ray diffraction, X-ray fluorescence and inductively coupled plasma mass spectrometry (ICP-MS) [28-30]. The chemical compositions of the different samples are also reported Tables II-2 and II-3. The X-ray measurements were conducted using around 1 g of sieved mineral dust and two complementary techniques: (i) X-ray diffraction (XRD; Bruker D2 phaser 2 theta analyzer) and (ii) X-ray fluorescence (XRF; Bruker AXS explorer S4 pioneer). Regarding the ICP-MS analysis, a few mg of the dusts were dissolved in an acidic solution (HF/HNO$_3$/HCl) and thermally pretreated at 220°C before analysis [31]. Since the quantity required for ICP-MS analyses is in the milligram range, three sets of measurements were performed for each sample to evaluate the sample homogeneity; the variation coefficients for the major elements never exceeded 10%.

Furthermore, nitrogen adsorption measurements were performed using a sorption analyzer, whose robustness has been previously demonstrated [32, 33]. The specific surface area, SSA, of the collected dust samples was determined employing the BET method within 0.05 to 0.3 relative pressures, P/P$_0$. At least three adsorption measurements were conducted for each sample, and the average values are presented in Table II-1.

2.1.3 Gas preparation

IPA concentrations are obtained from calibrated gas cylinders (PRAXAIR) at 10 and 507 ppm$_v$ in N_2, which are further diluted in zero dry air. The IPA dilution factor in the experiments ranges between 2 and 170 which allows the variation of IPA concentrations from $(0.15 - 615) \times 10^{13}$ molecules cm^{-3}. The zero air is generated by a classical air compressor, and then sent into a catalytic zero air generator (Claind AZ-2020, Lenno, Italy) which is coupled to a pressure swing adsorption (PSA) device. The remaining impurity levels in the air stream are always lower than the analytical system detection limits, that is to say VOCs < 0.1 ppb, CO_2 < 10 ppb, CO < 80 ppb and H_2O < 2 ppm. The relative humidity is controlled by changing the mixing ratio of dry and humid air. In particular, the zero air flow is moistened after passing through a H_2O bubbler and is further diluted with dry air to obtain the desired RH level. The exact relative humidity in our gas flow is recorded using a temperature and moisture meter (KIMO HQ 210).

2.2   Methods

2.2.1   Experimental setup

A detailed schematic of the experimental setup is presented in Figure III-1 and has been described in details previously [11, 34]. Briefly, it consists of three parts: (i) the gas flow generation system (ii) the U-shaped flow reactor, and (iii) the analytical device. The gas flow generation line is made of stainless steel and Teflon. Calibrated mass flow controllers (Bronkhorst) are used to introduce IPA that is further diluted in zero air to achieve a total flow rate of 700 sccm. The reactor consists of two parts: the upper one is a bypass line with a total volume of 15 cm^3; it is used to monitor the IPA concentration in the absence of dust. The lower part, with similar volume of 15 cm^3, is equipped with a quartz wool sample-holder (geometric surface area 4.95 cm^2), on top of which the mineral sample is placed. The two parts are connected via two 3-way valves. The exact temperature of the sample is recorded using a K-type thermocouple inserted inside the U-shaped reactor. A known amount of mineral dust is placed on the top of a porous quartz wool sample-holder as shown in Figure III-1. The residence time of IPA in the reactor is estimated to be around 1 second. The monitoring of IPA is achieved employing a Selected-Ion Flow-Tube Mass Spectrometer (Voice 200 SIFT-MS). The SIFT-MS is an analytical technique based on the chemical ionization of the analytes using three reagent ions: H_3O^+, NO^+ and O_2^+. IPA is detected using H_3O^+ and NO^+ ions at mass peaks 43 ($C_3H_7^+$)

and 59 ($C_3H_7O^+$), respectively. The detection limits of the recorded mass peaks are found to be around 2 ppb under our experimental conditions.
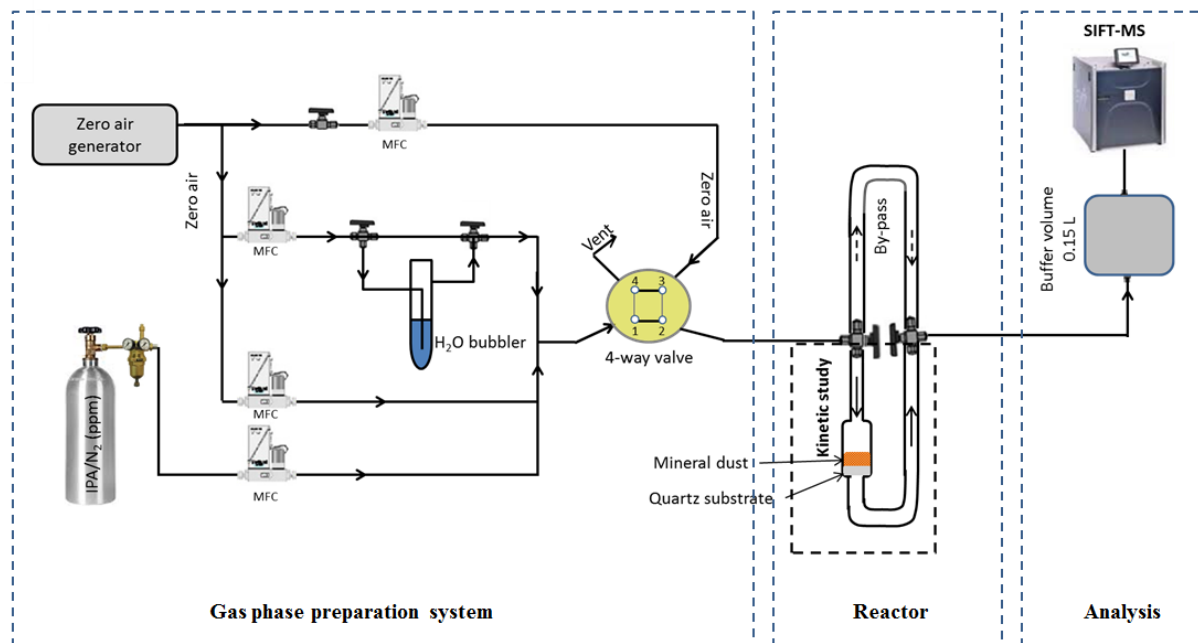
Figure III-1. Schematic representation of the experimental setup used for the kinetic studies. MFC: Mass flow controller.

2.2.2 Experimental protocol

Before each experiment the dust of interest is placed into the reactor and thermally pre-treated under dry zero air at 200°C to remove any pre-adsorbed species (e.g. removal of strongly adsorbed water, or other VOCs). Thereafter, the sample is cooled down to room temperature while still under zero air.
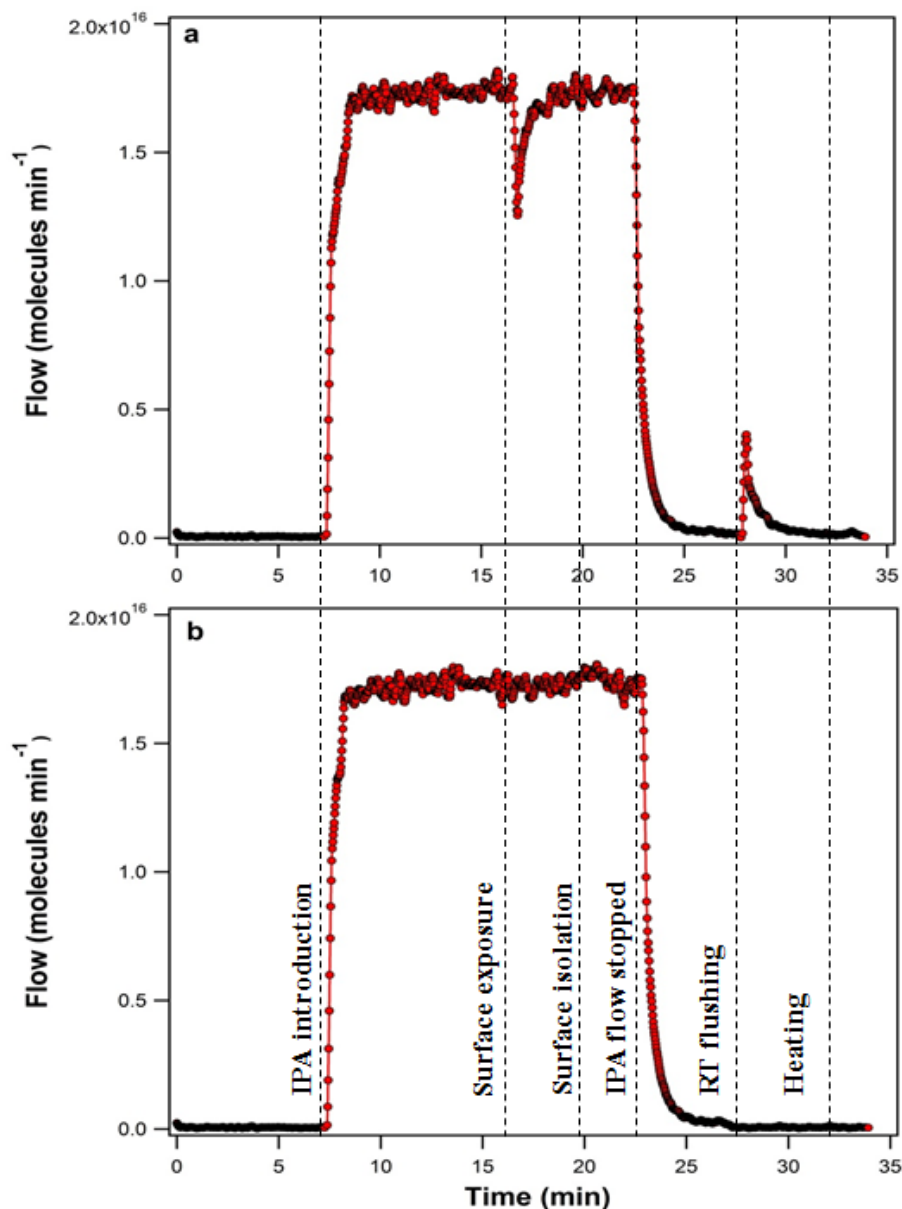
Figure III-2. Typical gas-phase profiles of IPA recorded with the SIFT-MS at 298 K and 30% RH in the presence (a) and absence (b) of dust, respectively. The H_3O^+ ion is used to monitor IPA with the SIFT-MS at the mass peak 69 ($C_5H_8H^+$). Step 1: background collection; step 2: IPA is introduced; step 3: dust surface exposure to IPA; step 4: surface isolation; step 5: RT flushing; step 6: heating the dust surface.

In case of dry conditions no other pretreatment takes place. However, under RH conditions and prior to IPA exposure, the freshly prepared mineral sample is exposed for about 10 min to water vapor present in the reactor during which the background is collected in the same experimental conditions. Longer (up to 30 min exposure) or even no exposure of samples to water vapor had no impact on the observed uptake data. Once room temperature is reached,

the background level of IPA is monitored using SIFT-MS as shown in Figure III-2, step 1. In step 2, the gas flow direction is changed to the 15 cm^3 by-pass line by means of the two 3-way valves and a known concentration of IPA is introduced. When a steady-state concentration is achieved, the flow is directed through the reactor (step 3), exposing the dust surface to IPA (Figure III-2a). The uptake of IPA by the sample promotes a decrease in IPA concentration, followed by a progressive increase towards the initial value. It should be noted that since the by-pass and the reactor have equal volumes, the observed decrease to IPA concentration during the adsorption experiment is not due to volume differences. The latter has been validated with complementary experiments in the absence of dust (Figure III-2b). Once the equilibrium between the adsorbed and gas phases is achieved, the reactor is isolated by changing the flow direction to the by-pass as shown in step 4 (Figure III-2a). Thereafter, the IPA flow is stopped and the lines are purged with air (step 5). Consequently, the IPA concentration reaches again the background level. Then, the flow is directed through the reactor to purge the surface and recover the weakly adsorbed fraction of IPA. Lastly, the surface is heated up to 110°C to remove the remaining quantity of adsorbed IPA (step 6).

2.2.3 Uptake measurements

In order to assess the affinity of the natural dust samples towards IPA the initial uptake coefficients, γ_0, are determined. γ expresses the probability of a colliding molecule to be taken up by the surface or to react with the surface [17]. The time resolution provided by the SIFT-MS is high enough to allow the determination of γ_0 within the first seconds of the interaction between IPA and dust. The uptake coefficient of IPA is derived from the following equations:

$$\frac{d(IPA)/dt}{V} = k_{het}[IPA] \qquad \textbf{(Equation III-1)}$$

$$k_{het=}\frac{d(IPA)/dt}{V[IPA]} = \omega\gamma_0 \qquad \textbf{(Equation III-2)}$$

with:

$$\omega = \frac{cA_s}{4V} \qquad \textbf{(Equation III-3)}$$

and finally:

$$\gamma_0 = \frac{4\{d(IPA)/dt\}}{cA_s[IPA]} \qquad \textbf{(Equation III-4)}$$

where (IPA) denotes the number of IPA molecules taken up by the dust surface at the beginning of exposure (molecule); k_{het}, the first-order rate coefficient of the heterogeneous degradation of IPA (s^{-1}); V, the volume of the reaction zone (cm^3); [IPA], the gas-phase IPA concentration (molecules cm^{-3}); ω, the collision frequency of IPA (s^{-1}); c, the mean molecular speed (cm s^{-1}); A_s, the effective surface area of the dust (cm^2), calculated as the product of SSA with the mass of the sample.

2.2.4 Adsorption isotherms

Beside uptake coefficients, the adsorption isotherms of IPA on the natural mineral samples are determined at 30% of RH in order to simulate atmospheric conditions. In particular, the total number of molecules taken up per surface unit, N_s (molecules cm^2), is derived from the integration of the area of the adsorption peak in a typical uptake experiment (Figure III-2a), divided by the effective surface area of the dust, calculated as the product of SSA with the mass of the sample, according to Equation III-5: [35]

$$N_s = \int_{\tau=0}^{\tau=1} \frac{F(t)}{A_s} dt \qquad \textbf{(Equation III-5)}$$

where F is the flow rate (molecules s^{-1}) of IPA molecules through the reactor.

3 Results and discussions

3.1 Initial uptake coefficients of IPA onto natural mineral dust samples

3.1.1 Concentration dependence of IPA uptake

The dependence of the initial uptake coefficient on IPA concentration is investigated in the range of $(0.15 - 615) \times 10^{13}$ molecules cm^{-3} at room temperature and under 30% RH (Figure III-3). It is observed that γ_0 values are independent of IPA concentration over the entire investigated range (Figure III-3). This behavior is expected since the initial uptake expresses the interaction of a gas molecule with the fresh, i.e. unexposed surface. In addition, it provides an experimental validation of first-order kinetics that is required for γ determination (Equations III-1 to III-4). The average values of the uptake coefficient for each sample studied at room temperature and 30% RH are:

$\gamma_0(\text{ATD}) = 8.67 \times 10^{-8}$, $\gamma_0(\text{Rawdat}) = 1.11 \times 10^{-7}$, $\gamma_0(\text{Mbour}) = 7.10 \times 10^{-8}$, $\gamma_0(\text{Nefta}) = 2.89 \times 10^{-8}$, $\gamma_0(\text{Gobi}) = 6.52 \times 10^{-7}$
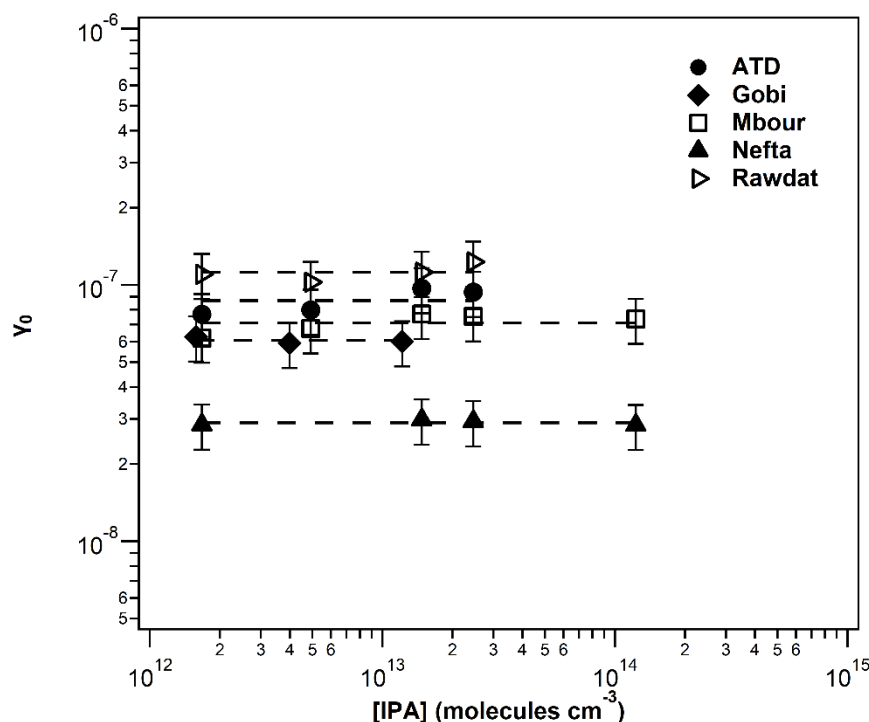
Figure III-3. Initial uptake coefficients, γ_0, determined at 296 K and 30% RH as a function of the IPA gas-phase concentration for the five different natural samples used. The error bars represent the overall estimated uncertainty on γ_0. Dashed lines are the average value for each sample.

3.1.2 Relative humidity dependence of IPA uptake

Laboratory studies have confirmed that heterogeneous reactions on mineral dust particles can be influenced by hygroscopicity[11, 19, 36]. In an attempt to address the effect of RH on the interaction of IPA with the dust samples, the IPA initial uptake coefficient is measured at room temperature in the RH range of <0.01 − 85%. A typical uptake experiment where Rawdat dust is exposed to 1 ppm of IPA at 30 % RH is shown in Figure III-2a. Under humid conditions the uptake of IPA is reversible and equilibrium between the adsorbed and gas phases is achieved after ~15 min of surface exposure. On the contrary, under dry conditions and

at lower concentrations the uptake process is longer and could require several hours to achieve equilibrium conditions as shown in Figures AS1 and AS2 of annex A.
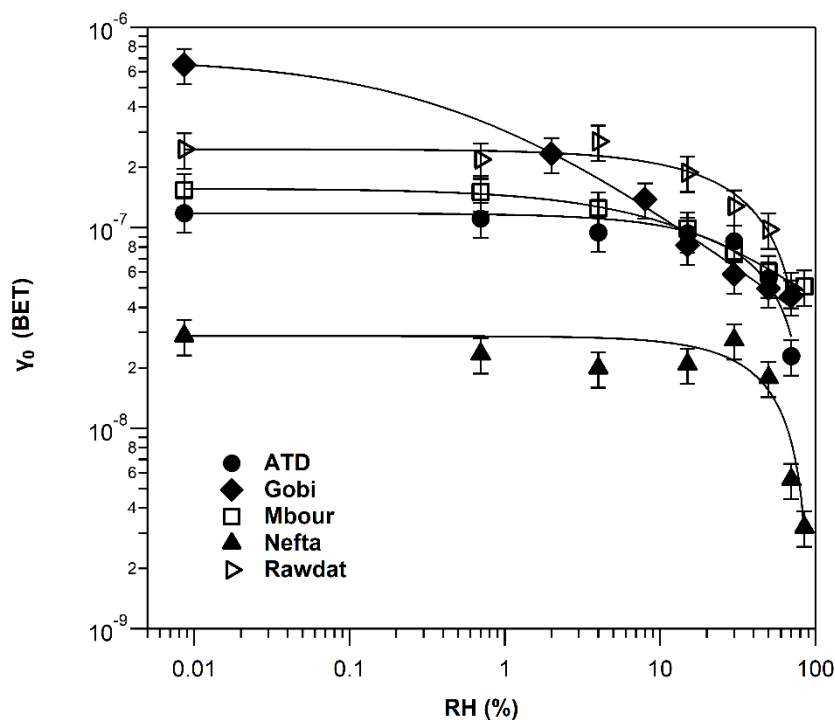
Figure III-4. Initial uptake coefficients, γ_0, of IPA onto the five different natural dust samples determined over the RH range 0.01 – 85%. The solid lines correspond to the fitting of experimental results with the following expression: $\gamma_{RH} = \gamma_{dry} - \alpha \, RH^b$ Error bars represent the overall estimated uncertainty on γ_0.

The RH dependence of the initial uptake coefficients is studied for the different samples and the results are displayed in Figure III-4. Each data point represents the average value of at least 3 measurements performed in the range where γ_0 is independent on the IPA concentration. From dry conditions up to around 20% RH the uptake coefficients are constant for all the studied dust samples. However, after this threshold a dramatic decrease is observed up to 80% of RH reflecting the competition between IPA and H_2O molecules for available adsorption sites. Besides, in a recent study performed in our laboratory, the hygroscopic properties of natural dust samples (using the same ones as in the current study) were determined using diffused reflectance infrared spectroscopy (DRIFTS) [33]. It was found that the water monolayer for Mbour and Nefta dust was formed at around 17% RH while for Rawdat, ATD and Gobi particles the water monolayer was formed at around 23% RH. Consequently, the sharp drop observed in the uptake coefficient at RH levels above 20% could be attributed to the formation of one or more water layers above the dust particles that blocks the active sites and inhibits the direct

interaction of IPA with mineral dust. It should be mentioned that in the literature, the surface coefficients for several VOCs on mineral oxides have been determined [37-40] as a function of RH. The results showed that they decrease significantly as RH increases in agreement with the results of the current study.

The RH dependence of the uptake coefficients for the different samples is fairly simulated using the empirical Equation III-6, that has already been used in the past to simulate the uptake of trace gases on mineral oxide surfaces [41, 42]:

$$\gamma_{RH} = \gamma_{dry} - aRH^b \qquad \qquad \textbf{(Equation III-6)}$$

where γ_{dry} is the uptake coefficient measured under dry conditions and a, b are variable parameters, whose values are given in Table AS1 of annex A. Since the initial uptake determined in our study is found independent of IPA concentration (see section on concentration dependence), then one can use Equation III-6 to extrapolate the uptake coefficient of IPA on each dust sample under relevant RH tropospheric conditions.

3.2   Adsorption isotherms of IPA onto natural mineral dust samples

The adsorption isotherms of IPA for all the mineral dust samples are determined at room temperature and 30% RH in the IPA concentration range of $0.15 - 615 \times 10^{13}$ molecules cm^{-3}. Results are presented in Figure III-5. One can note that the Nefta sample has the lowest adsorption efficiency leading to low surface coverage values, N_s, as well as the lowest uptake coefficients. It could be attributed to the significant high Si content (around 98% Si), in the form of quartz, which has been reported in the literature as the less reactive/adsorptive component of dust [17].
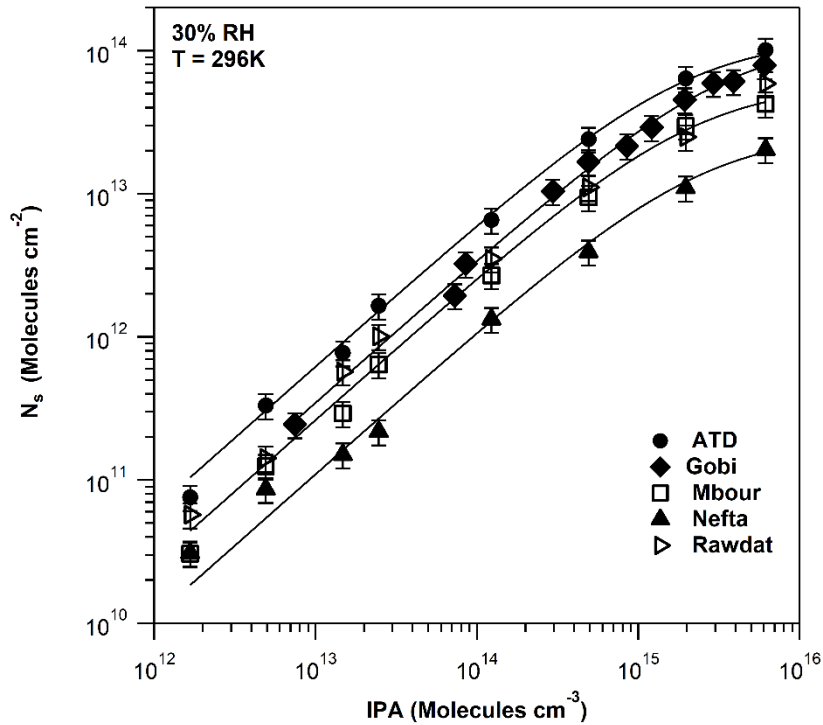
Figure III- 5. Adsorption isotherms of IPA for the five natural dust samples determined at 296K and 30% RH. The error bars represent the overall uncertainty on Ns determination. The solid lines are non-weighted fits through the data using the Langmuir expression.

Among the five samples compared, ATD and Gobi have the highest adsorption efficiency. Both dusts are rich in Al and Ca mainly in the form of Al_2O_3 and $CaCO_3/CaO$ forms respectively. Furthermore, comparing the adsorption isotherm profiles shown in Figure III-5, it is evidenced that the number of IPA molecules adsorbed increases as concentration increases, approaching a plateau for IPA concentrations beyond 5×10^{15} molecules cm^{-3} [11]. This behavior is characteristic of a monolayer adsorption process, allowing our experimental data to be fitted employing the Langmuir adsorption model that is valid for monolayer adsorption on solid surfaces and insignificant gas-adsorbate and adsorbate-adsorbate interactions. This model is described by Equation III-7:

$$\theta = \frac{N_S}{N_{max}} = \frac{K_{Lang} \times [IPA]}{1 + K_{Lang} \times [IPA]}$$
(Equation III-7)

where θ is the fractional coverage of IPA molecules on the dust surface, N_s is the number of IPA molecules adsorbed (molecules cm^{-2}), N_{max} is the monolayer saturation surface coverage (molecules cm^{-2}) and K_{Lang} (cm^3 $molecule^{-1}$) is the Langmuir equilibrium constant, which

describes the partitioning between the gas and adsorbed phases. The model fits well the experimental results. Furthermore Equation 7 can be rearranged to:

$$\frac{[IPA]}{N_S} = \frac{1}{N_{max} \times K_{Lang}} + \frac{1}{N_{max}} \times [IPA]$$ **(Equation III-8)**

Therefore the linear least-squares fit of the plots [IPA]/N_s versus [IPA] provides N_{max}, K_{Lang} and the partition coefficient K_{Lin} ($K_{Lin} = K_{Lang} \times N_{max}$) for the different dust samples [17]. The results are given in Table III-1. ATD has the highest monolayer coverage with $N_{max} = (1.65 \pm 0.26) \times 10^{14}$ molecules cm^{-2}, followed by Gobi desert dust ($N_{max} = (1.35 \pm 0.16) \times 10^{14}$ molecules cm^{-2}). Regarding the other samples, N_{max} values are by a factor of 4 lower, around 3 $\times 10^{13}$ molecules cm^{-2}. Since the monolayer coverage varies between samples, a direct comparison of the equilibrium constants K_{Lang} is not representative. It is suggested to compare the partitioning constants K_{Lin} that include the effect of monolayer coverage [17]. The highest K_{Lin} values are observed for ATD, Rawdat and Gobi dusts.

Table III-1. Saturation surface coverage, N_{max}, and partitioning constants K_{Lang} and K_{Lin} values for IPA adsorption on several studied dust samples at 30% RH and at 296 K. The overall uncertainty for N_{max} and K_{Lang} is estimated to be around 16% while that for K_{Lin} is around 20%.

Dust sample	[IPA] (10^{13} molecules cm^{-3})	N_{max} (10^{13} molecules cm^{-2})	K_{Lang} (10^{-16} cm^3 molecule^{-1})	K_{Lin} (10^{-2} cm)
Mbour	0.15 – 615	4.27 ± 0.68	5.59 ± 0.89	2.39 ± 0.47
Nefta	0.15 – 615	2.77 ± 0.44	4.09 ± 0.65	1.13 ± 0.22
ATD	0.15 – 615	16.5 ± 0.26	3.14 ± 0.50	5.18 ± 1.04
Rawdat	0.15 – 615	3.91 ± 0.62	8.73 ± 0.40	3.41 ± 0.68
Gobi	0.1 – 601	13.5 ± 0.16	2.68 ± 0.32	3.60 ± 0.70

The impact of RH to the number of IPA molecules adsorbed after exposing the dust samples to a fixed IPA concentration (i.e. 2.46×10^{13} molecules cm^{-3}) is given by Figure S4. Clearly, an inverse dependence is observed, indicating the competition between IPA and water molecules on the available sites. Nefta and Mbour samples appear to have the lowest adsorption capacity over the entire range of RH used. On the contrary for the other dusts and under ambient

RH conditions, no significant variation is observed. Furthermore, in order to simulate the dependence of surface coverage with RH, results are simulated by the following empirical equation:

$$N_S = \frac{a}{b + (RH^c)}$$

(Equation III-9)

where the values of parameters a, b and c are displayed in Table AS1 of annex A.

3.3   Impact of the chemical composition of the dust on IPA uptake

Attempting to correlate the chemical composition with the initial uptake coefficients determined for each dust, the principal elements of the studied samples, namely Si, Al, Ca, and Fe are investigated. As shown in Figures III-6a and III-6b under dry conditions a linear trend of γ with Al/Si and Fe/Si ratios is observed while no trend is observed with Ca. More precisely, including the commercial ATD sample the correlation coefficient R^2 of the linear fit (dashed line) is 0.65 for Al/Si and 0.83 Fe/Si ratios. However, excluding ATD, an excellent correlation between the uptakes and the corresponding elemental ratios is observed (solid line) with R^2 values of 0.93 for Al/Si and 0.97 Fe/Si ratios. In general the ATD sample does not follow the trends observed for the other natural samples. The observed deviation in its γ values could be attributed to several parameters, such as morphology and particle size or to the sieving protocol followed by the supplier, or even to the presence of low but non negligible amounts of MgO and K_2O in ATD compared to other samples that could affect its adsorption efficiency.
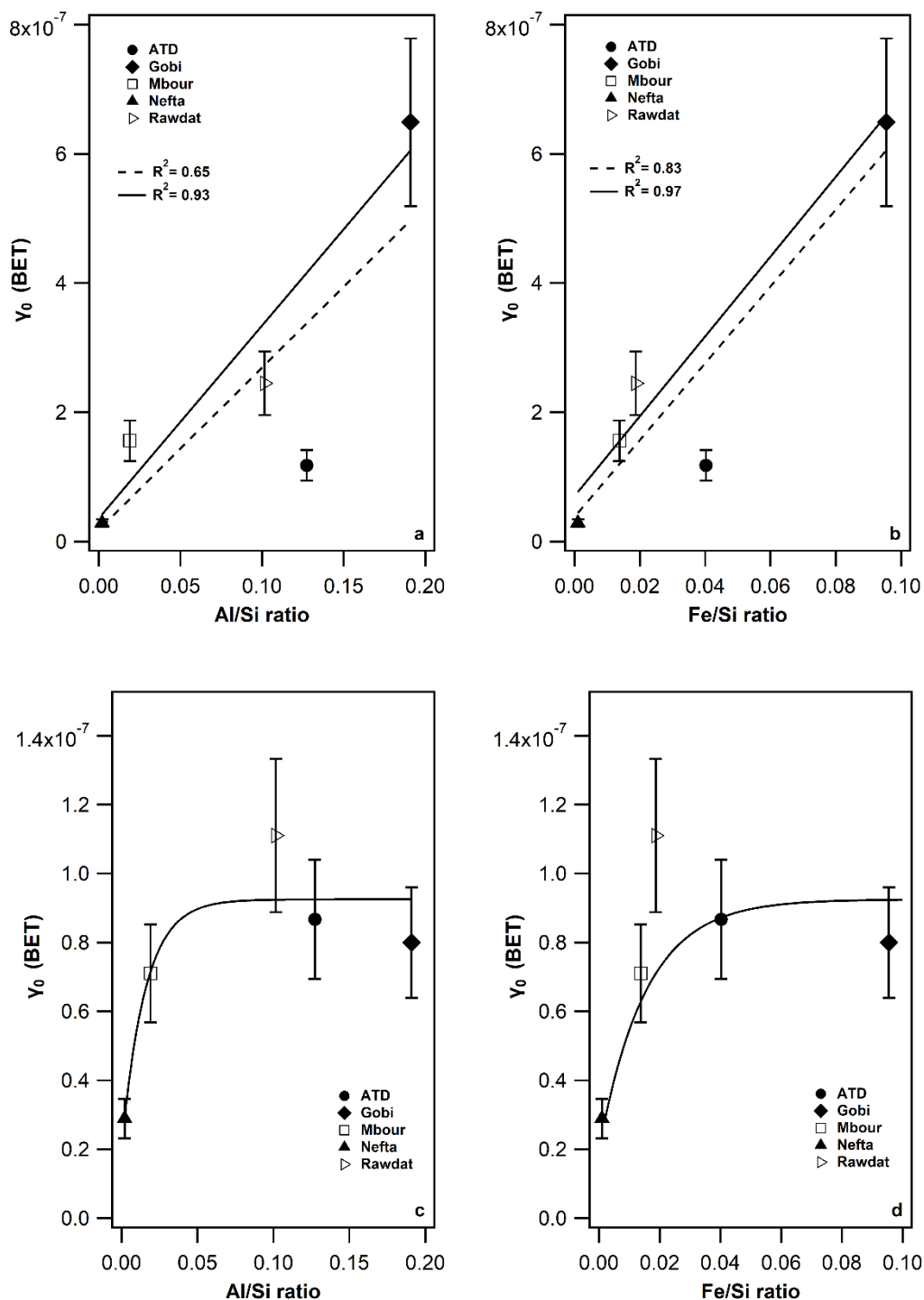
Figure III-6. Initial uptakes of IPA under dry (a-b) and 30% RH conditions (c-d) for all studied dust samples as a function of Al/Si and Fe/Si ratios. The error bars represent the overall uncertainty on the uptake and K_{Lin} determination. The lines in (a-b) correspond to the linear fit of the experimental data with (dashed) or without (solid) the commercial ATD sample. The solid lines in (c-d) correspond to the exponential fitting of experimental results

Since there are no literature data correlating the uptake/reactivity of VOCs with the chemical composition of mineral dusts, we collected the uptake coefficients reported in the literature for the main inorganic species, i.e. NO_2, O_3 and SO_2, on mineral oxides and natural dusts and tried to correlate them with respect to Al/Si ratio. The collected results are shown in Table AS2 of annex A.

In the case of NO_2 (Figure III-7a), a linear increase ($R^2 = 0.99$), similar to our study, can be observed when plotting γ_0 reported by Underwood et al. [43] as a function of Al/Si, whereas much lower values (2-3 orders of magnitude) were obtained by Ndour et al. [44] but at 25% RH and for steady state uptakes.

Concerning ozone, γ_0 reported by Hanish et al. [45] and Michel et al. [46] also exhibit a linear trend with the Al/Si ratio (Figure III-7b; $R^2 = 0.93$). Similarly, an excellent correlation of the SO_2 uptake (Figure III-7c) with the Al/Si ratio is observed ($R^2 = 0.99$) for the data of Usher et al. [47] and Adams et al. [48] Consequently, the Al/Si ratio appears as a determining factor for the adsorption efficiency of dust which can be linearly correlated with the initial uptake coefficients of both organic and inorganic species.

At 30% RH, as shown in Figures III-6c and III-d, a linear trend for γ is observed up to ratios of Al/Si and Fe/Si of 0.1 and 0.03, respectively. Above these limits γ is independent of the respective elemental ratios and a plateau is reached. The latter indicates that the impact of water on the observed kinetics is highly dependent on the chemical composition of dust; the dust surface possibly becomes more hydrophilic as the Al and Fe contents of the dust increase. However, to validate this assumption, a higher number of samples is required and the hygroscopic properties of various Al/Si and Fe/Si fractions should be examined as well.
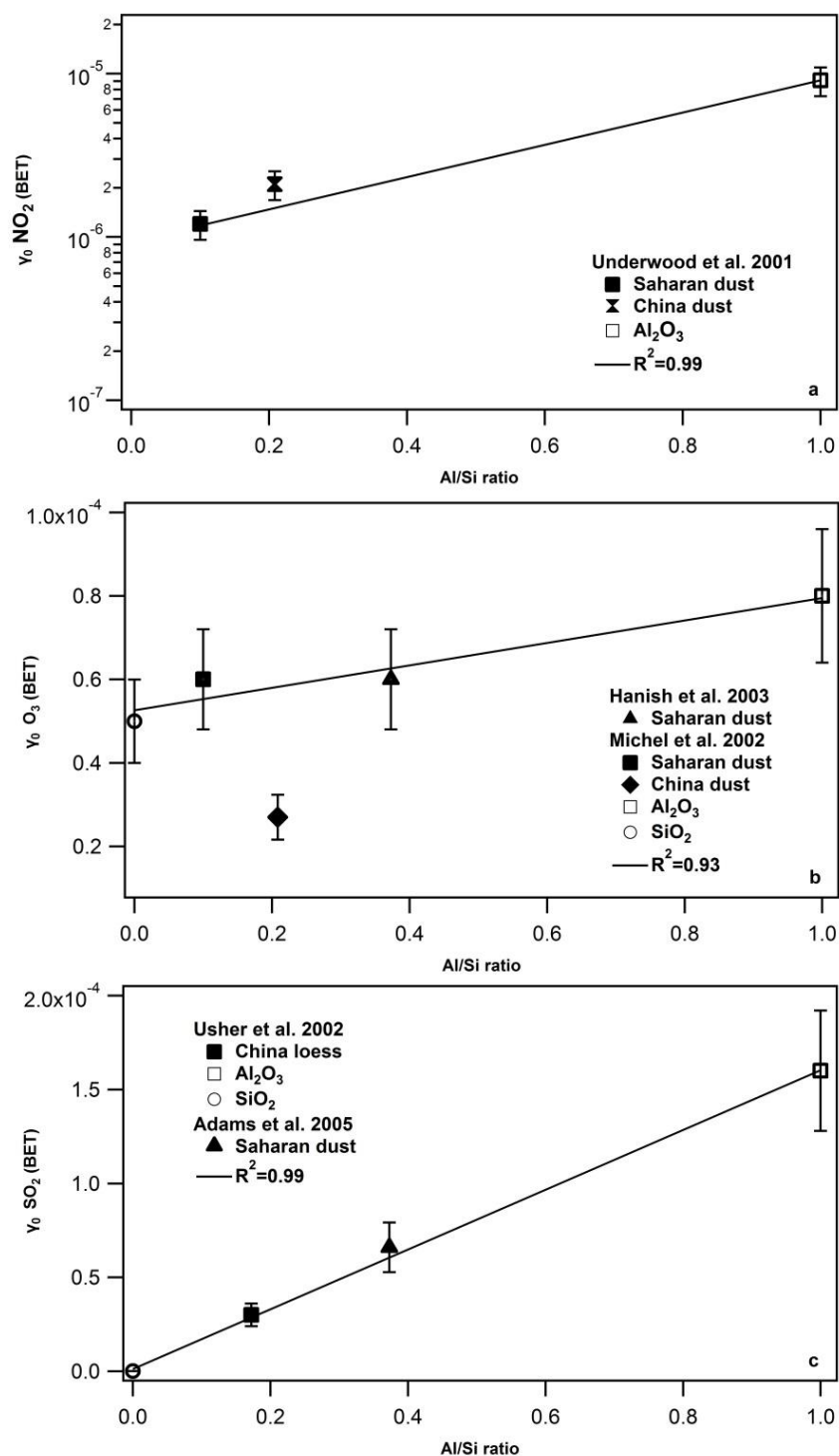
Figure III-7. Effect of Al/Si ratio on the uptake of (a) NO₂, (b) O₃, and (c) SO₂, respectively. The solid lines correspond to the linear fit of the experimental data. Open symbols denote data obtained on individual mineral oxides (open circles: SiO₂; open squares: Al₂O₃). The error bars represent the overall uncertainty on the uptake determination as given by the authors.

3.4   Desorption profiles of IPA from natural mineral dust samples

The IPA desorption profiles are recorded at (i) room temperature, and (ii) under thermal treatment of dust. It is observed that under dry conditions and RT flushing, the recovered fraction is always lower than the adsorbed one. However, by heating up the surface to 110°C the remaining quantity of IPA is recovered in the gas phase (Figure AS1 in annex A) pointing out that IPA is adsorbed onto at least two distinct types of sites with different adsorption enthalpies.
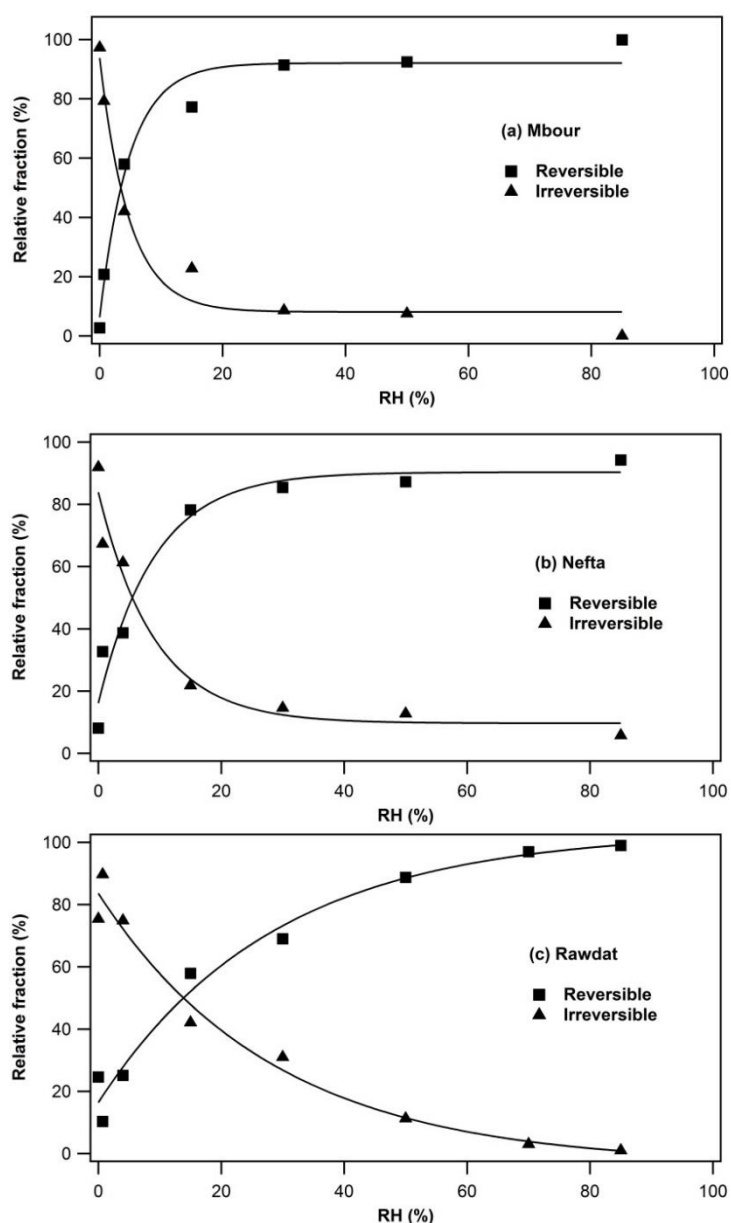
Figure III-8. Reversibly and irreversibly adsorbed fractions at 296 K from dry to 85% RH for three of the natural dust samples: (a) Mbour, (b) Nefta and (c) Rawdat. The solid lines represent the power fitting through the data.

More information could be obtained about the nature of the interaction by investigating the reversible and irreversible fractions of IPA as a function of RH for Nefta, Rawdat, and Mbour samples are shown in Figure III-8. It is observed that as RH increases the reversible fraction increases until a plateau is reached at around 20% for Nefta (Figure III-8a), Mbour (Figure III-8b) and at higher levels for Rawdat (Figure III-8c), while the opposite trend is noted for the irreversibly adsorbed IPA. Considering that the water monolayer is formed at around 20% of RH for all the dust samples, [33] it seems that water molecules compete and block the active sites that lead to irreversibly adsorbed IPA. Especially above the water monolayer formation the number of sites where IPA can be irreversibly adsorbed is almost non-existent.

To further evaluate the results of the desorption curves, the reversibly adsorbed fractions of IPA at room temperature are determined at 30% RH in the IPA concentration range of $0.15 - 615 \times 10^{13}$ molecules cm^{-3} (Figure AS3 in annex A). Similarly to adsorption, it is evidenced that the higher the IPA concentration, the higher the number of IPA molecules desorbed, approaching a plateau for IPA concentrations beyond 5×10^{15} molecules cm^{-3} [11]. This behaviour is characteristic of a monolayer adsorption process hence the experimental data are fitted employing the Langmuir model and results are given in Table AS3 of annex A. No difference is observed in the partition coefficient K_{Lin} from the analysis of adsorption and desorption curves for Nefta and Mbour samples (K_{lin} desorption ~ K_{lin} adsorption), while in the case of Rawdat and ATD the agreement was better than 85%.

4   Conclusions on probing natural dust samples with IPA

In this study the heterogeneous interactions of IPA with several dust samples collected over various regions of the world are studied at several IPA concentrations and in the RH range $0.01 - 85\%$. The initial uptake coefficients are independent of the IPA initial concentration. Furthermore, γ is independent of RH up to ca. 20% then dramatically decreases, which reflects the competition between water molecules and IPA after the formation of a water monolayer on the dust surface. The uptake coefficients under any RH tropospheric conditions can be derived from an empirical expression, $\gamma_{RH} = \gamma_{dry} - aRH^{b}$. In addition, investigating the effect of chemical composition on IPA uptake coefficients, a linear correlation with the Al/Si and Fe/Si elemental ratios for the different dust samples is observed. Reviewing the initial uptake coefficients for inorganic species from the literature and plotting them versus the Al/Si ratio also highlighted significant linear correlations, thus revealing that the bulk chemical composition could be an indicator of the adsorption efficiency of mineral samples. Finally, the

analysis of the IPA adsorption isotherms using the Langmuir model allowed us to determine the monolayer surface coverage N_{max} and the partitioning coefficients K_{lin}. In summary, in the current study it is shown for the first time that the chemical composition of the mineral dust surfaces can be correlated with kinetic and surface equilibrium parameters for both VOCs and inorganic compounds. This study also highlights the interest of working with natural samples of different origins, for which the kinetic parameters can be evaluated with regard to aerosol composition.

5 References of Chapter III

1. Satheesh, S. K.; Krishna Moorthy, K., *Radiative Effects of Natural Aerosols: A Review.* Atmospheric Environment, 2005. **39**(11): p. 2089-2110.

2. Usher, C. R.; Michel, A. E.; Grassian, V. H., *Reactions on Mineral Dust.* Chemical Reviews, 2003. **103**(12): p. 4883-4940.

3. Cwiertny, D. M.; Young, M. A.; Grassian, V. H., *Chemistry and Photochemistry of Mineral Dust Aerosol.* Annual Review of Physical Chemistry, 2008. **59**(1): p. 27-51.

4. McNaughton, C. S.; Clarke, A. D.; Kapustin, V.; Shinozuka, Y.; Howell, S. G.; Anderson, B. E.; Winstead, E.; Dibb, J.; Scheuer, E.; Cohen, R. C.; Wooldridge, P.; Perring, A.; Huey, L. G.; Kim, S.; Jimenez, J. L.; Dunlea, E. J.; DeCarlo, P. F.; Wennberg, P. O.; Crounse, J. D.; Weinheimer, A. J.; Flocke, F., *Observations of Heterogeneous Reactions Between Asian Pollution and Mineral Dust Over the Eastern North Pacific During INTEX-B.* Atmospheric Chemistry and Physics, 2009. **9**(21): p. 8283-8308.

5. Li, J.; Han, Z., *A Modeling Study of the Impact of Heterogeneous Reactions on Mineral Aerosol Surfaces on Tropospheric Chemistry Over East Asia.* Particuology, 2010. **8**(5): p. 433-441.

6. Zhu, S.; Butler, T.; Sander, R.; Ma, J.; Lawrence, M. G., *Impact of Dust on Tropospheric Chemistry Over Polluted Regions: A Case Study of the Beijing Megacity.* Atmospheric Chemistry and Physics, 2010. **10**(8): p. 3855-3873.

7. Fitzgerald, E.; Ault, A. P.; Zauscher, M. D.; Mayol-Bracero, O. L.; Prather, K. A., *Comparison of the Mixing State of Long-range Transported Asian and African Mineral Dust.* Atmospheric Environment, 2015. **115**: p. 19-25.

8. Formenti, P.; Caquineau, S.; Desboeufs, K.; Klaver, A.; Chevaillier, S.; Journet, E.; Rajot, J. L., *Mapping the Physico-chemical Properties of Mineral Dust in Western Africa: Mineralogical Composition.* Atmospheric Chemistry and Physics, 2014. **14**(19): p. 10663-10686.

9. Formenti, P.; Schütz, L.; Balkanski, Y.; Desboeufs, K.; Ebert, M.; Kandler, K.; Petzold, A.; Scheuvens, D.; Weinbruch, S.; Zhang, D., *Recent Progress in Understanding Physical and Chemical Properties of African and Asian Mineral Dust.* Atmospheric Chemistry and Physics, 2011. **11**(16): p. 8231-8256.

10. Journet, E.; Balkanski, Y.; Harrison, S. P., *A New Data Set of Soil Mineralogy for Dust-cycle Modeling.* Atmospheric Chemistry and Physics, 2014. **14**(8): p. 3801-3816.

11. Romanias, M. N.; Zeineddine, M. N.; Gaudion, V.; Lun, X.; Thevenet, F.; Riffault, V., *Heterogeneous Interaction of Isopropanol with Natural Gobi Dust.* Environmental Science & Technology, 2016. **50**(21): p. 11714-11722.

12. Goudie, A. S.; Middleton, N. J., *Desert Dust in the Global System.* 2006: Springer.

13. Scheuvens, D.; Schütz, L.; Kandler, K.; Ebert, M.; Weinbruch, S., *Bulk Composition of Northern African Dust and its Source Sediments — A Compilation.* Earth-Science Reviews, 2013. **116**: p. 170-194.

14. Goudie, A. S.; Middleton, N. J., *Saharan Dust Storms: Nature and Consequences.* Earth-Science Reviews, 2001. **56**(1–4): p. 179-204.

15. Klaver, A.; Formenti, P.; Caquineau, S.; Chevaillier, S.; Ausset, P.; Calzolai, G.; Osborne, S.; Johnson, B.; Harrison, M.; Dubovik, O., *Physico-chemical and Optical Properties of Sahelian and Saharan Mineral Dust: In-situ Measurements During the GERBILS Campaign.* Quarterly Journal of the Royal Meteorological Society, 2011. **137**(658): p. 1193-1210.

16.   Scheuvens, D.; Kandler, K.; KÜPper, M.; Lieke, K.; Zorn, S. R.; Ebert, M.; SchÜTz, L.; Weinbruch, S., *Individual-particle Analysis of Airborne Dust Samples Collected Over Morocco in 2006 During SAMUM 1.* Tellus B, 2011. **63**(4): p. 512-530.

17.   Crowley, J. N.; Ammann, M.; Cox, R. A.; Hynes, R. G.; Jenkin, M. E.; Mellouki, A.; Rossi, M. J.; Troe, J.; Wallington, T. J., *Evaluated Kinetic and Photochemical Data for Atmospheric Chemistry: Volume V - Heterogeneous Reactions on Solid Substrates.* Atmospheric Chemistry and Physics, 2010. **10**(18): p. 9059-9223.

18.   Volkamer, R.; San Martini, F.; Molina, L. T.; Salcedo, D.; Jimenez, J. L.; Molina, M. J., *A Missing Sink for Gas-phase Glyoxal in Mexico City: Formation of Secondary Organic Aerosol.* Geophysical Research Letters, 2007. **34**(19): p. n/a-n/a.

19.   Zhao, Y.; Chen, Z.; Zhao, J., *Heterogeneous Reactions of Methacrolein and Methyl Vinyl Ketone on α-Al$_2$O$_3$ Particles.* Environmental Science & Technology, 2010. **44**(6): p. 2035-2041.

20.   Romanias, M. N.; Ourrad, H.; Thévenet, F.; Riffault, V., *Investigating the Heterogeneous Interaction of VOCs with Natural Atmospheric Particles: Adsorption of Limonene and Toluene on Saharan Mineral Dusts.* The Journal of Physical Chemistry A, 2016. **120**(8): p. 1197-1212.

21.   Kolb, C. E.; Cox, R. A.; Abbatt, J. P. D.; Ammann, M.; Davis, E. J.; Donaldson, D. J.; Garrett, B. C.; George, C.; Griffiths, P. T.; Hanson, D. R.; Kulmala, M.; McFiggans, G.; Pöschl, U.; Riipinen, I.; Rossi, M. J.; Rudich, Y.; Wagner, P. E.; Winkler, P. M.; Worsnop, D. R.; O' Dowd, C. D., *An Overview of Current Issues in the Uptake of Amospheric Trace Gases by Aerosols and Clouds* Atmospheric Chemistry and Physics, 2010. **10**(21): p. 10561-10605.

22.   Khalizov, A. F.; Cruz-Quinones, M.; Zhang, R., *Heterogeneous Reaction of NO$_2$ on Fresh and Coated Soot Surfaces.* The Journal of Physical Chemistry A, 2010. **114**(28): p. 7516-7524.

23.   Shen, X.; Zhao, Y.; Chen, Z.; Huang, D., *Heterogeneous Reactions of Volatile Organic Compounds in the Atmosphere.* Atmospheric Environment. **68**(0): p. 297-314.

24.   Fairlie, T. D.; Jacob, D. J.; Dibb, J. E.; Alexander, B.; Avery, M. A.; van Donkelaar, A.; Zhang, L., *Impact of Mineral Dust on Nitrate, Sulfate, and Ozone in Transpacific Asian Pollution Plumes.* Atmospheric Chemistry and Physics, 2010. **10**(8): p. 3999-4012.

25.   Sivachandiran, L.; Thevenet, F.; Gravejat, P.; Rousseau, A., *Isopropanol Saturated TiO$_2$ Surface Regeneration by Non-thermal Plasma: Influence of Air Relative Humidity.* Chemical Engineering Journal, 2013. **214**(Supplement C): p. 17-26.

26.   Barakat, C.; Gravejat, P.; Guaitella, O.; Thevenet, F.; Rousseau, A., *Oxidation of Isopropanol and Acetone Adsorbed on TiO$_2$ Under Plasma Generated Ozone Flow: Gas Phase and Adsorbed Species Monitoring.* Applied Catalysis B: Environmental, 2014. **147**(Supplement C): p. 302-313.

27.   Sivachandiran, L.; Thevenet, F.; Rousseau, A., *Regeneration of Isopropyl Alcohol Saturated Mn$_X$O$_Y$ Surface: Comparison of Thermal, Ozonolysis and Non-thermal Plasma Treatments.* Chemical Engineering Journal, 2014. **246**(Supplement C): p. 184-195.

28.   Fultz, B.; Howe, J., Diffraction and the X-Ray Powder Diffractometer. In *Transmission Electron Microscopy and Diffractometry of Materials*, Springer Berlin Heidelberg: 2013; pp 1-57.

29.   Hill, S. J.; Fisher, A.; Liezers, M., Plasma Generation, Ion Sampling and Focusing. In *Inductively Coupled Plasma Mass Spectrometry Handbook*, Blackwell Publishing Ltd.: 2009; pp 1-25.

30.   Jenkins, R., *X-ray Fluorescence Spectrometry*. Second edition. Vol. 152. 1999: John Wiley & Sons, Inc.

31.   Alleman, L. Y.; Lamaison, L.; Perdrix, E.; Robache, A.; Galloo, J.-C., *PM10 Metal Concentrations and Source Identification Using Positive Matrix Factorization and Wind Sectoring in a French Industrial Zone.* Atmospheric Research, 2010. **96**(4): p. 612-625.

32.   Thevenet, F.; Olivier, L.; Batault, F.; Sivachandiran, L.; Locoge, N., *Acetaldehyde Adsorption on TiO_2: Influence of NO_2 Preliminary Adsorption.* Chemical Engineering Journal, 2015. **281**: p. 126-133.

33.   Joshi, N.; Romanias, M. N.; Riffault, V.; Thevenet, F., *Investigating Water Adsorption onto Natural Mineral Dust Particles: Linking DRIFTS Experiments and BET Theory.* Aeolian Research, 2017. **27**(Supplement C): p. 35-45.

34.   Zeineddine, M. N.; Romanias, M. N.; Gaudion, V.; Riffault, V.; Thévenet, F., *Heterogeneous Interaction of Isoprene with Natural Gobi Dust.* ACS Earth and Space Chemistry, 2017. **1**(5): p. 236-243.

35.   Bedjanian, Y.; Morin, J.; Romanias, M. N., *Gas-Phase Reaction of Hydroxyl Radical with p-Cymene over an Extended Temperature Range.* The Journal of Physical Chemistry A, 2015. **119**(45): p. 11076-11083.

36.   Navea, J. G.; Xu, S.; Stanier, C. O.; Young, M. A.; Grassian, V. H., *Heterogeneous Uptake of Octamethylcyclotetrasiloxane (D4) and Decamethylcyclopentasiloxane (D5) onto Mineral Dust Aerosol Under Variable RH Conditions.* Atmospheric Environment, 2009. **43**(26): p. 4060-4069.

37.   Goss, K.-U.; Schwarzenbach, R. P., *Quantification of the Effect of Humidity on the Gas/Mineral Oxide and Gas/Salt Adsorption of Organic Compounds.* Environmental Science & Technology, 1999. **33**(22): p. 4073-4078.

38.   Goss, K.-U.; Eisenreich, S. J., *Adsorption of VOCs from the Gas Phase to Different Minerals and a Mineral Mixture.* Environmental Science & Technology, 1996. **30**(7): p. 2135-2142.

39.   Goss, K. U., *Effects of Temperature and Relative Humidity on the Sorption of Organic Vapors on Clay Minerals.* Environmental Science & Technology, 1993. **27**(10): p. 2127-2132.

40.   Goss, K. U., *Effects of Temperature and Relative Humidity on the Sorption of Organic Vapors on Quartz Sand.* Environmental Science & Technology, 1992. **26**(11): p. 2287-2294.

41.   El Zein, A.; Romanias, M. N.; Bedjanian, Y., *Kinetics and Products of Heterogeneous Reaction of HONO with Fe2O3 and Arizona Test Dust.* Environmental Science and Technology, 2013. **47**(12): p. 6325-6331.

42.   Romanias, M. N.; El Zein, A.; Bedjanian, Y., *Reactive Uptake of HONO on Aluminium Oxide Surface.* Journal of Photochemistry and Photobiology A: Chemistry, 2012. **250**: p. 50-57.

43.   Underwood, G. M.; Song, C. H.; Phadnis, M.; Carmichael, G. R.; Grassian, V. H., *Heterogeneous Reactions of NO_2 and HNO_3 on Oxides and Mineral Dust: A Combined Laboratory and Modeling Study.* Journal of Geophysical Research: Atmospheres, 2001. **106**(D16): p. 18055-18066.

44.   Ndour, M.; Nicolas, M.; D'Anna, B.; Ka, O.; George, C., *Photoreactivity of NO_2 on Mineral Dusts Originating from Different Locations of the Sahara Desert.* Physical Chemistry Chemical Physics, 2009. **11**(9): p. 1312-1319.

45.   Hanisch, F.; Crowley, J., *Ozone Decomposition on Saharan dust: An Experimental Investigation.* Atmospheric Chemistry and Physics, 2003. **3**(1): p. 119-130.

46.   Michel, A. E.; Usher, C. R.; Grassian, V. H., *Heterogeneous and Catalytic Uptake of Ozone on Mineral Oxides and Dusts: A Knudsen Cell Investigation.* Geophysical Research Letters, 2002. **29**(14): p. 10-1-10-4.

47. Usher, C. R.; Al-Hosney, H.; Carlos-Cuellar, S.; Grassian, V. H., *A Laboratory Study of the Heterogeneous Uptake and Oxidation of Sulfur Dioxide on Mineral Dust Particles.* Journal of Geophysical Research: Atmospheres, 2002. **107**(D23): p. ACH 16-1-ACH 16-9.

48. Adams, J. W.; Rodriguez, D.; Cox, R. A., *The Uptake of SO₂ on Saharan Dust: A Flow Tube Study.* Atmospheric Chemistry and Physics, 2005. **5**(10): p. 2679-2689.

Chapter IV. Effect of temperature and relative humidity on the heterogeneous interaction of isopropanol with natural Gobi dust.

Table of content

List of Table

List of Table

List of Figures

In the previous chapter, several natural mineral dust samples were screened using isopropanol (IPA) as a probe molecule. IPA has been proved to be efficiently interacting with dust, and due to its reactivity it may lead to acetone and other lighter compounds therefore being suitable to check for any product formation [1-3].

In this chapter, a more thorough study is carried out with this VOC and the natural Gobi dust sample under atmospherically relevant conditions, in order to assess the importance that such an interaction could have on the global VOC budget concentrations in the atmosphere and to check whether this interaction can lead to the significant formation of oxygenated VOCs.

The choice of this particular dust sample is based on the conclusions drawn from Chapter 3, Section 3.3 dealing with the effect of the mineral dust chemical composition on the kinetics and surface equilibrium. The uptake coefficient of IPA on the available natural dust samples showed a linear correlation with the dust elemental Al/Si and Fe/Si ratios. Therefore the natural dust from the Gobi desert is chosen herein since among the samples available in our laboratory it is the richest in Al and Fe (see Table II-2) and we have seen that is has the highest IPA uptake.

*The results of this study were published in an article entiteld "**Heterogeneous Interaction of Isopropanol with Natural Gobi Dust"** in the Journal of **Environmental Science and Technology** on September 28, 2016.*

In this article, the interaction of IPA with natural Gobi dust is investigated under atmospheric conditions. The adsorption isotherms and the uptake coefficients are determined over a wide range of (i) concentrations (0.1-730 $\times$ 10^{13} molecule cm^{-3}), (ii) temperatures (273 – 348 K), and (iii) relative humidity (<0.01 – 70%). Furthermore, a detailed reaction product study is performed in a dedicated photochemical reactor under dark and UV light irradiation conditions.

The supporting information of this chapter can be found in Annex B at the end of this manuscript. The tables and figures of the supporting information in this chapter are noted as "BS" before their number (e.g. "Table BS1").

Full citation:

M. N. ROMANIAS, **M. N. ZEINEDDINE**, V. GAUDION, F. THEVENET, V. RIFFAULT, *Heterogeneous interaction of isopropanol with natural Gobi dust*, Environmental Science and Technology (50), 11714–11722 (2016), DOI 10.1021/acs.est.6b03708

1 Materials and methods

1.1 Materials

This section summarizes the characteristics of the natural dust sample from Gobi desert and the technical specifications of the experiments.

1.1.1 Gas preparation

IPA concentrations are obtained from calibrated gas cylinders (PRAXAIR) at 10 and 507 ppm_v in N_2 diluted in dry zero air. The IPA dilution factor in the experiments ranges between 2 and 170 which allowed the variation of IPA concentrations by 4 orders of magnitude. The zero air is generated by a classical air compressor, and then sent into a catalytic zero air generator (Claind, AZ-2020, Lenno, Italy). The remaining impurity levels in the air stream are lower than the analytical system detection limits: VOCs < 0.1 ppb, CO_2 < 10 ppb, CO < 80 ppb and H_2O ~ 2 ppm.

1.1.2 Gobi dust collection, and physical and chemical characterizations

Natural Gobi dust was collected in Yanchi, Ningxia province in China (107.475211°E, 36.487333°N). The adsorption of IPA on Gobi dust is studied using the smallest sieved size fraction of the dust batch (< 100 µm) that can be suspended in air. The specific surface area of Gobi (10.5 ± 2.0 m^2 g^{-1}) is measured employing the BET method using a sorption analyzer and nitrogen as adsorbate gas. The chemical characterization of the sample is determined employing X-ray spectroscopy and inductively coupled plasma mass spectrometry (ICP-MS). Results have been previously reported in Table II-2 and Table II-3.

1.1.3 Pretreatment of natural Gobi dust particles

Prior to the kinetic and product investigation each dust sample is thermally pretreated at 150°C for 20 minutes and purged with zero dry air to remove any pre-adsorbed species. The mass of each sample is weighed before and after the experiments with an accuracy of ±0.1mg. The difference between two measurements never exceeded 3%. Regarding the experiments performed under different relative humidity conditions, the dust surface was pre-exposed to humid air flow for 15 minutes prior to any experiment.

1.2   Experimental methods
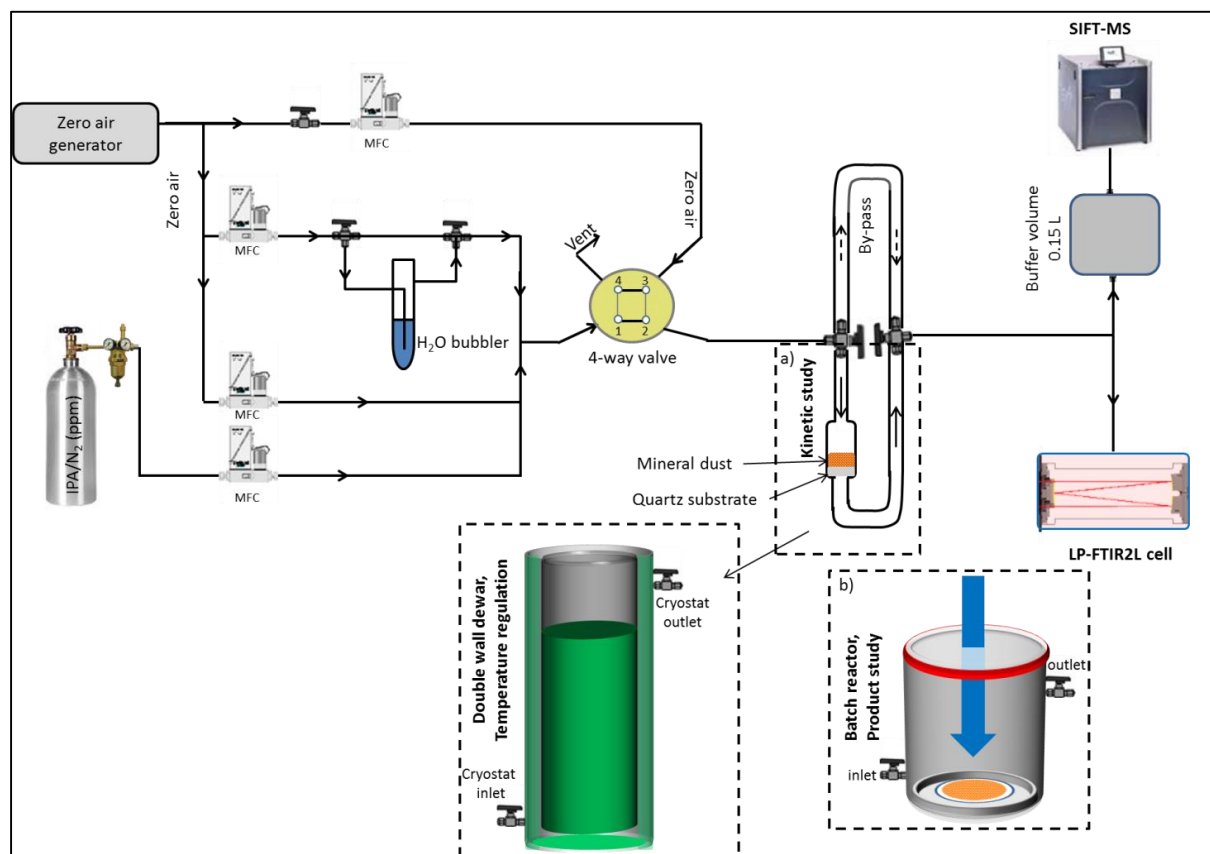
Figure IV-1. General scheme of the experimental setups. (a) U-shaped reactor for kinetic experiments, (b) double wall reactor for studying possible product formations.

A detailed scheme of the experimental setups is presented in Figure IV-1. It consists of (i) a gas flow generation system with stainless steel and Teflon tubings, (ii) a U-shaped reactor or a double wall photochemical reactor and (iii) the analytical devices. The descriptions of the different types of reactors used and the protocols followed for the kinetic and mechanistic experiments and the reaction product study are presented below in separate subsections. Regarding the analytical instrumentation used, details are presented in Section 2.1 of chapter 2, and only the necessary information are given herein. Particularly, the gas-phase is monitored employing either a long-path FTIR or a SIFT-MS. The FTIR is equipped with a 2 L White cell coupled to a liquid N_2-cooled MCT detector. The optical path length is 10 m. IR spectra are collected within the wavenumber range 400-4000 cm^{-1} every 10 sec. Each spectrum corresponds to the average of 16 co-added scans with a resolution of 1 cm^{-1}. IPA is monitored in three different regions, using the broad absorption bands at 897-1000, 1307-1432 and 2920-3028 cm^{-1}, respectively. The detection limit is estimated as 5×10^{13} molecule cm^{-3} (~2 ppm). Alternatively, the gas-phase is monitored employing a SIFT-MS which is essentially a double quadrupole chemical ionization mass spectrometer that uses three precursor ions, H_3O^+, NO^+

120

and O_2^+. The major advantage is that upto 30 VOCs can be monitored simultaneously eliminating the effect of mass peak overlapping. The sensitivity of SIFT-MS for most VOCs is in the ppb level.

1.2.1 Monitoring of IPA adsorption on Gobi dust sample

The uptake study is conducted inside a 15 cm^3 U-shaped flow reactor. A double-wall thermostatic Dewar filled with water and glycol solution is used to regulate the temperature; the reactor is immersed in the thermostated solution while the inlet and outlet of the Dewar are connected to a thermostat (Huber ministat 230).

The temperature of the sample is recorded using a K-type thermocouple. A known amount of mineral dust (50-430 mg) is placed on the top of a porous quartz wool sample-holder as shown in Figure IV-1. Calibrated mass flow controllers (Bronkhorst) are used to introduce the IPA and zero air in the reactor at a total flow rate of 650-850 sccm. The residence time of IPA in the reactor is estimated as ca. 1 second.

In a typical experiment (see also Figure IV-2) zero air is flown through the reactor to record the background level of IPA. Subsequently, by means of two 3-way valves, the gas flow direction is changed to a 15 cm^3 by-pass line.
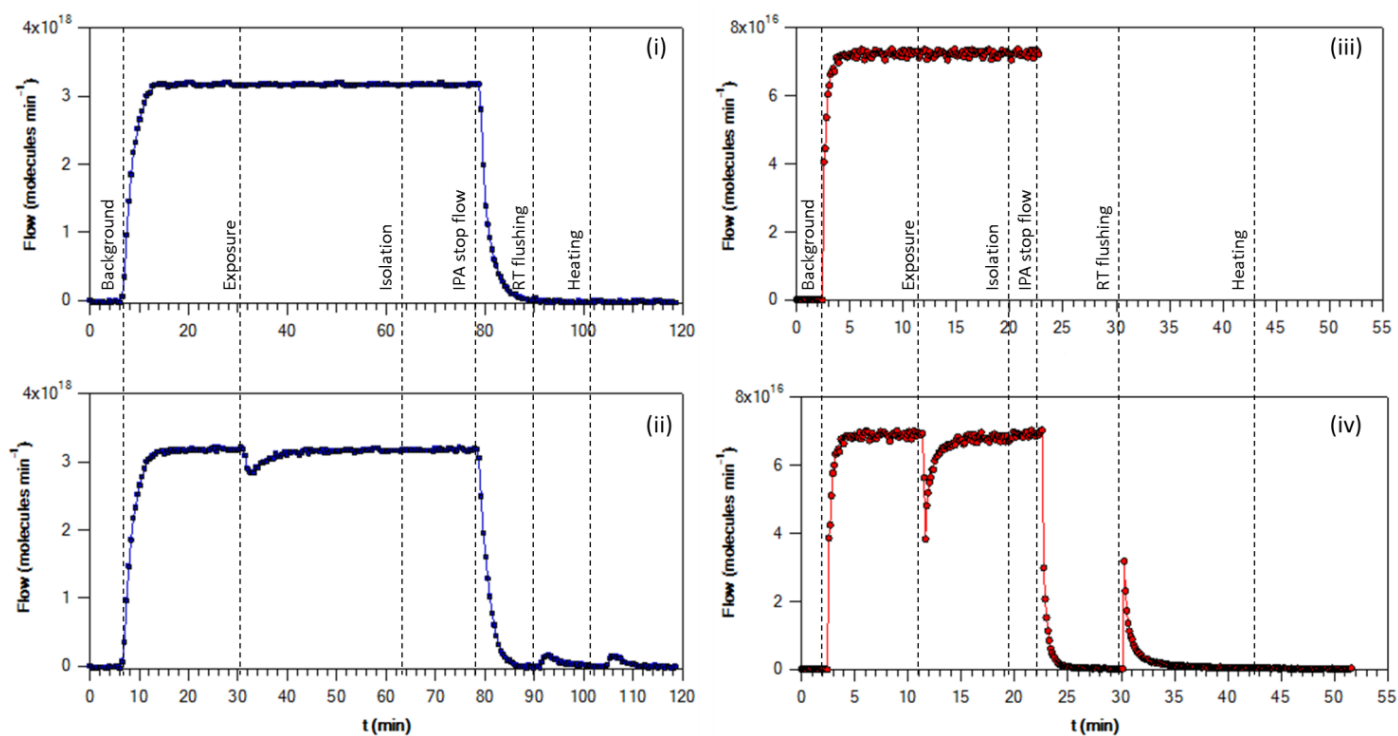
Figure IV-2. Typical gas-phase profiles of IPA. On the left side recorded with the FTIR at 320 K under dry conditions and on the right side recorded by SIFT-MS at 293K and 30% of RH in the (i), (iii) absence and (ii), (iv) presence of dust, respectively.

Thereafter, a known amount of isopropanol is introduced flowing through the by-pass. Upon achievement of steady state conditions, the flow is again directed through the reactor, exposing the Gobi dust surface to IPA. A rapid decrease of IPA concentration is recorded, due to the uptake of IPA on the dust surface. It should be noted that since the by-pass and the reactor have equal volumes, the decrease observed in IPA concentration during the exposure experiment is not contributed by any volume difference. In addition, when the gas-phase is recorded by the FTIR, the 2 L cell is used as a buffer volume that could not be influenced by any small volume variations upon changing from by-pass to the reactor and vice versa. For the same reason a 150 cm^3 buffer volume is positioned upstream the SIFT-MS (Figure IV-1). Reference experiments are conducted in the absence of dust (Figure IV-2, i and iii) showing that IPA concentration profiles are not influenced by volume changes and that IPA adsorption on the quartz wool substrate is lower than the experimental detection limit.

Subsequently, when the equilibrium between the adsorbed and the gas phase is achieved the IPA gas concentration returns to the initial pre-exposure level. The reactor is then isolated, i.e. switched to by-pass configuration, the IPA flow is stopped and the lines are purged with air. Consequently, the IPA concentration returns to the background level. Thereafter, the zero air flow is directed through the reactor to purge the surface and recover the weakly bonded fraction of IPA. Lastly, the surface is heated up to 110°C to remove the remaining adsorbed fraction of IPA.

1.2.2 IPA side-product study

The reactivity of IPA on the natural Gobi dust sample is studied at room temperature inside a 600 cm^3 double-wall reactor made of Pyrex and equipped with a quartz window at the top attached with a metallic clamp and two gas connections. A glass plate containing the dust is placed at the bottom of the reactor. Three UV lamps (UVA, PL-L18W, Philips) are used to irradiate the dust from above (Figure IV-1). The total gas flow is varied from 300 to 500 sccm. IPA breakthrough curves are used in this series of experiments [4, 5]. The product study requires a two-step procedure where the temporal gas-phase concentration of IPA is recorded: (i) in the absence of dust to define the mixing curve, corresponding to blank experiment, and (ii) in the presence of the natural Gobi dust sample to determine the VOC breakthrough curve. The equilibrium is reached when IPA outlet concentration remains constant and corresponds to the

inlet concentration. Under this condition, the dust surface is equilibrated with IPA. Typical breakthrough curves have been previously reported [4].

Complemantarily, after IPA surface equilibration, the surface of the Gobi dust sample is irradiated with UV light and the gas-phase is simultaneously monitored with SIFT-MS and FTIR. In addition, experiments are conducted inside a DRIFT optical cell [4] to monitor *in-situ* the coverage of the Gobi dust sample by IPA and potential side-products formed under dark and UV irradiation conditions.

2   Results and discussion

Typical IPA adsorption and desorption profiles in the absence and presence of dust, presented in Figure IV-2. Desorption profiles are recorded at room temperature, RT, and when heating the dust. It is observed that under dry conditions and RT flushing, the recovered fraction is always lower than the adsorbed one. However, by heating up the surface to $110^{o}C$ the remaining quantity of IPA is recovered in the gas phase (Figure IV-2, ii), pointing out that IPA is adsorbed onto at least two distinct types of sites with different adsorption enthalpies. On the other hand, under humid conditions, the entire adsorbed quantity of IPA is recovered by RT flushing (Figure IV-2, iv) highlighting the competition between H_2O and IPA molecules for the same adsorption sites.

2.1   Investigation of IPA initial uptake onto natural Gobi dust samples

The SIFT-MS gas-phase analyses at the outlet of the U-shape reactor were fast enough to allow the determination of the initial uptake coefficient, γ_0, within the first seconds of the interaction between IPA and dust [6]. Note that due to the high buffer volume of the FTIR cell the time resolution is longer than for SIFT-MS by a factor of 10. In addition, SIFT-MS was also preferred because of lower detection limits that enables γ_0 determination close to atmospherically relevant IPA concentrations. The uptake coefficient of IPA can be derived from the following expressions:

$$\frac{d(IPA)/dt}{V} = k_{het}[IPA] \qquad\qquad \textbf{(Equation IV-1)}$$

$$k_{het=}\frac{d(IPA)/dt}{V[IPA]} = \omega\gamma_0 \qquad\qquad \textbf{(Equation IV-2)}$$

with:

$$\omega = \frac{cA_s}{4V}$$ **(Equation IV-3)**

and finally:

$$\gamma_0 = \frac{4\{d(IPA)/dt\}}{cA_s[IPA]}$$ **(Equation IV-4)**

where (IPA) denotes the number of IPA molecules taken up by the dust surface at the beginning of exposure (molecule); k_{het}, the first-order rate coefficient of the heterogeneous loss of IPA (s^{-1}); V, the volume of the interaction zone (cm^3); [IPA], the gas-phase concentration of IPA (molecules cm^{-3}); ω, the collision frequency of IPA (s^{-1}); c, the mean molecular speed ($cm\ s^{-1}$); A_s, the effective surface area of the dust sample, calculated as the product of SSA with the mass of the sample (cm^2).

2.1.1 Dependence of IPA initial uptake on the mass of natural Gobi dust sample

In order to determine the effective surface area of Gobi dust involved in the interaction with IPA, the geometric γ_0 is determined as a function of the mass of dust exposed. Results of the measurements carried out at room temperature and under dry conditions are shown in Figure IV-3.
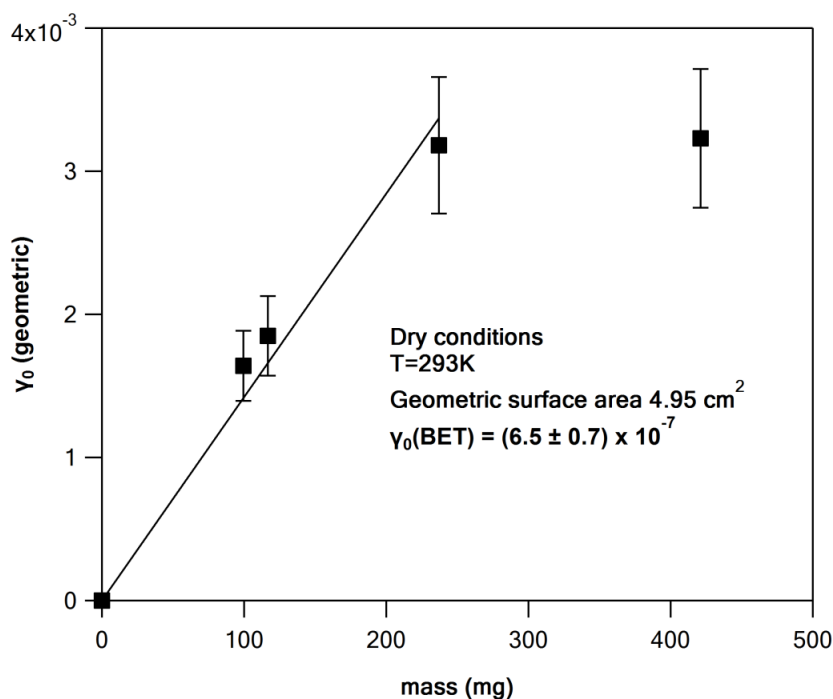
Figure IV-3. Dependence of the geometric initial uptake coefficient of IPA as a function of Gobi dust mass exposed. The error bars represent the overall uncertainty on γ_0. The solid line is the non-weighted least-square fit of the data, forced through zero.

γ_0 linearly increases with the exposed mass till a saturation regime for masses higher than 230 mg. The linear dependence of the uptake probability on mass is considered as an indication

124

that the entire surface area of the solid sample is accessible to IPA, and consequently, the BET surface area can be used for γ_0 determination [7, 8]. Consequently, the kinetic measurements in the U-shape reactor are conducted in the linear regime using dust masses lower than 230 mg.

2.1.2 Dependences of IPA initial uptake on temperature and IPA concentration

Figure IV-4 illustrates the effect of IPA concentrations and temperature on γ_0 determined under dry conditions. In all cases, γ_0 is found to be $\left(6.52 \pm_{1.15}^{2.00}\right) \times 10^{-7}$, irrespectively of IPA gas-phase concentration, [IPA] = $(0.12$-$2.5) \times 10^{13}$ molecule cm^{-3}, and temperature (273 – 320 K). The reported uncertainties correspond to the extreme values of γ_0 determined on the investigated ranges of IPA concentration and temperature.
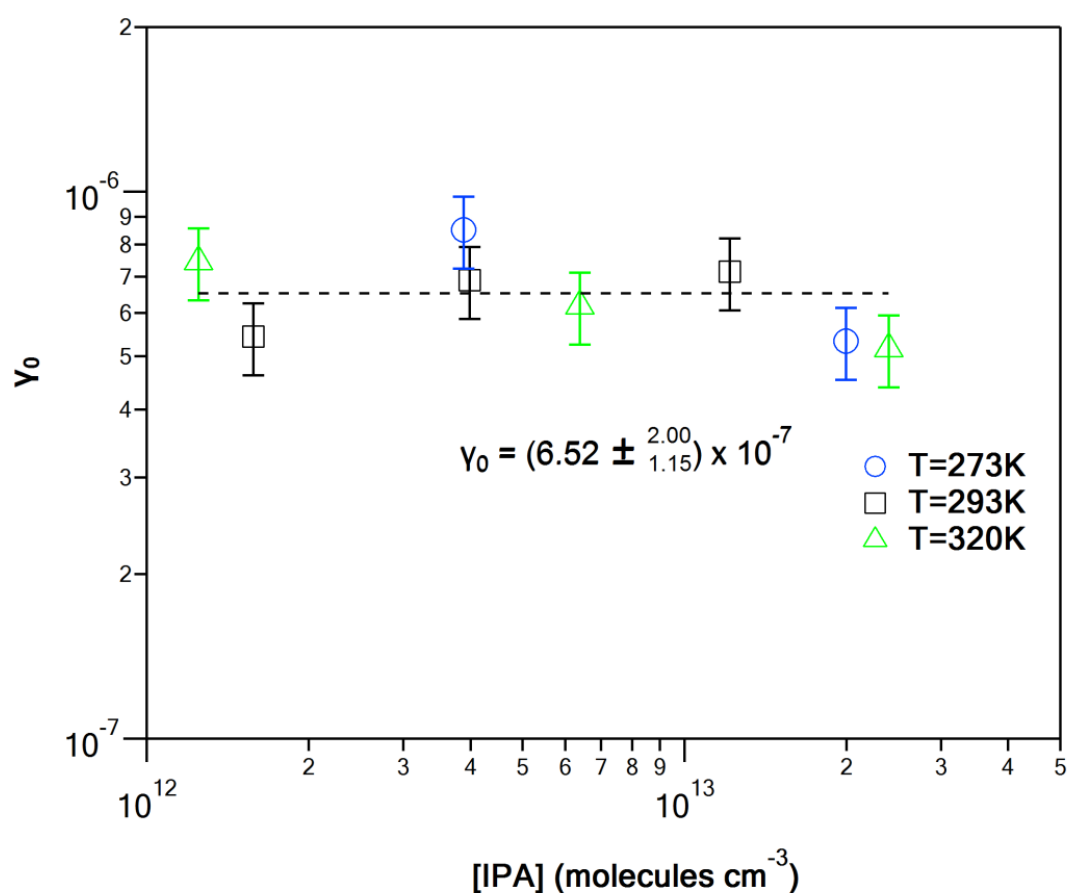
Figure IV-4. Initial uptake coefficients determined over the temperature range 273-320 K as a function of the IPA gas-phase concentration, monitored by SIFT-MS. The error bars represent the overall estimated uncertainties on γ_0.

By definition, the initial uptake coefficient expresses the very first steps of the interaction between a gas molecule and a fresh surface, thus, it is expected to be independent on the gas-phase concentration. The observed independence of γ_0 on temperature could be

attributed to the limited T range where experiments are conducted. Note that similar temperature trends of γ_0 on mineral dust surfaces have been reported in the literature [8].

2.2 Adsorption isotherms of IPA on natural Gobi dust sample

The surface coverage of Gobi dust by IPA is investigated as a function of temperature from 273 to 348 K, and relative humidity from 0.01 to 50%. In this set of experiments the U-shaped reactor is combined either with the FTIR or the SIFT-MS.

2.2.1 Dependence of IPA adsorption isotherm on temperature
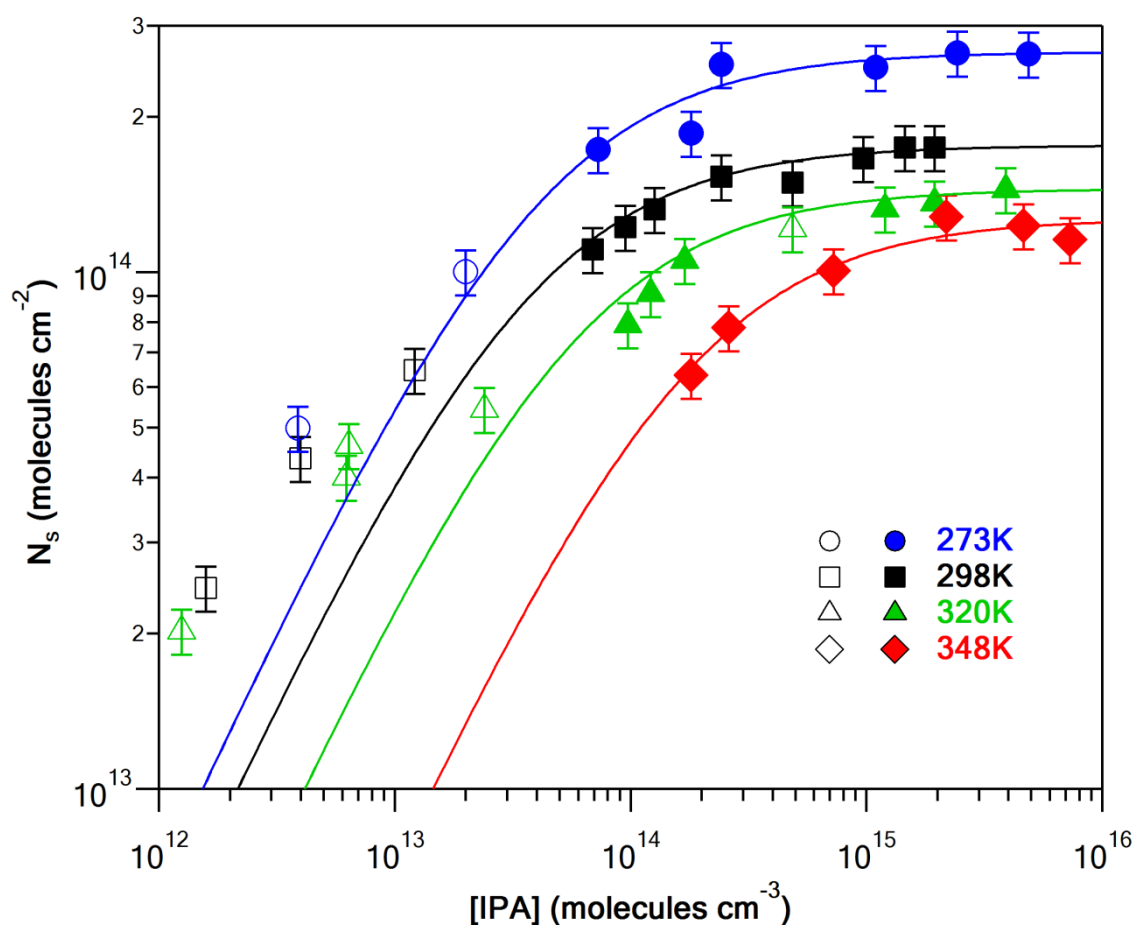
Figure IV-5. Adsorption isotherms of IPA on Gobi dust determined in the temperature range 273 – 348 K under dry conditions (<0.01%). Open symbols: experiments performed with SIFT-MS using H_3O^+ and NO^+ ions to monitor IPA at the mass peaks 43 ($C_3H_7^+$) and 59 ($C_3H_7O^+$) respectively. Filled symbols: experiments with long path FTIR Error bars represent the overall uncertainty on N_s determination. The lines are non-weighted fits through the data using the Langmuir expression.

The adsorption isotherms of IPA on Gobi dust under dry conditions and at different temperatures are presented in Figure IV-5. The uptake of IPA increases with decreasing temperature. In addition, the quantity of IPA adsorbed reaches a plateau where the IPA concentration threshold depends on each temperature, for instance 1×10^{14} molecules cm^{-3} at 273 K. This threshold increases as a function of temperature suggesting the complete coverage of the surface for the considered temperature. Experimental results are simulated with Langmuir model which is described in details in Section 3.1 of Chapter 1. The number of IPA molecules adsorbed per surface unit depends on the IPA gas-phase concentration according to Equation IV-5:

$$\theta = \frac{N_S}{N_{max}} = \frac{K_{Lang} \times [IPA]}{1 + K_{Lang} \times [IPA]}$$
(Equation IV-5)

where θ is the Gobi dust surface coverage by IPA, N_s is the number of IPA molecules adsorbed per surface unite (molecule cm^{-2}), N_{max} is the maximum surface coverage reached for a given temperature (molecule cm^{-2}) and K_{Lang} (cm^3 molecule^{-1}) is the Langmuir equilibrium constant, which describes the partitioning of IPA between the gas phase and the adsorbed phase. The model fits well the experimental results at concentrations above 1×10^{13} molecule cm^{-3}. However below that limit, the Langmuir model underestimates the surface concentration of molecule adsorbed. As previously shown (Figure IV-2), under dry conditions, the RT flushing does not remove the entire quantity of IPA adsorbed; it is necessary to heat the surface to recover the total adsorbed fraction. This behavior was attributed to the presence of at least two types of adsorption sites for IPA onto Gobi. Therefore, it can be assumed that at low concentrations, IPA molecules are adsorbed on the sites for which the binding energy is higher, further called "highly active sites", and the Langmuir isotherm fails to simulate that adsorption behaviour because the hypotheses related to pure physisorption of the gas onto the solid surface may not be fully satisfied.

Proper rearrangement of Equation IV-5 leads to Equation IV-6:

$$\frac{[IPA]}{N_S} = \frac{1}{N_{max} \times K_{Lang}} + \frac{1}{N_{max}} \times [IPA]$$
(Equation IV-6)

A linear fit of the [IPA]/N_s ratio versus [IPA] provides N_{max} and K_{Lang} values for each temperature [9]. The values obtained, excluding concentrations lower than 1×10^{13} molecule cm^{-2}, are reported in Table IV-1. The values obtained N_{max} and K_{Lang} are used to calculate the

partition coefficient K_{Lin} which is the equilibrium constant that was introduced by the IUPAC panel in order to include the temperature dependence of surface coverage [10]. The temperature dependence of K_{Lin} is given by the Van't Hoff expression (Equation IV-7):

$$K_{Lin} = A \, exp[-\Delta H_{ads}/RT]$$
(Equation IV-7)

where A is the pre-exponential factor and R is the ideal gas constant. The plot of K_{Lin} versus 1000/T is displayed in Figure IV-6 and the Equation IV-8 is obtained:

$$K_{Lin} = (1.1 \pm 0.3) \times 10^{-2} \, exp[1764 \pm 132/RT]$$
(Equation IV-8)
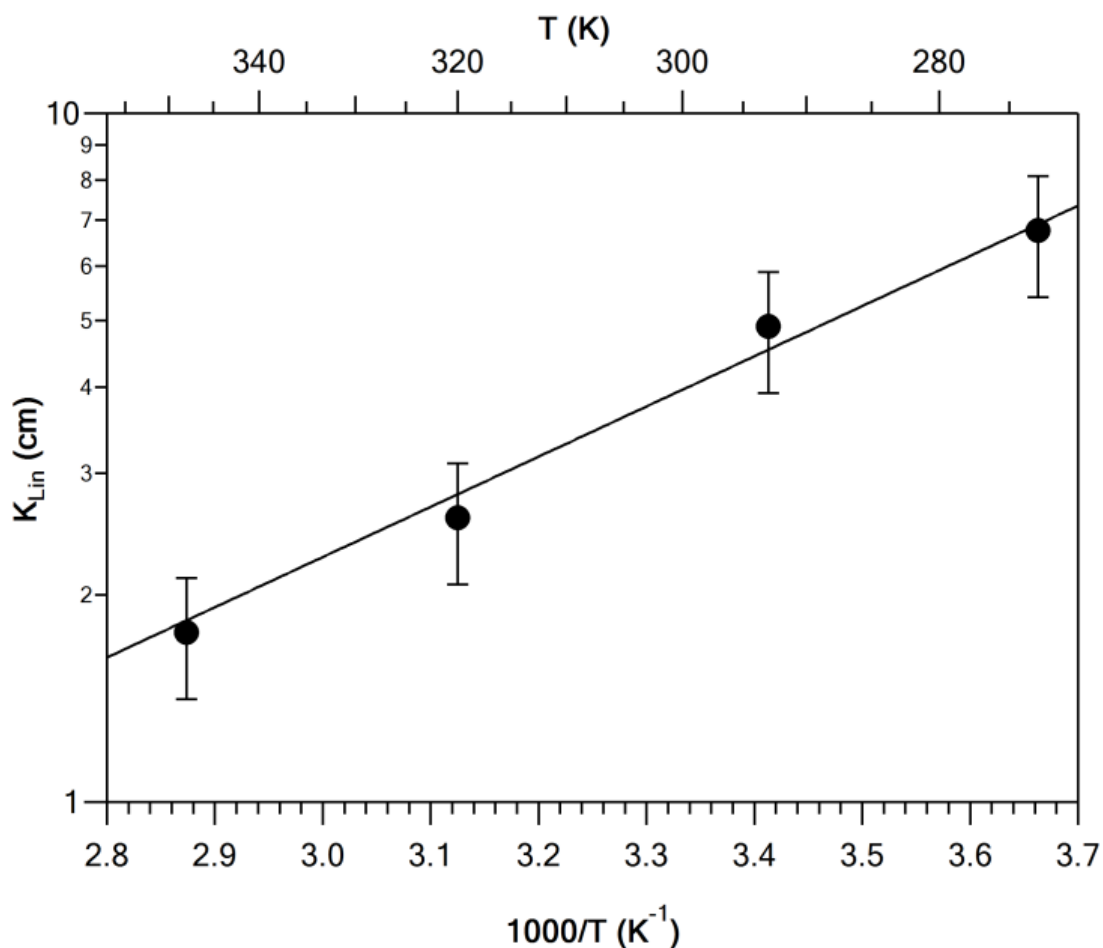
Figure IV-6. Plot of K_{Lin} as a function of 1000/T. K_{Lin} values are derived from the Langmuir fitting of the experimental results under dry conditions. Error bars represent the overall uncertainty on K_{Lin} determination. Solid line is the non-weighted exponential fit using the Van't Hoff equation.

The uncertainties on the exponential factor reflect the 1σ precision of the fit of $\ln(K_{Lin})$ versus 1000/T, while the error limit on A is related to the intercept of the fit based on the expression $dA = A \times d(\ln A)$. All the systematic uncertainties have been added in quadrature for the pre-exponential factor. The IPA adsorption enthalpy derived from the slope of the fit is determined as ΔH_{ads} = -14.7 ± 1.1 kJ mol^{-1}. The relatively low negative value of ΔH_{ads} indicates that isopropanol is mostly physisorbed on the surface of the natural Gobi dust sample.

Table IV-1. Maximum surface coverage, N_{max}, and partitioning constants K_{Lang} and K_{Lin} values for IPA adsorption on Gobi dust as a function of temperature (under dry conditions) and relative humidity (at 293 K). The given uncertainty for N_{max} and K_{Lang} includes the estimated systematic uncertainties (ca. 12%). The overall uncertainty for K_{Lin} was estimated to be ca. 20%.

T (K)	[IPA] (10^{13} molecule cm^{-3})	N_{max} (10^{14} molecule cm^{-2})	K_{Lang} (10^{-14} cm^{3}molecule^{-1})	K_{Lin} (10^{-2} cm)
273	2-485	2.67 ± 0.32	2.53 ± 0.30	676 ± 135
293	1-194	1.76 ± 0.21	2.78 ± 0.33	491 ± 98
320	2-389	1.45 ± 0.17	1.79 ± 0.21	259 ± 52
348	18-729	1.19 ± 0.14	1.48 ± 0.18	176 ± 35
$K_{Lin} = (1.1 \pm 0.3) \times 10^{-2} \exp[(1764 \pm 132)/T]$				
RH (%)	[IPA] (10^{13} molecule cm^{-3})	N_{max} (10^{14} molecule cm^{-2})	K_{Lang} (10^{-16} cm^{3}molecule^{-1})	K_{Lin} (10^{-2} cm)
<0.01	1-194	1.76 ± 0.21	278 ± 33	491 ± 98
15	0.1-436	1.67 ± 0.20	7.62 ± 0.91	12.7 ± 2.5
30	0.7-601	1.35 ± 0.16	2.68 ± 0.32	3.6 ± 0.7
50	0.4-630	0.66 ± 0.08	2.74 ± 0.49	1.81 ± 0.4
$K_{Lin} = 15.75/(3.21 + RH^{1.77})$				

2.2.2 Dependence of IPA adsorption isotherm on relative humidity
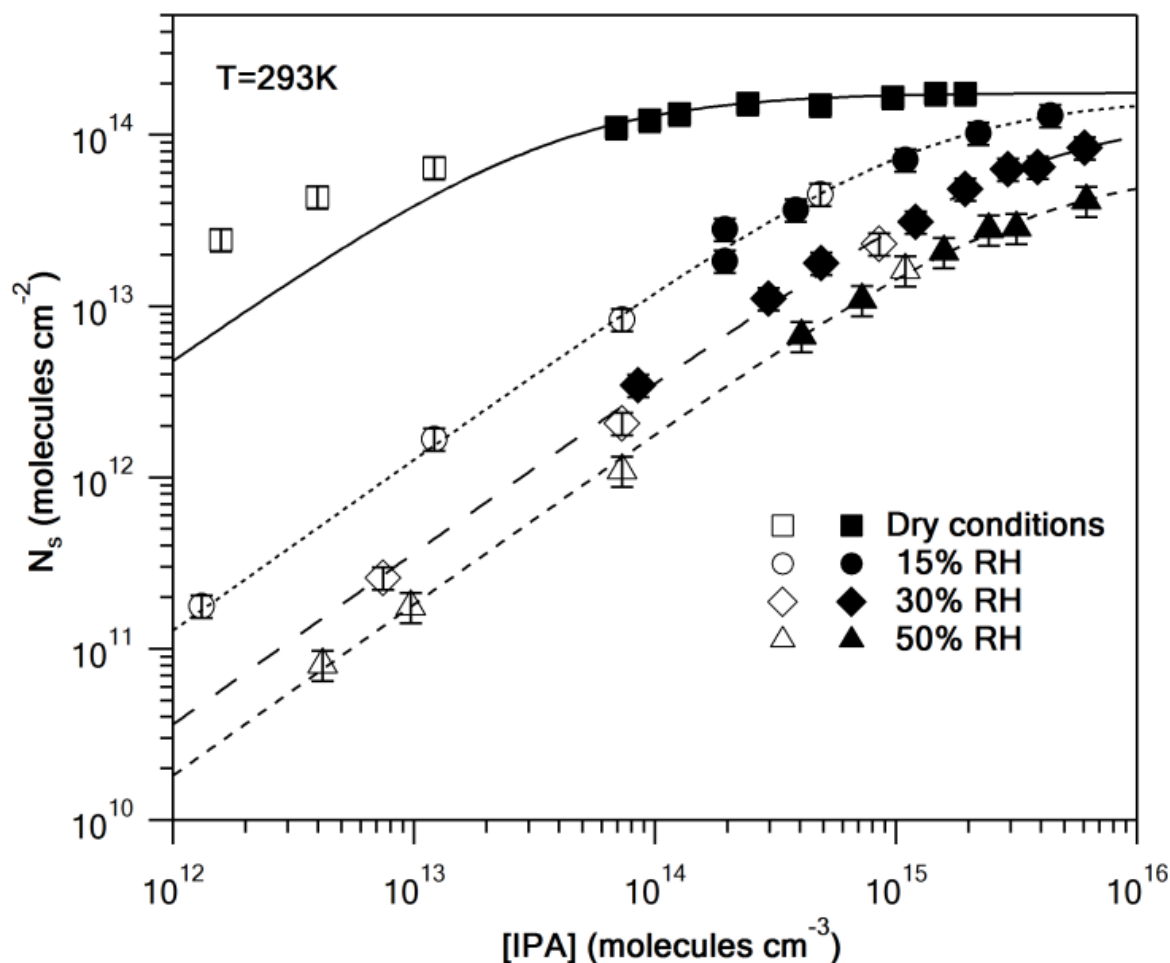
Figure IV-7. Adsorption isotherms of IPA on Gobi dust determined in the relative humidity range <0.01– 50% at 293 K. Open symbols: experiments performed with SIFT-MS. Filled symbols: experiments with long path FTIR. Error bars represent the overall uncertainty on Ns determination. The lines are non-weighted fits through the data according to the Langmuir expression.

The adsorption isotherms of IPA as a function of relative humidity are determined at 293 K and results are reported in Figure IV-7. The consistency of the data obtained with both analytical techniques was crosschecked and they obviously provide consistent values within the range of experimental uncertainties. IPA adsorption is diminished with increasing relative humidity. Clearly, H_2O molecules compete with IPA for the adsorption sites. The adsorption measurements are simulated with the Langmuir model and an excellent agreement is obtained under humid conditions even at low IPA concentrations, but not under dry conditions. This observation indicates that H_2O molecules occupy preferentially and quickly the "highly active sites" of the surface, thus leaving IPA weakly bonding on adsorption sites that can be well simulated with the Langmuir model. Plotting the results with Equation IV-6 (Figure BS1 of

annex B) provides N_{max}, K_{Lang}, and K_{Lin} values over the RH range (Table IV-1). The dependence of K_{Lin} on RH is displayed in Figure BS2 of annex B, it can be described by Equation IV-9:

$$K_{Lin} = 15.75/(3.21 + RH^{1.77})$$ **(Equation IV-9)**

2.3 Investigation of reaction products

The effect of Gobi dust surface irradiation during IPA adsorption is investigated at room temperature under dry and 50% RH conditions. Typical IPA breakthrough curves recorded using the SIFT-MS at 50 % RH are presented in Figure IV-8.
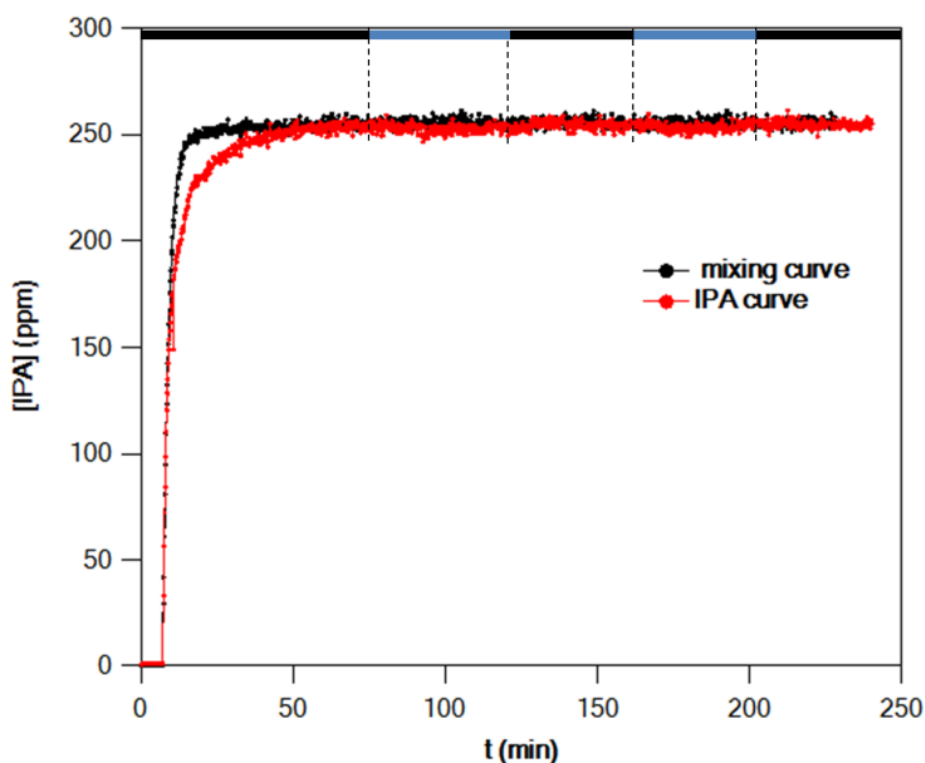
Figure IV-8. IPA breakthrough curves under dark and UV light conditions (indicated with black and blue rectangles, respectively) in the absence (black) and presence (red) of Gobi dust. The experiments are performed under 253.5 ppm of IPA concentration and under 50% RH.

The delayed recovery of the signal in the presence of dust (red line) is due to IPA uptake on dust. Upon achieving steady state conditions the surface is illuminated with UV light. Figure IV-9 focuses on the concentration profiles of IPA and identified products formed. Due to the extremely low yields of gaseous products, in this series of experiments the dust is exposed to high concentrations of IPA ranging from 50 to 253.5 ppm and high dust mass of around 800

mg. Irradiation of the surface in the absence of dust did not cause any decrease to IPA signal (Figure IV-9).
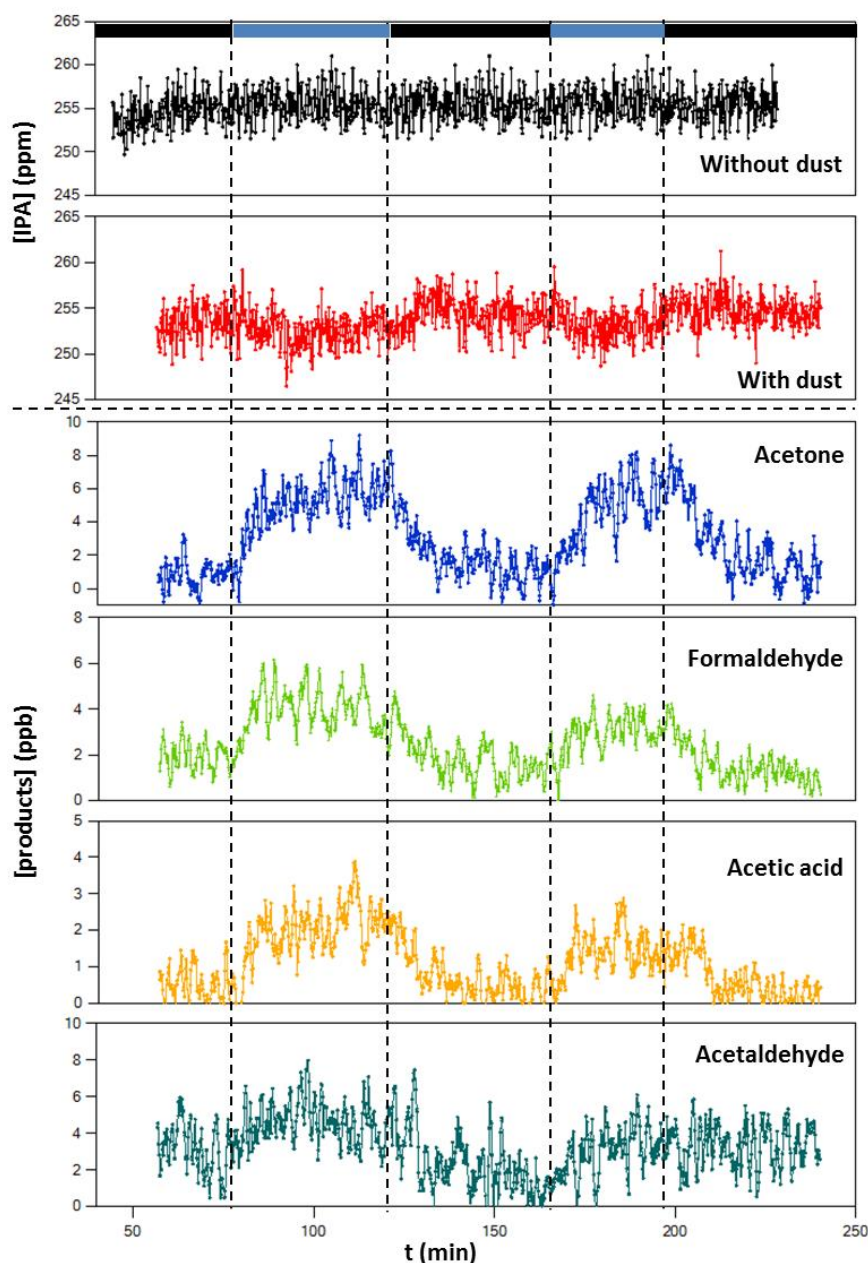
Figure IV-9. Concentration profiles of IPA in the absence and presence of dust and those of the products formed under dark and UV light irradiation conditions employing the SIFT-MS. The experimental conditions were: 800 mg of Gobi dust exposed to 253.5 ppm of IPA at 293K and 50% RH in the batch reactor. IPA was detected using H_3O^+ and NO^+ ions at the mass peaks 43 ($C_3H_7^+$) and 59 ($C_3H_7O^+$) respectively. Acetone was monitored at the mass peak 88 ($NO^+C_3H_6O$) while formaldehyde at mass 31 (CH_3O^+) using the H_3O^+ ion. In addition, the H_3O^+ and NO^+ ions were used for acetic acid and acetaldehyde monitoring at the mass peaks 61 ($CH_3COOH_2^+$), 90 (NO^+CH_3COOH) and 45 ($C_2H_5O^+$), 43 (CH_3CO^+) respectively.

On the other hand, in the presence of dust, a slight but systematic decrease of IPA is observed, which is attributed to a photoactivated process. Simultaneously, acetone, formaldehyde, acetic acid and possibly acetaldehyde are monitored in the gas phase at yields lower than 0.1 % (see Table BS1, annex B). Besides the oxygenated VOCs, H_2O [11] and CO_2 (<15%) [11] are identified as gas-phase products by infrared spectroscopy under dry conditions as show in Figure IV-10. Therefore the interaction of IPA on Gobi dust can be considered as a source of oxygenated VOCs in the atmosphere.
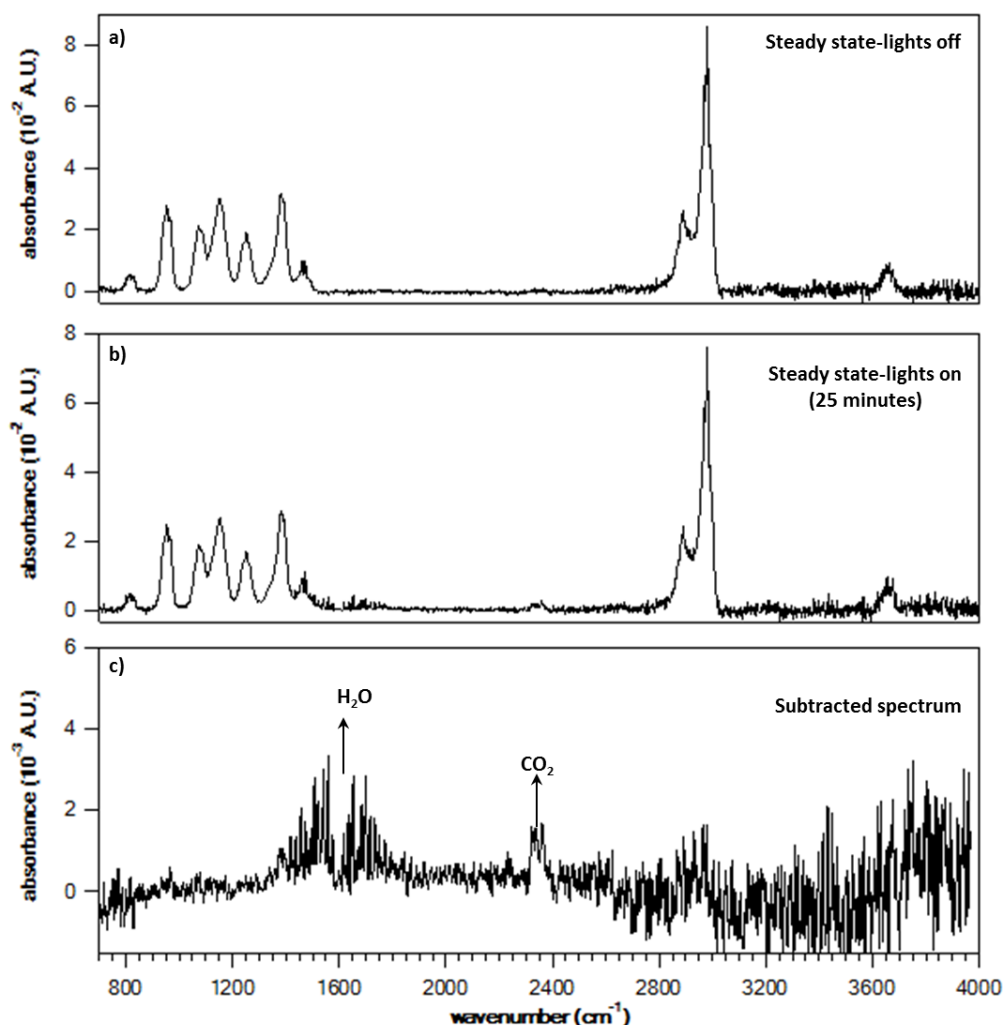
Figure IV-10. IR spectra collected after exposure of 1.4 g of Gobi dust to 20 ppm of IPA at room temperature and dry conditions, a) with lights off, b) after 25 minutes of UV irradiation of the surface. The subtracted spectrum, c), is also presented. CO_2 and H_2O were identified as products.

To investigate the possible formation of surface products, a second series of experiments are conducted where the IPA breakthrough curves are recorded (i) in the absence of dust (ii) in the presence of dust and dark conditions, and (iii) in the presence of dust under UV light

irradiation. At the end of each breakthrough curve, the reactor is flushed with zero air till IPA signal returns to background levels. Then, the temperature of the reactor is gradually increased to reach 80 °C. No products are detected in the gas-phase without dust or without light. On the contrary, several ppb of formaldehyde are monitored in the gas phase when the dust covered by IPA is previously exposed to UV light.

In a third series of experiments, the interaction of IPA with Gobi is studied inside the DRIFTs optical cell under dry and humid conditions. It is observed that upon UV irradiation of the surface the dust is photo-activated enhancing the IPA consumption (Figure IV-11).
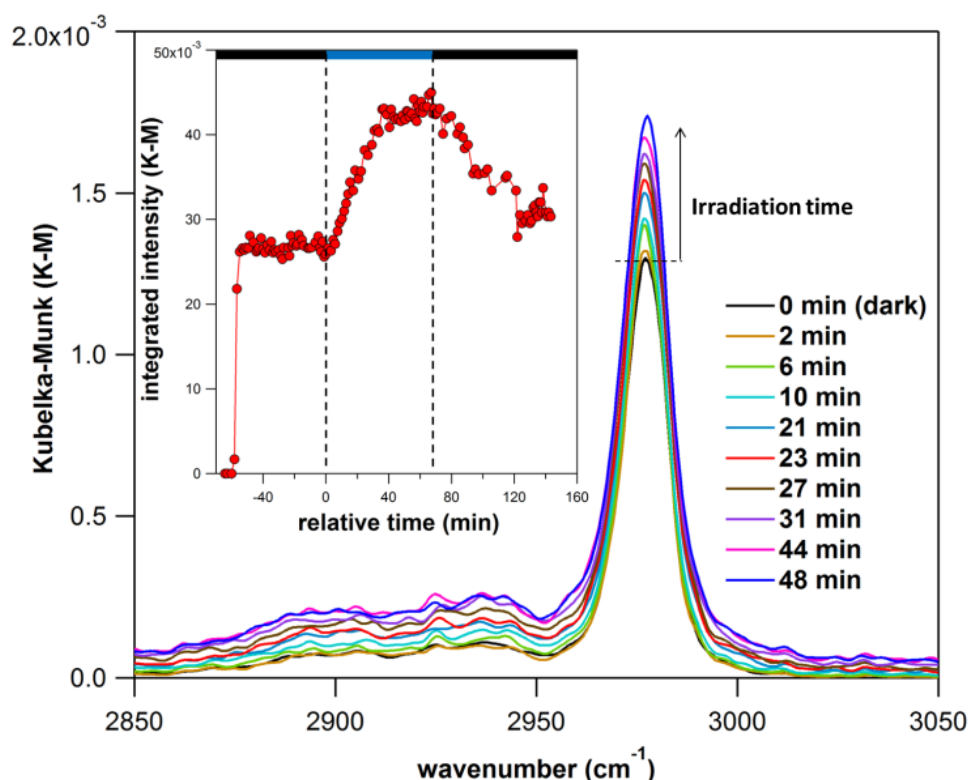
Figure IV-11. Sequential DRIFTs spectra showing the temporal evolution of IPA coverage on Gobi dust under UV light irradiation. The time dependent profile of IPA under dark and UV light conditions is enclosed. The experimental conditions were: 150 mg of Gobi dust exposed to 150 ppm of IPA at room temperature, 50% RH in the DRIFTs optical cell.

However, no surface products are observed using DRIFTs. The latter is attributed to the low sensitivity of the instrument, which is the main drawback of DRIFTs. In addition, the mineral sample has been exposed to IPA for several hours under UV irradiation conditions inside the DRIFTs optical cell that was coupled with the SIFT-MS for gas phase monitoring. At the end of the experiment, the surface-adsorbed IPA and products are extracted using acetonitrile as a solvent and 2,4 dinitrophenylhydrazine (2,4-DNPH) as the derivatization agent.

The solution has been analysed using HPLC coupled with a UV detector. The HPLC instrument is dedicated to the detection of aldehydes and ketones and therefore regularly calibrated using commercially available standards. Hydroxyacetone, formaldehyde, acetaldehyde, acetone and methylglyoxal have been identified as surface products (Figure IV-12) while the formation of several other compounds are observed but not identified. In order to provide quantitative results, the calibration factor of each compound identified has been determined except hydroxyacetone where standard was not readily available and thus its calibration factor could not be determined within the same batch of analytical samples. Nevertheless, the standards of the remaining identified compounds were available and used to obtain the calibration factors of each compound. Moreover we used former HPLC chromatograms where the instrument was calibrated with all same standards (including hydroxyacetone) to confirm that the observed peak at ~3.8 min (see Figure IV-12) corresponds to hydroxyacetone and to estimate a calibration factor.
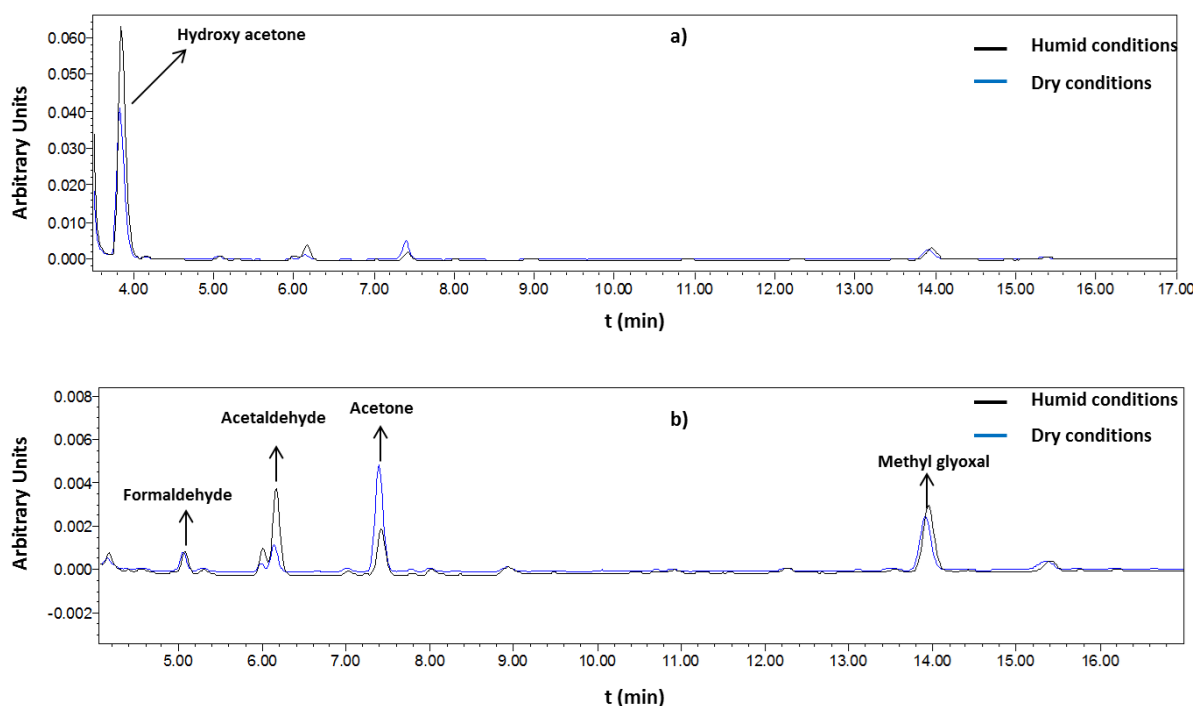
Figure IV-12. a) HPLC chromatogram obtained by extraction of surface products formed after 6 hours of UV irradiation of ~150 mg of Gobi dust exposed on 253.5 ppm of IPA under dry and humid conditions. b) Focus of chromatogram a.

As can be seen in Figure IV-12, the most intense peak corresponds to hydroxyacetone, and the upper limits of its formation under dry (<0.01% RH) and humid conditions (50% RH), were <30% and <50%, respectively. Regarding the other surface products the response coefficients are obtained using standards and the upper limits determined under dry and humid

conditions are, a) formaldehyde under dry and humid < 1%, b) acetaldehyde, dry: <2%, humid: <8%, c) acetone, dry: <11%, humid: <4%, d) methylglyoxal under dry and humid <10%. Finally, it should be noted that no experiments were conducted to evaluate the evolution of the products with the irradiation time. Moreover, other pathways have to be considered, for instance the UV enhanced adsorption of IPA as shown in Figure IV-11 or the conversion of most of CO_2 to carbonates promoted by moisture [12, 13].

2.4 Atmospheric implications

The fraction of IPA molecules (α) expected to be removed from the atmosphere onto mineral dust is given by the ratio of adsorbed-to-total IPA according to Equation IV-10 [14]:

$$\alpha = \frac{K_{Lin} \times A}{1 + K_{Lin} \times A}$$ **(Equation IV-10)**

where A is the dust surface area density (cm^2 cm^{-3}). Considering high mineral dust mass loads occurring during dust storms (12,400 μg m^{-3}) [15], and the BET surface area of Gobi dust, A is estimated to be around 1.2×10^{-3} cm^2 cm^{-3}. Hence, according to Equation IV-11, up to 38% of IPA could be expected to be depleted under dry conditions typical of a dust storm, whereas it would appear negligible under 50% RH ($\alpha < 1\%$). However, the formation of small amounts of OVOCs due to the heterogeneous reactivity of IPA with Gobi dust under UV irradiation could be an important process in some environments. For instance, the formation rates of the products at 50% of RH considering a 12 hour day-time interval have been estimated in two cases, that is to say considering (i) monthly averages of dust mass loads [16], and (ii) high mass loads recorded under dust storms [15]. Results are presented in Table BS1 of annex B. Several ppt of OVOCs can be produced under these conditions. Although in the case of IPA, these rough estimations are not enough to account for a missing source of OVOCs in the troposphere [17] this work is to the best of our knowledge the first one to demonstrate that natural mineral dust can be activated under light conditions and act as a potential source of OVOCs. Even though the photoreactivity of this particular dust sample seems relatively low, it does not preclude that with other natural samples and/or other abundant VOCs, heterogeneous processes on dust could influence the VOCs distribution of the troposphere, and thus its oxidation capacity under specific environmental conditions.

3 Conclusion

In this chapter the interaction of IPA with natural dust from the Gobi desert is investigated under atmospherically relevant conditions. γ_0 is found to be independent of

temperature. Furthermore, the adsorption isotherms of isopropanol are determined and the results are simulated with the Langmuir adsorption model to obtain the partitioning constant, K_{Lin}, as a function of temperature and relative humidity. Beside the kinetics, a detailed product study is conducted under UV irradiation conditions (350−420 nm) in a double wall reactor. Acetone, formaldehyde, acetic acid, acetaldehyde, carbon dioxide, and water are identified as gas-phase products. In addition, several surface products are extracted and identified employing HPLC: Hydroxyacetone, formaldehyde, acetaldehyde, acetone, and methylglyoxal. The results presented in this chapter evidence that the interaction of anthropogenic VOCs with natural mineral dust in the atmosphere could lead to the formation of oxygenated VOCs. What about the interaction of more abundant biogenic VOCs? In the following chapter the interaction of a biogenic VOC with natural dust sample is investigated.

4 References of Chapter IV

1. Sivachandiran, L.; Thevenet, F.; Gravejat, P.; Rousseau, A., *Isopropanol Saturated TiO₂ Surface Regeneration by Non-thermal Plasma: Influence of Air Relative Humidity.* Chemical Engineering Journal, 2013. **214**(Supplement C): p. 17-26.

2. Barakat, C.; Gravejat, P.; Guaitella, O.; Thevenet, F.; Rousseau, A., *Oxidation of Isopropanol and Acetone Adsorbed on TiO₂ Under Plasma Generated Ozone Flow: Gas Phase and Adsorbed Species Monitoring.* Applied Catalysis B: Environmental, 2014. **147**(Supplement C): p. 302-313.

3. Sivachandiran, L.; Thevenet, F.; Rousseau, A., *Regeneration of Isopropyl Alcohol Saturated MnₓOᵧ Surface: Comparison of Thermal, Ozonolysis and Non-thermal Plasma Treatments.* Chemical Engineering Journal, 2014. **246**(Supplement C): p. 184-195.

4. Romanias, M. N.; Ourrad, H.; Thévenet, F.; Riffault, V., *Investigating the Heterogeneous Interaction of VOCs with Natural Atmospheric Particles: Adsorption of Limonene and Toluene on Saharan Mineral Dusts.* The Journal of Physical Chemistry A, 2016. **120**(8): p. 1197-1212.

5. Thevenet, F.; Olivier, L.; Batault, F.; Sivachandiran, L.; Locoge, N., *Acetaldehyde Adsorption on TiO₂: Influence of NO₂ Preliminary Adsorption.* Chemical Engineering Journal, 2015. **281**: p. 126-133.

6. Huthwelker, T.; Ammann, M.; Peter, T., *The Uptake of Acidic Gases on Ice.* Chemical Reviews, 2006. **106**(4): p. 1375-1444.

7. Usher, C. R.; Michel, A. E.; Grassian, V. H., *Reactions on Mineral Dust.* Chemical Reviews, 2003. **103**(12): p. 4883-4940.

8. Romanias, M. N.; El Zein, A.; Bedjanian, Y., *Uptake of Hydrogen Peroxide on the Surface of Al₂O₃ and Fe₂O₃.* Atmospheric Environment, 2013. **77**: p. 1-8.

9. Romanias, M. N.; Zogka, A. G.; Papadimitriou, V. C.; Papagiannakopoulos, P., *Uptake Measurements of Acetic Acid on Ice and Nitric Acid-doped Thin Ice Films over Upper Troposphere/lower Stratosphere Temperatures.* Journal of Physical Chemistry A, 2012. **116**(9): p. 2198-2208.

10. Crowley, J. N.; Ammann, M.; Cox, R. A.; Hynes, R. G.; Jenkin, M. E.; Mellouki, A.; Rossi, M. J.; Troe, J.; Wallington, T. J., *Evaluated Kinetic and Photochemical Data for Atmospheric Chemistry: Volume V - Heterogeneous Reactions on Solid Substrates.* Atmospheric Chemistry and Physics, 2010. **10**(18): p. 9059-9223.

11. Coates, J., Interpretation of Infrared Spectra, A Practical Approach. In *Encyclopedia of Analytical Chemistry*, John Wiley & Sons, Ltd: 2006.

12. Zevenhoven, R.; Teir, S.; Eloneva, S., *Heat Optimisation of a Staged Gas–solid Mineral Carbonation Process for Long-term CO₂ Storage.* Energy, 2008. **33**(2): p. 362-370.

13. Bhardwaj, R.; van Ommen, J. R.; Nugteren, H. W.; Geerlings, H., *Accelerating Natural CO₂ Mineralization in a Fluidized Bed.* Industrial & Engineering Chemistry Research, 2016. **55**(11): p. 2946-2951.

14. von Hessberg, P.; Pouvesle, N.; Winkler, A. K.; Schuster, G.; Crowley, J. N., *Interaction of Formic and Acetic Acid with Ice Surfaces Between 187 and 227 K. Investigation of Single Species- and Competitive Adsorption.* Physical Chemistry Chemical Physics, 2008. **10**(17): p. 2345-2355.

15. Gillies, J. A.; Nickling, W. G.; McTainsh, G. H., *Dust Concentrations and Particle-size Characteristics of an Intense Dust Haze Event: Inland Delta Region, Mali, West Africa.* Atmospheric Environment, 1996. **30**(7): p. 1081-1090.

16.   Zhang, R.; Wang, M.; Sheng, L.; Kanai, Y.; Ohta, A., *Seasonal Characterization of Dust Days, Mass Concentration and Dry Deposition of Atmospheric Aerosols Over Qingdao, China.* China Particuology, 2004. **2**(5): p. 196-199.

17.   Singh, H.; Chen, Y.; Staudt, A.; Jacob, D.; Blake, D.; Heikes, B.; Snow, J., *Evidence From the Pacific Troposphere for Large Global Sources of Oxygenated Organic Compounds.* Nature, 2001. **410**(6832): p. 1078-1081.

Chapter V. Heterogeneous interaction of isoprene with natural Gobi dust.

Table of content

List of Tables

List of Figures

In the previous chapter, an investigation of the interaction of an anthropogenic VOC on natural Gobi dust sample showed that such heterogeneous processes should not be ruled out in the atmosphere. Indeed up to 38% of IPA could be depleted from the atmosphere by the effect of its heterogeneous removal by mineral dust under dry conditions typical of a dust storm. Moreover, the heterogeneous reactivity of IPA with Gobi dust under UV irradiation led to the formation of several ppt of oxygenated VOCs which could be an important process in some specific environments. But what about the interaction of natural dust sample with a typical biogenic VOC?

In order to investigate the interaction of a biogenic VOC with natural dust samples and evaluate whether this interaction is reactive or purely sorptive, isoprene (ISP) has been selected as a biogenic VOC of interest. Indeed, this VOC is the highest emitted biogenic VOC in the atmosphere and the impact of heterogeneous processes on that VOC requires a deeper investigation.

*In a first approach, the heterogeneous interaction of isoprene with TiO_2 has been investigated. The study of isoprene uptake and reactivity on TiO_2 under dark and irradiated conditions has been considered as a first step toward the investigation of isoprene interaction with natural samples. This initial study allowed the validation of experimental setups and analytical devices. The results evidenced that isoprene can be significantly taken up on TiO_2, and oxidized under UV-irradiation. This study also highlighted the potential side-products that can be formed from isoprene heterogeneous oxidation and justified additional experiments with the natural Gobi dust sample. The results have been published in an article entitled **"Isoprene heterogeneous uptake and reactivity on TiO_2: a kinetic study and product study"** in the **International Journal of Chemical Kinetics [1].** Since the scope of this Ph.D is dedicated to the heterogeneous processes related to natural dust samples, this article only centered on a synthetic single metal oxide is not included in the main body of the manuscript but available as Annex C.*

Based on results obtained on ISP interaction with TiO_2, the interaction of ISP on natural Gobi dust has been addressed. The objectives of this study are: (i) to provide a quantitative evaluation of ISP uptake onto a natural dust sample under typical environmental conditions; and (ii) to determine whether heterogeneous processes may have an impact on the budget of

*the most abundant biogenic VOC. The results of this study are published in an article entitled "**Heterogeneous Interaction of Isoprene with Natural Gobi Dust**" in **ACS Earth and Space Chemistry** on the 23rd of May 2017. In this article the uptake of ISP on natural Gobi dust sample is investigated from 253 to 358 K and from <0.01 to 10% RH. The kinetic measurements are performed under atmospheric pressure and for inlet concentrations of isoprene ranging from 0.05 to 140 × 10^{14} molecules cm^{-3}, corresponding to 200 ppb and 570 ppm. The initial uptake coefficients, γ$_0$ of ISP are determined as a function of environmental parameters such as ISP concentration, dust mass, temperature, and relative humidity. Furthermore, the adsorption isotherms of ISP onto natural Gobi dust sample are determined.*

The supporting information of this chapter are reported in Annex D of the manuscript. The tables and figures of the supporting information in this chapter are noted by DS before there number.

Full citation:

M. N. ZEINEDDINE, M. N. ROMANIAS, V. RIFFAULT, F. THEVENET, *Heterogeneous Interaction of Isoprene with Natural Gobi Dust*. **ACS Earth and Space Chemistry** *1 (5)*, 236-243 (2017), DOI 10.1021/acsearthspacechem.7b00050

1   Introduction to isoprene interaction with natural Gobi dust

Volatile organic compounds (VOCs) are emitted into the atmosphere from both anthropogenic and biogenic sources [2]. Once emitted, major transformation pathways include photolysis, reactions in the gas phase with atmospheric oxidants such as OH radicals, NO_3 radicals and O_3 molecules, or uptake onto particles depending on their volatility [3]. Subsequently, VOCs participate in various sequential oxidation cycles leading to the formation of new radicals, secondary VOCs and secondary organic aerosols (SOA) [4].

The current approach used in atmospheric chemistry models mainly relies on homogeneous gas-phase mechanisms eventually leading to underestimated concentrations of oxygenated volatile organic compounds (OVOCs) when compared to field observations [5]. Modelers have thus suggested that other processes acting as sources of oxygenated compounds, and not yet taken into account in reaction schemes may exist; heterogeneous oxidation processes may be one of them and it is therefore critical to evaluate the possibility of such reactions to occur under atmospheric conditions, and form OVOCs.

Mineral dust is the highest emitted type of aerosol in the atmosphere with ca. 1600 Tg released per year. It can undergo long-range transportation to remote areas [6]. Dust surfaces provide the seedbed for specific interactions with atmospheric trace gas molecules, and can subsequently play a key role in the transformation and environmental fate of many atmospheric gaseous species [7, 8]. Some of the Earth's primary dust source areas are the arid and semiarid regions of China and southern Mongolia such as Gobi desert. The Gobi desert generates large quantities of mineral dust that are carried by winds over vast areas of Asia [9], across the Pacific Ocean [10] to North America [11] and even to the Arctic region [12].

The assumption that heterogeneous processes on dust can complement the missing sinks of VOCs and the missing sources of oxygenated VOCs in the atmosphere is supported by various observations. Previous field campaigns reported a significant correlation between high dust loads and low mixing ratios for O_3 and HNO_3 [13, 14]. Besides, it has been established that dust-poor air masses originating from North Africa are characterized by significantly higher ozone concentrations than dust-rich ones [15]. Several modeling studies have investigated the potential effect of dust on O_3, inorganic nitrogen-containing species, and HO_x (OH and HO_2) [16, 17]. Bain et al. investigated the effect of reduced photolysis rates and heterogeneous

chemistry on the tropospheric trace gas mixing ratios [18]. They concluded that both processes cause a combined decrease in global mean concentrations of O_3, OH, HO_2 and HNO_3 of 0.7, 11.1, 5.2 and 3.5 %, respectively. Moreover, they evidenced that the effects of heterogeneous reactions clearly dominated over the reduced photolysis rates. Considering the relatively well-documented impact of dust storms on the atmospheric chemistry of ozone and other inorganic trace gases, [16-18] a similar effort should be undertaken to assess the impact on the global budgets of some organic trace gases, as well as the potential changes in the oxidative capacity of the troposphere. Former investigations from our research group evidenced the effective heterogeneous interactions of limonene ($C_{10}H_{16}$), toluene (C_7H_8) and isopropanol on natural Saharan and Asian dust samples [7, 8] and the subsequent formation and release of OVOCs as side-products under UV irradiation.

In this study, the heterogeneous interaction of isoprene (ISP) with natural dust from Gobi desert is investigated. ISP is the most emitted biogenic VOC in the troposphere with emission rates exceeding 500 Tg per year; it corresponds to one-third of the annual global VOC emissions [19]. The primary sources of isoprene are natural, with deciduous trees being large emitters. Isoprene predominantly reacts with the oxidants of the atmosphere in the gas phase and its estimated lifetime is in the range of a few hours. Nevertheless, literature suggests that isoprene degradation on humic-like particles could account for a major fraction of organic aerosols and possibly to OVOC formation [20]. Furthermore, it is reported in the literature that isoprene is significantly taken up by soils [21].

Therefore, the main objective of the present study is to investigate whether isoprene can be taken up and reacts on the surface of natural dust samples and how far it impacts the budget of isoprene and could contribute to the formation of OVOCs, especially during intense dust events.

Consequently, in the framework of the current study, the heterogeneous interaction of ISP with Gobi dust is examined under atmospheric pressure in a U-shaped flow reactor. The gas phase is monitored by Selected Ion Flow Tube Mass Spectrometry (SIFT-MS). The adsorption isotherms and the uptake coefficients are determined over a range of concentrations from 0.05 to 140×10^{14} molecule cm^{-3}, in the relative humidity range < 0.01 - 10%, and in the temperature range 253 - 358 K. To the best of our knowledge, this is the first experimental study

reporting the heterogeneous kinetics of isoprene with natural atmospheric dust under typical atmospheric conditions.

2   Materials and methods

2.1   Materials

Isoprene gas mixture preparation

Various concentrations of ISP are prepared inside an 18 L stainless steel canister by injecting precise volumes of liquid ISP ranging from 1 µL to 0.1 mL (Sigma-Aldrich; purity $\geq$ 99 %). Then, the canister is filled with dry zero air. The concentration of ISP inside the canister can be adjusted from 13 ppm to 1340 ppm. The canister outlet flow is then diluted with dry zero air to allow the variation of ISP concentrations within 5 orders of magnitude. Zero air is generated from an air compressor, and sent into a catalytic zero air generator. The remaining impurity levels in the air stream are lower than the analytical system detection limits: VOCs < 0.1 ppb, CO_2 < 10 ppb, CO < 80 ppb and H_2O ~ 2 ppm. The relative humidity is controlled by changing the mixing ratio of dry and humid air. In particular, the zero air flow is moistened after passing through a H_2O bubbler and is further diluted with dry air to obtain the targeted RH level. The exact relative humidity in the gas flow is monitored using a temperature and moisture probe (KIMO HQ 210).

Natural Gobi dust characterizations

Natural Gobi dust has been collected from aeolian deposits in Yanchi, Ningxia province in China (107.475211° E, 36.487333°N). The uptake of ISP on Gobi dust is studied using the smallest sieved size fraction of the dust batch (< 100 µm) that can be suspended in air [22], Its specific surface area (SSA) is determined employing the BET method. At least three adsorption measurements are conducted on different samples and SSA is determined as: SSA= 10.5 ± 2.0 $m^2 \, g^{-1}$.

The Gobi dust sample has also been chemically characterized employing X-ray diffraction and fluorescence techniques, as well as Inductively Coupled Plasma Mass Spectrometry (ICP-MS). The mineralogy and elemental composition of the Gobi sample have already been provided in Table II-2 and Table II-3.

Pretreatment of natural Gobi dust samples

Prior to the experiments, each dust sample is thermally pretreated at 423 K for 10 minutes and purged with dry zero air to remove any pre-adsorbed species. Regarding experiments performed under different relative humidity conditions, the dust surface is pre-exposed to a corresponding humid air flow for 10 minutes prior to any experiment.

2.2 Methods

Experimental setup

The experimental setup is composed of three parts: (i) the gas flow generation system, (ii) the U-shaped flow reactor, and (iii) the analytical device. A detailed scheme of the experimental setup is presented in Figure V-1. The gas flow generation line is made of stainless steel and Teflon. Calibrated mass flow controllers (Bronkhorst) are used to introduce ISP and dilute it with zero air upstream the reactor at a total flow rate of that can be adjusted from 500 to 600 sccm.
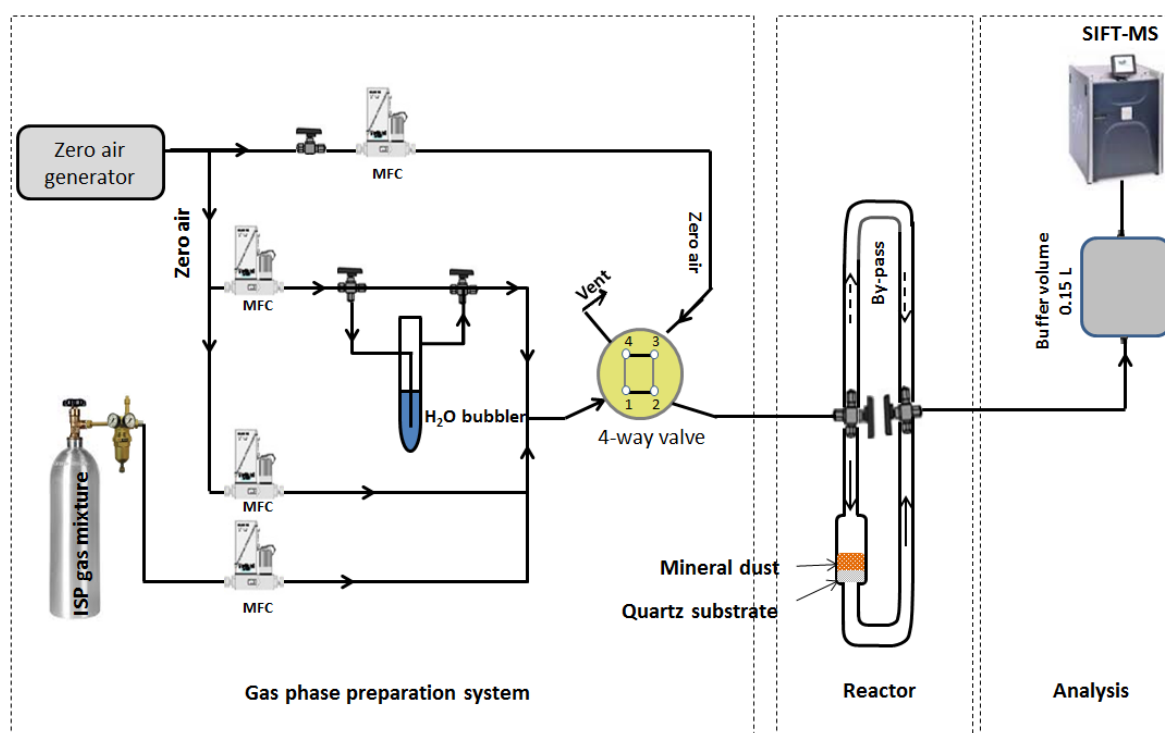
Figure V-1. Schematic representation of the experimental setup used for the kinetic studies. MFC: Mass Flow Controller.

The reactor itself consists in two parts: the upper one is a bypass line with a total volume of 15 cm^3. The lower part, with an equivalent volume of 15 cm^3, is equipped with a quartz wool

sample-holder with a geometric surface area of 4.95 cm^2, on top of which the sample is placed. Both sections are connected via two 3-way valves. The lower part of the reactor with the dust sample is immersed in a thermostated bath (Huber ministat 230) filled with ethanol or water, which allows varying the temperature from 253 to 358 K i.e. from -20 to 85°C. The bypass line is also thermostated, by wrapping it up either with a thin flex tube circulating the thermostatic liquid, or using a heating tape. The exact temperature of the dust sample is recorded using a K-type thermocouple inserted inside the U-shaped reactor.

A known amount of mineral dust is placed on top of the porous quartz wool sample-holder as shown in Figure V-1. The residence time of ISP in the reactor is estimated to be ca. 1 second. The real time monitoring of ISP concentration at the reactor outlet is achieved employing a Selected Ion Flow Tube Mass Spectrometer, Voice 200 SIFT-MS. The SIFT-MS is an analytical technique based on the chemical ionization of the analytes using three reagent ions: H_3O^+, NO^+ and O_2^+. ISP is detected using H_3O^+ and NO^+ ions at mass peaks 69 ($C_5H_8H^+$) and 68 ($C_5H_8^+$), respectively.

Experimental protocol

Typical concentration profiles of ISP in the absence and presence of Gobi dust are presented in Figure V-2. In order to record the background level of ISP, zero air is flown through the reactor. Then the gas flow direction is changed to the bypass line using the two 3-way valves, and a known concentration of ISP is introduced at the reactor inlet. When the inlet concentration is monitored at the outlet of the bypass line, the dust sample is exposed to ISP by allowing the gas mixture to flow through the reactor. An uptake peak can be observed on ISP concentration profile; it has to be mentioned that in the absence of dust and with the same protocol, no variation in the signal is recorded (Figure V-2), confirming the absence of impact of the reactor volume (15 cm^3) and showing that ISP adsorption on the quartz wool substrate remains below the detection limit. However, for temperatures lower than 280 K, a slight adsorption of ISP on the quartz wool can be noticed. Under these condition, the uptake of ISP on the substrate is subtracted in the subsequent data analysis. The observed adsorption peak is proportional to the number of molecules of ISP adsorbed on the natural dust sample. As equilibrium between the adsorbate and the natural dust surface is achieved, the ISP concentration at the outlet of the reactor is equal to the inlet concentration. Then, the reactor is isolated, i.e. switched to bypass.
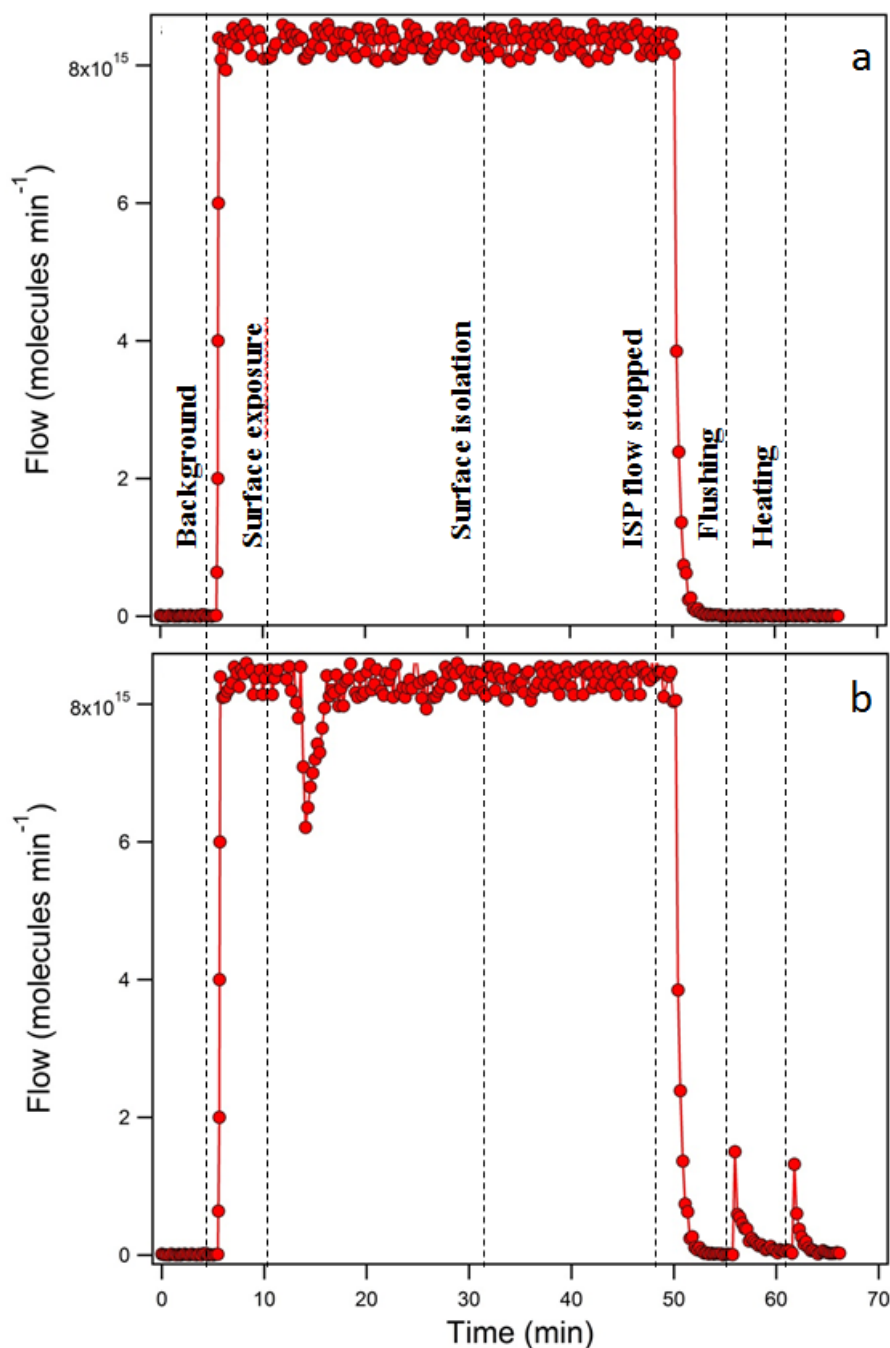
Figure V-2. Typical gas-phase profiles of ISP recorded with the SIFT-MS at 298 K and dry conditions in the absence (a) and presence (b) of dust. The H_3O^+ ion was used to monitor ISP profile with the SIFT-MS using the mass peak 69 ($C_5H_8H^+$).

The ISP flow is then stopped and the lines are purged with zero air under the corresponding RH level. Consequently, the ISP concentration returns back to its background

153

level. Then, the zero air flow is directed through the reactor to purge the surface and recover the weakly adsorbed fraction of ISP. This first flushing step is always conducted under the same temperature as the adsorption experiment. Lastly, the surface is heated up to 473 K to remove the remaining strongly adsorbed fraction of ISP. It is to be noted that the sample is changed with every changing condition, i.e temperature or RH, and that the carbon mass balance of isoprene adsorbed on the dust is always completely retrieved after heating.

Furthermore, various analytical techniques are used to characterize the gas phase and the adsorbed phase. The gas phase is studied employing the U-shaped reactor coupled to a SIFT-MS. The adsorbed phase is monitored using a DRIFTs optical cell and offline analysis with HPLC chromatography. The aim of using different reactors and analytical instruments is to investigate the possible formation of products in the gas and adsorbed phases, although none could be observed. This means that either the interaction of ISP with Gobi dust does not lead to any product formation or the products formed are below the detection limit of the analytical instruments used. Detection limits of the instruments have been previously discussed in Section 2.1 of Chapter 2.

The initial uptake coefficient, γ_0, is a time-dependent kinetic parameter that can be determined from the initial stage of a typical experiment on fresh surfaces, i.e. previously unexposed. The online monitoring of the gas phase by SIFT-MS allowed the determination of γ_0 within the first seconds of interaction between ISP and Gobi dust [23]. The uptake coefficient can be derived from Equation V-1 to V-4.

$$\frac{d(IPA)/dt}{V} = k_{het}[IPA] \qquad \textbf{(Equation V-1)}$$

$$k_{het=} \frac{d(IPA)/dt}{V[IPA]} = \omega\gamma_0 \qquad \textbf{(Equation V-2)}$$

with:

$$\omega = \frac{cA_s}{4V} \qquad \textbf{(Equation V-3)}$$

and finally:

$$\gamma_0 = \frac{4\{d(IPA)/dt\}}{cA_s[IPA]} \qquad \textbf{(Equation V-4)}$$

where (ISP) denotes the number of ISP molecules taken up by the dust surface at the beginning of exposure (molecule); k_{het}, the first-order rate coefficient of the heterogeneous removal of ISP (s^{-1}); V, the volume (cm^3); [ISP], the ISP gas-phase concentration (molecule

cm^{-3}); ω, the collision frequency (s^{-1}); c, the mean molecular velocity (cm s^{-1}); A_s, the effective surface area (cm^2), calculated as the product of SSA with the mass of the sample.

3 Results and discussion

3.1 Initial uptake coefficients of isoprene on Gobi dust sample

3.1.1 Dependence of isoprene uptake on the mass of Gobi dust

The mass dependence experiments of the initial uptake of isoprene are carried out to determine the limit of accessible sites of Gobi dust samples. Initial uptake coefficients are determined as a function of the exposed dust sample mass. Figure V-3 reports the geometric initial uptake coefficient of ISP as a function of the mass of Gobi dust exposed. It is calculated using two different ions detected by SIFT-MS obtained from the reaction of isoprene with H_3O^+ and NO^+, at mass peaks 69 ($C_5H_8H^+$) and 68 ($C_5H_8^+$), respectively.
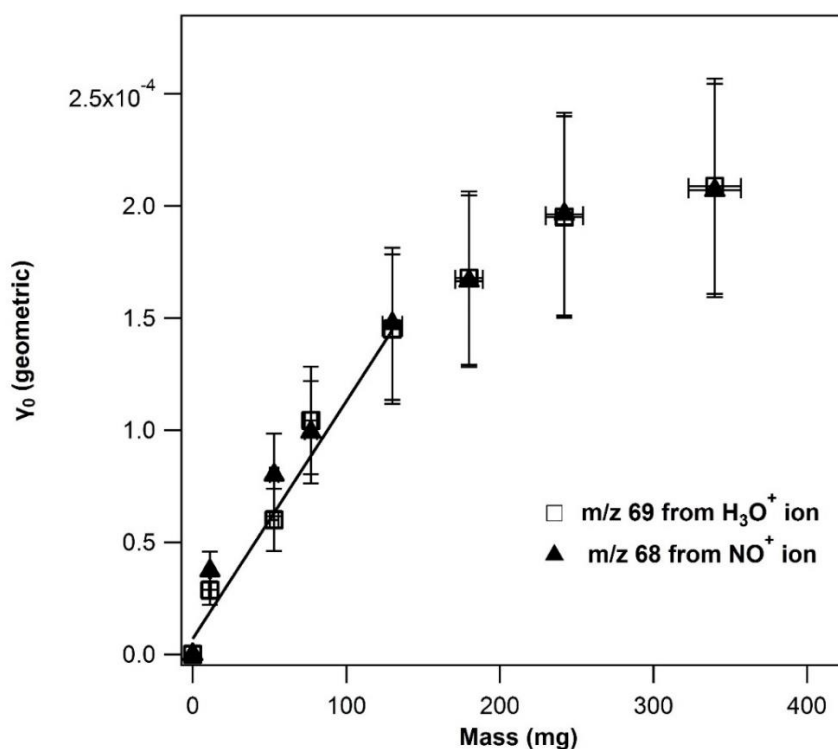
Figure V-3. Dependence of the geometric initial uptake coefficient of ISP as a function of the Gobi dust mass exposed. The error bars represent the overall uncertainty on γ_0. The solid line is the linear fit through the experimental points within the range where the uptake is proportional to the mass of Gobi dust, i.e. for dust masses lower than 150 mg.

The experiments are carried out at room temperature and under dry conditions. As long as the geometric uptake linearly varies with the mass of dust exposed, i.e. below 150 mg, it can be assumed that the entire surface of the dust sample remains accessible to isoprene, and the BET surface area can be used for the determination of the specific uptake coefficient [23]. Thus, the kinetic measurements performed inside the U-shaped reactor are carried out with a mass of Gobi dust lower than 150 mg.

3.1.2 Dependences of isoprene uptake on concentration and relative humidity

ISP initial uptake has been determined at room temperature as a function of ISP concentration for inlet concentrations ranging from 0.05 to 4.92×10^{14} molecule cm^{-3} and under relative humidity ranging from < 0.01 to 10%.
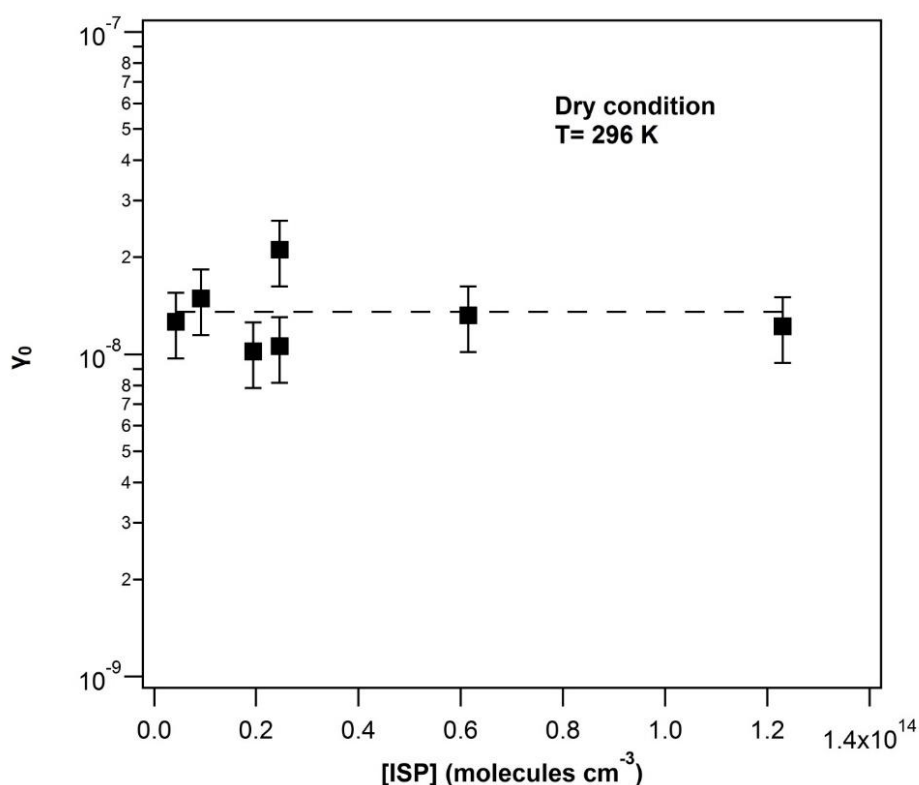
Figure V-4. Initial uptake coefficients determined at 296 K and under 3 % RH as a function of the ISP gas-phase concentration. The error bars represent the overall estimated uncertainty on γ_0.

Regarding the impact of isoprene concentration, γ_0 is found to be independent on ISP initial concentration; results are presented in Figure V-4. This behavior is expected since the initial uptake expresses the interaction of a gas molecule with a fresh and unexposed surface. A similar behavior was observed for isopropanol as seen in Section 2.1.2 of Chapter 4. However

the initial uptake of IPA is found to be higher than of that ISP by around one order of magnitude. The presence of the OH functional group could be an important factor controlling the strength of the uptakes.

Regarding the impact of relative humidity, γ_0 is found to be inversely dependent on RH as reported in Figure V-5. Experimental results are simulated with the empirical Equation V-5 in order to be able to extrapolate the initial uptake at any targeted RH. Above 10 % RH the initial uptake is significantly decreased and isoprene uptake induces a concentration drop on concentration profile that cannot be detected by analytical techniques used. The uptake process is below the detection limit of our instrument. An inverse dependence of the initial uptake with RH on different substrates, especially mineral oxides and ice, has already been reported in previous studies where similar trends were observed [8, 24].

$$\gamma_0 = 2.7 \times 10^{-10}/(0.005 + RH^{1.4}) \qquad \textbf{(Equation V-5)}$$
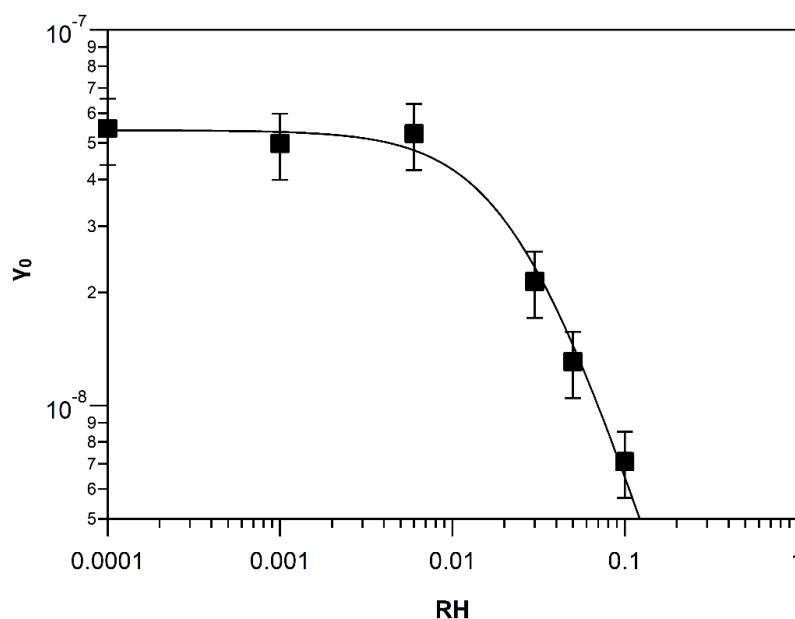
Figure V-5. Initial uptake coefficients of ISP determined over the RH range 0.01 - 10% as a function of the ISP gas-phase concentration, monitored by SIFT-MS. The error bars represent the overall estimated uncertainty on γ_0. The uptake coefficient was found to be inversely dependent on RH according to the empirical equation (solid line fitting the experimental points): $\gamma_0 = (2.7 \times 10^{-10}) / (0.005 + RH^{1.44})$

3.1.3   Dependence of isoprene uptake on temperature

The temperature dependence of ISP initial uptake coefficients γ_0 on Gobi dust is determined on the ISP concentration range $(0.05 - 4.92) \times 10^{14}$ molecule cm^{-3} and over 253 - 358 K. The corresponding Arrhenius plot is reported in Figure V-6. Each point represents an average of four different experiments at each temperature. The initial uptake coefficients of ISP on Gobi dust are fitted by the Arrhenius Equation V-6 so that the initial uptake can be extrapolated at any targeted temperature. These types of equations are also needed to import the impact of ISP interaction with mineral dust in an atmospheric model.

$$\gamma_0 = (5.30 \pm 1.50) \times 10^{-7} exp\,[(1376 \pm 133)/\,T \qquad \textbf{(Equation V-6)}$$
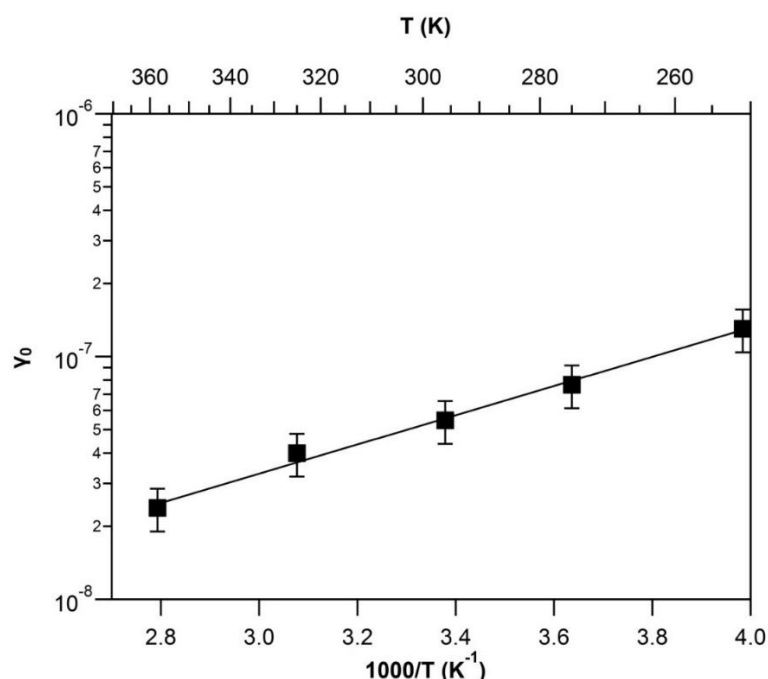
Figure V-6. Initial uptake coefficients determined over the range 253 - 358 K as a function of 1000/T, monitored by SIFT-MS. The error bars represent the overall estimated uncertainty on γ_0. The solid line is the exponential fit through the experimental results according to the Arrhenius equation. The uptake coefficient is found to be dependent on T according to the following equation: $\gamma_0 = (5.30 \pm 1.5) \times 10^{-7}$ exp [(1376 $\pm$ 133)/T].

The uncertainties on the exponential factor reflects the 2σ precision of the fit of ln(γ_0) versus 1000/T, while the error limit on the pre-exponential factor, A, expressed in the same unit than γ_0, is related to the intercept of the fit based on the expression dA = A $\times$ d(lnA). The

activation energy of ISP uptake derived from the slope of the fit is determined as E_a = -11.4 ± 2.2 kJ mol^{-1}. The negative activation energy corresponds to the overall energy barrier for the colliding gas molecules to undergo adsorption on the Gobi dust surface via the formation of an intermediate state on dust. Low and negative activation energies indicate less stable intermediate state and/or higher energy barrier between the intermediate precursor state and the transition state for adsorption on the dust surface. The negative activation energy values provide a qualitative estimate of (i) the surface ability to diffuse the kinetic energy of colliding molecules and stabilize them on the surface, and (ii) the intensity of the gas-surface interaction.

3.2 Adsorption isotherms of isoprene on natural Gobi dust samples

3.2.1 Dependence of isoprene adsorption isotherm on temperature
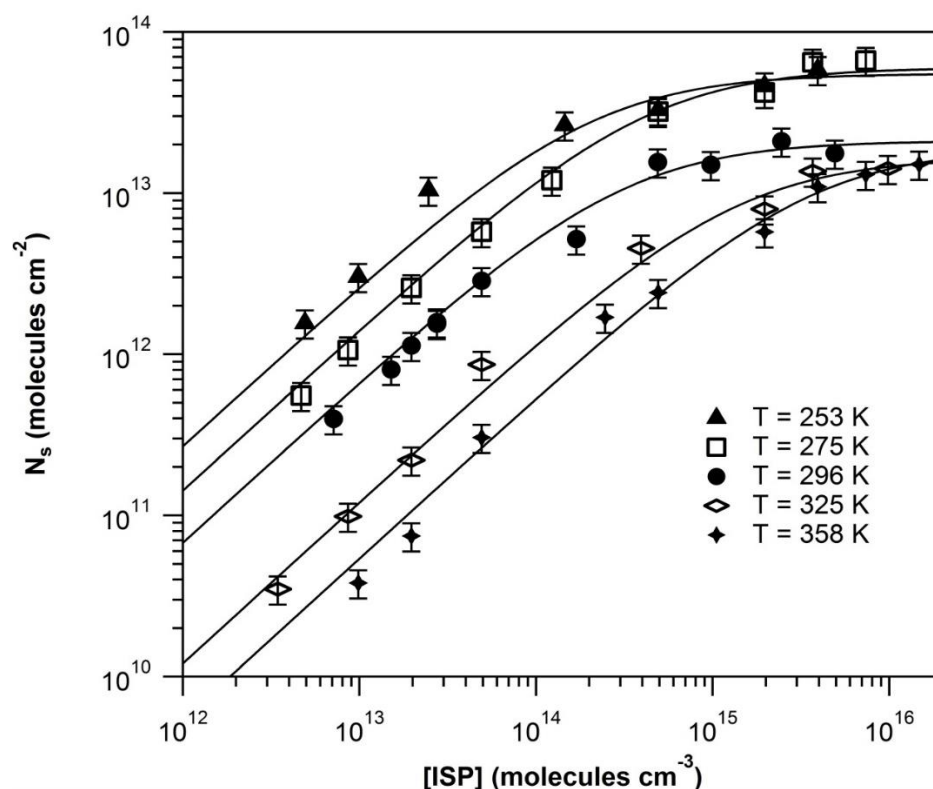
Figure V-7. Adsorption isotherms of ISP on Gobi dust determined in the temperature range 253 - 358 K under dry conditions (< 0.01%). The error bars represent the overall uncertainty on N_s determination. The lines are non-weighted fits through the data using the Langmuir equation.

The adsorption isotherms of ISP on Gobi dust under dry conditions and from 253 to 358 K are presented in Figure V-7. The number of ISP molecules adsorbed per unite surface on

Gobi dust increases with decreasing temperature. In addition, a surface concentration plateau is reached for ISP concentration higher than 10^{15} molecules cm^{-3}, This plateau indicates the highest coverage of the dust surface by ISP for a given temperature. This behaviour is characteristic of a Langmuir adsorption process, and results have been fitted using the corresponding model. It assumes that (i) all sites are equivalent and (ii) the uptake of a gas molecule on a solid surface cannot proceed beyond monolayer coverage. Based on Langmuir model, the number of ISP molecules adsorbed per specific surface unit is related to the gas-phase concentration according to Equation V-7:

$$\theta = \frac{N_S}{N_{max}} = \frac{K_{Lang} \times [ISP]}{1 + K_{Lang} \times [ISP]}$$

(Equation V-7)

In Equation V-7, θ is the surface coverage; N_s the number of ISP molecules adsorbed (molecule cm^{-2}); N_{max} the surface saturation coverage (molecule cm^{-2}) and K_{Lang} (cm^3 molecule^{-1}) the Langmuir equilibrium constant, which describes the partitioning between the gas phase and the adsorbed phase.

Proper rearrangement of Equation V-7 leads to Equation V-8:

$$\frac{[ISP]}{N_S} = \frac{1}{N_{max} \times K_{Lang}} + \frac{1}{N_{max}} \times [ISP]$$

(Equation V-8)

A linear fit of the [ISP]/N_s ratio versus [ISP] provides N_{max} and K_{Lang} values for each temperature. The obtained values are reported in Table V-1, as well as K_{Lin} calculated as:

$$K_{Lin} = K_{Lang} \times N_{max}$$

(Equation V-9)

where K_{Lin} is an equilibrium constant introduced by the IUPAC panel in order to include the temperature dependence of surface coverage [25]. The temperature dependence of K_{Lin} is given by the Van't Hoff Equation V-10:

$$K_{Lin} = A\, exp[-\Delta H_{ads}/RT]$$

(Equation V-10)

where A is the pre-exponential factor and R the ideal gas constant. The plot of K_{Lin} versus 1000/T is displayed in Figure V-8 and Equation V-11 is obtained by fitting the data through and exponential fit that helps calculating the enthalpy of adsorption:

160

$$K_{Lin} = (1.39 \pm 0.33) \times 10^{-7} \, exp[3732 \pm 140/RT] \qquad \textbf{(Equation V-11)}$$

Table V-1. Saturation surface coverage, N_{max}, and partitioning constants K_{Lang} and K_{Lin} values for ISP adsorption on Gobi dust as a function of relative humidity, at 296 K and under dry conditions. The overall uncertainty for N_{max} and K_{Lang} is estimated to be ca. 16 % while for K_{Lin} it is ca. 20 % for relative humidity dependence and ca. 23 % for temperature dependence.

RH (%)	[ISP] (10^{13} molecule cm^{-3})	N_{max} (10^{13} molecule cm^{-2})	K_{Lang} (10^{-16} cm^3 molecule^{-1})	K_{Lin} (10^{-3} cm)
< 0.01	0.32 - 615	1.97 ± 0.39	24.1 ± 3.9	47.5 ± 10.9
3	0.41 - 2533	1.77 ± 0.35	2.66 ± 0.53	4.71 ± 0.94
5	0.34 - 3296	1.55 ± 0.31	1.43 ± 0.28	2.22 ± 0.44
10	0.42 - 1476	1.14 ± 0.23	0.74 ± 0.48	0.84 ± 0.17
$K_{Lin} = 0.028 / (0.604 + RH^{1.54})$				
T (K)	[ISP] (10^{13} molecule cm^{-3})	N_{max} (10^{13} molecule cm^{-2})	K_{Lang} (10^{-16} cm^3 molecule^{-1})	K_{Lin} (10^{-2} cm)
253	0.49 - 615	4.66 ± 0.93	72.8 ± 11.7	33.9 ± 7.8
275	0.46 - 728	6.41 ± 1.28	17.3 ± 2.8	11.1 ± 2.6
296	0.71 - 615	1.97 ± 0.39	24.1 ± 3.9	4.75 ± 1.09
325	0.34 - 984	1.66 ± 0.33	6.91 ± 1.10	1.15 ± 0.26
358	0.98 - 1476	2.36 ± 0.47	2.08 ± 0.33	0.49 ± 0.11
$K_{Lin} = (1.39 \pm 0.33) \times 10^{-7} \, exp\,[(3732 \pm 140)/T]$				

The quoted uncertainties on the exponential factor reflect the 2σ precision of the fit of $ln(K_{Lin})$ versus 1000/T, while the one on the pre-exponential factor, A, is related to the intercept of the fit based on the expression $dA = A \times d(lnA)$ where $d(lnA)$ comes from the 2σ precision as well. The ISP adsorption enthalpy derived from the slope of the fit is determined as $\Delta H_{ads} = -31.0 \pm 2.3$ kJ mol^{-1}. It can be noted that the total heat content of the heterogeneous interaction

161

of ISP with Gobi dust is lower than that of isopropanol with the same dust sample -14.7 ± 1.1 kJ mol^{-1} [8]. This indicates that ΔH_{ads} can vary widely for the same substrate.
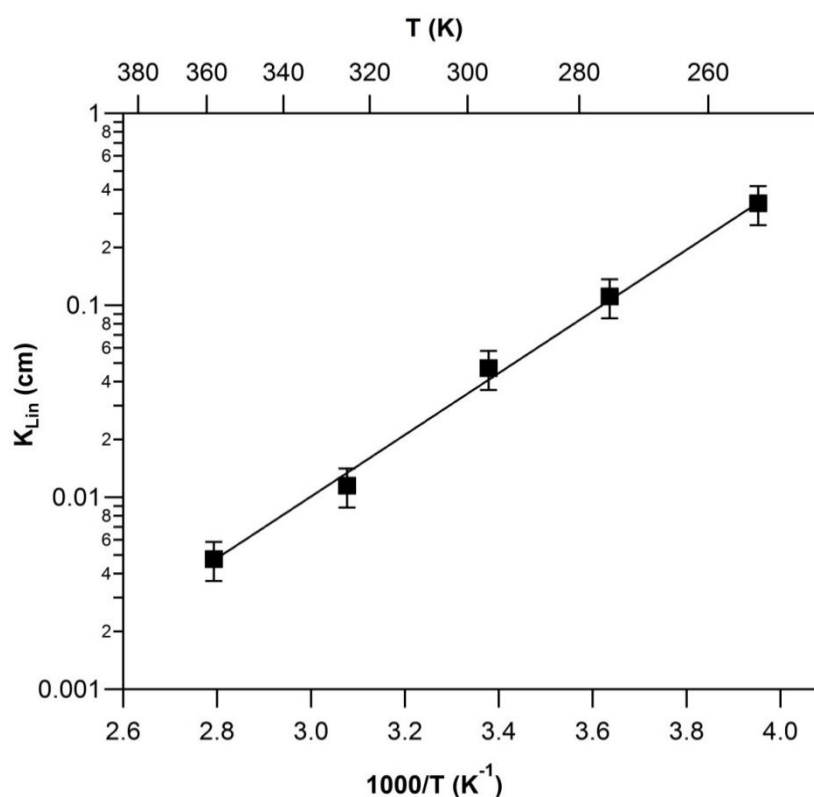
Figure V-8. Dependence of K_{Lin} on temperature in dry conditions. The error bars represent the overall uncertainty on K_{Lin} determination. The solid line is the non-weighted Van't Hoff fit through the calculated data and is represented by the equation $K_{Lin} = (1.39 \pm 0.33) \times 10^{-7} \exp [(3732 \pm 140)/T]$.

Moreover, previous work from our group [26] studied the adsorption isotherms of water and derived ΔH_{ads} for the same natural mineral dust sample. The authors used the 3-parameter BET expression and integrated band intensities to simulate the water adsorption isotherms on different natural mineral surfaces, allowing to determine the number of water layers formed and to retrieve thermodynamical parameters (the published article is attached as annex E in this manuscript). The enthalpy of adsorption of water on the Gobi dust sample was found to be -49.2 kJ mol^{-1}. This value is lower than the adsorption enthalpies of IPA and ISP on the same dust sample. So water could be expected to play a critical role whenever considering any VOC interaction with natural dust samples.

3.2.2 Dependence of isoprene adsorption isotherm on relative humidity

The adsorption isotherms of ISP as a function of relative humidity are investigated at 296 K and results are reported in Figure V-9. ISP adsorption is considerably impacted with

162

increasing relative humidity. Clearly, H_2O molecules compete with ISP for the adsorption sites. This is consistent with the fact that the formation of the first monolayer of water occurs at 24% RH as reported by a previous work from our group investigating water adsorption on various dust samples including the one used in that study [26]. Therefore, highlighting the importance of relative humidity on the interaction of VOCs with natural dust samples. Plotting the results with the linear form of the Langmuir equation (Equation V-8) allows the determination of N_{max}, K_{Lang}, and K_{Lin} over the entire RH range. Results are reported in Table V-1 as well. The dependence of K_{Lin} on RH is displayed in Figure DS1 of annex D and is described by the empirical Equation V-12 so that K_{lin} could be extrapolated at any targeted RH:

$$K_{Lin} = 0.028/ (0.604 + RH^{1.54})$$ **(Equation V-12)**
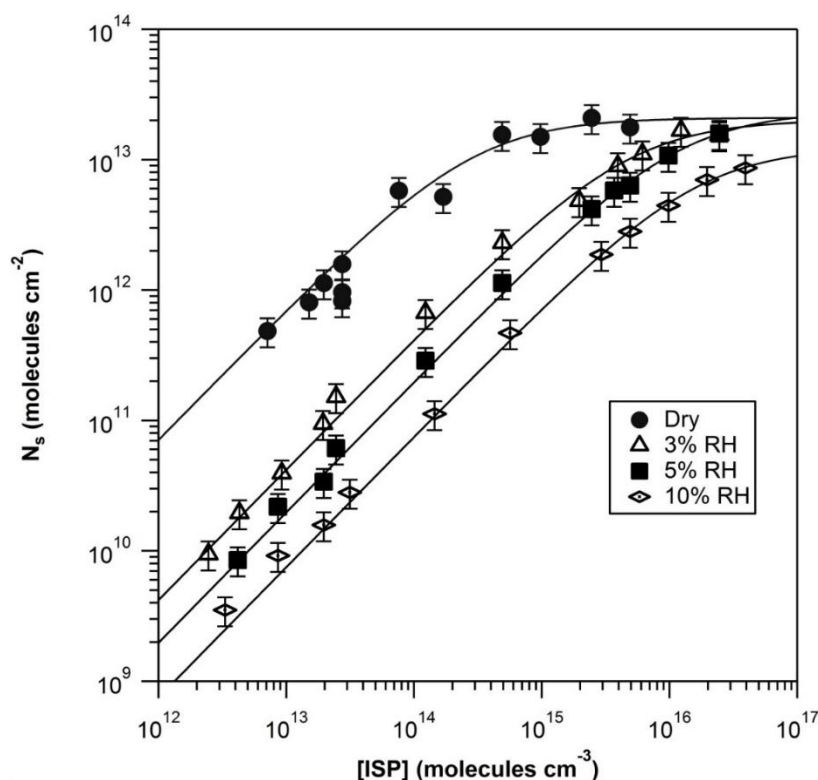
Figure V-9. Adsorption isotherms of ISP on Gobi dust determined in the relative humidity range < 0.01 - 10% at 296 K. The error bars represent the overall uncertainty on N_s determination. The lines are non-weighted fits through the data according to the Langmuir equation.

3.3   Reversibility of isoprene uptake on natural Gobi dust

In dry conditions not all the entire adsorbed fraction of ISP interaction with Gobi dust sample is desorbed by flushing the dust surface with zero air at room temperature (see Figure

V-2). Therefore, the dust sample was heated at 473 K in order to desorb the remaining fraction. Under humid condition the heating step is not needed since all the adsorbed fraction is reversible. Figure V-10 is a bar chart representing the evolution of both the reversibly and irreversibly adsorbed fractions of ISP on Gobi dust samples as a function of temperature under dry conditions. The reversible fraction is deduced from the irreversible ones considering 100% recovery. The irreversible fraction decreases as a function of temperature until almost all the adsorbed molecules can be recovered by one single flushing step, which is expected in accordance with the Langmuir isotherm.
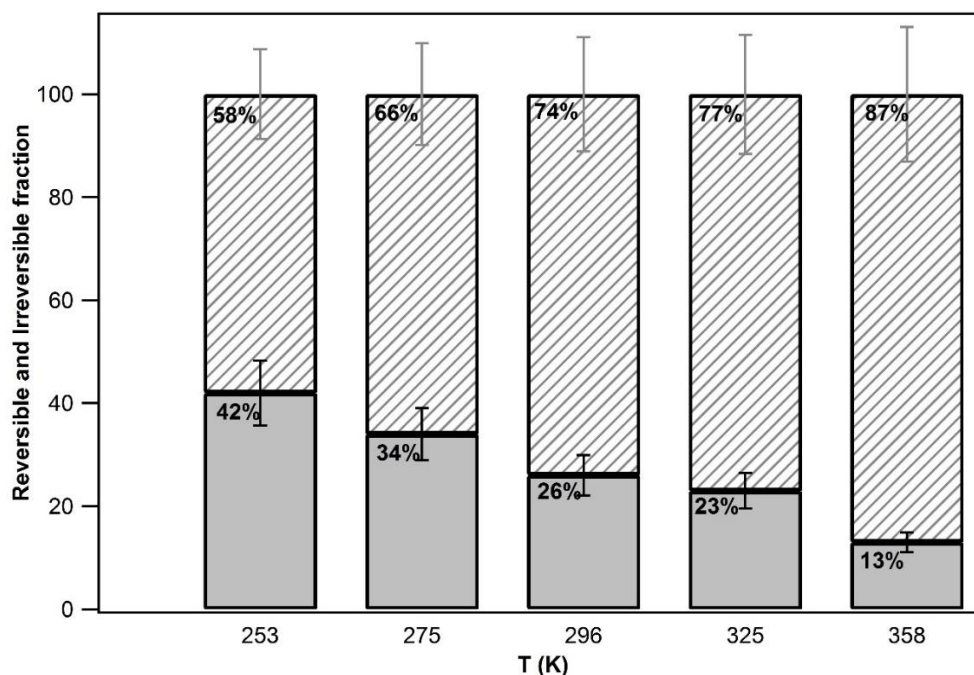
Figure V-10. Irreversible fractions (solid bars) of adsorbed ISP calculated from ISP recovery after flushing at 473 K. The reversible fractions (dashed bars) are deduced considering 100% recovery. Errors quoted represent the 1σ precision of the average of all the experiments at each temperature.

4   Atmospheric implications

The atmospheric lifetime of isoprene due to its heterogeneous loss onto a dust surface can be calculated using Equation V-13:

$$\tau_{het} = \frac{4}{\gamma \, c \, D} \qquad\qquad \textbf{(Equation V-13)}$$

where γ is the uptake coefficient, c the mean molecular velocity (cm s^{-1}), and D the Gobi dust surface area density (cm^2 cm^{-3}). Considering (i) concentrations of Gobi dust

transported to forested regions of 1400 µg m^{-3} [27], and (ii) the SSA of the natural sample A_S = 10.5 ± 2.0 m^2 g^{-1}, D can be calculated by the direct multiplication of the dust concentration and the specific surface area of the dust sample used and was found to be 1.47×10^{-4} cm^2 cm^{-3}; besides, the uptake coefficient of ISP onto Gobi dust (γ_{BET}) at 30% RH and 296 K can be extrapolated to 1.5×10^{-9} using Equation V-5. It has to be noted that the extrapolated value should be considered as a lower limit [25]. This leads to a calculated lifetime of ISP due to its heterogeneous loss on Gobi dust of several years. However, using the geometric surface area of the dust (4.95 cm^2) instead of the SSA allows deriving an upper limit of the atmospheric lifetime: The geometric uptake coefficient for RH < 30% is then estimated to be 2×10^{-5} and the lifetime is in the range of 13 hours. Based on these calculations, it appears that the heterogeneous uptake of ISP on natural dust particles is a negligible process compared to fast gas-phase oxidation processes (atmospheric lifetimes of 50 min, 1.4 and 22 hours with NO$_3$, OH radicals and ozone, respectively).

The lifetime of isopropanol removal by heterogeneous interaction with the same Gobi dust sample was found to be 9.2 days, using the BET surface area of the dust sample, in urban areas where dust could be transported [8]. The difference between isopropanol and ISP may be attributed to the presence of the hydroxyl group in isopropanol structure. The considerable difference in lifetime values between these two compounds on the same natural sample indicates that the interactions of VOCs onto mineral dust is different from one VOC to another and should be experimentally determined in order to assess VOC individual significances in the atmosphere through heterogeneous pathways. The fate and reactivity of VOCs via heterogeneous processes appear closely related to their structures, constraining their interactions with the considered mineral surfaces, and not directly to their atmospheric abundances.

5   Conclusion

Within the framework of the current study, the adsorption of isoprene on Gobi dust was investigated in the temperature and relative humidity ranges of 253 - 358 K and <0.01 − 10%, respectively. The initial uptake coefficient, γ_0, of isoprene was measured as a function of several parameters (isoprene mass, temperature, and relative humidity). γ_0 is inversely dependent on relative humidity and dependent on temperature. It is evidenced that ISP is rather sorptive and not reactive on dust surfaces; the activation energy and the enthalpy of adsorption are equal to

E_a = -11.4 ± 2.2 kJ mol^{-1} and ΔH_{ads} = -31.4 kJ mol^{-1}. Thus the interaction of ISP on Gobi dust is weak. The lifetime of ISP heterogeneous removal on Gobi dust is almost negligible compared to its removal from gas-phase reactions. Therefore, in the following chapter an examination of a VOC that has a longer gas-phase lifetime in the atmosphere is investigated.

6 References of Chapter V

1. Romanias, M. N.; Zeineddine, M. N.; Riffault, V.; Thevenet, F., *Isoprene Heterogeneous Uptake and Reactivity on TiO2: A Kinetic and Product Study.* International Journal of Chemical Kinetics, 2017. **49**(11): p. 773-788.

2. Koppmann, R., *Volatile Organic Compounds In The Atmosphere.* 2008: John Wiley & Sons.

3. Atkinson, R.; Arey, J., *Atmospheric Degradation of Volatile Organic Compounds.* Chemical Reviews, 2003. **103**(12): p. 4605-4638.

4. Singh, H. B.; Kanakidou, M.; Crutzen, P. J.; Jacob, D. J., *High Concentrations and Photochemical Fate of Oxygenated Hydrocarbons in the Global Troposphere.* Nature, 1995. **378**(6552): p. 50-54.

5. Karl, T.; Potosnak, M.; Guenther, A.; Clark, D.; Walker, J.; Herrick, J. D.; Geron, C., *Exchange Processes of Volatile Organic Compounds Above a Tropical Rain Forest: Implications for Modeling Tropospheric Chemistry Above Dense Vegetation.* Journal of Geophysical Research: Atmospheres, 2004. **109**(D18).

6. Satheesh, S. K.; Krishna Moorthy, K., *Radiative Effects of Natural Aerosols: A Review.* Atmospheric Environment, 2005. **39**(11): p. 2089-2110.

7. Romanias, M. N.; Ourrad, H.; Thévenet, F.; Riffault, V., *Investigating the Heterogeneous Interaction of VOCs with Natural Atmospheric Particles: Adsorption of Limonene and Toluene on Saharan Mineral Dusts.* The Journal of Physical Chemistry A, 2016. **120**(8): p. 1197-1212.

8. Romanias, M. N.; Zeineddine, M. N.; Gaudion, V.; Lun, X.; Thevenet, F.; Riffault, V., *Heterogeneous Interaction of Isopropanol with Natural Gobi Dust.* Environmental Science & Technology, 2016. **50**(21): p. 11714-11722.

9. Husar, R. B.; Tratt, D. M.; Schichtel, B. A.; Falke, S. R.; Li, F.; Jaffe, D.; Gassó, S.; Gill, T.; Laulainen, N. S.; Lu, F.; Reheis, M. C.; Chun, Y.; Westphal, D.; Holben, B. N.; Gueymard, C.; McKendry, I.; Kuring, N.; Feldman, G. C.; McClain, C.; Frouin, R. J.; Merrill, J.; DuBois, D.; Vignola, F.; Murayama, T.; Nickovic, S.; Wilson, W. E.; Sassen, K.; Sugimoto, N.; Malm, W. C., *Asian Dust Events of April 1998.* Journal of Geophysical Research: Atmospheres, 2001. **106**(D16): p. 18317-18330.

10. KeYi Chen , Z. P., *Monitoring Mongolia Gobi Dust Transport Using OMI Data.* Sciences in Cold and Arid Regions, 2012. **31**(3): p. 798-803.

11. Sassen, K., *Indirect Climate Forcing Over the Western US from Asian Dust Storms.* Geophysical Research Letters, 2002. **29**(10): p. 103-1-103-4.

12. Bory, A. J. M.; Biscaye, P. E.; Svensson, A.; Grousset, F. E., *Seasonal Variability in the Origin of Recent Atmospheric Mineral Dust at NorthGRIP, Greenland.* Earth and Planetary Science Letters, 2002. **196**(3–4): p. 123-134.

13. de Reus, M.; Dentener, F.; Thomas, A.; Borrmann, S.; Ström, J.; Lelieveld, J., *Airborne Observations of Dust Aerosol over the North Atlantic Ocean During ACE 2: Indications for Heterogeneous Ozone Destruction.* Journal of Geophysical Research: Atmospheres, 2000. **105**(D12): p. 15263-15275.

14. Hanke, M.; Umann, B.; Uecker, J.; Arnold, F.; Bunz, H., *Atmospheric Measurements of Gas-Phase HNO_3 and SO_2 Using Chemical Ionization Mass Spectrometry During the MINATROC Field Campaign 2000 on Monte Cimone.* Atmospheric Chemistry and Physics, 2003. **3**(2): p. 417-436.

15. Bonasoni, P.; Cristofanelli, P.; Calzolari, F.; Bonafè, U.; Evangelisti, F.; Stohl, A.; Zauli Sajani, S.; van Dingenen, R.; Colombo, T.; Balkanski, Y., *Aerosol-Ozone Correlations*

During Dust Transport Episodes. Atmospheric Chemistry and Physics, 2004. **4**(5): p. 1201-1215.

16. Zhang, Y.; Sunwoo, Y.; Kotamarthi, V.; Carmichael, G. R., *Photochemical Oxidant Processes in the Presence of Dust: An Evaluation of the Impact of Dust on Particulate Nitrate and Ozone Formation.* Journal of Applied Meteorology, 1994. **33**(7): p. 813-824.

17. Zhang, Y.; Carmichael, G. R., *The Role of Mineral Aerosol in Tropospheric Chemistry in East Asia: A Model Study.* Journal of Applied Meteorology, 1999. **38**(3): p. 353-366.

18. Bian, H.; Zender, C. S., *Mineral Dust and Global Tropospheric Chemistry: Relative Roles of Photolysis and Heterogeneous Uptake.* Journal of Geophysical Research: Atmospheres, 2003. **108**(D21).

19. Guenther, A.; Karl, T.; Harley, P.; Wiedinmyer, C.; Palmer, P. I.; Geron, C., *Estimates of Global Terrestrial Isoprene Emissions Using MEGAN (Model of Emissions of Gases and Aerosols from Nature).* Atmospheric Chemistry and Physics, 2006. **6**(11): p. 3181-3210.

20. Limbeck, A.; Kulmala, M.; Puxbaum, H., *Secondary Organic Aerosol Formation in the Atmosphere Via Heterogeneous Reaction of Gaseous Isoprene on Acidic Particles.* Geophysical Research Letters, 2003. **30**(19).

21. Cleveland, C. C.; Yavitt, J. B., *Consumption of Atmospheric Isoprene in Soil.* Geophysical Research Letters, 1997. **24**(19): p. 2379-2382.

22. Johnston, H., *Reduction of Stratospheric Ozone by Nitrogen Oxide Catalysts from Supersonic Transport Exhaust.* Science, 1971. **173**(3996): p. 517-522.

23. Usher, C. R.; Michel, A. E.; Grassian, V. H., *Reactions on Mineral Dust.* Chemical Reviews, 2003. **103**(12): p. 4883-4940.

24. Romanias, M. N.; El Zein, A.; Bedjanian, Y., *Reactive Uptake of HONO on Aluminium Oxide Surface.* Journal of Photochemistry and Photobiology A: Chemistry, 2012. **250**: p. 50-57.

25. Crowley, J. N.; Ammann, M.; Cox, R. A.; Hynes, R. G.; Jenkin, M. E.; Mellouki, A.; Rossi, M. J.; Troe, J.; Wallington, T. J., *Evaluated Kinetic and Photochemical Data for Atmospheric Chemistry: Volume V - Heterogeneous Reactions on Solid Substrates.* Atmospheric Chemistry and Physics, 2010. **10**(18): p. 9059-9223.

26. Joshi, N.; Romanias, M. N.; Riffault, V.; Thevenet, F., *Investigating Water Adsorption onto Natural Mineral Dust Particles: Linking DRIFTS Experiments and BET Theory.* Aeolian Research, 2017. **27**(Supplement C): p. 35-45.

27. *Dust and Sand storms*. 2008, Japanese ministry of environment: Japan. p. 8.

Chapter VI. Uptake and reactivity of acetic acid on natural dust from the Gobi desert.

Chapter VI. Uptake and reactivity of acetic acid on natural dust from the Gobi desert.

Table of content

List of Tables

List of Figures

Studies presented in the previous chapters showed the effective and contrasted heterogeneous interactions of selected VOCs on natural Saharan and Asian mineral dust samples. Moreover, the formation and the release of oxygenated volatile organic compounds, OVOCs, as gas phase side-products under UV irradiation was evidenced. In particular, Gobi dust had the highest uptake towards a probe VOC, isopropanol (IPA), compared to other natural dust samples collected from various places in the world. Nevertheless, our understanding of such heterogeneous processes is still limited especially because of the low number of VOCs and mineral dusts that have been investigated so far. Even though the lifetime from the heterogeneous processes investigated could be significant under major dust events, it is clearly negligible compared to the gas phase removal under background daily dust events. The investigation of relevant "VOC-dust" systems could allow identifying effective heterogeneous sinks and sources of VOCs in the atmosphere and provide greater understanding of the soil-atmosphere interaction.

For this reason, the carboxylic acid family was chosen to assess its interaction with natural Gobi dust. Due to their relatively low gas-phase reactivity, carboxylic acids are not significantly removed by homogeneous processes in the atmosphere [1]. The major loss mechanism in the gas phase is their reaction with HO° radicals with corresponding lifetimes of 25 days for formic and 14 days for acetic acid [1]. As a result, their main atmospheric removal pathway proceeds through dry and wet depositions [2], with a lifetime of ca. 4 days for formic acid and 3 days for acetic acid [2]. What about the lifetime of carboxylic acids removal by heterogeneous processes? Is it significant? Does it lead to the formation of oxygenated VOCs?

In this framework, the heterogeneous interaction of acetic acid on natural Gobi dust is studied under dark conditions. The experiments are conducted at room temperature and in the relative humidity range (< 0.01 – 90% RH) using zero air as bath gas. The experiments are performed using a U-shaped reactor coupled to a Selected-Ion Flow-Tube Mass Spectrometer (SIFT-MS) for gas-phase monitoring.

Although not yet published, these results are similarly presented as the draft of a publication hereafter.

1   Introduction

Formic and acetic acids are the first and second most abundant carboxylic acids in the atmosphere [3]. They are found in concentrations varying from 0.1 to 40 ppb and from 0.5 to 16 ppb for formic and acetic acids, respectively [3]. Major sources of these organic acids include direct anthropogenic sources, such as vehicular emissions [3], and biogenic sources, such as ants [4], and plants [2]. Due to their relatively low gas phase reactivity, carboxylic acids are not significantly removed by gas phase reactions in the atmosphere [1]. The major loss mechanism in the gas phase is their reaction with HO° radicals with corresponding lifetimes of 25 day for formic and 14 days acetic acid [1]. As a result, their main atmospheric removal pathway proceeds through dry and wet depositions [2], with a lifetime of ca. 4 days for formic acid and 3 days for acetic acid [2].

Carlos-Cuellar et al.[5] and Al-Hosney et al.[6] used a Knudsen reactor to determine the uptake coefficients of formic and acetic acid on mineral oxides under dry conditions. Prince et al.[7] studied the reactivity of acetic acid on calcite aerosols as a function of relative humidity (RH) in an environmental reaction chamber and found that the uptake of acetic acid is enhanced with increasing RH. Moreover, CO_2 is continuously produced from carbonate conversion, highlighting the possible reactive nature of this heterogeneous interaction. Tong et al.[8] studied the heterogeneous chemistry of monocarboxylic acids on α-Al_2O_3 under humid conditions using diffuse reflectance infrared Fourier transform spectroscopy (DRIFTs). These authors evidenced that the heterogeneous removal rates are 25, 12, and 21 hours for formic, acetic and propanoic acids, respectively, which is lower than the wet deposition removal of the same acids. In summary, results reported in the literature regarding acetic acid interaction with metal oxides suggest (i) significant uptake coefficients, (ii) reactive processes and (iii) possible side-product generation. As a consequence, the heterogeneous behavior of such a carboxylic acid should be deeper investigated. However, most of the studies are focused on the uptake of acetic acid on individual mineral oxides or carbonate. The use of these synthetic materials, as surrogate natural mineral dusts, provides an approximation and allows evaluating the atmospheric relevance of the simulated heterogeneous processes. Synthetic minerals are often present as bulk samples in laboratory experiments, which require careful analysis to take into account interstitial surface areas. They do not necessarily mimic the interaction of natural dust. Nevertheless, researchers assume that the bulk composition of the natural sample is the same as the surface composition. This is an assumption that is not yet validated.

Hence, the present study focuses for the first time on the interaction of acetic acid (AcA) with natural Gobi dust sample. This interaction is characterized through the determination of the adsorption isotherms and uptakes coefficients of AcA onto the Gobi sample under simulated atmospheric conditions regarding pressure and relative humidity. Furthermore, a detailed study of the reaction products is performed under dark conditions to characterize the reactive uptake of AcA onto Gobi dust. Specific investigations are carried out to understand the underlying contributions of the various mineral phases present in the natural sample to the uptake, the sorption, and the reactivity of AcA onto Gobi dust.

2   Materials and methods

2.1   Materials

Material characterization

Natural Gobi dust consists of aeolian deposits collected in Yanchi, Ningxia province in China (107.475211° E, 36.487333°N). The interaction of AcA on Gobi dust is studied using the smallest sieved size fraction of the dust batch that can be suspended in air, that is to say < 100 μm. Its specific surface area (SSA) is determined as 10.5 ± 2.0 m^2 g^{-1}, employing the BET method. Besides, the morphology of the sieved fraction is evaluated using scanning electron microscopy (SEM). This approach reveals that particles are irregular and exhibit various sizes (Figure VI-1). Indeed, most of the particles are bulky in shape with mean diameters ranging from a few μm to 50 μm. Nevertheless, flat particles are observed as well, suggesting the presence of distinct crystalline phases.

The phase identification and elemental composition are characterized employing X-ray diffraction (XRD) and X-ray fluorescence, Results have been previously reported in Table II-2 and Table II-3.

Synthetic metal oxides and carbonate: Complementarily to the natural dust sample, four synthetic materials corresponding to the major individual mineral phases identified in the Gobi dust sample have been used as received. The SSA values of TiO$_2$ powder (Degussa, Aeroxide-P25; diameter lower than 50 nm) and Al$_2$O$_3$ powder (Sigma-Aldrich; diameter lower than 200 μm) are determined as 52 ± 6 m^2 g^{-1} and 118 ± 21 m^2 g^{-1}, respectively, in agreement with the suppliers specifications (50 ± 15 m^2 g^{-1} and 120-190 m^2 g^{-1}, respectively). CaCO$_3$ powder (Sigma-Aldrich; diameter $\leq$ 30 μm) SSA is determined as 0.6 ± 0.3 m^2 g^{-1}. The

carbonate material is characterized by a specific surface area lower by two order of magnitude than TiO_2 and Al_2O_3. Finally, Fe_3O_4 powder (Sigma-Aldrich 99.99% trace metal) with a diameter lower than ≤ 5 µm) SSA is determined as 3.4 ± 0.4 $m^2 g^{-1}$.
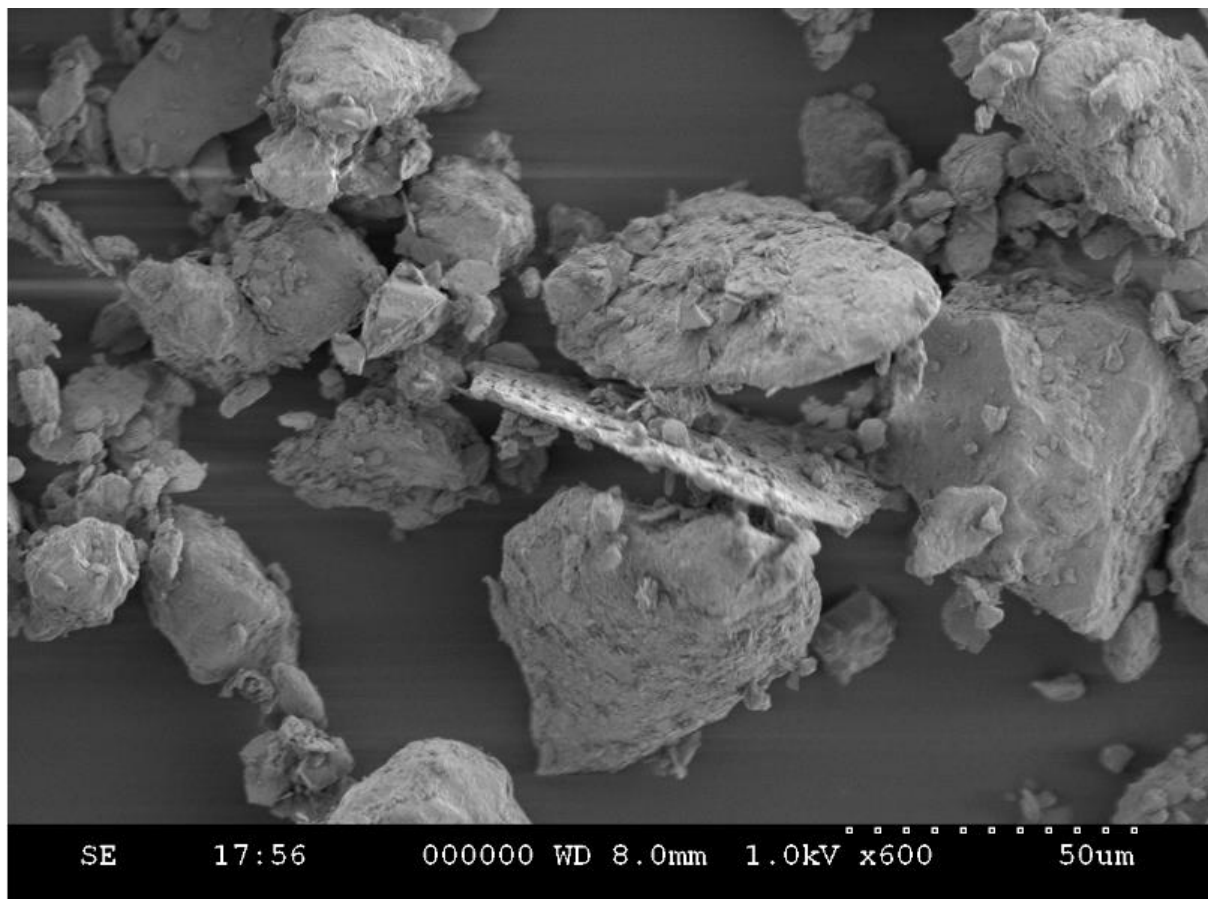
Figure VI-1. SEM image of the sieved Gobi dust sample (< 100 µm).

Gas preparation

Zero air is generated using compressed air sent into a catalytic zero air generator (Claind AZ-2020) to mineralize trace VOCs. The zero air generator is coupled with a pressure swing adsorption (PSA) system used for H_2O and CO_2 removal. The remaining impurity levels in the obtained air stream are lower than the detection limits of the analytical systems, i.e. VOCs < 0.1 ppb, CO_2 < 10 ppb, CO < 80 ppb and H_2O < 2 ppm. The relative humidity is controlled by changing the mixing ratio between dry and humid air. In particular, the zero air flow is humidified passing through a H_2O bubbler and is further diluted with dry air to obtain the targeted RH level. The relative humidity level in the obtained gas flow is monitored using

temperature and relative humidity probes (KIMO HQ 210) measuring RH from 3 to 98% and temperature from 253 to 353 K with an accuracy of ± 1.5% and ± 0.3%, respectively.

AcA is generated from a calibrated gas cylinder (Praxair) with a nominal concentration of 106 ± 2 ppm in N_2. It is further diluted in zero dry/humid air. The dilution of AcA allows the variation of its concentrations between 1.2 and 39.4 × 10^{13} molecules cm^{-3}, i.e. 500 ppb to 16 ppm) at the reactor inlet. Other chemicals used are commercially available with stated purities. More precisely, several oxygenated VOCs, namely acetaldehyde, acetone and methanol, observed as products, are calibrated as well. Acetaldehyde is generated and calibrated using a certified gas cylinder (Praxair) with a nominal concentration of 98 ± 4.9 ppm in N_2. Acetone (Sigma Aldrich, Europe; ≥ 99%) and methanol (Sigma Aldrich, Europe; ≥ 99%) are generated and calibrated from the individual injection and vaporization of a defined liquid volume in an 18 L canister further diluted using dry zero air.

2.2   Methods

Experimental setup

A detailed scheme of the experimental setup is presented in Figure VI-2 and has been described in previous articles [9-11]. It consists of three parts: (i) the gas flow generation system (ii) the U-shaped flow reactor, and (iii) the analytical device. The gas flow generation line is made of stainless steel and Teflon. Calibrated mass flow controllers (Bronkhorst) are used to dilute and introduce AcA at a total flow rate of 1000 sccm. The reactor consists of two parts: the upper one is a bypass line with a total volume of 15 cm^3; it is used to monitor AcA concentration profile in the absence of dust. The lower part, with a similar volume of 15 cm^3, is equipped with a quartz wool sample holder characterized by a geometric surface area of 4.95 cm^2. The investigated sample is dispersed on the top of this sample holder (Figure VI-2). Both parts of the reactor are connected via two 3-way valves. The temperature of the sample is recorded using a K-type thermocouple inserted inside the U-shaped reactor in the vicinity of the investigated sample. The contact time of AcA with the dust in the reactor is estimated to be ca. 1 second.
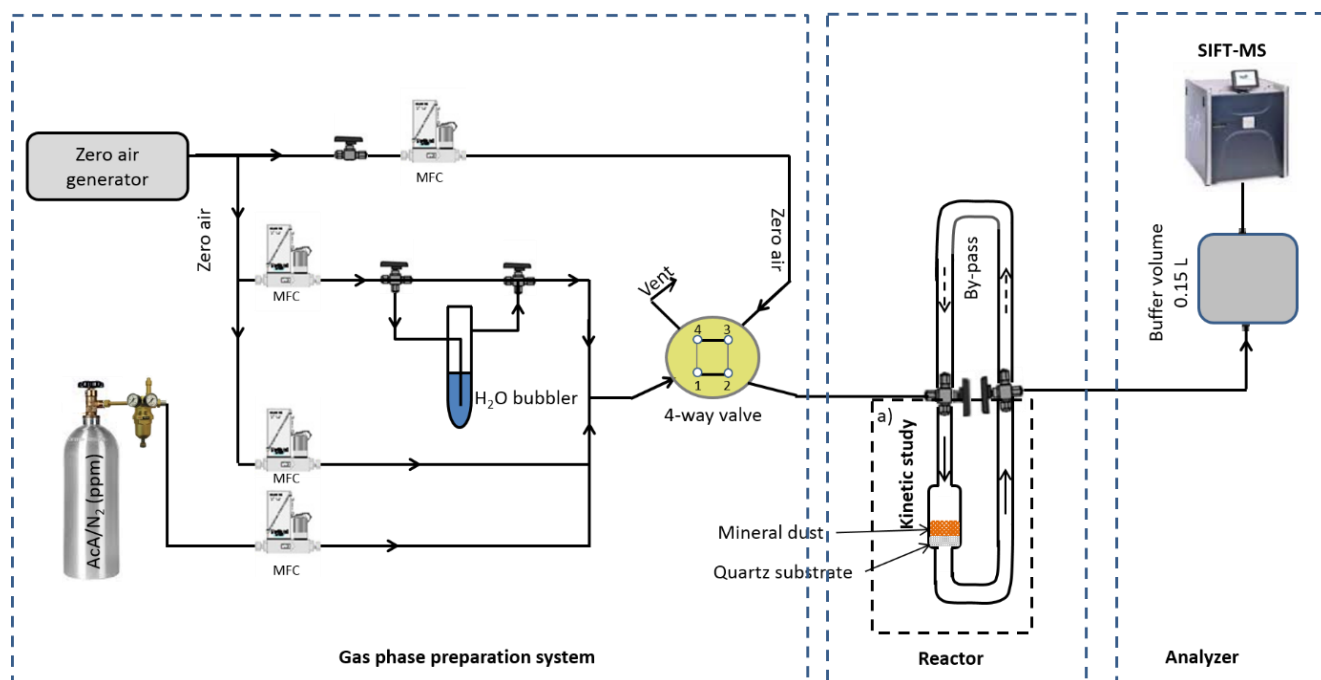
Figure VI-2. General scheme of the experimental setup used for the kinetic studies (MFC: mass flow controller).

VOC monitoring

The monitoring of VOCs at the outlet of the reactor is performed using a Selected-Ion Flow-Tube Mass Spectrometer (Voice 200, SYFT-Technology). The SIFT-MS is an analytical technique based on the chemical ionization of the analytes using three reagent ions: H_3O^+, NO^+ and O_2^+. The compounds identified in the current study as well as mass peaks used to monitor their real time gas-phase concentrations, and detection limits (DL) under dry and 50% RH conditions, are reported in Table II-6. During preliminary experiments, each compound of interest is introduced individually to check any possible contribution of other compounds to the mass peaks. The limit of detection is determined based on the standard deviation of the response and using the slope of the calibration curve.

Experimental protocol

Before each experiment the sample of interest is placed into the reactor and thermally pre-treated under dry zero air at 200 °C to remove any contamination such as H_2O. Thereafter, the sample is cooled down to room temperature under zero air. In case of dry conditions no other pretreatment is applied. However, under humid conditions and prior to AcA exposure, the freshly prepared mineral sample is exposed for ca. 10 min to the targeted RH level to equilibrate the surface with H_2O molecules.
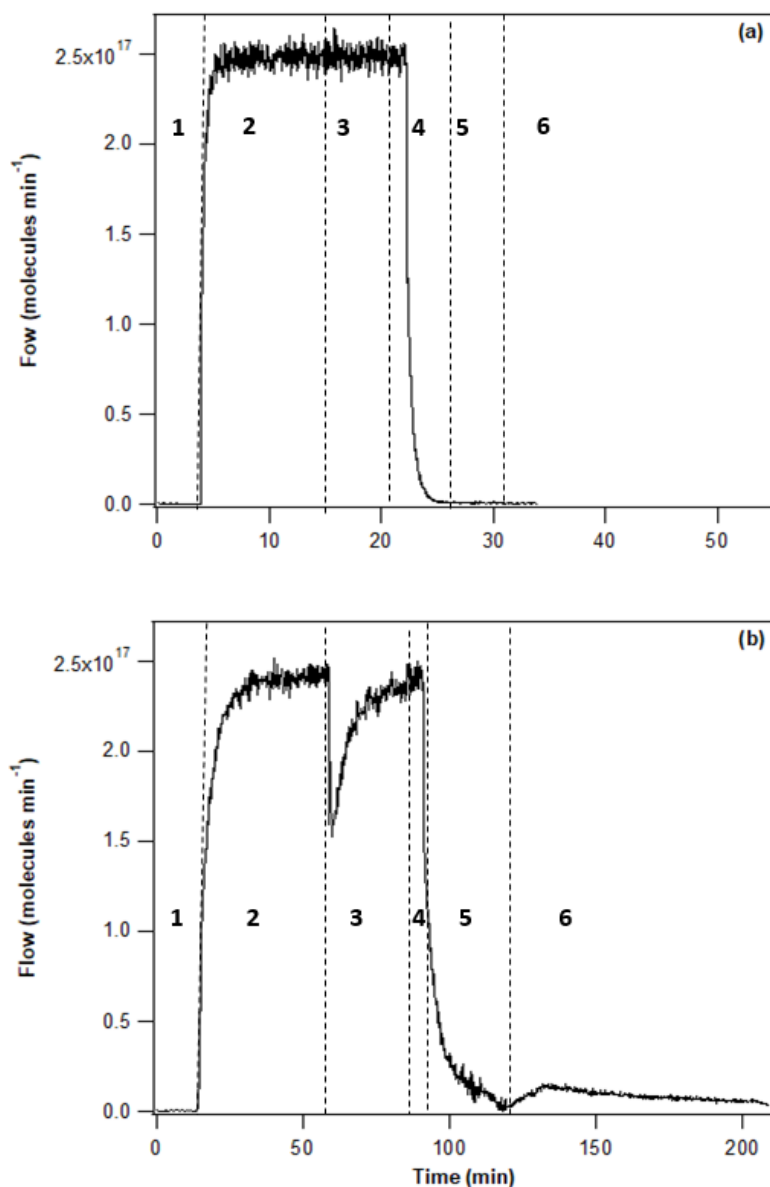
Figure VI-3. Typical temporal profile of AcA recorded with the SIFT-MS at the reactor outlet under 295 K and 50 % RH in the absence (a) and presence (b) of the Gobi dust sample. The NO$^+$ ion is used to monitor AcA using SIFT-MS at the mass peak 90 (NO$^+$CH$_3$COOH). Step 1: background collection; Step 2: AcA is sent to the by-pass line; Step 3: AcA is sent through the reactor (exposure of dust surface); Step 4: reactor isolation; Step 5: AcA flow is stopped and the gas lines are purged with zero air; Step 6: zero air flow is directed through the reactor to flush the surface then the reactor is heated up to 150 °C under zero air to possibly desorb the remaining quantity of adsorbed AcA.

This equilibration time has been optimized and longer exposure times do not impact the further determined uptake data. First, the reactor is still flushed with zero air and the background level of AcA is monitored using SIFT-MS as shown in Figure VI-3 (step 1). In step 2, the flow of AcA at a defined concentration is sent to the bypass line. When a steady-state concentration of AcA is monitored at the reactor outlet, the AcA flow is directed through the reactor (step 3),

exposing the reactor, containing (Figure VI-3 (b)) or not (Figure VI-3 (a)) the dust sample to AcA.

In the presence of the natural dust in the reactor, AcA can be taken up by the sample surface, inducing a decrease in AcA concentration profile, followed by a progressive increase towards the initial value as the sample surface is equilibrated with the AcA gas phase concentration (Step 3, Figure VI-3 (b)). It has to be noted that since the bypass and the reactor have equal volumes, the drop of AcA concentration during the adsorption experiment is not due to volume differences. This point has been validated with complementary experiments in the absence of dust (Figure VI-3 (a)). Once the sorptive equilibrium in AcA is reached, the reactor is isolated by changing the flow direction to the bypass as shown in step 4 (Figure VI-3 (b)). Then, the AcA flow is stopped and the gas lines are purged with zero air (step 5). Thus, AcA concentration returns to the background level. Then, the zero air flow is directed through the reactor to flush the surface and eventually recover the reversibly adsorbed fraction of AcA. Finally, the reactor is heated up to 150°C under zero air to possibly desorb the remaining quantity of adsorbed AcA (step 6).

Determination of uptake coefficients

Heterogeneous processes can be described by the uptake coefficient. It characterizes the probability for a gas phase molecule to be lost on the surface. This parameter is determined to assess the affinity of AcA towards the selected natural dust samples. The uptake coefficient, γ, is defined as the ratio of the number of gas molecules taken up by the surface to the total number of gas-surface collisions [12]. The uptake coefficient can be determined under two different experimental conditions. First in the initial stage of an experiment on fresh (i.e., previously unexposed) surfaces, where it is named "initial uptake coefficient" and noted, γ_0. The initial uptake described a transient process occurring along the very first seconds of interactions between the gas and the solid surface. Second, after long exposure of the surface with the gas pollutant if steady state conditions are achieved, then it is named steady-state uptake coefficient and noted, γ_{ss}. The steady state uptake regime indicates that a continuous consumption of the gas occurs on the solid surface and suggests a regeneration of the surface sites involved in the loss of the gas phase species. In this study only an initial uptake is observed. The equations for the determination of the initial uptake are presented [13]. The initial uptake coefficient of AcA is derived from Equations VI (1-4) where a first order kinetics is assumed:

$$\frac{d(AcA)/dt}{V} = k_{het}[AcA] \qquad \textbf{(Equation VI-1)}$$

$$k_{het=}\frac{d(AcA)/dt}{V[AcA]} = \omega\gamma_0 \qquad \textbf{(Equation VI-2)}$$

with:

$$\omega = \frac{cA_s}{4V} \qquad \textbf{(Equation VI-3)}$$

and finally:

$$\gamma_0 = \frac{4\{d(AcA)/dt\}}{cA_s[AcA]} \qquad \textbf{(Equation VI-4)}$$

where (AcA) denotes the number of AcA molecules taken up by the dust surface at the beginning of exposure (molecules); k_{het}, is the first-order rate coefficient of the heterogeneous interaction of AcA with Gobi dust (s^{-1}); V is the volume of the interaction zone (cm^3); [AcA] stands for the gas-phase concentration of AcA (molecules cm^{-3}); ω is the collision frequency of AcA (s^{-1}); c is the mean molecular speed of AcA (cm s^{-1}) and finally A_s corresponds to the effective surface area of the sample in the reactor (cm^2).

Determination of the number of molecules adsorbed

Since the initial uptakes are determined to assess the affinity of AcA towards the selected natural dust sample in the initial stage interaction, information about this interaction throughout the whole process is critical. This information can be provided by the number of molecules adsorbed per surface unit, N_s (molecules cm^2). It can be investigated as a function of RH. Ns is derived from the integration of the adsorption peak in a typical uptake experiment (Figure VI-3 (b)), and divided by the effective surface area of the sample, A_s, according to Equation VI-5: [14]

$$N_s = \int_{\tau=0}^{\tau=1} \frac{F(t)}{A_s} dt \qquad \textbf{(Equation VI-5)}$$

where F is the flow rate (molecules s^{-1}) of AcA molecules inside the reactor. The time $\tau = 0$ denotes the initial time of exposure of the sample surface to the AcA gas flow and $\tau = t$ corresponds to the time where the uptake equilibrium is reached.

3 Results and discussion

3.1 Determination of AcA initial uptake coefficient on natural Gobi dust

Effect of relative humidity on AcA uptake on Gobi dust sample

As mentioned in the introduction the interaction of AcA with minerals has been mostly studied under dry conditions. However, several literature studies have shown that adsorbed water molecules play an important role in the heterogeneous chemistry of trace atmospheric gases [9-11, 15, 16]. In particular recent studies from our group [17, 18] investigated the effect of relative humidity on natural mineral samples and experimentally evidenced that under ambient RH conditions natural mineral samples are always covered with at least one layer of adsorbed water molecules as RH exceeds a threshold of 15 or 25% depending on the composition of the dust. As a result, under atmospheric conditions the surface of natural mineral dust sample is covered by water molecules, which makes essential to consider the effect of relative humidity to characterize the uptake of atmospheric trace gases.

The initial uptake coefficients and the number of AcA molecules adsorbed on the Gobi sample are determined at room temperature (295 K), with AcA concentration of 2.46×10^{14} molecules cm^{-3} (10 ppm) at the reactor inlet. Relative humidity is varied from dry conditions (0.01) to 90% RH. Results are plotted in Figures VI-4 and VI-5.

As observed in Figure VI-4, γ_0 is inversely dependent on RH. Results are fitted using the empirical Equation VI-6 that permits extrapolating the initial uptake at any targeted RH:

$$\gamma_0 = \gamma_{dry} - (1.3 \times 10^{-8})RH^{0.42} \qquad \textbf{(Equation VI-6)}$$

From 0 to around 20% RH. There is a strong decrease of the initial uptake with the relative humidity. Nevertheless, at the impact of RH is weaker over 30%. These behavior can be related to the water monolayer formed at around 20 % RH on the surface of natural Gobi dust [17].

The graph shows γ_0 (BET) on the y-axis versus RH (%) on the x-axis, with the fit equation:

$$\gamma_0 = \gamma_{dry} - (1.3 \times 10^{-8}) \, RH^{0.42}$$

Weighted fit
2.46×10^{14} molecules cm^{-3}
T = 295 K
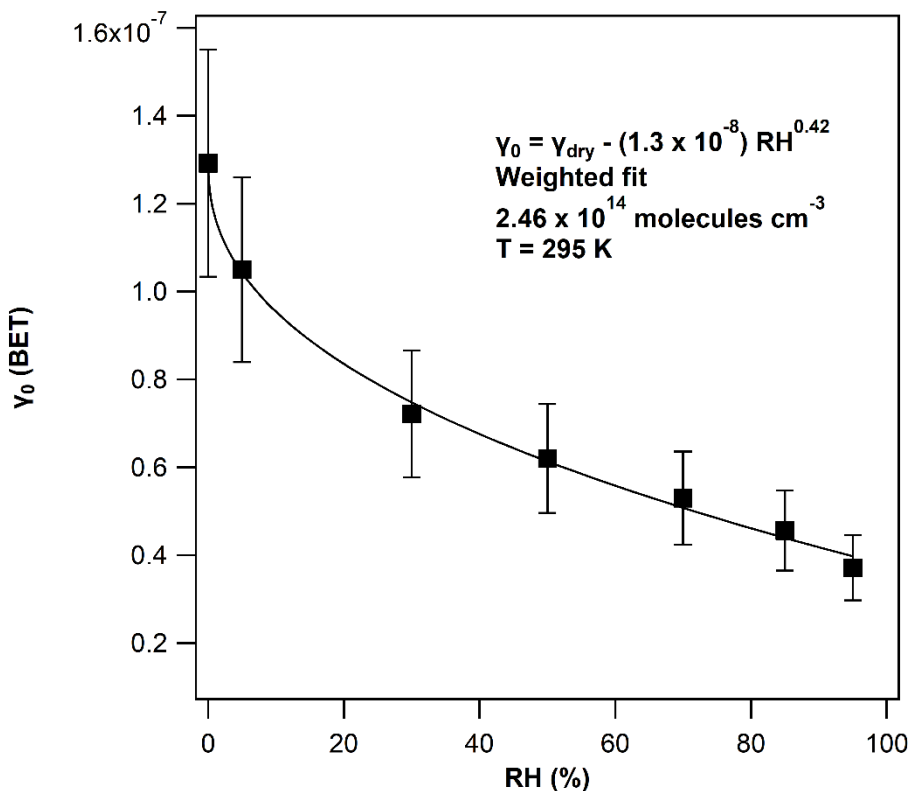
Figure VI-4. Initial uptake coefficients, γ_0, of AcA onto Gobi dust determined at 295 K, with an AcA inlet concentration of 2.46×10^{14} molecules cm^{-3} and over the RH range 0.01 – 90%. The solid lines correspond to the fitting of experimental results with the empirical expression (6). Error bars represent the overall estimated uncertainty on γ_0.

The decrease of γ_0 with relative humidity suggests a competition between AcA and H_2O molecules to access the surface sites of the natural Gobi dust sample. An inverse dependence of the initial uptake of VOC with RH on dust surfaces has already been reported in previous studies where similar trends are observed [9, 11, 19-23]. Particularly, Zeineddine et al.[9] and Romanias et al.[11] studied the uptake of isoprene and isopropanol, respectively, on the same sample. The authors report an inverse dependence of the uptake on RH similar to the one presented herein.

Moreover, Tang et al.[15] investigated the role of water on the uptake of AcA on SiO_2 and Al_2O_3. The authors reported an increase by a factor of 3-5 for γ-Al_2O_3 when RH increases from 0% to 15%, whereas acetic acid and water were found to compete for adsorption surface sites on SiO_2 particles. The main constituent of the Gobi dust is SiO_2 and therefore the results present herein are considered in good agreement with Tang et al. [15] considering the outcome of the interaction of AcA on Gobi dust will be dominated by the effect of its highest constituent

SiO₂. However, the results reported by Tang et al. [15] highlight the contrasted roles of individual oxides in the heterogeneous processes.
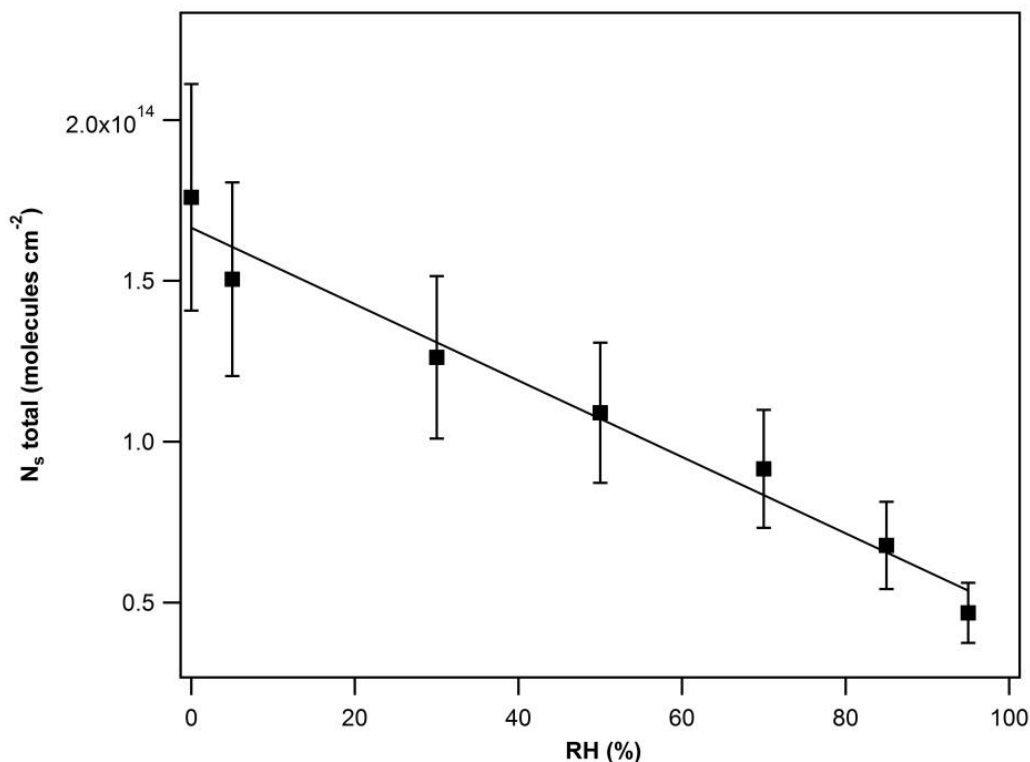
Figure VI-5. Number of molecules adsorbed per surface unit, N$_s$, of AcA on Gobi dust determined in the relative humidity range < 0.01 - 90% at 295 K. The error bars represent the overall uncertainty on N$_s$ determination. The line is the linear least-squares fit through the data.

The uptake approach used to describe the loss of AcA on the solid aerosol relies on the probability of AcA to resid on the dust surface. It can be completed by a quantitative approach that consists in quantifying the effective surface concentration of AcA on the dust surface. As observed in Figure VI-5, AcA surface concentration decreases linearly with increasing relative humidity. Similarly to the initial uptake, the surface concentration of AcA is divided by ca. 3 as RH increases from 0.01 to 90 % RH. However, no threshold related to water monolayer formation on the dust surface can be evidenced from the quantification of sorbed AcA in Figure VI-5. Indeed, the inhibitive impact of water molecules on AcA adsorbed amount is directly proportional to RH value.

Effect of initial AcA concentration on AcA uptake on Gobi sample

Experiments are carried out as a function of AcA concentration in the range $(1.2 - 39.4) \times 10^{13}$ molecules cm^{-3}, i.e. from 16 to 500 ppm, at 295K and 85% RH. The results obtained for the initial uptake coefficient are reported in Figure VI-6.
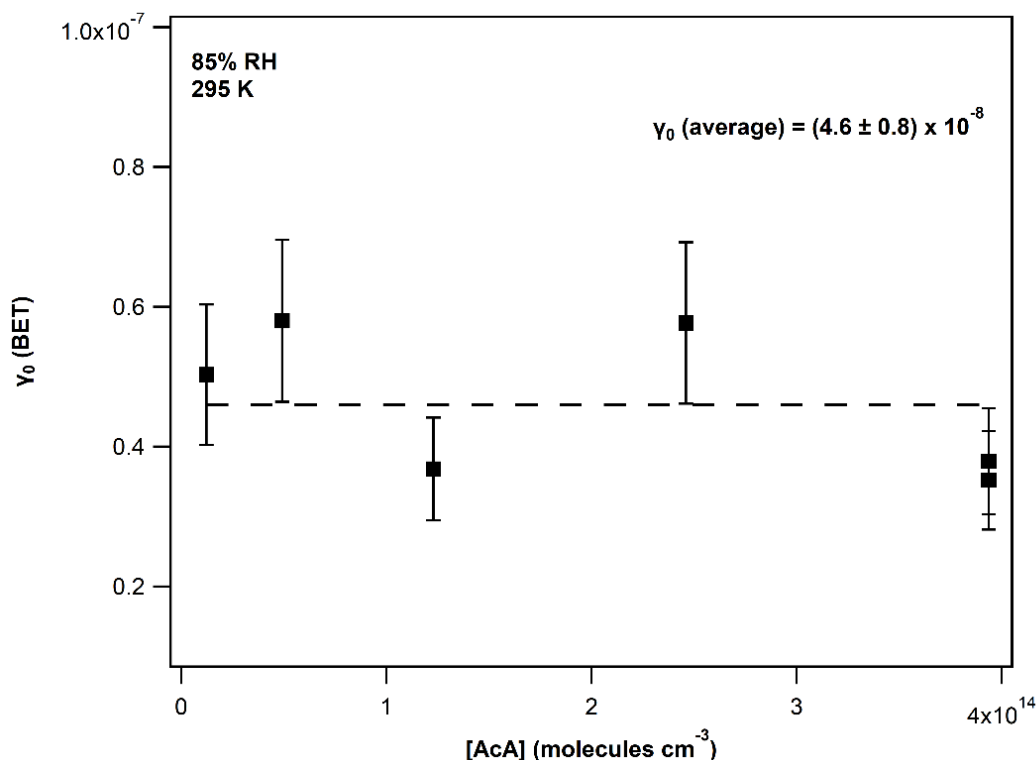
Figure VI-6. Initial uptake coefficients, γ_0, determined at 295 K and 85% RH as a function of the gas-phase concentration of AcA. The error bars represent the overall estimated uncertainty on γ_0. The dashed line represents the average uptake value over the investigated concentration range.

As observed in Figure VI-6, γ_0 values are independent on AcA concentration over the investigated concentration range, with an average value at 85 % RH of $\gamma_0 = (4.6 \pm 0.8) \times 10^{-8}$. As stated in the method section, a first-order kinetic is assumed to derive the uptake coefficient (Equations VI (1-4)). These results provide an experimental validation of this assumption. This behavior is expected since the initial uptake expresses the interaction of a gas molecule with the fresh, i.e. unexposed surface.

The number of molecules taken up per surface unit, N_s, is investigated as a function of AcA inlet concentration (Figure VI-7). The results reported in Figure VI-7 evidence that the number of AcA molecules adsorbed increases linearly as AcA concentration increases. In a first approach, this linear behavior could be interpreted using a typical Langmuir adsorption

isotherm on low concentration range. However, the intercept at the origin is not zero but 1.77 $\times 10^{13}$ molecules cm^{-2} indicating a significant and fast adsorption of AcA at concentration lower than 1.2×10^{13} molecules cm^{-3}.
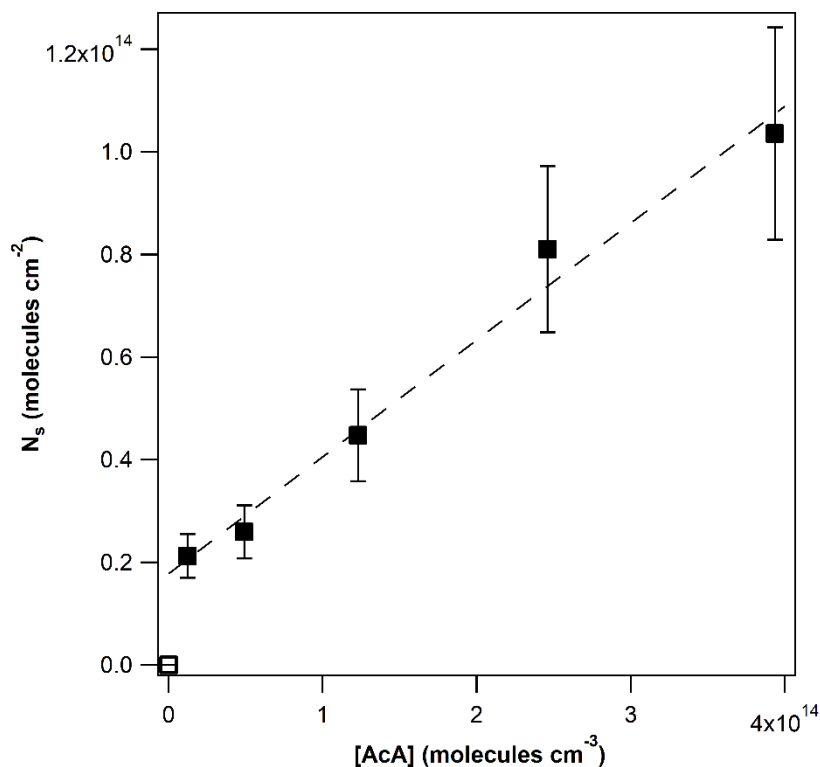
Figure VI-7. Number of molecules, N$_s$, of AcA adsorbed on Gobi dust per unit surface area determined at 295K and 85% RH. The error bars represent the overall uncertainty on N$_s$ determination. The data point displayed at the origin corresponds to a blank experiment (performed in the absence of dust). The dashed line is only there to guide the eye and has no physical meaning.

The behavior of N$_s$ as a function of AcA concentration reported on Figure VI-7 suggests the combination of two sorptive processes: (i) a fast and massive sorption, independent of the inlet concentration, that could correspond to a chemisorptive process and involve a reaction of AcA on the dust surface; (ii) a concentration-controlled sorption process that could be described by a typical Langmuir model and may correspond to a physisorptive process. These hypotheses would suggest the existence of at least two distinct surface sorption sites for AcA onto natural Gobi dust samples. They are further explored thereafter.

3.2 Interaction of AcA with Gobi dust individual mineral phases: uptakes and number of molecules adsorbed

As reported in Table II-3, SiO_2 is the major phase of the selected natural Gobi dust sample, followed by calcite ($CaCO_3$; 17.8%) and albite ($NaAlSi_3O_8$; 10.5 %). Individual metal oxides such as TiO_2, Al_2O_3 and Fe_3O_4, contribute only to a minor extent with abundances ranging from 1 to 7 %. In order to assess the individual contribution of the main components of natural Gobi dust and to clarify their respective roles in Gobi dust surface properties toward AcA, experiments with the individual Gobi dust mineral phases are performed.

The initial uptakes of AcA on SiO_2, $CaCO_3$, Al_2O_3, Fe_3O_4, and TiO_2 have been investigated under the same experimental conditions than with the natural Gobi dust sample (295K, 2.46×10^{14} molecules cm^{-3}) and under two distinct RH levels: 50 and 85 %. Results are reported in Figure VI-8 and compared with data obtained on the Gobi natural sample.
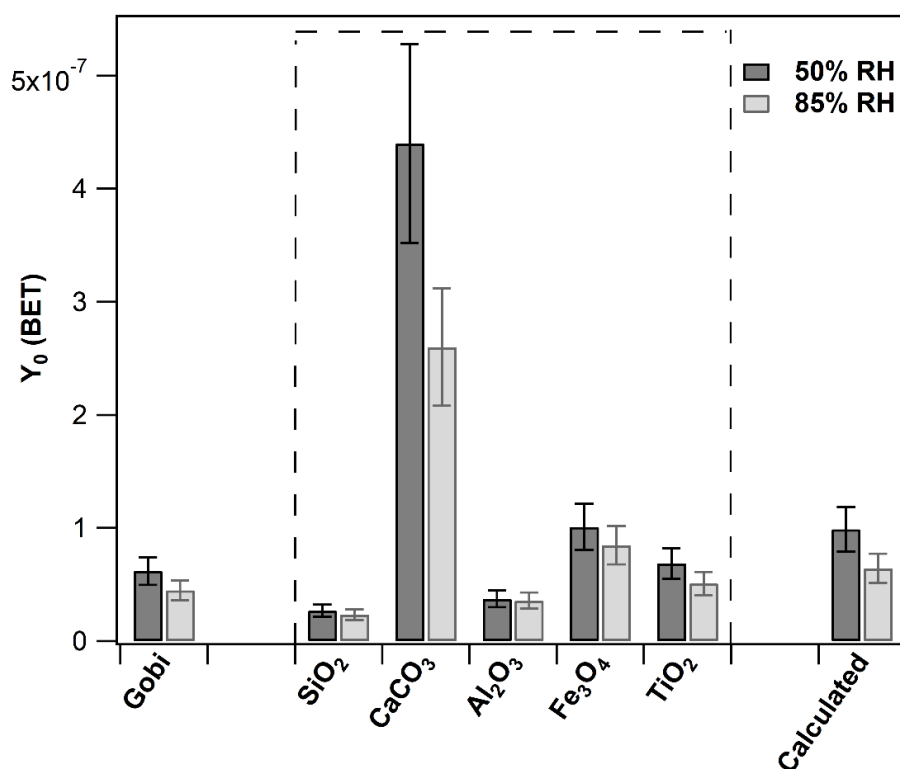
Figure VI-8. Initial uptake coefficients, γ_0, determined at 295 K and under 50 and 85 % RH for natural Gobi dust sample, and its mineral phases ordered by their respective abundances inside the dashed box. Data labeled with "Calculated" correspond to the initial uptake determined from the sum of the initial uptakes of each component. The error bars represent the overall estimated uncertainty on γ_0.

The uptakes of AcA on any investigated mineral phases decrease as a function of RH, similarly to the trend observed on natural Gobi dust sample. Irrespectively of the RH level, the highest uptake value is observed for $CaCO_3$: $\gamma_0 = 4.5 \times 10^{-7}$ at 50 % RH. It isfrom 4 to 8 times higher than on other individual minerals. This result suggests that $CaCO_3$ is the most contributing the phase of the natural dust sample to the uptake of AcA. This a behavior can be correlated to the acid-base interaction between AcA and $CaCO_3$. Al- Hosney et al.[6] reported that formic acid is strongly adsorbed on the surface of $CaCO_3$ in the form of formate and carbonic acid, and that the latter dissociates into CO_2 and H_2O in the presence of adsorbed water. The high abundance of carbonates is a specificity of dust samples from the Gobi desert [24]. Natural Gobi dust was also previously characterized by the highest uptake coefficient regarding isopropanol, compared to four other dusts with different origins. It can be suggested that $CaCO_3$ is the mineral phase responsible for the high uptake capacity of Gobi desert samples.

Fe_3O_4 and TiO_2 are characterized by AcA initial uptake coefficients ranging from ca. 0.5×10^{-7} to 1×10^{-7}, while Al_2O_3 and SiO_2 lead to values lower than 0.5×10^{-7}, i.e. lower than the natural Gobi dust sample itself. In spite of the fact that SiO_2 is the most abundant oxide in the natural dust sample, it is the less contributing phase to the uptake of AcA. This result is in accordance with the observations of Zeineddine et al. [25] concerning the linear increase of isopropanol initial uptake with the abundances of metal elements other than Si.

The number of AcA molecules reversibly and irreversibly adsorbed on Gobi mineral phases is assessed at 295 K, 2.46×10^{14} molecules cm^{-3} and 50 % RH. The results are reported in Figure VI-9.

The highest total N_s is observed for AcA interaction on $CaCO_3$ and the lowest on SiO_2. SiO_2 is not only characterized by the lowest total surface concentration of AcA but also by the fact that AcA adsorption on silica is almost fully reversible. This observation could be correlated with the fact that SiO_2 has no basic properties, thus AcA molecules can only weakly interact with SiO_2 surface. Unlike SiO2, other individual minerals are characterized by reversible and irreversible fractions of AcA on their surfaces.

The determination of total N_s onto TiO_2, 1.46×10^{14} molecules cm^{-2}, is in agreement with Ngo et al.[26] and Batault et al.[27] who reported values of 1.82×10^{14} and 1.74×10^{14} molecules cm^{-2}, respectively. More precisely, around one third of the adsorbed fraction on TiO_2 is reversible, which corresponds to the observations of Batault et al.[27]. TiO_2 is partially acidic

which may explain the higher contribution of the reversible fraction compared to other individual minerals.

The highest contributions of the irreversible fractions of AcA are observed for $CaCO_3$, Fe_3O_4, and Al_2O_3 with ca. 90 %. These oxides are amphoteric, they can behave as an acid or a base. Since the surfaces studied herein are exposed to an acid, they are playing a role of a base, which could explain a stronger bonding of AcA to the studied surfaces and lower reversible fractions.
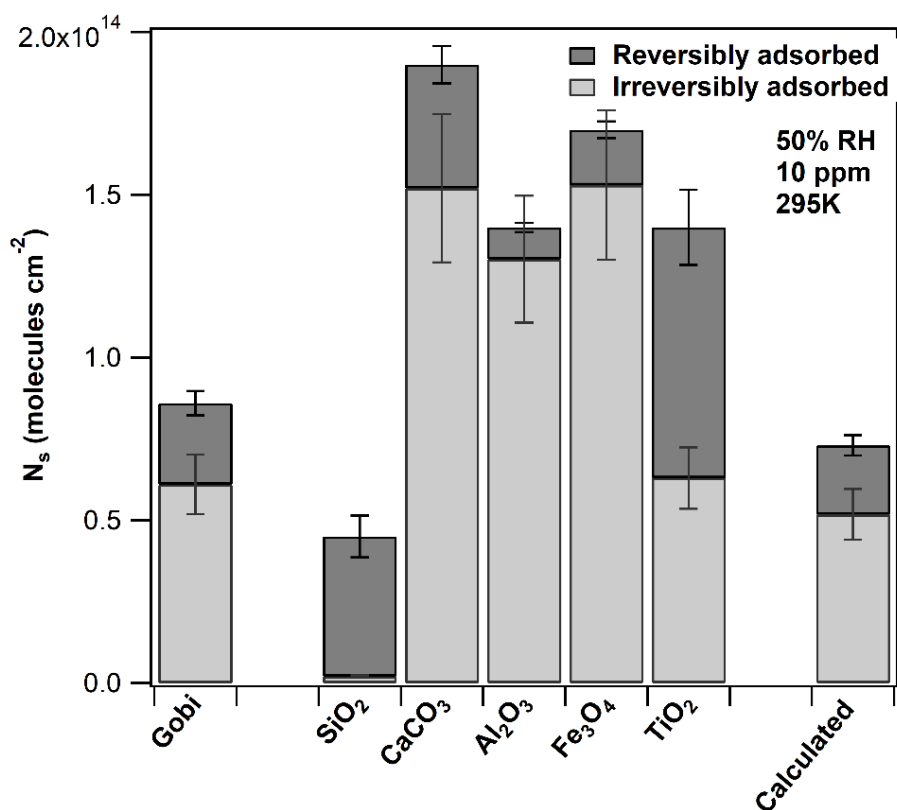
Figure VI-9. Reversibly and irreversibly adsorbed fractions and surface concentrations of AcA on Gobi natural dust samples and its individual minerals determined at 295 K, 2.46×10^{14} molecules cm^{-3} and 50 % RH. The error bars represent the overall uncertainty on N_s determination. Data labeled with "Calculated" correspond to the N_s determined from the sum of N_s of each component, weighted by their respective abundances in the natural sample.

In order to determine whether the use of single constituents can simulate or not the behavior of the natural dust sample, the uptake coefficients and the number of molecules adsorbed of oxides and carbonate phases are taken into account in Equation VI-7 to model the behavior of the natural Gobi dust sample from its individual components:

$$F_{(x),calculated} = \sum_{x} [F(x) \times RA(x)]$$

(Equation VI-7)

where F(x) is either γ_0 or N_s and RA is the relative abundance of the corresponding mineral x (x = Al_2O_3, SiO_2, TiO_2, $CaCO_3$ and Fe_3O_4). This calculation assumes that the distribution of the different phases between the surface and the bulk of a natural Gobi particle is homogeneous.

The results are reported in Figures VI-8 and VI-9 for the initial uptake and N_s, respectively. They are labelled as "calculated" on the corresponding graphs. The initial uptake on Gobi at 85 % RH with a gas phase concentration of 2.46×10^{-14} molecules cm^{-3} is $\gamma_0 = (4.6 \pm 0.9) \times 10^{-8}$. The calculated value obtained from Equation VI-7 is: $\gamma_0 = (6.4 \pm 1.2) \times 10^{-8}$. A difference of around 25 % is obtained between the experimental determination of γ_0 using the natural sample compared to the sum of individual oxides and carbonate.

N_s on Gobi dust is experimentally determined as 8.6×10^{13} molecules cm^{-2} under 50 % RH with a gas phase concentration of 2.46×10^{-14} molecules cm^{-3}. The calculated value using Equation VI-7 is 7.3×10^{13} molecules cm^{-2}. The difference is lower than 16 %. Therefore, in the case of AcA and Gobi dust, the discrimination of the natural sample into its individual components provides a good approximation of the behavior of the natural sample. However, this does not preclude that similar trends will be observed for other trace gases and dust samples and this observation requires further investigation to be used more widely.

3.3 Investigation of AcA reactivity on natural Gobi dust sample

3.3.1 First insight into AcA reactivity

In order to address the reactivity of AcA on the natural Gobi dust sample, special attention has been paid to the gas phase monitoring of possible side-products. This experimental approach, focused on the characterization of the gas phase, complements the investigation of surface reactivity performed using *in-situ* spectroscopic techniques.[6, 8, 15, 28]

The possible formation of gaseous side-products during the interaction of AcA with 100 mg of the natural Gobi dust sample has been examined using online SIFT mass spectrometry, at room temperature, under 85 % RH and with an AcA inlet concentration of 2.46×10^{14} molecules cm^{-3}. Under these conditions, methanol, acetaldehyde and acetone are formed in the gas phase during the first minutes of AcA interaction with the Gobi dust sample, providing

evidence of the reactive nature of the uptake. Figure VI-10 illustrates the typical profiles of AcA uptake on the natural Gobi dust sample and the concomitant formation of the oxygenated side-products. The temporal profiles of these species evidence a transient production limited to a maximum of 4 minutes. The fact that the duration of AcA uptake on the natural sample highly exceeds the formation of the side-products suggests the coexistence of distinct processes on the dust surface and subsequently at least two different AcA surface sites that can be considered: sorptive (S1) and reactive sites (S2), supporting and clarifying the hypotheses proposed above, Sorptive sites (S1) are gradually covered by AcA molecules from the introduction of AcA in the reactor till the recovery of the AcA concentration to pre-exposure level; they contribute to the surface loss of AcA but not to the release of side-products in the gas phase. Reactive sites (S2) lead to the formation of gas-phase side-products, and their complete coverage is confirmed by the monitoring of gaseous species.

Irrespectively of their contrasted chemical nature, neither (S1) nor (S2) sites are regenerated since they do not lead to a steady-state uptake/reaction; they both get depleted over time as supported by Figure VI-10.

Complementarily to (S1) and (S2), two distinct fractions of AcA taken up by the Gobi dust surface can be distinguished on Figure VI-10: (i) AcA taken up concomitantly with the formation of side-product is further named as "reactive AcA fraction", and (ii) AcA taken up while no side-products are monitored in the gas phase is designated as "non-reactive AcA fraction". The latter is solely contributed by the coverage of (S1)-type sites, while the former encompasses the coverage of (S2) as well as (S1) sites.
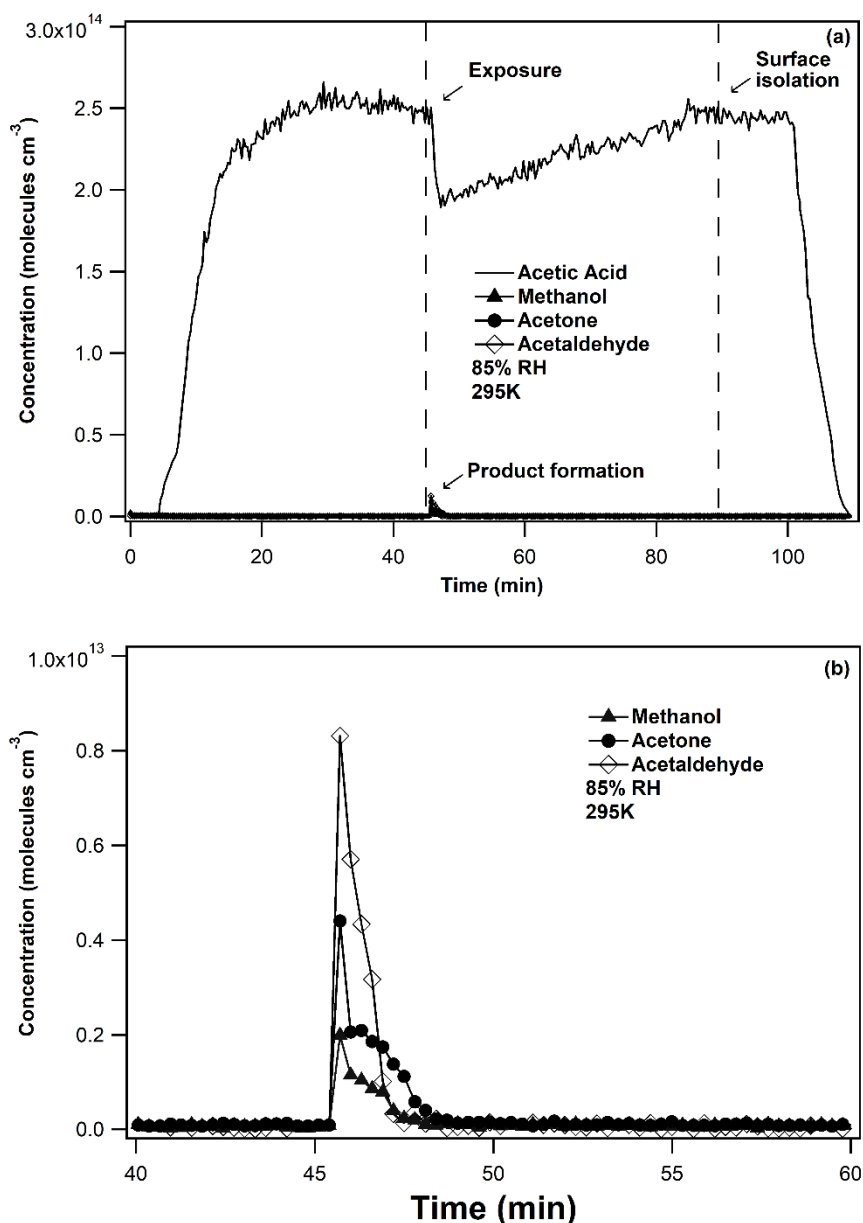
Figure VI-10. (a) Global gas-phase profiles of 2.46 × 10^14 molecules cm^-3 AcA interaction on Gobi dust and concomitant gas phase product formation: methanol, acetaldehyde, and acetone monitored by SIFT-MS under 85% RH and 295K. (b) Zoom-in area of the product formation.

3.3.2   Influence of relative humidity on the formation of gas-phase side-products

In order to assess the influence of relative humidity on the formation of side-products, the interaction of AcA with natural Gobi dust sample is examined under RH ranging from 0.01 to 85 % RH, at room temperature, with an AcA inlet concentration of 2.46 × 10^14 molecules cm^-3 and in the presence of 100 mg of Gobi dust sample. Based on the side-product concentration profiles (Figure VI-10), the integrated area of each peak is used to determine its

amount expressed in molecules. Because of heterogeneous formation, their production may depend on the effective specific surface available to AcA in the reactor. As a consequence, the amount is normalized by the effective specific surface (expressed in cm²) provided by the natural dust sample, as displayed on the y-axis of Figure VI-11 which do not refer to a surface concentration of side-products (since species are monitored in the gas phase), but to the ability of the natural sample to produce an amount of gas-phase side-products per specific surface unit. The obtained data are reported in Figure VI-11 as a function of RH.
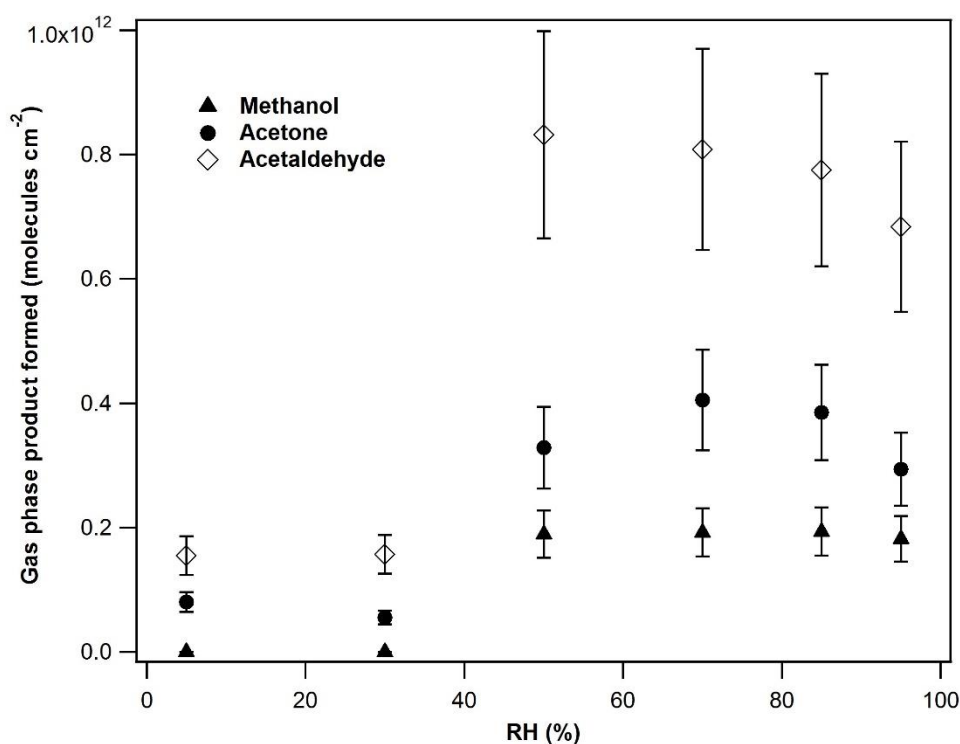
Figure VI-11. Variation of the gas-phase product formation as a function of RH. All experiments are carried out at 295 K, 2.46×10^{14} molecules cm^{-3} and 100 mg of sample mass. The error bars represent the overall uncertainty on the product determination.

The influence of RH on the formation of side-products is clearly characterized by a threshold effect somewhere between 30 and 50 % RH. Indeed, two distinct regimes can be observed: (i) below the threshold, the formation of side-products is not influenced by RH and remains lower than 0.2×10^{12} molecules cm^{-2} (Figure VI-11); (ii) above the threshold, acetaldehyde, acetone and methanol formation is multiplied by a factor of 6, 4 and 10, respectively, and further RH increase does not alter their formation (Figure VI-11).

Joshi et al. [17] investigated *in-situ* the coverage of the same natural Gobi dust sample by water molecules as a function of RH using Diffuse Reflectance Fourier Transform Infrared Spectroscopy (DRIFTS). They determined the number of water layers present on the surface of the dust particles as a function of RH to address their hygroscopic properties under atmospheric conditions. They experimentally determined that the RH threshold corresponding to the formation of a monolayer of water molecules on the surface of the Gobi dust sample is ca. 25 %. The threshold observed in the formation of the side-products (Figure VI-11) could be correlated with the formation of a water monolayer on the Gobi dust surface [17]. For that purpose, two interpretations can be proposed:

(i)   the completion of the water monolayer above 30% impacts the reaction pathway of side-products and enhances their formation,

(ii)   the completion of the water monolayer on the dust sample prevents the adsorption of the side-products formed on the surface and promotes their transfer to the gas phase.

Both phenomena would result in an increase of the side-product concentrations above 30% RH, however, the first hypothesis considers a modification of the reaction pathway, while the second hypothesis suggests a modification of the sorption equilibrium of the side-products.

It is important to recall that the number of AcA molecules taken up also decreases with RH. Therefore, it seems that H_2O plays a key role in the product formation and the reaction mechanism but more investigation is needed to understand exactly how the presence of an H_2O monolayer alters the surface and leads to the formation and/or release of the side-products we have observed.

3.3.3   Influence of AcA concentration on the formation of side-products

In order to investigate the reactivity of AcA onto the natural Gobi dust sample, AcA inlet concentration is varied from 1.2 to 39.4×10^{13} molecules cm^{-3} i.e. from 16 to 500 ppm; the gas-phase concentrations of the side-products are monitored at the reactor outlet.
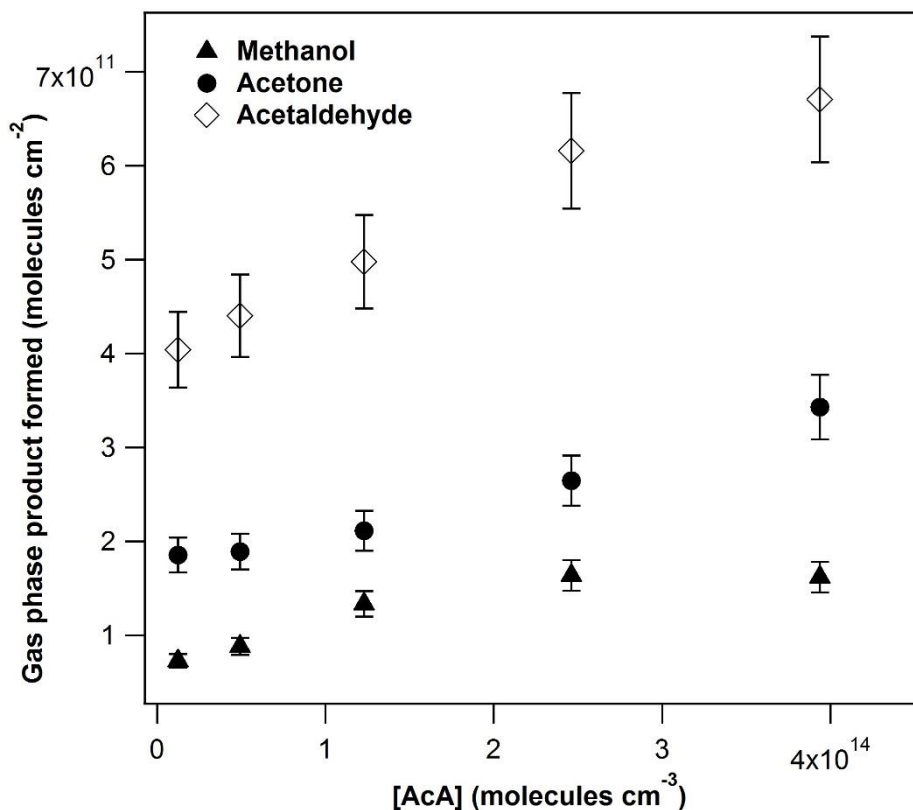
Figure VI-12. Evolution of the concentrations of the gas-phase products as a function of AcA inlet concentration. Experiments are carried out at 295 K, under 85 % RH and in the presence of 100 mg of sample mass. The error bars represent the overall uncertainty on the product determination.

Experiments are performed at room temperature, under 85 % RH and in the presence of 100 mg of Gobi dust. The gas phase side-products formed are normalized by the effective specific surface (expressed in cm²) provided by the natural dust sample. The results are shown in Figure VI-12 where the data displayed on the y-axis are expressed in molecules cm^{-2}.

It can be observed in Figure VI-12 that the amount of each side-products formed per specific surface unit globally increases with AcA concentration. However, while the AcA inlet concentration increases by a factor of 20 over the investigated concentration range, the amounts of methanol, acetaldehyde and acetone observed in the gas phase only increase by a factor lower than 2, and even tend to stabilize towards asymptotic values for methanol and acetaldehyde. Nevertheless, as reported in Figure VI-7, the number of AcA molecules adsorbed on the Gobi dust surface linearly increases with AcA initial concentration on the same investigated concentration range. This behavior suggests that the formation of side-products is only weakly controlled by AcA concentration (and consequently by AcA molecules adsorbed on the dust

surface), but it is mostly defined by a number of reactive surface sites, which could correspond to (S2) surface sites.

3.3.4 Identification of Gobi componental minerals responsible for side product formation

In order to determine the respective contributions of the components of Gobi dust to the observed reactivity and the subsequent formation of gas-phase product, a series of experiments has been carried out using individual minerals: SiO_2, Al_2O_3, Fe_3O_4, TiO_2, and $CaCO_3$. They are exposed to 2.46×10^{14} molecules cm^{-3} AcA at 295 K, and under 50% RH. The results are reported in Figure VI-13.

It is observed that none of the side-products previously detected along the uptake of AcA onto Gobi dust (i.e. methanol, acetaldehyde and acetone) is produced in the presence of $CaCO_3$, SiO_2, and Fe_3O_4. On the contrary, as TiO_2 is used, acetaldehyde, acetone and methanol are formed. In the case of Al_2O_3 only methanol and acetone are detected. As a consequence, TiO_2 and Al_2O_3 can be pointed out as the two oxides responsible for the gas-phase product formation when considering AcA interaction on natural Gobi dust.

The above results do not preclude that other mineral phases are not reactive towards AcA. Indeed, they may lead to the formation of side-products in the adsorbed phase. However, only gas-phase products are addressed in the present experimental approach. For instance, the adsorption of acetaldehyde on TiO_2 has been studied by Batault et al. [27] under 50% RH. The authors found that at this relative humidity the amount of acetaldehyde adsorbed on TiO_2 is totally reversible. Thus, in case acetaldehyde was produced as an effect of AcA interaction on TiO_2, it would be detected since it is completely released in the gas phase. However in the case of Al_2O_3, acetaldehyde is found to be characterized by an irreversible adsorption onto the surface of Al_2O_3. [29] Therefore, acetaldehyde might be formed on the surface on Al_2O_3 but it is not detectable because it remains adsorbed on the surface on the considered mineral. In the case of $CaCO_3$, Al-Hosney et al. [6] also report that the adsorbed carbonic acid dissociates into CO_2 and H_2O in the presence of adsorbed water. Therefore it is possible that AcA reacts with $CaCO_3$ in a similar manner under our experimental conditions. However, this study focuses only on VOCs and gaseous CO_2 formation is not investigated.
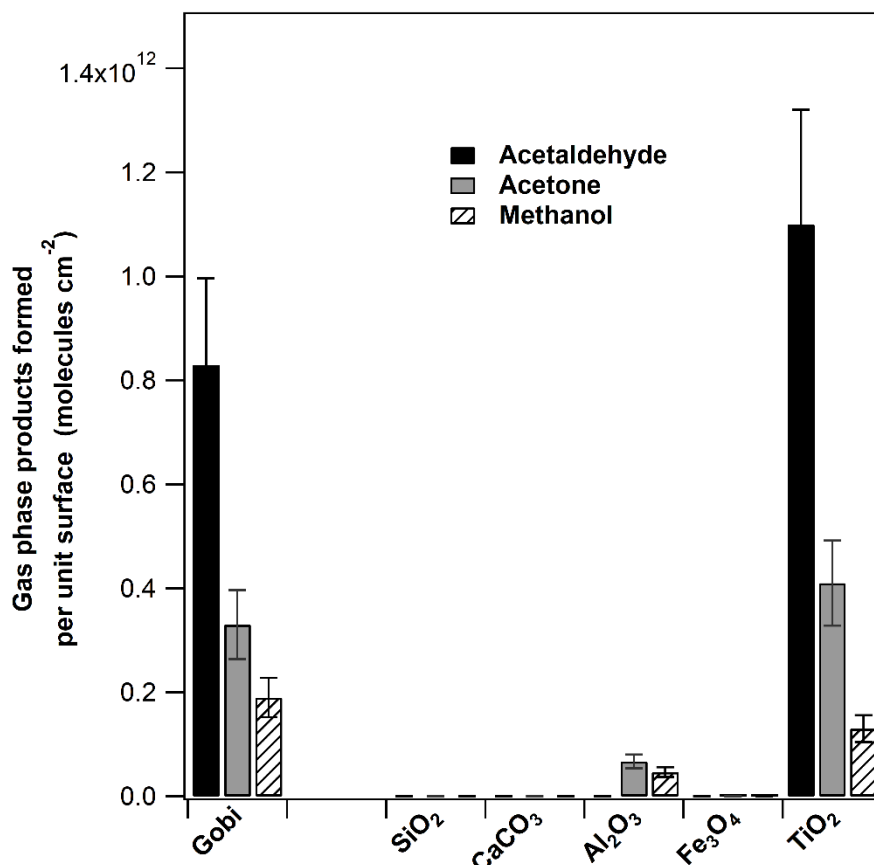
Figure VI-13. Evolution of the concentrations of the gas-phase products as a function of AcA inlet concentration. Experiments are carried out at 295 K, under 85% RH and in the presence of 100 mg of sample mass. The error bars represent the overall uncertainty on the product determination.

4 Atmospheric implications

Several atmospheric implications can be inferred from the current work that may point out the role of heterogeneous processes in the atmospheric cycle of AcA. First, the loss of atmospheric AcA due to its uptake on natural dust should be taken into account. More precisely, the estimated lifetime (τ_{het}) for the heterogeneous removal of AcA is calculated based on Equation VI-8:

$$\tau_{het} = \frac{4}{\gamma_0 D c} \qquad \textbf{(Equation VI-8)}$$

where γ_0 is the uptake coefficient, c is the mean molecular velocity (cm s^{-1}), and D is the dust density (cm^2 cm^{-3}). In the literature and for atmospheric implication purposes, besides the uptake coefficient normalized by the specific surface area, γ_0(BET), the geometric uptake coefficient γ_0(geom) – which indicates that in the initial stage of the uptake process only a

limited fraction of the dust is accessible to the gas environment for interaction [12] – is also widely used.

Actually, γ_0(BET) can be considered as a lower limit and γ_0(geom) as an upper limit of the heterogeneous process [12]. Therefore, aiming to assess the boundaries of the heterogeneous lifetime both parameters are considered. The results are presented in Table VI. Considering that γ_0 is independent of AcA concentration (Figure VI-6) and under atmospheric relevant RH conditions (50 % RH), three different scenarios are taken into account to calculate the heterogeneous lifetime (Table VI-1). In the first scenario using background dust loads, the removal of acetic acid can be assessed as important only if γ_0(geom) is considered (lifetime ca. 2 hours). Although an upper limit, this value is then faster than the gas-phase removal process of AcA with OH radicals (about 14 days), [1] and actually confirms that dry deposition is one of the major removal process of AcA [2]. Regarding the second and third scenarios, where high mineral particle loads, typical for dust storm conditions, are considered, it is evidenced that the heterogeneous removal of AcA is significantly enhanced and clearly becomes the dominant process.

Table VI-1. Calculated heterogeneous lifetimes of AcA under several density of dust (D) conditions, at 295 K and 50% RH.

	During background dust load (D = 6 × 10⁻⁷) [30]	During high dust loads (D = 1.8 × 10⁻⁵) [30]	During dust storm (D = 1.2 × 10⁻³) [31]
γ_0(geom)	τ = 2 hours	τ = 4 min	τ = 4 s
γ_0(BET)	τ = 160 days	τ = 5 days	τ = 2 hours

The amount of AcA converted to gas-phase products, AcA$_{tr}$, can be calculated using Equation VI-9 that also includes the carbon balance. More precisely, to estimate the AcA$_{tr}$ fraction, we considered the results obtained after exposing Gobi dust to various AcA concentrations at room temperature and 85% RH (Figures VI-7 and VI-12).

$$AcA_{tr} = \frac{2N_s(methanol) + \frac{2}{3}N_s(acetone) + N_s(acetaldehyde)}{N_S(acetic\ acid)} \times 100 \qquad \textbf{(Equation VI-9)}$$

where N_s(methanol/acetone/acetaldehyde) corresponds to the total number of molecules of the side-product formed per specific surface unit of the solid and N_s(acetic acid) corresponds to the total AcA amount taken up per specific surface unit of the solid, after exposing Gobi dust to various AcA concentrations. The results are reported in Figure VI-14.
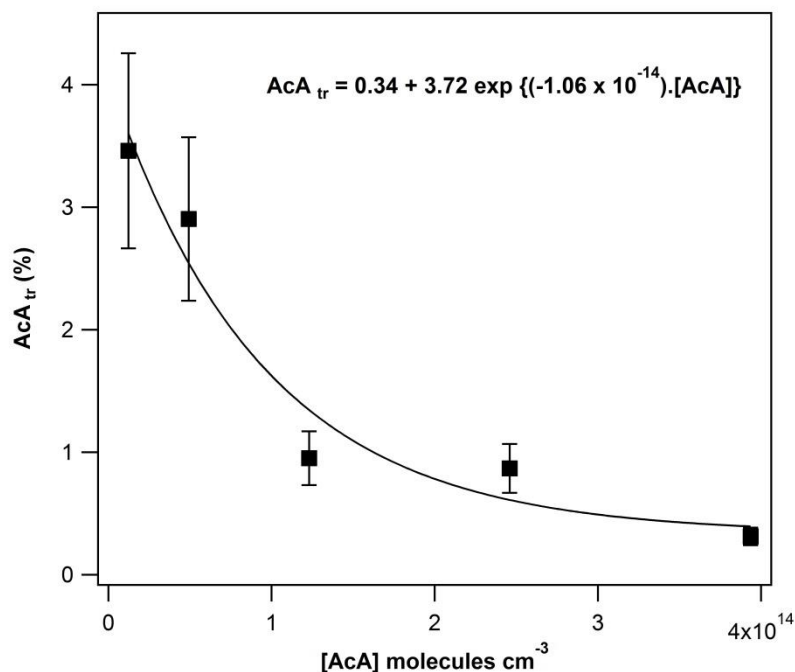
Figure VI-14. Amount of AcA transformed to gas-phase OVOCs as a function of AcA concentration. The error bars represent the overall uncertainty on the product determination. The solid line corresponds to an exponential fit of the results.

An exponential decrease of AcA_{tr} with the AcA gas phase concentration can be observed and fitted with the following equation:

$$AcA_{tr}(\%) = 0.34 + 3.72 \exp\{(-1.06 \times 10^{-14}) \times [AcA]\} \qquad \textbf{(Equation VI-10)}$$

where [AcA] is the concentration of acetic acid in molecules cm^{-3}

Equation VI-10 is used to extrapolate the amount of AcA transformed to OVOCs under relevant atmospheric concentrations of AcA (i.e. around 20 ppb, or 4.92×10^{11} molecules cm^{-3}). It can be inferred that ca. 4 % of AcA can be converted into gas-phase OVOCs. Although this estimation has been extrapolated using an equation derived from higher concentration experimental data, it evidences that the heterogeneous reaction of organic carboxylic acids on selected mineral aerosols can be a source of OVOCs in the atmosphere.

5   Conclusion

This study investigates the heterogeneous interaction of AcA on natural Gobi dust under simulated atmospheric conditions for the first time. The uptake coefficient and the product yields are determined as a function of AcA concentration and RH. The initial uptake coefficient is found to be independent on concentration and reversibly dependent on RH.

The originality of this study relies on the determination of the relative contributions of each mineral phase of Gobi dust to the global behavior of the dust. More precisely, it has been evidenced that $CaCO_3$ is from far the most contributing mineral to the uptake of AcA by Gobi dust. Metal oxides have lower contributions, especially silica. This phenomenon has been correlated to the surface chemistry of the considered phases.

Methanol, acetone and acetaldehyde are identified as gas-phase products. It is found that the reactivity of such an interaction is enhanced as concentration decreases and RH increases. Interestingly the mineral phases contributing to the reactivity and the formation of side-products are different from the mineral phase mostly contributing to the uptake. Indeed, TiO_2, under dark conditions, and to a minor extent Al_2O_3 are the most contributive mineral phases to the formation of side products.

Using these results, the atmospheric lifetimes and the carbon mass balance can be assessed. The heterogeneous interaction of AcA on natural Gobi dust could be considered as a significant removal process of AcA from the atmosphere under specific environmental conditions.

This study focused on the determination of the gas-phase products under dark conditions and understanding the precise mechanism of the gas-phase product formation is still ongoing. Therefore, an important future perspective is to focus on the adsorbed-phase products to help proposing a mechanism of such reactivity.

6   References of Chapter VI

1.   Khare, P.; Kumar, N.; Kumari, K. M.; Srivastava, S. S., *Atmospheric Formic and Acetic Acids: An Overview.* Reviews of Geophysics, 1999. **37**(2): p. 227-248.

2.   Talbot, R. W.; Andreae, M. O.; Berresheim, H.; Jacob, D. J.; Beecher, K. M., *Sources and Sinks of Formic, Acetic, and Pyruvic acids over Central Amazonia: 2. Wet Season.* Journal of Geophysical Research: Atmospheres, 1990. **95**(D10): p. 16799-16811.

3.   Talbot, R. W.; Beecher, K. M.; Harriss, R. C.; Cofer, W. R., *Atmospheric Geochemistry of Formic and Acetic Acids at a Mid-latitude Temperate Site.* Journal of Geophysical Research: Atmospheres, 1988. **93**(D2): p. 1638-1652.

4.   Graedel, T. E.; Eisner, T., *Atmospheric Formic Acid from Formicine Ants: A Preliminary Assessment.* Tellus B, 1988. **40B**(5): p. 335-339.

5.   Carlos-Cuellar, S.; Li, P.; Christensen, A. P.; Krueger, B. J.; Burrichter, C.; Grassian, V. H., *Heterogeneous Uptake Kinetics of Volatile Organic Compounds on Oxide Surfaces Using a Knudsen Cell Reactor: Adsorption of Acetic Acid, Formaldehyde, and Methanol on Alpha-Fe$_2$O$_3$, Alpha-Al$_2$O$_3$, and SiO$_2$.* The Journal of Physical Chemistry A, 2003. **107**(21): p. 4250-4261.

6.   Al-Hosney, H. A.; Carlos-Cuellar, S.; Baltrusaitis, J.; Grassian, V. H., *Heterogeneous Uptake and Reactivity of Formic Acid on Calcium Carbonate Particles: a Knudsen cell Reactor, FTIR and SEM study.* Physical Chemistry Chemical Physics, 2005. **7**(20): p. 3587-3595.

7.   Prince, A. P.; Kleiber, P. D.; Grassian, V. H.; Young, M. A., *Reactive Uptake of Acetic Acid on Calcite and Nitric Acid Reacted Calcite Aerosol in an Environmental Reaction Chamber.* Physical Chemistry Chemical Physics, 2008. **10**(1): p. 142-152.

8.   Tong, S. R.; Wu, L. Y.; Ge, M. F.; Wang, W. G.; Pu, Z. F., *Heterogeneous Chemistry of Monocarboxylic Acids on Alpha - Al$_2$O$_3$ at Different Relative Humidities.* Atmospheric Chemistry and Physics, 2010. **10**(16).

9.   Zeineddine, M. N.; Romanias, M. N.; Gaudion, V.; Riffault, V.; Thévenet, F., *Heterogeneous Interaction of Isoprene with Natural Gobi Dust.* ACS Earth and Space Chemistry, 2017. **1**(5): p. 236-243.

10.   Romanias, M. N.; Zeineddine, M. N.; Riffault, V.; Thevenet, F., *Isoprene Heterogeneous Uptake and Reactivity on TiO$_2$: A Kinetic and Product Study.* International Journal of Chemical Kinetics, 2017. **49**(11): p. 773-788.

11.   Romanias, M. N.; Zeineddine, M. N.; Gaudion, V.; Lun, X.; Thevenet, F.; Riffault, V., *Heterogeneous Interaction of Isopropanol with Natural Gobi Dust.* Environmental Science & Technology, 2016. **50**(21): p. 11714-11722.

12.   Crowley, J. N.; Ammann, M.; Cox, R. A.; Hynes, R. G.; Jenkin, M. E.; Mellouki, A.; Rossi, M. J.; Troe, J.; Wallington, T. J., *Evaluated Kinetic and Photochemical Data for Atmospheric Chemistry: Volume V - Heterogeneous Reactions on Solid Substrates.* Atmospheric Chemistry and Physics, 2010. **10**(18): p. 9059-9223.

13.   Huthwelker, T.; Ammann, M.; Peter, T., *The Uptake of Acidic Gases on Ice.* Chemical Reviews, 2006. **106**(4): p. 1375-1444.

14.   Romanías, M. N.; Dagaut, P.; Bedjanian, Y.; Andrade-Eiroa, A.; Shahla, R.; Emmanouil, K. S.; Papadimitriou, V. C.; Spyros, A., *Investigation of the Photochemical Reactivity of Soot Particles Derived from Biofuels Toward NO$_2$. A Kinetic and Product Study.* Journal of Physical Chemistry A, 2015. **119**(10): p. 2006-2015.

15.   Tang, M.; Larish, W. A.; Fang, Y.; Gankanda, A.; Grassian, V. H., *Heterogeneous Reactions of Acetic Acid with Oxide Surfaces: Effects of Mineralogy and Relative Humidity.* The Journal of Physical Chemistry A, 2016. **120**(28): p. 5609-5616.

16. Roscoe, J. M.; Abbatt, J. P. D., *Diffuse Reflectance FTIR Study of the Interaction of Alumina Surfaces with Ozone and Water Vapor.* The Journal of Physical Chemistry A, 2005. **109**(40): p. 9028-9034.

17. Joshi, N.; Romanias, M. N.; Riffault, V.; Thevenet, F., *Investigating Water Adsorption onto Natural Mineral Dust Particles: Linking DRIFTS Experiments and BET Theory.* Aeolian Research, 2017. **27**(Supplement C): p. 35-45.

18. Ibrahim, S.; Romanias, M. N.; Alleman, L. Y.; Zeineddine, M. N.; Angeli, G. K.; Trikalitis, P. N.; Thevenet, F., *Water Interaction with Mineral Dust Aerosol: Particle Size and Hygroscopic Properties of Dust.* ACS Earth and Space Chemistry, 2018. **2**(4): p. 376-386.

19. Goss, K.-U.; Schwarzenbach, R. P., *Quantification of the Effect of Humidity on the Gas/Mineral Oxide and Gas/Salt Adsorption of Organic Compounds.* Environmental Science & Technology, 1999. **33**(22): p. 4073-4078.

20. Goss, K.-U.; Schwarzenbach, R. P., *Empirical prediction of heats of vaporization and heats of adsorption of organic compounds.* Environmental Science & Technology, 1999. **33**(19): p. 3390-3393.

21. Goss, K.-U.; Eisenreich, S. J., *Adsorption of VOCs from the Gas Phase to Different Minerals and a Mineral Mixture.* Environmental Science & Technology, 1996. **30**(7): p. 2135-2142.

22. Goss, K. U., *Effects of Temperature and Relative Humidity on the Sorption of Organic Vapors on Clay Minerals.* Environmental Science & Technology, 1993. **27**(10): p. 2127-2132.

23. Goss, K. U., *Effects of Temperature and Relative Humidity on the Sorption of Organic Vapors on Quartz Sand.* Environmental Science & Technology, 1992. **26**(11): p. 2287-2294.

24. Tungsheng, L.; Shouxin, Z.; Jiaomao, H., *Stratigraphy and Paleoenvironmental Changes in the Loess of Central China.* Quaternary Science Reviews, 1986. **5**: p. 489-495.

25. Zeineddine, M. N.; Romanias, M. N.; Riffault, V.; Thévenet, F., *Heterogeneous Interaction of Various Natural Dust Samples with Isopropyl Alcohol as a Probe VOC.* The Journal of Physical Chemistry A, 2018. **122**(22): p. 4911-4919.

26. Ngo, S.; Betts, L. M.; Dappozze, F.; Ponczek, M.; George, C.; Guillard, C., *Kinetics and Mechanism of the Photocatalytic Degradation of Acetic Acid in Absence or Presence of O_2.* Journal of Photochemistry and Photobiology A: Chemistry, 2017. **339**: p. 80-88.

27. Batault, F.; Thevenet, F.; Hequet, V.; Rillard, C.; Le Coq, L.; Locoge, N., *Acetaldehyde and Acetic Acid Adsorption on TiO_2 under Dry and Humid Conditions.* Chemical Engineering Journal, 2015. **264**: p. 197-210.

28. Rubasinghege, G.; Ogden, S.; Baltrusaitis, J.; Grassian, V. H., *Heterogeneous Uptake and Adsorption of Gas-Phase Formic Acid on Oxide and Clay Particle Surfaces: The Roles of Surface Hydroxyl Groups and Adsorbed Water in Formic Acid Adsorption and the Impact of Formic Acid Adsorption on Water Uptake.* The Journal of Physical Chemistry A, 2013. **117**(44): p. 11316-11327.

29. Li, P., K. A. Perreau, E. Covington, C. H. Song, G. R. Carmichael, and V. H. Grassian, *Heterogeneous Reactions of Volatile Organic Compounds on Oxide Particles of the Most Abundant Crustal Elements: Surface Reactions of Acetaldehyde, Acetone, and Propionaldehyde on SiO_2, Al_2O_3, Fe_2O_3, TiO_2, and CaO.* Journal of Geophysical Research: Atmospheres, 2001. **106**(D6): p. 5517-5529.

30.   Aymoz, G.; Jaffrezo, J. L.; Jacob, V.; Colomb, A.; George, C., *Evolution of Organic and Inorganic Components of Aerosol During a Saharan Dust Episode Observed in the French Alps.* Atmospheric Chemistry and Physics, 2004. **4**(11/12): p. 2499-2512.

31.   Gillies, J. A.; Nickling, W. G.; McTainsh, G. H., *Dust Concentrations and Particle-size Characteristics of an Intense Dust Haze Event: Inland Delta Region, Mali, West Africa.* Atmospheric Environment, 1996. **30**(7): p. 1081-1090.

General conclusion and perspectives

The main purpose of this thesis is to investigate the interaction of VOCs with natural mineral dust under atmospheric conditions. The following section summarizes the results obtained in this thesis and future perspective in six different aspects: (1) impact of the origin and chemical composition of mineral dust on the interaction of VOCs with natural dust samples (2) initial uptakes of VOCs on natural dust samples (3) adsorption isotherms of VOCs on natural dust samples (4) reactivity of VOCs on natural dust surfaces under dark and UV irradiation (5) Atmospheric implications (6) perspective towards future approaches.

1. Effect of mineral dust origin and chemical composition on the interaction of VOCs with natural dust samples

The adsorption efficiencies of natural dust samples collected from North and West Africa, Saudi Arabia, Gobi and Arizona desert regions toward isopropanol (IPA), used as a probe molecule, are investigated. Result evidenced a difference of one order of magnitude between the lowest and the highest uptakes determined. Gobi dust are characterized by the highest initial uptake while that of Nefta desert showed the lowest. A linear correlation of the initial uptake coefficients has been experimentally evidenced with the Al/Si and Fe/Si elemental ratios for the different dust samples from different origins. Interestingly, reviewing the initial uptake coefficients for inorganic species from the literature and plotting them versus the Al/Si ratio also highlighted significant linear correlations. This behaviour underlines the key role of metal centres other than Si in the mineral phases. The chemical composition of the mineral dust surfaces directly controls the uptake of VOCs and inorganic species.

2. Initial uptakes of VOCs on natural dust samples

Dependence of VOC uptake on VOC concentration

The initial uptake of IPA, ISP and AcA on natural dust samples has been evidenced to be independent on the gases inlet concentration. This behavior is expected since the initial uptake expresses the interaction of a gas molecule with a fresh and unexposed surface. Moreover, under dry conditions the contrasted initial uptake values of IPA, AcA, and ISP on the same natural Gobi sample highlighted the role of the functional groups of the VOC, i.e. the VOC structure, in controlling the interaction with the considered dust sample.

Dependence of VOC uptake on relative humidity

It has been experimentally evidenced that the initial uptake of IPA, ISP and AcA on natural dust samples is inversely dependent on RH. Fitted experimental results enabled to extrapolate the initial uptakes at any targeted RH. This work can help importing the result in atmospheric models in order to be able to evaluate heterogeneous processes on a regional or global scale. The impact of relative humidity on the uptake of IPA and ISP is higher than on AcA, showing the significance of the VOC-dust interaction intensity in competitive sorptive processes.

From dry conditions up to ca. 20% RH the initial uptake coefficients are poorly impacted by the presence of water molecules for all the studied dust samples. However, after this threshold a dramatic decrease is observed up to 80% of RH reflecting the competition between VOCs and H_2O molecules for surface sites. The drop of initial uptake coefficients above 20% RH is proposed to be correlated to the formation of one or more water layers on the surface of the dust particles, blocking the active sites and inhibiting the direct interaction of VOCs with mineral dust.

Dependence of VOC uptake on temperature

The temperature dependence the initial uptake coefficients of ISP and IPA on Gobi dust is investigated for the first time. For IPA, the initial uptake is found to be independent of temperature. The observed independence of γ_0 on temperature could be attributed to the limited T range where experiments are conducted. For ISP, the initial uptake is found to be decreasing with increasing temperature. The initial uptake coefficients of ISP on Gobi dust are fitted by the Arrhenius equation that enables the calculation of the activation energy. The activation energy of ISP uptake is determined as Ea = -11.4 ± 2.2 kJ mol^{-1}. The negative activation energy corresponds to the overall energy barrier for the colliding gas molecules to undergo adsorption on the Gobi dust surface via the formation of an intermediate state on dust. The impact of temperature should be deepened in the future in order to improve our ability to address realistic atmospheric conditions.

Adsorption isotherms of VOCs on natural dust samples

Dependence of VOC adsorption isotherm on relative humidity

The adsorption isotherms of IPA, ISP, and AcA on natural Gobi dust are constructed as a function of RH. In general VOC adsorption is diminished with increasing relative humidity.

H$_2$O molecules compete with VOC for the adsorption sites. This is consistent with the fact that the formation of the first monolayer of water occurs at around 20% RH. Therefore, highlighting the importance of relative humidity on the interaction of VOCs with natural dust samples. Furthermore, RH also impacts the reversibly adsorbed fraction. In the case of IPA and ISP flushing the surface with humid air induces the complete desorption of the adsorbed molecules, while in the case of AcA the intensity of the interaction is higher and only a fraction lower than 10% is desorbed. This approach emphasized the fact that beyond the characterization of heterogeneous process through uptake coefficient, the fate of taken up species can be highly contrasted. It helps understanding the role a gas-surface interaction from a sink-and-source point of view. Weakly interacting species can be easily desorbed depending on atmospheric conditions while strongly interacting species can be irreversibly lost.

Dependence of VOC adsorption isotherm on temperature

The adsorption isotherms of IPA and ISP on Gobi dust are constructed at different temperatures. The adsorption of both used VOCs is enhanced with decreasing temperature. The experimental results are simulated with Langmuir model that enables the calculation of the partition coefficient K_{Lin}. The temperature dependence of K_{Lin} is given by the Van't Hoff expression and allows the calculation of the adsorption of enthalpy. The adsorption of enthalpy is found to be ΔH_{ads} = -14.7 ± 1.1 kJ mol^{-1} for IPA and ΔH_{ads} = -31.0 ± 2.3 kJ mol^{-1} for ISP. This indicates that ΔH_{ads} can vary widely for the same substrate and no value can be predicted for the interaction of any VOC with the same dust sample. The enthalpy of adsorption of water on the Gobi dust sample was found to be -49.2 kJ mol^{-1}. This value is lower than the adsorption of enthalpy of IPA and ISP interaction on the same dust sample. That might be the reason why water plays an important role whenever considering VOC interaction with natural dust samples.

4. Reactivity of VOC on natural dust surfaces under dark and UV irradiation

The interaction of ISP on Gobi dust did not lead to any product formation neither in the gas nor in the adsorbed phase under our experimental conditions. This means that either the interaction of ISP with fresh Gobi dust does not lead to any product formation in the gas phase or the products formed are below the detection limit of the analytical instruments used.

The interaction of IPA on Gobi dust led to a minor formation of acetone, formaldehyde, acetic acid, and acetaldehyde as gas phase products under UV-A irradiation of

the dust surface. The adsorbed phase was also analyzed and several aldehydes and ketones are detected as adsorbed phase products. It has to be noted that under dark condition no products are detected neither in the gas nor in the adsorbed phase, underlying the role a photo-activated processes in the observed reactivity.

The interaction of AcA on Gobi dust led to the formation of methanol, acetaldehyde and acetone in the gas phase. These products are characterized as a function on AcA concentration and relative humidity. The formation of the products is enhanced by decreasing AcA gas concentration and by the formation of the water monolayer.

These results show that in some cases, the VOC-dust interaction can effectively lead to the formation of reaction products in the adsorbed phase or in the gas phase. These reactive processes are highly dependent on (i) the structure of the considered VOC and its subsequent interaction with the dust sample, (ii) the chemical composition of the considered dust and its surface reactivity, and (iii) the environmental condition (RH, irradiation) that can induce reactive processes or promote the transfer a surface products to the gas phase. Considering the sensitivity of the reactive process to the selected VOC, dust and conditions, no general conclusion can be extracted, but the contribution of such processes among the sink s and sources of VOCs in the atmosphere should be further considered.

5. Atmospheric implications

This work is the first one to experimentally evidence that natural mineral dust samples can act as potential sources of OVOCs under specific conditions. Even though the photoreactivity of the Gobi dust sample seems to be relatively low, it does not preclude that with other natural samples and/or other abundant VOCs it should be identical. The heterogeneous processes on dust could influence the VOC distribution and balance in the troposphere, and thus its oxidation capacity under specific environmental conditions.

The loss of atmospheric VOCs due to the uptake on natural dust strongly vary from one compound to another. For instance the lifetime of ISP and IPA from their heterogeneous interactions with dust are low compared to the main removal with OH reaction (estimated around 1.4 hours for ISP). However the lifetime from the heterogeneous interaction of AcA on dust sample should not be ruled out in the atmosphere. It is determine to range from several

days under background dust to only few hours under major dust events, meaning that it could be a significant removal process of AcA from the atmosphere.

6. Perspective towards future approaches

The short term perspectives from this thesis are:

(i)   Investigating the heterogeneous reaction of AcA on Gobi dust using the DRIFTs in order to determine the adsorbed phase products and can also help figuring out the mechanism of product formations

(ii)   Investigating the heterogeneous reaction   of AcA on Gobi dust under UV irradiation

(iii)   Investigating the heterogeneous interaction of formic acid on natural mineral dust

The long term perspectives of this thesis are:

(i)   Studying other groups of VOC compound interactions on natural dust samples

(ii)   Implementing the results obtained in this and other studies in atmospheric models in order to evaluate the importance of the heterogeneous process on global atmospheric scale

(iii)   Studying the interaction of VOCs with other possible substrates. For instance, the interaction of VOCs with liquid particles that contribute to the heterogeneous and multi-phase chemistry in the atmosphere.

List of publications related to this thesis

Journal publications

1) **M. N. ZEINEDDINE**, M. N. ROMANIAS, V. GAUDION, V. RIFFAULT, F. THEVENET, *Heterogeneous interaction of isoprene with natural Gobi dust*, ACS Earth and Space Chemistry 1(5), 236–243 (2017), DOI 10.1021/acsearthspacechem.7b00050

2) **M. N. ZEINEDDINE**, M. N. ROMANIAS, V. RIFFAULT, F. THEVENET, *Heterogeneous interaction of various dust samples with isopropanol as a probe molecule*, The Journal of Physical Chemistry A *122*(22), 4911-4919, (2018) DOI: 10.1021/acs.jpca.8b02034

3) **M. N. ZEINEDDINE**, M. N. ROMANIAS, V. RIFFAULT, F. THEVENET, *Uptake and reactivity of acetic acid on natural gobi dust (**In progress**)*

4) M. N. ROMANIAS, **M. N. ZEINEDDINE**, V. GAUDION, X. LUN, F. THEVENET, V. RIFFAULT, *Heterogeneous Interaction of Isopropanol with Natural Gobi Dust*, Environmental Science and Technology, 50 (21), 11714–11722 (2016), DOI 10.1021/acs.est.6b03708

5) M. N. ROMANIAS, **M. N. ZEINEDDINE**, V. GAUDION, V. RIFFAULT, F. THEVENET, *Isoprene heterogeneous uptake and reactivity on TiO$_2$: A kinetic and product study*, International Journal of Chemical Kinetics 49(11), 773-788 (2017), DOI 10.1002/kin.21114

6) S. IBRAHIM, M. N. ROMANIAS, **M. N. ZEINEDDINE**, L. Y. ALLEMAN, G. K. ANGELI, P. N. TRIKALITIS, F. THEVENET, Water Interaction with Mineral Dust Aerosol: Particle Size and Hygroscopic Properties of Dust. *ACS Earth and Space Chemistry, 2*(4), 376-386, (2018). DOI: 10.1021/acsearthspacechem.7b00152

International conferences

1) M. N. ROMANIAS, **M. N. ZEINEDDINE**, V. GAUDION, V. RIFFAULT, <u>F. THEVENET</u>, *Heterogeneous interaction of isopropanol with Gobi mineral dusts under simulated atmospheric conditions*, **Oral communication**, 8th International Workshop on Sand/Duststorms and Associated Dustfall, Lisbonne (Portugal), 1-4 May 2016.

2) <u>M. N. ROMANIAS</u>, **M. N. ZEINEDDINE**, V. GAUDION, F. THEVENET, V. RIFFAULT, *Heterogeneous interaction of isopropanol with mineral dust surfaces under simulated atmospheric conditions*, **Oral communication,** 2nd International Conference on Atmospheric Dust, Castellaneta Marina (Italie), 12-17 juin 2016.

3) M. N. ROMANIAS, N. JOSHI, **<u>M. N. ZEINEDDINE</u>**, H. OURRAD, M. CHOËL, F. THEVENET, V. RIFFAULT, *Investigating the composition and morphology of natural mineral dust samples*, **Poster**, European Aerosol Conference, Tours (France), 4-9 septembre 2016.

4) M. N. ROMANIAS, **<u>M. N. ZEINEDDINE</u>**, V. GAUDION, F. THEVENET, V. RIFFAULT, Heterogeneous interaction of volatile organic compounds with natural mineral dust surfaces under simulated atmospheric conditions, **Poster**, European Aerosol Conference, Tours (France), 4-9 Sep 2016.

5) **<u>M. N. ZEINEDDINE</u>**, M. N. ROMANIAS, V. GAUDION, V. RIFFAULT, F. THEVENET, *Heterogeneous interaction of isoprene with natural Gobi dust*, **Poster**, International Conference on Aerosol Cycle, Villeneuve d'Ascq (France), 21-23 mars 2017.

6) <u>M. N. ROMANIAS</u>, J. LASNE, **M. N. ZEINEDDINE**, V. RIFFAULT, F. THEVENET, *Heterogeneous reaction of NO_2 with volcanic dust in the atmosphere: uptake coefficients and HONO formation yields*, **Oral communication,** American Geosciences Union General Assembly 2017, New Orleans (US), 11-15 Dec 2017.

7) **<u>M. N. ZEINEDDINE</u>**, M. N. <u>ROMANIAS</u>, V. RIFFAULT, F. THEVENET, *Uptake and reactivity of acetic acid on natural gobi dust*, **Oral communication,** Dust 2018 Conference, Bari (Italy), 29-31 may 2018.

Annex A

Table AS1. Summary of parameter values obtained after fitting the RH dependence of initial uptakes, γ_0, and partitioning constants, K_{Lin}, with the respective empirical expressions

$\gamma_{RH} = \gamma_{dry} - aRH^b$ and $N_s = \dfrac{a}{b + (RH)^c}$.

Dust sample	$\gamma_{RH} = \gamma_{dry} - aRH^b$			$N_s = \dfrac{a}{b + (RH)^c}$		
	γ_{dry} (10^{-7})	a (10^{-9})	b	a (10^{13})	b	c
Mbour	1.54	17.1	0.42	4.3	3.0	1.2
Nefta	0.29	0.11	1.24	1.2	3.8	1.1
Rawdat	2.46	5.65	0.84	1.5	6.8	1.4
Gobi [1]	-	-	-	3.8	5.3	1.8
ATD	1.18	2.10	0.89	5.5	11.9	1.7

Table AS2. Uptake values and RH conditions for NO_2, O_3, and SO_2 interaction with several dust samples or mineral oxides.

	Sample	Uptake	RH	Reference
NO$_2$				
	Saharan dust	1.2×10^{-6}	Dry	Underwood et al. [2]
	China dust	2.1×10^{-6}		
	Al_2O_3	9.1×10^{-6}		
	Mauritania dust	1.6×10^{-8}	25%	Ndour et al. [3]
	Tunisia dust	5.9×10^{-9}		
	Morocco dust	9.4×10^{-9}		
	Algeria dust	4.3×10^{-9}		
O$_3$				
	Saharan dust	6×10^{-5}	Dry	Hanish et al. [4]
	China dust	2.7×10^{-5}	Dry	Michel et al. [5]
	Saharan dust	6×10^{-5}		
	Al_2O_3	8×10^{-5}		
	SiO_2	5×10^{-5}		
SO$_2$				
	China loess	3×10^{-5}	Dry	Usher et al.[6]
	Al_2O_3	1.6×10^{-4}		
	SiO_2	1×10^{-7}		
	Saharan dust	6.65×10^{-5}	Dry	Adams et al. [7]

Table AS3. Saturation surface coverage, N_{max}, and partitioning constants K_{Lang} and K_{Lin} values for IPA desorption (concentrations in the range $(0.15 - 615) \times 10^{13}$ molecules cm^{-3}) on several dust samples at 30% RH and 296 K. The overall uncertainty for N_{max} and K_{Lang} is estimated to be around 16% while that for K_{Lin} (desorption) is around 20%. K_{Lin} (adsorption) is given for comparison purposes.

Dust sample	N_{max} (10^{13} molecules cm^{-2})	K_{Lang} (10^{-16} cm^3 molecule^{-1})	K_{Lin} (desorption) (10^{-2} cm)	K_{Lin} (adsorption) (10^{-2} cm)	K_{Lin}(des)/ K_{Lin}(ads)
Mbour	4.11 ± 0.64	5.89 ± 0.91	2.42 ± 0.49	2.39 ± 0.47	~1
Nefta	2.70 ± 0.44	4.25 ± 0.68	1.14 ± 0.21	1.13 ± 0.22	~1
ATD	14.5 ± 2.3	2.97 ± 0.46	4.34 ± 0.89	5.18 ± 1.04	0.86
Rawdat	3.52 ± 0.62	8.81 ± 0.40	3.10 ± 0.64	3.41 ± 0.68	0.84
Gobi	6.66 ± 0.81	2.74 ± 0.49	1.61 ± 0.28	1.81 ± 0.40	0.88

Figure AS1. IPA interaction with Rawdat dust at 1 ppm of IPA under (a) dry conditions and (b) 30% RH showing the differences in step durations between both experiments. Step 1: background collection; step 2: IPA introduction; step 3: dust surface exposure to IPA; step 4: surface isolation; step 5: room temperature flushing; step 6: dust surface heating.
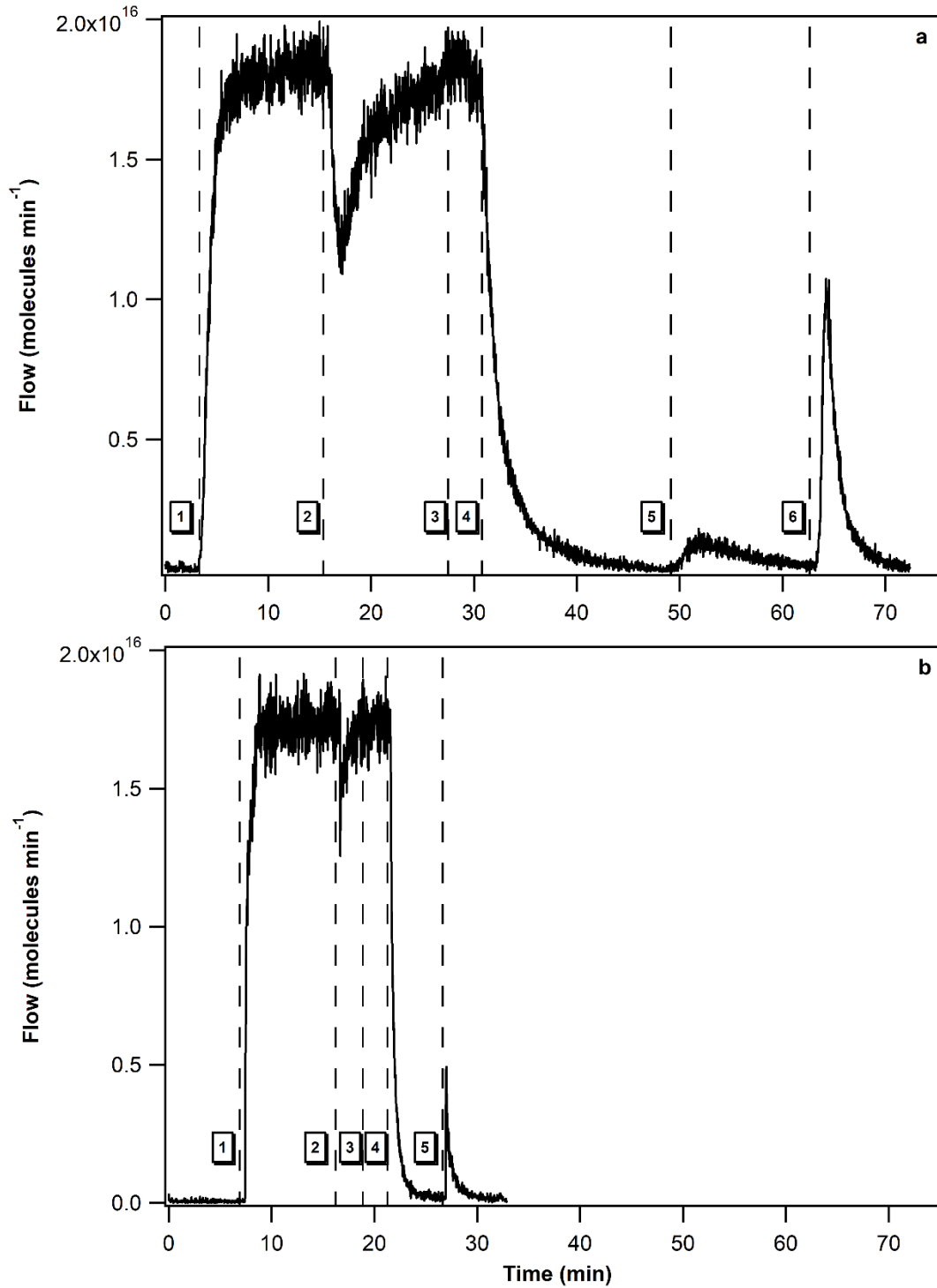
Figure AS2. IPA interaction with Mbour dust under low concentration of IPA (70 ppb) and dry

conditions highlighting the duration of the surface exposure step in this experiment
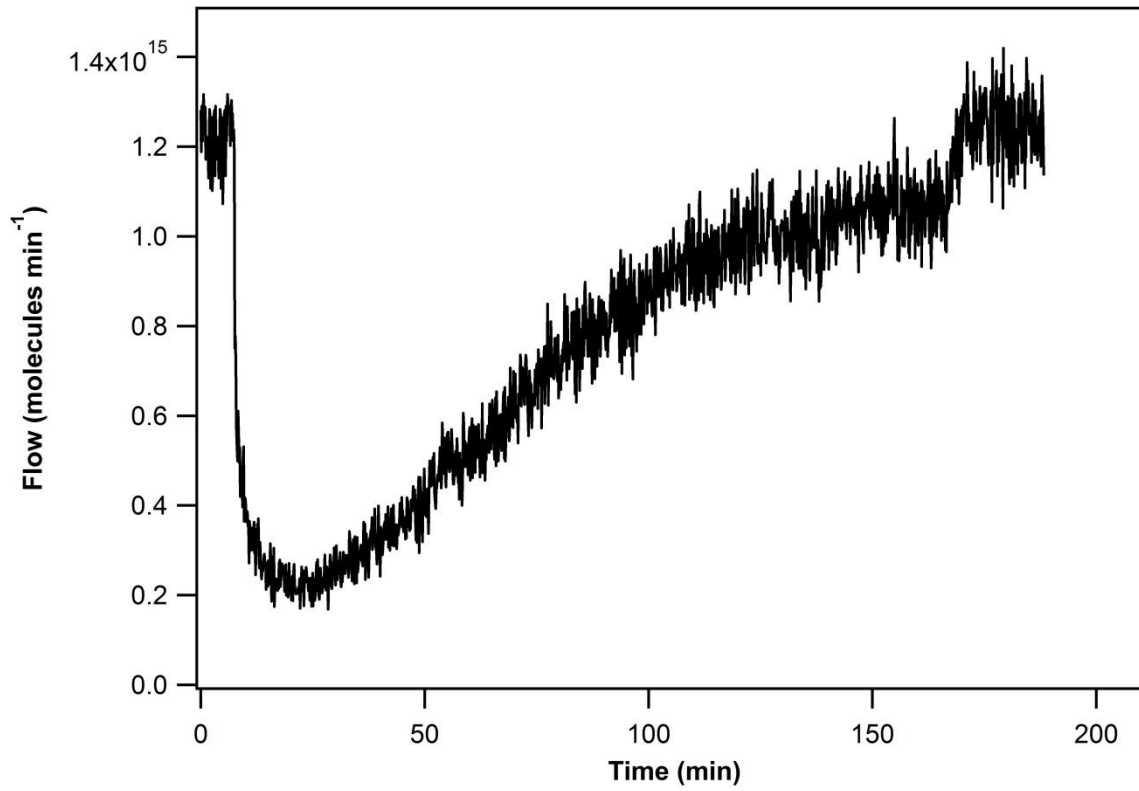
Figure AS3. Number of molecules adsorbed per surface unit, N_S, at 1 ppm of IPA for the different studied samples as a function of RH. The error bars represent the overall uncertainty on N_S determination (20%).
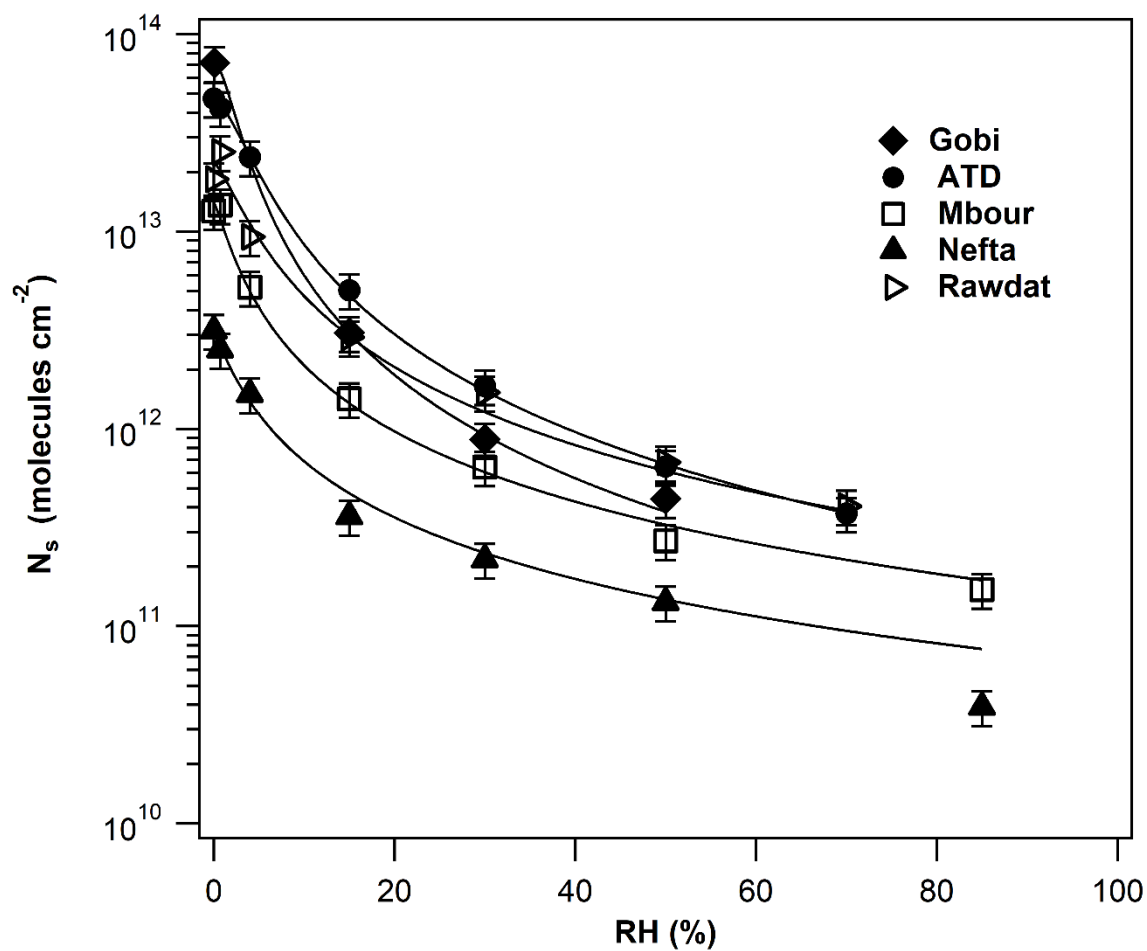
Figure AS4 Desorption isotherms of IPA for the four natural dust samples determined at 296 K and 30% RH. The error bars represent the overall uncertainty on N_s determination. The solid lines are non-weighted fits through the data using the Langmuir expression.
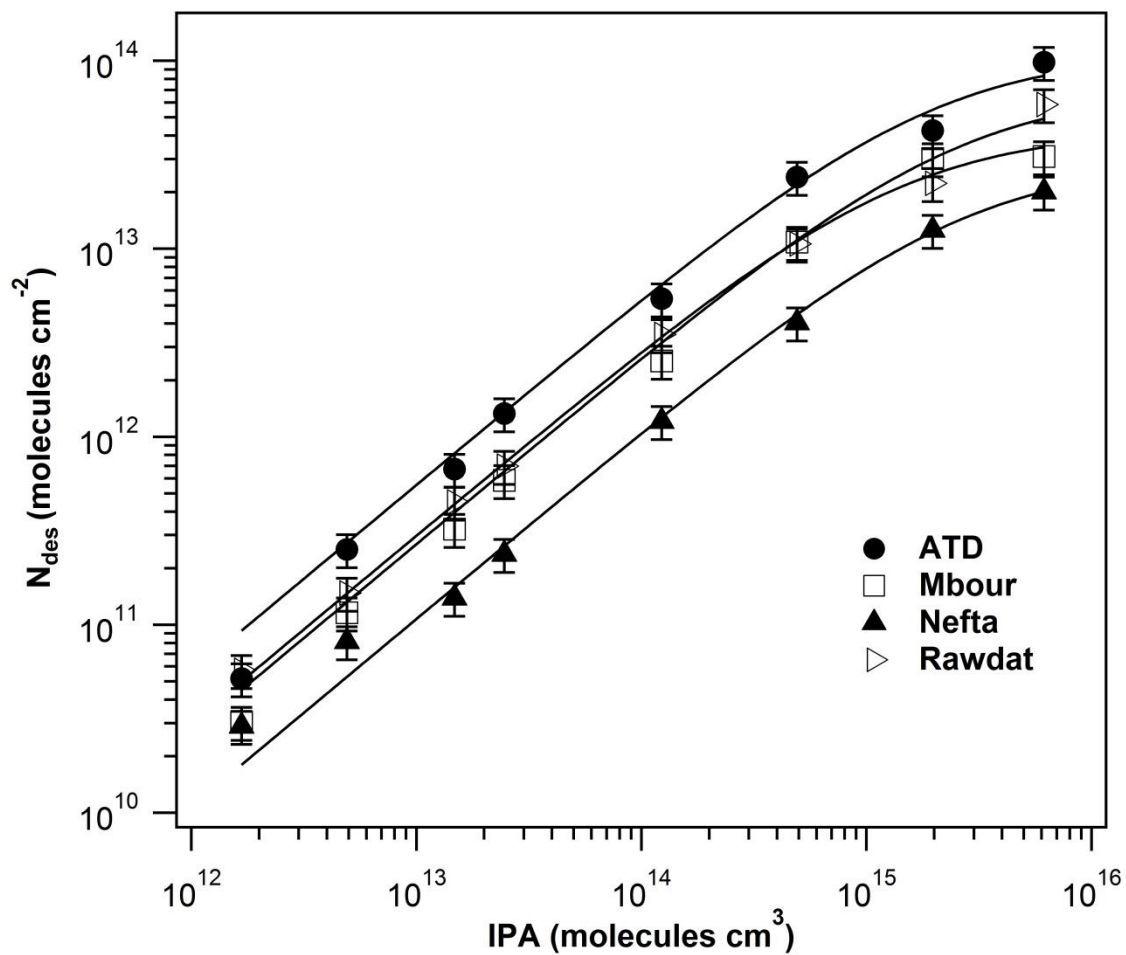
References of Annex A

1. Romanias, M. N.; Zeineddine, M. N.; Gaudion, V.; Lun, X.; Thevenet, F.; Riffault, V., *Heterogeneous Interaction of Isopropanol with Natural Gobi Dust.* Environ. Sci. Tech., 2016. **50**: p. 11714-11722.

2. Underwood, G. M.; Song, C. H.; Phadnis, M.; Carmichael, G. R.; Grassian, V. H., *Heterogeneous Reactions of NO_2 and HNO_3 on Oxides and Mineral Dust: A Combined Laboratory and Modeling Study.* J Geophys. Res. Atmos., 2001. **106**: p. 18055-18066.

3. Ndour, M.; Nicolas, M.; D'Anna, B.; Ka, O.; George, C., *Photoreactivity of NO_2 on Mineral Dusts Originating from Different Locations of the Sahara Desert.* Phys. Chem. Chem. Phys., 2009. **11**: p. 1312-1319.

4. Hanisch, F.; Crowley, J. N., *Ozone Decomposition on Saharan Dust: An Experimental Investigation.* Atmos. Chem. Phys., 2003. **3**: p. 119-130.

5. Michel, A. E.; Usher, C. R.; Grassian, V. H., *Heterogeneous and Catalytic Uptake of Ozone on Mineral Oxides and Dusts: A Knudsen Cell Investigation.* Geophys. Res. Lett., 2002. **29**: p. 10-1-10-4.

6. Usher, C. R.; Al-Hosney, H.; Carlos-Cuellar, S.; Grassian, V. H., *A laboratory Study of the Heterogeneous Uptake and Oxidation of Sulfur Dioxide on Mineral Dust Particles.* J Geophys. Res. Atmos., 2002. **107**: p. ACH 16-1-ACH 16-9.

7. Adams, J. W.; Rodriguez, D.; Cox, R. A., *The Uptake of SO_2 on Saharan Dust: A Flow Tube Study.* Atmos. Chem. Phys., 2005. **5**: p. 2679-2689.

Annex B

Figure BS1. Plot of [IPA]/N_s versus [IPA] for isopropanol adsorption on Gobi dust under various RH conditions: dry (<0.01), 15, 30 and 50%. The lines are linear least-square fits through the data according to the modified Langmuir expression.
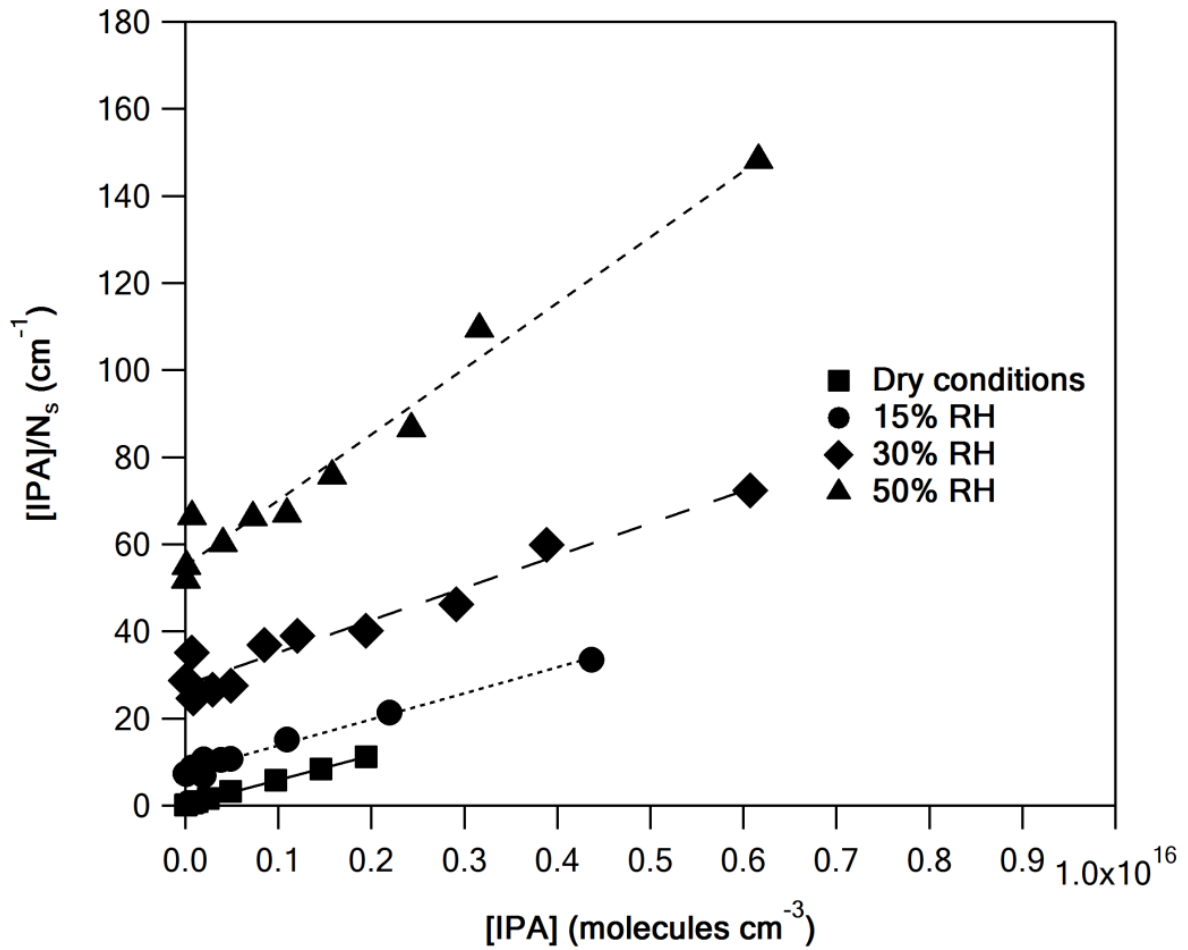
Figure BS2. Dependence of K_{Lin} on relative humidity at T = 293 K. The solid line is the fit of the experimentally determined K_{Lin} equilibrium constants based on the equation: $K_{Lin} = a / (b + RH^c)$, where a, b and c are empirical parameters. The error bars represent the overall uncertainty on K_{Lin} determination (corresponding to the estimated systematic uncertainties and the 2σ precision of the fit).

$$K_{Lin}=15.75/(3.21+RH^{1.77})$$
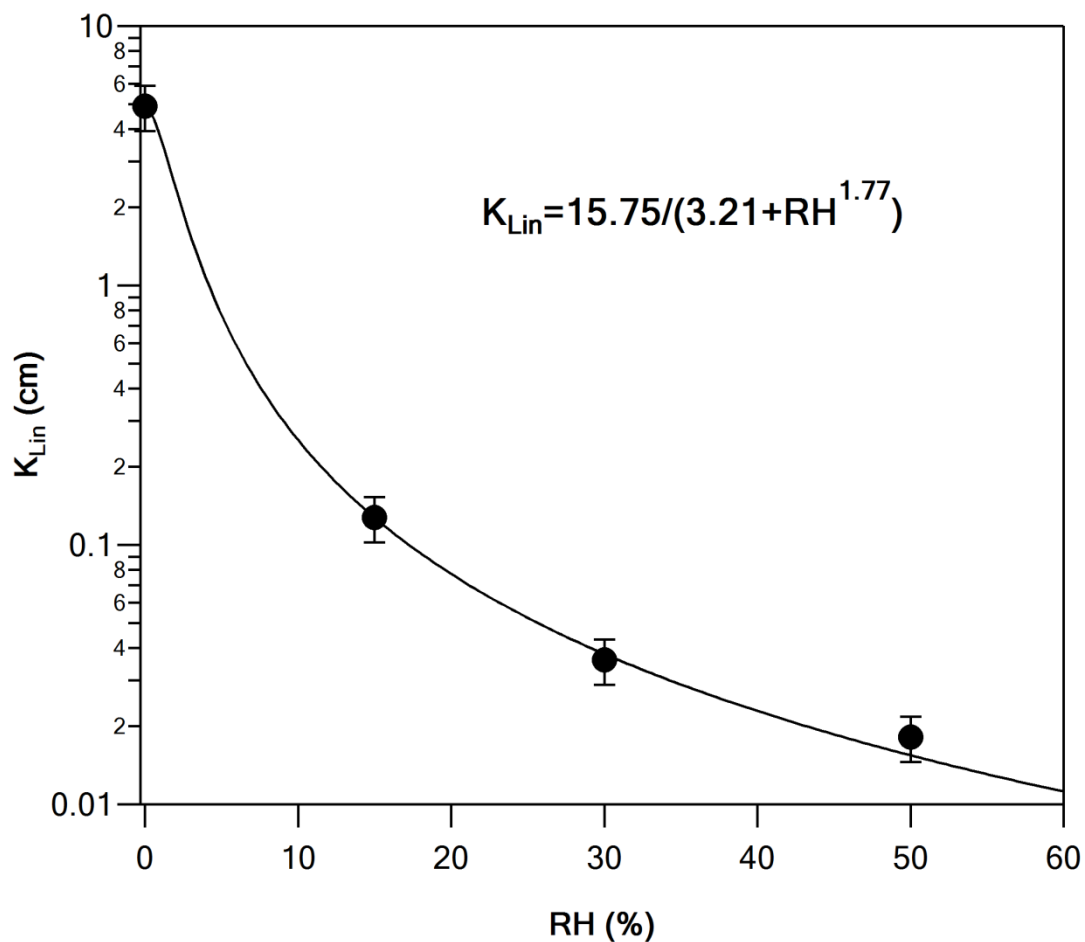
Table BS1. Average concentrations consumed/produced under UV light irradiation for isopropanol and identified products. The yield of the products formed and their estimated additional concentrations under atmospheric conditions are also presented.

Compound	Experimental results		Atmospheric implications	
	Average concentration produced/consumed (ppb)	Formation yields (%)	Additional amounts in the atmosphere (ppt/m^3)[a]	
			Monthly average[b]	Dust storm[c]
IPA	1175	-	-	-
Acetone	5.46	0.46	1.43	38.5
Formaldehyde	1.73	0.15	0.465	12.6
Acetic acid	1.68	0.14	0.43	11.7
Acetaldehyde	1.55	0.13	0.40	10.9

[a] estimated using an average IPA concentration of 45 ppb$_v$ for 12-hour irradiation (average daylight hours) and considering that the yields of the products formed are independent on IPA gas phase concentration.

[b] dust mass loads of 460 μg m^{-3}

[c] dust storm loads of 12,400 μg m^{-3}

Annex C

Isoprene Heterogeneous Uptake and Reactivity on TiO$_2$: A Kinetic and Product Study

MANOLIS N. ROMANIAS, MOHAMAD N. ZEINEDDINE, VERONIQUE RIFFAULT, FREDERIC THEVENET

IMT Lille Douai, Univ. Lille, SAGE–Département Sciences de l'Atmosphère et Génie de l'Environnement, F-59000, Lille, France

ABSTRACT: The heterogeneous interaction of isoprene with TiO$_2$ surfaces was studied under dark and UV light irradiation conditions. The experiments were conducted at room temperature, using zero air as bath gas, in a flow reactor coupled with a SIFT-MS (selected-ion flow-tube mass spectrometer) and a FTIR spectrometer for the gas-phase monitoring of reactants and products. The steady-state uptake coefficient and the yields of the products formed were measured as a function of TiO$_2$ mass (9–120 mg), light intensity (37–112 W m^{-2}), isoprene concentration (36–12000 ppb), and relative humidity (0.01–90% of RH). Under dark and dry conditions, isoprene was efficiently and reversibly adsorbed on TiO$_2$. In contrast, under humid conditions, isoprene uptake was diminished, pointing to competitive adsorption with water molecules. In the presence of UV light irradiation, isoprene reacted on the surface of TiO$_2$. The reactive steady-state uptake coefficient, γ_{ss}, was independent of RH under most ambient relative humidity conditions (>50%). However, γ_{ss} was strongly dependent on isoprene initial concentration according to the empirical expression: $\gamma_{ss} = (2.0 \times 10^{-4}) \times [\text{isoprene}]_0^{-n}$ with $n = 0.35$ and 0.28 for 37 and 112 W m^{-2} irradiation conditions, respectively. In addition to the kinetics, a detailed product study was performed. The gas-phase oxidation products were mostly CO$_2$ (ca. 90% of the carbon mass balance) and a large variety of carbonyl compounds (methyl vinyl ketone, acetone, methacrolein, formaldehyde, acetaldehyde, propanal, traces of butanal, and pentanal), the distribution of which was investigated as a function of mineral oxide mass, isoprene concentration, and RH. Furthermore, the surface-adsorbed products were determined employing off-line HPLC chromatography; their concentrations were inversely dependent on

Correspondence to: Manolis N. Romanias; e-mail: emmanouil.romanias@imt-lille-douai.fr; Frédéric Thévenet; e-mail: frederic.thevenet@imt-lille-douai.fr.

RH and decreased to background levels at RH greater than 30%. Finally, the reaction mechanism and possible implications of isoprene reaction on TiO_2 are briefly discussed. © 2017 Wiley Periodicals, Inc. Int J Chem Kinet 49: 773–788, 2017

INTRODUCTION

Titanium dioxide (TiO_2) is a semiconductor material widely used as a photocatalyst for the UV-induced oxidation of pollutants. Particularly, due to its chemical stability, low cost, and strong oxidizing potential under UV irradiation [1], TiO_2 photocatalysis has been applied to air purification, especially for volatile organic compound (VOC) conversion into CO_2 and H_2O, i.e., mineralization. When TiO_2 absorbs a photon with an energy equal to or higher than the energy band gap of 3.2 eV (corresponding to $\lambda \leq 387$ nm), an electron (e^-) is promoted from the valence band to the conduction band leaving a hole (h^+) behind, which initiates a series of oxidation−reduction reactions between TiO_2 particles and the adsorbed donor and/or acceptor molecules [2,3].

TiO_2 is also a key component of natural atmospheric mineral dust. Mineral dust represents the largest mass emission rate of aerosol particles on a global scale [4,5]. TiO_2 mass mixing ratios in natural dust samples range from 0.1% to 4.5%, depending on their origins [6,7]. Despite its relatively low abundance, TiO_2 may have a significant contribution to the reactivity of atmospheric mineral aerosols due to its photocatalytic properties [8]. Moreover, mineral dust can undergo long-range transportation to remote areas; recently, Yu et al. reported that Saharan dust reaches the Amazon basin and represents the dominant source of phosphorus that fertilizes the Amazon rainforest [9]. Furthermore, field and modeling studies have evidenced that mineral dust can influence the mixing ratios of key atmospheric species such O_3 and HNO_3 [10–12] as well as HO_x [13,14] budget on regional and global scales [15]. However, the impact on the chemistry and the global budgets of organic trace species has not been addressed yet.

VOCs are released into the atmosphere as a result of direct and indirect anthropogenic and biogenic emissions [16]. These compounds are of environmental importance because they significantly influence the oxidation capacity of the troposphere [16]. Isoprene is the most emitted biogenic VOC (BVOC) in the atmosphere and comprises around one third of the total VOC emissions. In forested areas, isoprene concentrations can reach up to 10 ppb, especially during daytime and under relatively dry conditions [17]. The lifetime of isoprene in the atmosphere is comparatively short, in the range of hours. Isoprene lifetime is defined by its gas-phase reactions with OH radicals during the day and with NO_3 radicals at nighttime. Nevertheless, compounds that were not concerned with heterogeneous reactions so far, such as isoprene, could be involved in heterogeneous processes [18–20]. Limbeck et al. observed that isoprene degradation on humic-like particles could account for a major identified fraction of organic aerosols and possibly to oxygenated VOC formation. Furthermore, it is well known in the literature that the uptake of isoprene on soils is a nonnegligible process that is now incorporated in global models [21]. Yet, the heterogeneous oxidation of isoprene on mineral dust particles has never been addressed in both lab and field studies. Since mineral particles are transported over long distances and interact with forested regions, a potential reaction of isoprene with mineral particles, especially during dust events, could influence the budget of oxygenated VOCs (OVOCs) at a regional scale.

Consequently, the aim of the current study is to evaluate whether the heterogeneous degradation of isoprene on mineral particles is a significant atmospheric process and if it can impact the budget of OVOCs in forest regions under intense dust events. Laboratory experiments were performed using TiO_2 as a mineral dust proxy under relevant atmospheric conditions. The isoprene uptake coefficients and the yields of the products formed were determined as a function of several environmental parameters (i.e., TiO_2 mass, isoprene concentration, relative humidity, and light intensity).

EXPERIMENTAL

Materials

Preparation of TiO_2 Samples. TiO_2 powder (Degussa, Aeroxide-P25) was used as purchased. The fractional content of anatase versus rutile has been determined in the literature to be ca. 85:15 [22]. Its specific surface area (SSA) was determined using a custom-built gas sorption analyzer ($52 \pm 6 \, m^2 \, g^{-1}$) and was in excellent agreement with that given by the supplier ($50 \pm 15 \, m^2 \, g^{-1}$). The mass of each sample was weighed before and after the photocatalytic experiments with a high accuracy mass balance (± 0.1 mg), and the difference between the two measurements never exceeded 5% for masses above 30 mg. Nevertheless, at masses below

Annex C
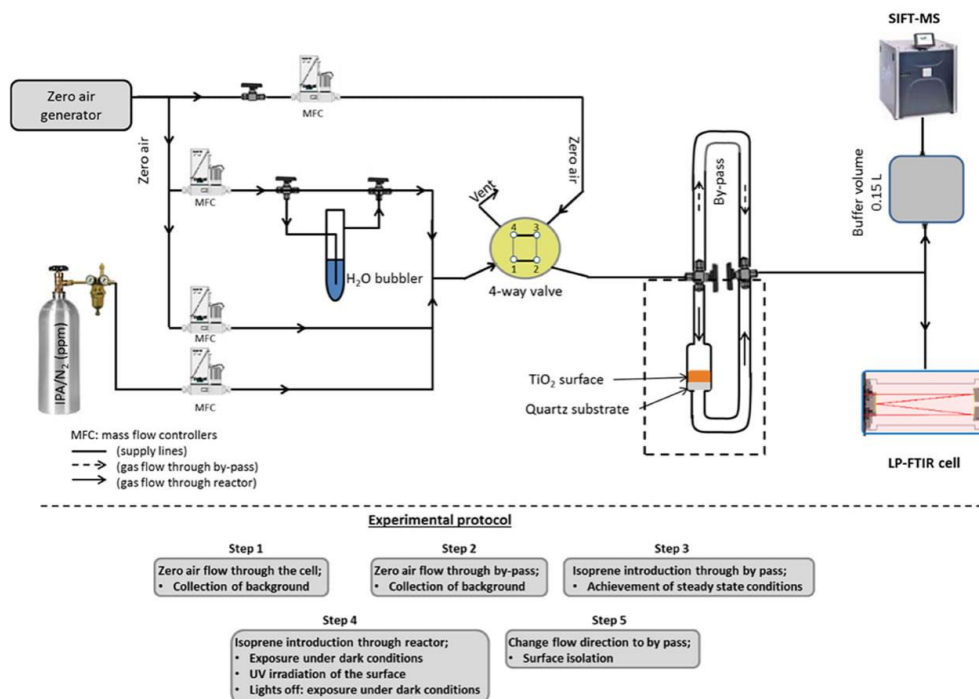
Figure 1 General scheme of the experimental setup used to investigate the heterogeneous interaction of isoprene with TiO$_2$ surface under dark and UV light irradiation conditions. [Color figure can be viewed at wileyonlinelibrary.com]

10 mg the uncertainty was higher and reached 15% in a few experiments.

Gas Preparation. All chemicals used were commercially available with stated purities. Known volumes of liquid isoprene (Sigma Aldrich, Europe; ≥99%) were injected inside an 18-L bulb and further diluted with zero air, to prepare known isoprene/zero air mixtures. A similar procedure was followed for mixtures of acetone (Sigma Aldrich, Europe; ≥99.9%), propanal (Sigma Aldrich, Europe; ≥97%), butanal (Sigma Aldrich, Europe; ≥99.5%), and pentanal (Sigma Aldrich, Europe; 97%) that were identified as gas-phase products of isoprene photooxidation. Regarding the other compounds studied, calibrated gas cylinders of (i) formaldehyde (Praxair, Europe 20 ppm), (ii) VOC mixture (Praxair; acetaldehyde 1.43 ppm, methacrolein – MACR – 1.65 ppm, methyl vinyl ketone – MVK – 1.54 ppm), and (iii) carbon dioxide, CO$_2$ (Linde, Europe; 997 ppm) balanced in nitrogen were used as sources. The flow of VOCs or CO$_2$ in a typical adsorption or calibration experiment was further diluted with zero air to

investigate a wide range of concentrations, which were calculated using the VOC or CO$_2$ mass flow rate, and the dilution factor. Zero air was generated by an air compressor combined with a catalytic zero air generator. The output impurity levels were always lower than the analytical system detection limits: VOCs < 0.1 ppb, CO$_2$ < 10 ppb, CO < 80 ppb, and H$_2$O ~ 2 ppm that corresponds to ca. 0.01% of relative humidity.

Experimental Setup

A detailed schematic of the experimental setup is presented in Fig. 1 and has been described in detail previously [23]. Briefly, it consists of (i) a gas flow generation system with stainless steel and Teflon tubings, (ii) a reactor, and (iii) the analytical devices. The experiments were conducted inside a 15-cm^3 U-shaped flow reactor. A known amount of TiO$_2$ (9–120 mg) was placed on top of a porous quartz wool sample holder with a geometric area of 4.95 cm^2. Calibrated mass flow controllers (Bronkhorst) were used to introduce isoprene and zero air (bath gas) in the reactor at a total

Table I   Summary of the Compounds Detected Employing SIFT-MS and FTIR Spectroscopy[a]

	SIFT-MS			
Compound	Reagent Ion	Ionized Species	Branching Ratio (%)	Mass Peak (m/z)
Isoprene	H_3O^+	$C_5H_8H^+$	100	69
	NO^+	$C_5H_8^+$	100	68
Formaldehyde	H_3O^+	CH_3O^+	100	31
Acetaldehyde	H_3O^+	$C_2H_5O^+$	100	45
	NO^+	$C_2H_3O^+$	100	43
Propanal	NO^+	$C_3H_5O^+$	100	57
Acetone	H_3O^+	$C_3H_7O^+$	100	59
	NO^+	$C_3H_6ONO^+$	100	88
Butanal/butanone	NO^+	$C_4H_7O^+$	100	71
	O_2^+	$C_4H_8O^+$	35	72
2-Methylprop-2-enal (Methacrolein, MACR)	NO^+	$C_4H_5O^+$	62	69
3-Butene-2-one (Methyl vinyl ketone, MVK)	H_3O^+	$C_4H_6O^+$	100	71
	NO^+	$C_4H_6ONO^+$	100	100
	O_2^+	$C_3H_3O^+$	48	55
Pentanal	H_3O^+	$C_5H_{11}O^+$	75	87
	NO^+	$C_5H_9O^+$	100	85
	FTIR			
Compound		Wavenumber		
Carbon dioxide		2300–2400 cm^{-1} (band integration)		

[a]The precursor reagent ions used for the identification of each VOC, the ionized species formed (and their yield of formation), as well as the recorded mass peaks are listed. Regarding CO_2, the IR wavelength range used for its identification is given.

flow rate of 250 sccm. The TiO$_2$ surface can be irradiated by means of three UV-A lamps (UVA, PL-L18W; Philips) contained in an open aluminum box. The irradiance intensity in the reactor was measured using a CCD-Spectrograph (999NN) and was found to be 37 and 112 W m^{-2} when operating 1 and 3 UV lamps, respectively. The intensity of one UV lamp is somewhat higher than the intensity of UV-A radiation reaching the Earth's surface (estimated to vary from 14 to 30 W m^{-2}) [24]. During the irradiation experiments, the reactor was cooled using fans to prevent any temperature increase and maintain room temperature conditions at 295 ± 3 K. Real-time monitoring of the gas phase was achieved employing simultaneously selective ion flow tube mass spectrometry (SIFT-MS, Voice 200; New Zealand) for the detection and quantification of VOCs and Fourier-transform infrared spectroscopy (FTIR, Thermo Scientific Antaris IGS; Europe) for CO$_2$ detection and quantification.

The SIFT-MS is a double quadrupole chemical ionization mass spectrometer. A microwave discharge of wet air is used for the generation of three precursor ions (H$_3$O$^+$, NO$^+$, and O$_2^+$), which are sequentially selected by a first quadrupole. Then, the precursor ions are injected inside a flow tube where they react with the analytes to produce new characteristic ionized species. Subsequently, both the precursor and product ions are analyzed by a second quadrupole mass filter and are

counted for identification and quantification. The major advantage of SIFT-MS is that many VOCs can be recorded simultaneously eliminating the effect of mass peak overlapping. For instance, when two species are identified at the same mass peak (equal m/z ratio) but originate from different precursor ions, the MS peak intensities recorded are free of contribution. Nevertheless, it is worth mentioning that in separate experiments standards of each identified compound were introduced individually to check for any possible contribution of other products to the species mass peaks.

The gas phase was also analyzed employing a transmission FTIR spectrometer coupled to a liquid N$_2$-cooled Mercury cadmium telluride (MCT) detector. The FTIR was used for the identification of compounds that can hardly be detected by SIFT−MS, such as CO and CO$_2$, which are expected as end products of isoprene oxidation with irradiated TiO$_2$ surfaces. IR spectra were collected within the wavenumber range 600−4000 cm^{-1} every 10 s using Result-3 software. Each IR spectrum corresponds to the average of 16 coadded scans with a resolution of 0.5 cm^{-1}. The compounds identified in the current study as well as the mass peaks or wavenumber range used to monitor their real-time gas-phase concentrations are presented in Table I.

Besides the gas phase, the adsorbed phase was investigated in a complementary series of experiments

Annex C
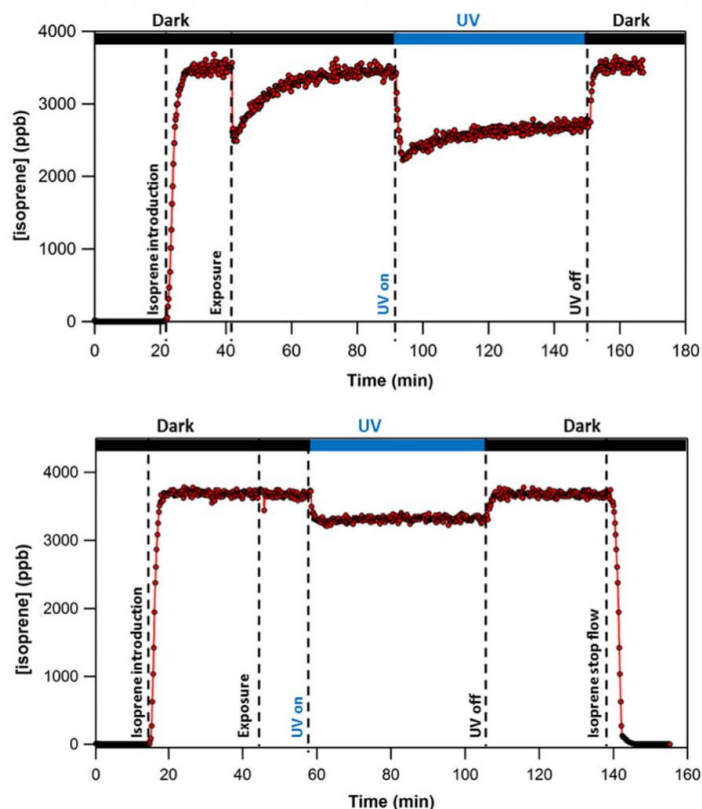
Figure 2 Typical gas-phase concentration profile of isoprene recorded at room temperature (a) under dry and (b) 70% of RH. The NO$^+$ ion was used to monitor the isoprene profile with the SIFT-MS at mass peak 68 (C$_5$H$_8^+$). [Color figure can be viewed at wileyonlinelibrary.com]

employing an off-line HPLC instrument dedicated to the detection of aldehydes and ketones. The surface-adsorbed species were extracted using acetonitrile as a solvent and 2,4-dinitrophenylhydrazine (2,4-DNPH) as the derivatization agent. The HPLC is regularly calibrated using commercially available standards [25].

Experimental Protocol

The experimental protocol is schematically presented in Fig. 1. Initially, zero air is flowed through the reactor to record the background level of isoprene (see also Fig. 2). Subsequently, the gas flow direction is changed to a by-pass line characterized by a volume equal to the reactor (i.e., 15 cm^3) by means of two three-way valves. Then a known amount of isoprene (mixed with zero air and further diluted with the bath gas) is flowed through

the by-pass. When steady-state conditions are reached, the flow is again directed through the reactor, exposing TiO$_2$ surface to isoprene under dark conditions (see also Fig. 2). Finally, the surface is exposed to UV-A irradiation to investigate the photocatalytic oxidation of isoprene, and then the lights are switched off to check for initial concentration levels. At the end of the experiment, the isoprene flow is stopped and the lines are flushed with zero air to record background level concentrations.

Measurement of the Steady-State Reactive Uptake Coefficient

One of the characteristic kinetic parameter that determines the affinity of a gas molecule for interacting with a solid surface is the uptake coefficient, γ [26].

γ expresses the probability of a colliding molecule (gas-kinetic collision with a surface) to be taken up by the surface or react with the surface [26]. The uptake coefficient can be measured at the initial stage of the surface exposure, γ_0, or at a later time, after the surface exposure to gas molecules has led to a steady state, γ_{ss}. For outdoor atmospheric implications, the determination of γ_{ss} is more relevant because atmospheric particles are processed for long periods of time before wet or dry deposition. However, the concept of γ_0 is complementary since it is measured on fresh samples and subsequently expresses the chemical affinity of a gas pollutant for a blank surface.

The uptake coefficient of isoprene on TiO_2 surfaces can be derived from the following expressions [26]:

$$\frac{d\{C_5H_8\}/dt}{V} = k_{het} [C_5H_8] \tag{1}$$

$$k_{het} = \frac{d\{C_5H_8\}/dt}{V[C_5H_8]} = \omega\gamma \tag{2}$$

where

$$\omega = \frac{cA_s}{4V} \tag{3}$$

and finally

$$\gamma = \frac{4(d\{C_5H_8\}/dt)}{cA_s[C_5H_8]} \tag{4}$$

with $\{C_5H_8\}$, the number of isoprene molecules reacted with the mineral oxide surface (molecule); k_{het}, the first-order rate coefficient of the heterogeneous degradation of isoprene measured at the initial stage (for γ_0) or after surface saturation (γ_{ss}) (s^{-1}); V, the volume (cm^3); $[C_5H_8]$, the gas-phase isoprene concentration (molecule cm^{-3}); ω, the collision frequency (s^{-1}); c, the mean molecular speed (cm s^{-1}); and A_s, the surface area available for reaction (cm^2). In the case where not all the surface is accessible for adsorption/reaction the geometric surface area, A_s(geom), of the sample is used for γ calculation [7,27–29]. Consequently, the geometric surface area represents a lower limit to A_s, and an upper limit to γ is obtained [6,26]. Alternatively, in the case where all the surface is accessible for adsorption or participates in the reaction, the use of the total sample surface area (e.g., the N_2-BET specific surface area, A_s (BET)), which is the maximum available surface area, including internal pore volume and bulk surface area of granular material, is used [6,30–33]. Therefore, the use of A_s(BET) provides a lower limit for γ [6,26].

RESULTS AND DISCUSSION

Adsorption of Isoprene on Quartz Substrate (Blank Experiments)

A series of test experiments were carried out to investigate the possible interaction of isoprene with the quartz substrate (i.e., in the absence of TiO_2) under dark and UV irradiation conditions. Various concentrations of isoprene were introduced in the reactor, and the gas phase was monitored by SIFT-MS. No decrease of the isoprene concentration was observed under dark conditions, indicating that isoprene uptake on the quartz substrate is below the detection limit of our technique and not significant. This observation is consistent with our recent study where the uptake of isopropanol on the quartz substrate was also found to be negligible [23]. Even under UV irradiation, no decrease of the isoprene concentration was detected evidencing that (i) isoprene is not photolyzed under UV-A irradiation and (ii) photo-induced reactions do not take place on the quartz substrate.

Adsorption and Conversion of Isoprene on TiO_2

Typical concentration profiles of isoprene at room temperature, under dry and humid conditions (70% of RH) using 60 mg of TiO_2, are presented in Fig. 2. Under dry and dark conditions (Fig. 2a), isoprene is strongly adsorbed on the surface of TiO_2 and adsorption equilibrium is achieved within 1 h of exposure. The integration of the adsorption peak provided the number of molecules adsorbed, N_s, equal to 2.4×10^{12} molecule cm^{-2} (using the SSA of the mineral oxide). On the contrary, under humid conditions, the uptake of isoprene was greatly decreased in the dark (Fig. 2b). The adsorption peak was sharp, and the equilibrium was achieved within a few seconds. The N_s value for the experiment presented in Fig. 2b was found to be 1.1×10^{10} molecule cm^{-2} (using the SSA of the mineral oxide) and thus lower by 2 orders of magnitude compared to dry conditions. Water molecules clearly block the TiO_2 sorptive surface sites.

UV irradiation of the TiO_2 surface caused a rapid consumption of isoprene under both dry and humid conditions (Fig. 2). This could be attributed to the production of radical species on the surface of TiO_2 that react and degrade isoprene [2,31,34]. Nevertheless, under dry conditions, the efficiency of isoprene degradation on the TiO_2 decreases with time and reaches a steady state after around 45 min of irradiation (Fig. 2a), whereas in the presence of water isoprene is steadily and continuously consumed during several hours
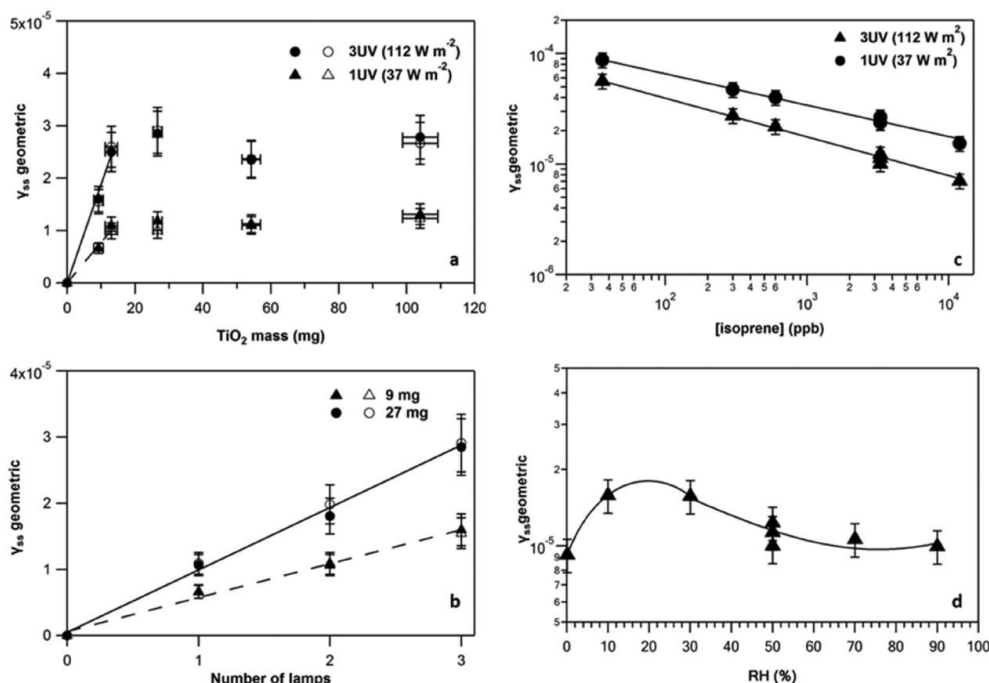
Figure 3 Reactive uptake coefficient as a function of (a) TiO$_2$ mass for two irradiation conditions (37 and 112 W m^{-2}) and 3.5 ppm of isoprene. (b) UV light intensity for two TiO$_2$ amounts (9 and 27 mg) and 3.5 ppm of isoprene. (c) isoprene initial concentration for two irradiation conditions (37 and 112 W m^{-2}) and 60 mg of TiO$_2$. The solid lines correspond to the fitting of experimental results with the empirical expressions: γ_{ss} (37 W m^{-2}) = (2.0 × 10^{-4}) × [isoprene]$^{-0.35}$ and γ_{ss} (112 W m^{-2}) = (2.4 × 10^{-4}) × [isoprene]$^{-0.28}$ where [isoprene] is expressed in ppb. (d) Relative humidity (0.01–90%) for 60 mg of TiO$_2$ and 3.5 ppm of isoprene under 1 UV lamp irradiation (37 W m^{-2}). The solid line is drawn to guide the eye and has no physical meaning. All experiments were carried out at room temperature and 50% of RH (except for (d)). The solid and dashed lines in (a, b) are the corresponding nonweighted least-square fits through the data. Filled and open symbols correspond to data obtained using either H$_3$O$^+$ or NO$^+$ ions to monitor isoprene concentration profiles. The y-axis error bars represent the overall uncertainty on γ (estimated to be ca. 15%). In (a), the x-axis error bars correspond to the uncertainty on mass determination.

(experiments up to 6 h were performed) from the first seconds of surface irradiation. Under dry conditions, adsorbed products may accumulate on the surface of TiO$_2$ reducing its efficiency with time or the reaction could proceed through other pathways (i.e., different reaction mechanisms). This is further discussed in the section RH Dependence.

Kinetic Study and Uptake Coefficient Determinations

TiO$_2$ Mass and Irradiance Dependencies. To determine the fraction of the TiO$_2$ surface involved in the reaction with isoprene, the steady-state uptake coefficient (γ_{SS}) was measured as a function of TiO$_2$ mass

placed into the reactor [30–33,35,36]. In this series of experiments, the geometric surface area of the reactor (i.e., 4.95 cm^2) was used for γ_{ss} calculation [31,36,37]. The results of the measurements carried out at room temperature, 50% RH, and 3.5 ppm of isoprene, irradiating TiO$_2$ with 1 and 3 UV lamps, are shown in Fig. 3a. The uptake increases linearly with the exposed mass until it saturates for masses above 13 mg.

The linear increase of the reaction probability with the mineral oxide mass is generally considered as an indication that the entire surface area of the solid sample is accessible for reaction [6,30–33,36] and that all exposed particles are totally illuminated [2]. This implies the use of TiO$_2$ specific surface area in the calculations of the uptake coefficient [6,33]. On the contrary, when

the reaction probability is independent of the mass exposed (plateau region), then it indicates that not all the surface is accessible for reaction or/and the particles are not totally irradiated in case of a photocatalytic process [2,27,38].

In the present study, the linear regime of the uptake coefficient was observed at relatively low masses of TiO_2, which would cause experimental difficulties, in particular to accurately weigh a few mg of TiO_2, thus leading to higher uncertainties (ca. 15% for mass weighing as noted above). In addition, the initial linear dependence of γ at very low TiO_2 masses could also be due to the incomplete coverage of the quartz substrate by TiO_2 although no uncovered area was visually observed. For all these reasons, uptake experiments were carried out with TiO_2 masses higher than 13 mg (where the uptake is independent of the sample mass), and the uptake coefficient of isoprene was calculated using the geometric surface area and should therefore be considered as an upper limit [26]. Nevertheless, a lower limit of the uptake coefficient could be derived using the BET surface area and the few experimental data obtained at low masses (in the linear regime), leading to uptake coefficients about 100 times lower than those obtained using the geometric surface area.

Figure 3b displays the impact of the UV light intensity on the uptake coefficient. The experiments were carried out at room temperature, 50% RH, and 3.5 ppm of isoprene irradiating 9 and 27 mg of TiO_2 with 37, 74, and 112 W m^{-2}, respectively. In the literature, it has been demonstrated that the photocatalytic efficiency of a semiconductor such as TiO_2 depends on the irradiance intensity of the incident light that activates the material [2]. A linear relationship between γ_{SS} and irradiation intensity was indeed observed, confirming the photoactivated nature of isoprene degradation on TiO_2 surfaces.

Isoprene Concentration Dependence. The dependence of the uptake coefficient on the initial gas-phase concentration of isoprene was studied in the range from 36 ppb to 12 ppm. The experiments were performed at room temperature, 50% RH, irradiating 60 mg of TiO_2 with 37 and 112 W m^{-2}, respectively. The results are displayed in Fig. 3c. Inverse dependences of γ_{SS} on the isoprene concentration could be fitted by an empirical expression that allows to determine the steady-state uptake coefficient at any atmospheric concentration of isoprene:

$$\gamma_{ss} = \left(2.0 \times 10^{-4}\right) \times \left[\text{isoprene}\right]_0^{-n} \qquad (5)$$

with $n = 0.35$ and 0.28 for 37 and 112 W m^{-2} irradiation conditions, respectively, and [isoprene]$_0$ in ppb. Consequently, based on expression (5) the steady-state uptake coefficient can be extracted at any atmospheric concentration level of isoprene. The reported trend may be due to surface saturation by the adsorbed precursor and/or depletion of photoproduced radical species that decrease the reaction probability. This also implies that under steady-state conditions the rate law of isoprene loss (i.e., γ_{ss}) on TiO_2 is not of first order although for initial uptakes, γ_0, no dependence on the initial isoprene concentration was observed. Similar trends have already been reported for the steady-state uptake of other trace gases with mineral oxides or dust surfaces [30,31,39]. The inverse effect of the gas-phase concentration toward reactive uptake has also been addressed in the latest IUPAC evaluation [26].

RH Dependence. The relative humidity dependence of isoprene uptake coefficient was investigated at room temperature, within the RH range 0.01–90%, irradiating 60 mg of TiO_2 with 1 UV lamp (37 W m^{-2}). To isolate the effect of RH on the kinetic measurements, the mass of TiO_2 and inlet isoprene concentration were kept constant at 60 mg and 3.5 ppm, respectively. Results are displayed in Fig. 3d. γ_{ss} was found to increase by a factor of 2 from 0.01 to 25–30% of RH, followed by a slight decrease to reach a plateau value for RH above 50%. This behavior highlights a twofold role of water in the system studied: (i) since H_2O is a well-known source of radicals on UV-irradiated TiO_2 surfaces, the enhancement of isoprene reactive uptake from dry to ca. 25% RH may be related to the increase of the surface concentrations of OH radicals or other reactive species (enhancing isoprene degradation) [2,31]; (ii) adsorbed water may also block some sorptive and reactive sites and induce a decrease in γ_{ss}. This second effect is expected to be noticeable at RH levels above 25%, since the first water monolayer on TiO_2 is observed at ca. 26% of RH [26], and would explain γ_{ss} decrease in the RH range of 25–50%. Finally, for RH above 50%, the blocking effect of water is probably compensated by its role as a source of OH radicals.

Product Study

The photoinduced reaction of isoprene on TiO_2 led to the formation of various gas- and adsorbed-phase products under both dry and humid conditions (Table II). As shown in Fig. 4, MVK, formaldehyde, MACR, acetone, and CO_2 were monitored in the gas phase concurrently with isoprene consumption. Besides, the formation of other aldehydes, such as

Table II List of Compounds Identified as Gas- or Adsorbed-phase Products under Dry and Humid (RH > 30%) Conditions. Quantification Was Performed Only for the Gas-Phase Products

	Gas Phase		Adsorbed Phase	
Compound	Dry	Humid	Dry	Humid
Formaldehyde	$\checkmark$	$\checkmark$	$\checkmark$	X
Acetaldehyde	$\checkmark$	$\checkmark$	$\checkmark$	X
Glyoxal	X	X	$\checkmark$	X
Propanal	L	$\checkmark$	$\checkmark$	X
Acetone	L	$\checkmark$	$\checkmark$	X
Butanal/butanone	L	$\checkmark$	$\checkmark$	X
2-Methylprop-2-enal (methacrolein, MACR)	$\checkmark$	$\checkmark$	$\checkmark$	X
3-Butene-2-one (methyl vinyl ketone, MVK)	L	$\checkmark$	$\checkmark$	X
Pentanal	L	$\checkmark$	$\checkmark$	X
Carbon dioxide	$\checkmark$	$\checkmark$	X	X
3 and 4 methylbenzaldehyde	X	X	$\checkmark$	X
2,5-Dimethylbenzaldehyde	X	X	$\checkmark$	X
Hexanal	X	X	$\checkmark$	X

$\checkmark$: identified.
^{L}: identified with yields lower than 1% (concerns only the gas phase).
^{X}: not identified (below the detection limit).

acetaldehyde, propanal, butanal, and pentanal, was observed at trace levels. The concentrations of the products reached their maximum levels within the first few minutes following surface irradiation, then stayed stable as isoprene was consumed. Switching off the light led to background concentrations of products while isoprene recovered to its initial level. The yields of reaction products formed were calculated as the ratio $\Delta[\text{product}]/\Delta[\text{isoprene}]$ [30,40,41].

Complementary to gas-phase analyses, adsorbed phase extractions combined with HPLC analyses allowed the identification of the above-mentioned products as well as glyoxal and other high molecular weight aldehydes (*m*- and *p*-toluldehydes, dimethyl benzaldehyde, hexanal) (Fig. 5). Their surface concentrations were found to strongly depend on RH and were greatly reduced at RH higher than 10%. Further discussion about RH dependence can be found in the preceding section.

TiO₂ Mass Dependence. The yields of the products formed were investigated for TiO₂ masses between 9 and 120 mg in the reactor. The experiments were performed at 50% RH, 3.5 ppm of isoprene and irradiating the surface with 1 UV lamp (37 W m^{-2}). The yields of formation for MVK, acetone, MACR, formaldehyde, and acetaldehyde, CO₂ and the carbon mass balance are displayed in Figs. 6(a)–6(f). Within the mass range 9–30 mg, the yields of the OVOC products decrease with TiO₂ increasing mass (Fig. 6a–6d), whereas the opposite trend was observed for CO₂, which was the

major degradation product (Fig. 6e). This behavior can be related to the fact that an increase in TiO₂ mass in the reactor induces an increase of available surface radical species (e.g., OH radicals) [2], enhancing the oxidation process advancement and mineralization into CO₂. However, above ca. 30 mg the product yields leveled off. This could be explained by an incomplete activation or access to TiO₂ sites: Either some TiO₂ particles are poorly irradiated due to packing effect, and any further increase of TiO₂ does not promote oxidation reaction advancement; or isoprene is accommodated on the surface of TiO₂ where it reacts directly with the active surface radical species [26]. The latter scenario implies a rapid scavenging of colliding/accommodated isoprene molecules by the photoinduced surface radical species [26]. The reaction pathway proposed is reinforced considering that under our experimental conditions (i.e., 50% RH) isoprene must be poorly adsorbed under dark conditions since water molecules already occupy most of the available adsorption sites. Ultimately, the yield of CO₂ at the plateau was 443 ± 6% corresponding ca. 90% of the carbon mass balance.

Isoprene Concentration Dependence. The yields of the gas-phase products were also examined as a function of the isoprene concentration, at room temperature, 50% RH, and irradiating 60 mg of TiO₂ with 1 UV lamp (37 W m^{-2}). The yields of the major OVOC products and CO₂ as well as the carbon mass balance are displayed in Figs. 6(g)–(6k). The product yields of MVK, acetone, and MACR progressively increased
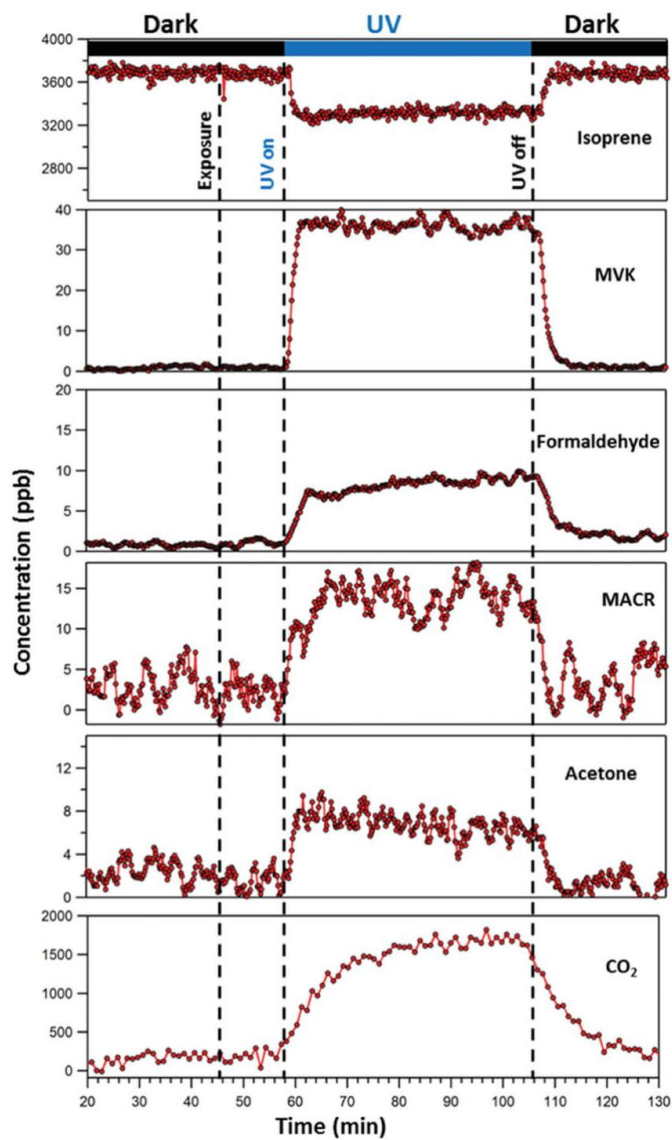
Figure 4 Typical gas-phase concentration profiles of isoprene and those of the major products formed under dark and UV light irradiation conditions. The experiments were carried out at room temperature, 70% of RH in the presence of 3.5 ppm of isoprene irradiating 60 mg of TiO_2 with 1 UV light (37 W m^{-2}). Isoprene and OVOCs were monitored with SIFT-MS and CO_2 with FTIR spectroscopy. [Color figure can be viewed at wileyonlinelibrary.com]

with the initial gas-phase concentration of isoprene, reaching a plateau for isoprene concentrations above 3 ppm. This upper limit could be attributed to com-

petitive reactions at the surface, in particular between isoprene and the products, for the radicals formed on the surface of TiO_2. As the isoprene concentration

Annex C
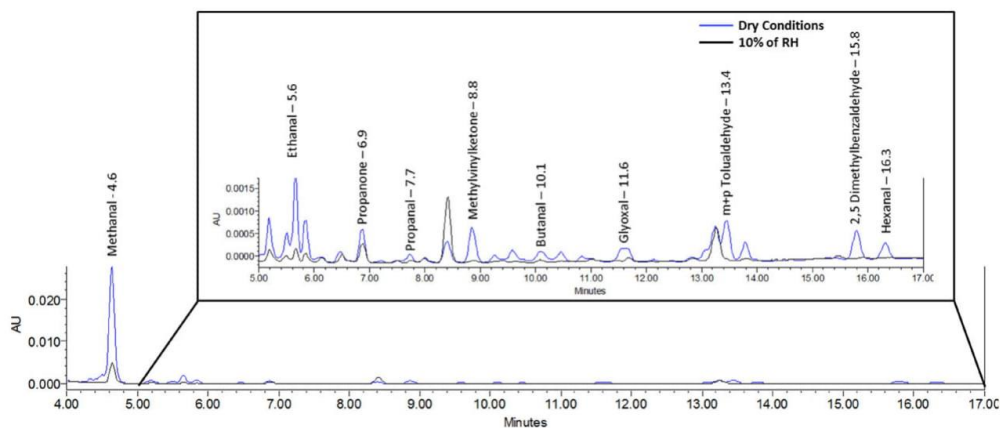
Figure 5 HPLC chromatograms obtained by extraction of surface products formed after 1 h of UV irradiation (37 W m^{-2}) of ~60 mg of TiO₂ exposed to 3.5 ppm of isoprene under dry and 10% of RH. The compounds identified and their elution times are noted in the graph. At higher RH, the surface concentrations of products were below the detection limits. For clarity, the chromatograph has been focused for retention times between 5 and 17 min. [Color figure can be viewed at wileyonlinelibrary.com]

increases, the surface radicals are predominantly consumed by isoprene leading to an increase of the product that reaches saturation at 3 ppm of isoprene.

Regarding the other products formed, the yields of formaldehyde and acetaldehyde (ca. 2.5%) were stable over the entire concentration range. Propanal ($\leq 1.5\%$), butanal ($<1.0\%$), and pentanal ($<1.0\%$) were detected only for isoprene concentrations above 600 ppb, due to their low yields and therefore no concentration dependence could be inferred. CO₂ was found to be the major degradation product of isoprene within the entire concentration range. The CO₂ formation yield was found to be $445 \pm 10\%$ (Fig. 6j) comprising ca. 90% of the carbon mass balance, implying the complete oxidation of reactant and products. Finally, the carbon mass balance closure was $101 \pm 6\%$ when considering the sum of the product contributions, indicating that all major products were identified.

RH Dependence. The effect of relative humidity on the distribution of reaction products and carbon mass balance is shown in Fig. 6l–p. The experiments were carried out at room temperature, 3.5 ppm of isoprene, irradiating 60 mg of TiO₂ with 1 UV lamp (37 W m^{-2}). Similar to the kinetic measurements, aiming to isolate the effect of RH to the kinetic measurements in this series of experiments the mass of TiO₂ and inlet isoprene concentration was kept constant at 60 mg and 3.5 ppm The gas-phase product yields of MVK, acetone, MACR, and CO₂ were found to increase up to

50% RH, and then level off at higher RH. The values in the saturation range (50%–90% RH) were: 10.2, 1.8, 3.6, and 450 % for MVK, acetone, MACR, and CO₂, respectively. On the contrary, the formation yields of formaldehyde (2.6%) and acetaldehyde (2.4%) were independent of RH. Regarding the other aldehydes, their yields were below 1.5% and it was not possible to detect any relative humidity dependence. Considering the distribution of the recorded gas-phase products, an imbalance of around 50% and 25% was observed in the carbon mass under dry conditions and 10% RH, respectively. However, above 30% RH, the distribution of the gas-phase products leads to complete carbon mass balance determination.

In an attempt to ascribe the observed carbon mass trends, we performed a series of experiments analyzing the adsorbed-phase products with offline HPLC, in which TiO₂ was exposed to 3.5 ppm of isoprene under 37 W m^{-2} light irradiation conditions for approximately 1 h. Thereafter, the surface products were extracted using acetonitrile as a solvent and 2,4-DNPH as a derivatization agent. The recorded HPLC chromatograms are shown in Fig. 5. The majority of the surface-adsorbed products had already been observed in the gas phase. Additionally, glyoxal and higher molecular weight aldehydes were also identified (Table II and Fig. 5). Interestingly, concentrations of adsorbed-phase products decreased by two orders of magnitude from dry conditions to 10% RH, whereas for RH above 30% no surface products were detected.

242

Consequently, it is shown that the carbon mass balance discrepancy at low RH could be attributed to the presence of surface-adsorbed compounds. This also explains the gas-phase concentration trends observed for MVK, acetone, MACR, and CO_2, related to the twofold impact of water onto the reaction system. On the one hand, water acts as a source of radicals on TiO_2 surface, oxidizing the adsorbed-phase products thus diminishing their concentrations and increasing the formation of CO_2. On the other hand, water competes with the products for the same adsorption sites, decreasing their adsorbed-phase concentrations.

In addition, it is important to note that since the gas- and adsorbed-phase products were identical under relatively dry ($\leq 10\%$) and higher RH conditions ($\geq 30\%$), it is highly probable that the reaction mechanism of isoprene degradation is similar over the entire experimental RH range. Note that even under dry conditions (0.01% RH), the absolute concentration of water is ca. 2 ppm, probably enough to preserve the catalytic mechanism. Under our experimental conditions, the major oxidation product of isoprene was CO_2, that is to say, the final oxidation product of organic compounds in the atmosphere. Minor compounds identified (MVK, MACR, formaldehyde, glyoxal in the adsorbed phase,
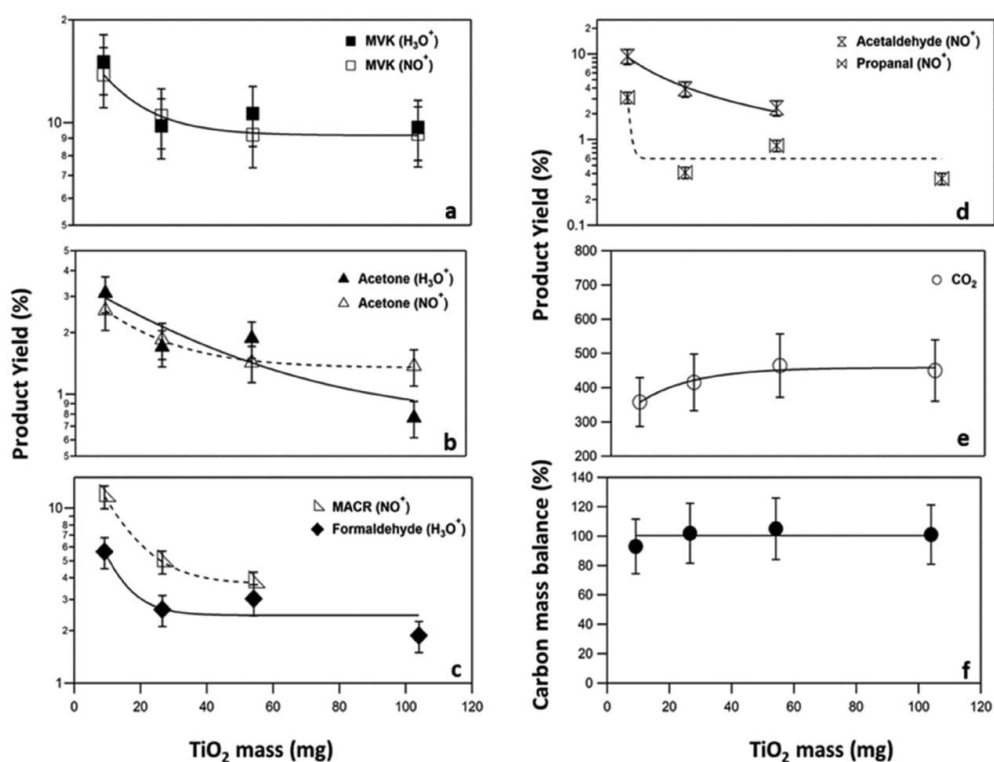
Figure 6 Variation of the gas-phase product yields and carbon mass balance as a function of (a–f) TiO_2 mass for 3.5 ppm of isoprene, (g–k) isoprene initial concentration for 60 mg of TiO_2, (l–p) relative humidity (0.01–90%) for 60 mg of TiO_2 and 3.5 ppm of isoprene. All experiments were carried out at room temperature and 50% of RH (except for (l-p)), irradiating TiO_2 with 1 UV lamp (37 W m^{-2}). The concentrations of isoprene and the OVOCs formed were monitored using SIFT-MS (see also Table I), whereas CO_2 was recorded employing FTIR spectroscopy. The error bars represent the overall uncertainty on product determinations. The curves of all product yields and CO_2 concentrations were drawn to guide the eye and have no physical meaning. The solid straight line in CO_2 plot (j) corresponds to the average value (445 ± 10). The carbon mass balance was calculated considering the gas-phase products. The average value is shown as the solid line fitting the experimental points in (f) and (k), found to be $100 \pm 6\%$ and 101 ± 6, respectively.
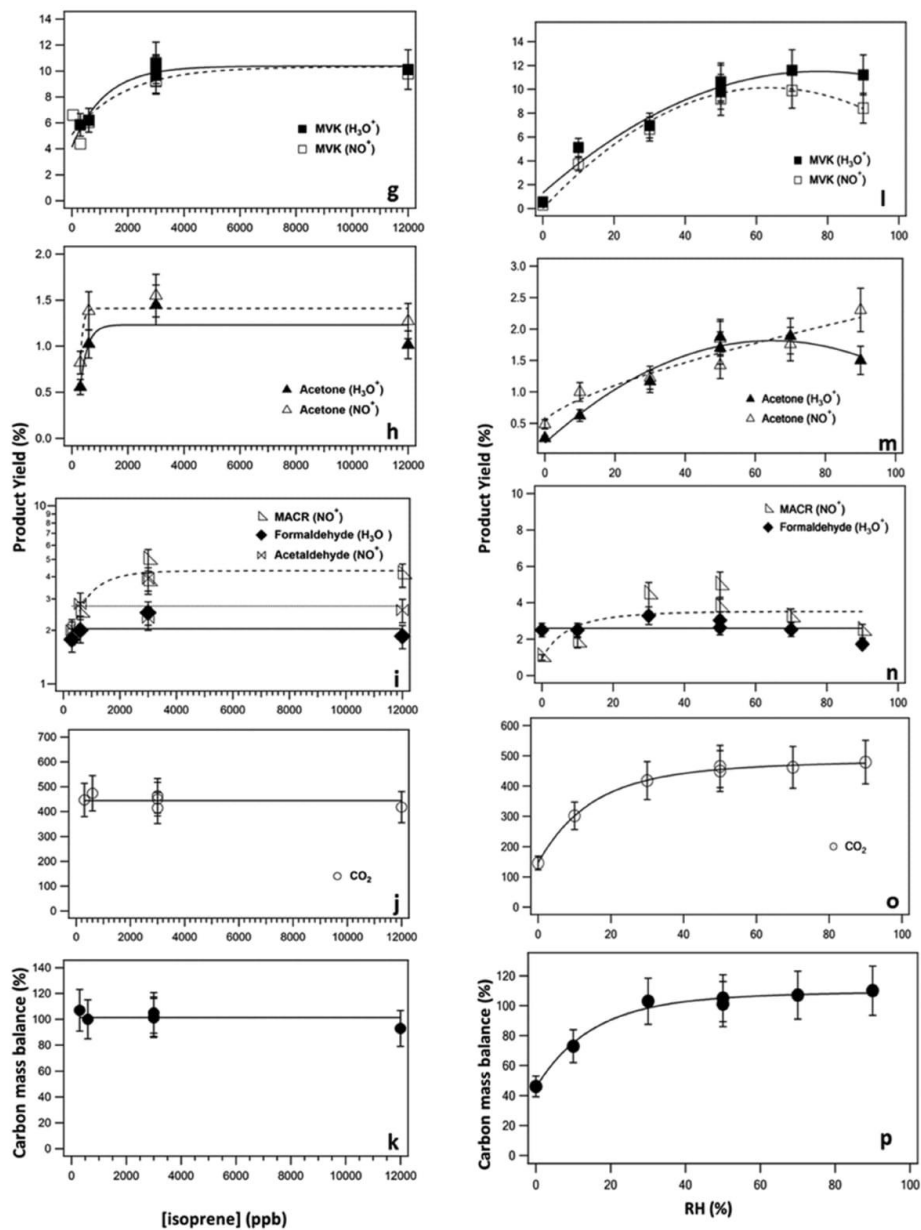
Figure 6   Continue

etc.) are similar to those observed for the gas-phase degradation of isoprene from OH radicals, suggesting a similar reaction mechanism [42]. However, the formation of several other aldehydes, such as acetaldehyde, propanal, pentanal, could indicate alternative oxidation pathways of isoprene on the surface of TiO$_2$. Although the observed product yield of aldehydes was low, these pathways may not be negligible, since the aldehydes

244

Annex C

formed could be rapidly oxidized on the surface of TiO_2 and account for a significant fraction of the CO_2 formed.

Reaction Mechanism

The observed photodegradation of isoprene is attributed to the formation of radical species on the surface of TiO_2. TiO_2 is a well-known semiconducting material that absorbs UV-A radiation (≤ 387 nm), initiating a sequence of redox reactions leading to VOC degradation [43,44]. Based on our experimental observations and literature data on VOC oxidation over TiO_2 or mineral particles, the following mechanistic scheme can be proposed:

$$TiO_2 + h\nu \rightarrow h^+ + e^- \quad (6)$$

$$h^+ + H_2O_{ads} \rightarrow HO^\bullet + H^+ \quad (7)$$

$$e^- + O_2 \rightarrow O_2^{\bullet-} \quad (8)$$

$$O_2^{\bullet-} + H_2O_{ads} \rightarrow HO_2^\bullet + HO^- \quad (9)$$

$$2HO_2^\bullet \rightarrow H_2O_2 + O_2 \quad (10)$$

$$H_2O_2 + O_2^{\bullet-} \rightarrow HO^- + HO^\bullet + O_2 \quad (11)$$

$$HO^- + h^+ \rightarrow HO^\bullet \quad (12)$$
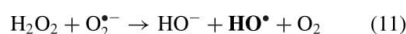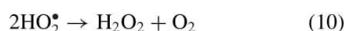
$$\mathbf{HO^\bullet + CH_2{=}C(CH_3)\,CH{=}CH_2}$$
$$\rightarrow \text{oxidation products (MVK, MACR, RCHO)}$$
$$\rightarrow\rightarrow CO_2 + H_2O \quad (13)$$

In particular, the UV irradiation of the surface activates TiO_2 that produce holes, h^+, and electrons e^-, on the conduction and valence bands, respectively (6). The holes react with adsorbed water, H_2O_{ads}, producing the highly reactive $HO^\bullet$ radicals through Reaction (7). Electrons could also react with O_2 producing superoxide radicals, $O_2^{\bullet-}$ (Reaction (8)) that could lead to $HO^\bullet$ radicals formation (Reactions (9)–(12)). Finally, the $HO^\bullet$ radicals react with isoprene (interfacial reaction) to produce a wide variety of degradation products that finally lead to CO_2 and H_2O formation that were identified via FTIR spectroscopy (Reaction (13)).

CONCLUSIONS AND ATMOSPHERIC IMPLICATIONS

This study investigated the heterogeneous oxidation of isoprene over TiO_2 surfaces under simulated atmospheric conditions for the first time. The uptake coefficient and the product yields were measured as a function of the mineral oxide mass, isoprene concentration, and RH. The steady-state geometric uptake coefficient was determined following the gas-phase concentration profile of isoprene and was parameterized using an empirical expression. Besides, the impact of water on the kinetics was evaluated in the RH range 0.01–90%, and the estimated reactive uptake coefficient of isoprene under ambient atmospheric conditions ($T = 293$ K, 50% RH, light intensity corresponding to clear sky conditions) is $\gamma_{ss} (37\,W\,m^{-2}) = 1.1 \times 10^{-4}$ and $\gamma_{ss} (37\,W\,m^{-2}) = 1.1 \times 10^{-6}$ considering the geometric and specific surface areas of TiO_2, respectively.

Furthermore, the temporal profiles of the products were investigated as a function of the same experimental parameters: TiO_2 mass, isoprene concentrations, and RH, to better understand their influence on the product yields. In all cases, the dominant oxidation product was CO_2 representing around 90% of the carbon mass balance, which clearly indicates that under our experimental conditions isoprene is completely oxidized on the surface of the TiO_2. Besides CO_2, several OVOC gas-phase products were identified and their contributions were found to be highly dependent on experimental conditions (yields in brackets given for ambient RH conditions): methyl vinyl ketone (10%), acetone (1.7%), methacrolein (4.3%), formaldehyde (2.8%), acetaldehyde (2.4%), propanal ($\leq 1.5\%$), and traces of butanal and pentanal ($<1.0\%$).

Regarding the atmospheric implications, the heterogeneous oxidation of isoprene appears to be negligible compared to its gas-phase degradation by the dominant tropospheric oxidants (O_3, OH, and NO_3 radicals). In particular, the atmospheric lifetime, τ_{het}, of isoprene due to the heterogeneous loss onto an aerosol surface can be calculated as $\tau_{het} = 4/(\gamma \omega A)$, where γ is the uptake coefficient, ω is the mean molecular velocity (cm s^{-1}), and A is the aerosol surface area density (cm^2 cm^{-3}), estimated to be around 1.5 $\times 10^{-6}$ cm^2 cm^{-3} representative of TiO_2 in a dust plume [10]. Considering an average concentration of 5 ppb of isoprene in forested regions [17,45], and using the concentration dependence of the uptake coefficient reported in the current study for 37 W m^{-2} and 50% RH, the extrapolated steady-state uptake coefficient is $\gamma_{ss} (37\,W\,m^{-2}) = 1.1 \times 10^{-4}$. Thus, the calculated lifetime due to heterogeneous loss of isoprene on TiO_2 is

Annex C

estimated to be around 9.2 days whereas it is ca. 1.4 h due to its gas-phase degradation with OH radicals. Even under extreme conditions, such as dust storms, the estimated lifetime is expected to be more than 1 day. Considering the results of the current study and those reported in the literature [23,46], it appears that the heterogeneous removal of volatile hydrocarbons is of minor importance compared with their gas-phase degradation. Consequently, we suggest that laboratory kinetic studies investigating heterogeneous phenomena should predominantly focus on high molecular weight organic compounds, for instance, semivolatile oxygenated molecules or multifunctional organics with a hydrophilic nature, which are expected to be characterized by higher uptake coefficient values onto metal oxide based minerals.

BIBLIOGRAPHY

1. Fujishima, A.; Zhang, X. C R Chim 2006, 9, 750–760.
2. Herrmann, J.-M. Top Catal 2005, 34, 49–65.
3. Linsebigler, A. L.; Lu, G.; Yates, J. T. Chem Rev 1995, 95, 735–758.
4. Satheesh, S. K.; Krishna Moorthy, K. Atmos Environ 2005, 39, 2089–2110.
5. Andreae, M. O.; Rosenfeld, D. Earth Sci Rev 2008, 89, 13–41.
6. Usher, C. R.; Michel, A. E.; Grassian, V. H. Chem Rev 2003, 103, 4883–4940.
7. Karagulian, F.; Santschi, C.; Rossi, M. J. Atmos Chem Phys 2006, 6, 1373–1388.
8. Chen, H.; Nanayakkara, C. E.; Grassian, V. H. Chem Rev 2012, 112, 5919–5948.
9. Yu, H.; Chin, M.; Yuan, T.; Bian, H.; Remer, L. A.; Prospero, J. M.; Omar, A.; Winker, D.; Yang, Y.; Zhang, Y.; Zhang, Z.; Zhao, C. Geophys Res Lett 2015, 42, 1984–1991.
10. de Reus, M.; Dentener, F.; Thomas, A.; Borrmann, S.; Ström, J.; Lelieveld, J. J Geophys Res: Atmos 2000, 105, 15263–15275.
11. Hanke, M.; Umann, B.; Uecker, J.; Arnold, F.; Bunz, H. Atmos Chem Phys 2003, 3, 417–436.
12. Bonasoni, P.; Cristofanelli, P.; Calzolari, F.; Bonafè, U.; Evangelisti, F.; Stohl, A.; Zauli Sajani, S.; van Dingenen, R.; Colombo, T.; Balkanski, Y. Atmos Chem Phys 2004, 4, 1201–1215.
13. Zhang, Y.; Sunwoo, Y.; Kotamarthi, V.; Carmichael, G. R. J Appl Meteorol 1994, 33, 813–824.
14. Zhang, Y.; Carmichael, G. R. J Appl Meteorol 1999, 38, 353–366.
15. Bian, H.; Zender, C. S. J Geophys Res: Atmos 2003, 108, n/a–n/a.
16. Williams, J.; Koppmann, R.; Koppmann, R., Volatile Organic Compounds in the Atmosphere, Chapter 1, Blackwell, UK, Ed.; 2007, pp. 1–19.
17. Kalogridis, C.; Gros, V.; Sarda-Esteve, R.; Langford, B.; Loubet, B.; Bonsang, B.; Bonnaire, N.; Nemitz, E.; Genard, A. C.; Boissard, C.; Fernandez, C.; Ormeño, E.; Baisnée, D.; Reiter, I.; Lathière, J. Atmos Chem Phys 2014, 14, 10085–10102.
18. Limbeck, A.; Kulmala, M.; Puxbaum, H. Geophys Res Lett 2003, 30, n/a–n/a.
19. Karl, T.; Potosnak, M.; Guenther, A.; Clark, D.; Walker, J.; Herrick, J. D.; Geron, C. J Geophys Res: Atmos 2004, 109, n/a–n/a.
20. Jang, M.; Kamens, R. M. Environ Sci Technol 2001, 35, 4758–4766.
21. Cleveland, C. C.; Yavitt, J. B. Geophys Res Lett 1997, 24, 2379–2382.
22. Ohtani, B.; Prieto-Mahaney, O. O.; Li, D.; Abe, R. J Photochem Photobiol A: Chem 2010, 216, 179–182.
23. Romanías, M. N.; Ourrad, H.; Thévenet, F.; Riffault, V. J Phys Chem A 2016, 120, 1197–1212.
24. Nunez, M.; Forgan, B.; Roy, C. Int J Biometeorol 1994, 38, 5–17.
25. Detournay, A.; Sauvage, S.; Riffault, V.; Wroblewski, A.; Locoge, N. Atmos Environ 2013, 77, 272–282.
26. Crowley, J. N.; Ammann, M.; Cox, R. A.; Hynes, R. G.; Jenkin, M. E.; Mellouki, A.; Rossi, M. J.; Troe, J.; Wallington, T. J. Atmos Chem Phys 2010, 10, 9059–9223.
27. Bedjanian, Y.; Romanias, M. N.; El Zein, A. Atmos Chem Phys 2013, 13, 6461–6471.
28. Fenter, F. F.; Caloz, F.; Rossi, M. J. Atmos Environ 1995, 29, 3365–3372.
29. Karagulian, F.; Rossi, M. J. Phys Chem Chem Phys 2005, 7, 3150–3162.
30. El Zein, A.; Romanias, M. N.; Bedjanian, Y. Environ Sci Technol 2013, 47, 6325–6331.
31. Romanias, M. N.; El Zein, A.; Bedjanian, Y. J Phys Chem A 2012, 116, 8191–8200.
32. Romanias, M. N.; El Zein, A.; Bedjanian, Y. Atmos Environ 2013, 77, 1–8.
33. Underwood, G. M.; Li, P.; Usher, C. R.; Grassian, V. H. J Phys Chem A 2000, 104, 819–829.
34. Chen, H.; Nanayakkara, C. E.; Grassian, V. H. Chem Rev 2012, 112, 5919–5948.
35. El Zein, A.; Bedjanian, Y.; Romanias, M. N. Atmos Environ 2013, 67, 203–210.
36. Underwood, G. M.; Li, P.; Al-Abadleh, H.; Grassian, V. H. J Phys Chem A 2001, 105, 6609–6620.
37. Caloz, F.; Fenter, F. F.; Rossi, M. J. J Phys Chem 1996, 100, 7494–7501.

788   ROMANIAS ET AL.

38. Bedjanian, Y.; Romanias, M. N.; El Zein, A. J Phys Chem A 2013, 117, 393–400.

39. Zein, A. E.; Romanias, M. N.; Bedjanian, Y. J Phys Chem A 2014, 118, 441–448.

40. Romanías, M. N.; Dagaut, P.; Bedjanian, Y.; Andrade-Eiroa, A.; Shahla, R.; Emmanouil, K. S.; Papadimitriou, V. C.; Spyros, A. J Phys Chem A 2015, 119, 2006–2015.

41. Romanias, M. N.; El Zein, A.; Bedjanian, Y. J Photochem Photobiol A 2012, 250, 50–57.

42. Ruppert, L.; Heinz Becker, K. Atmos Environ 2000, 34, 1529–1542.

43. Wang, S.; Ang, H. M.; Tade, M. O. Environ Int 2007, 33, 694–705.

44. Demeestere, K.; Dewulf, J.; Van Langenhove, H. Crit Rev Environ Sci Technol 2007, 37, 489–538.

45. Liu, Y.; Brito, J.; Dorris, M. R.; Rivera-Rios, J. C.; Seco, R.; Bates, K. H.; Artaxo, P.; Duvoisin, S.; Keutsch, F. N.; Kim, S.; Goldstein, A. H.; Guenther, A. B.; Manzi, A. O.; Souza, R. A. F.; Springston, S. R.; Watson, T. B.; McKinney, K. A.; Martin, S. T. Proc Natl Acad Sci 2016, 113, 6125–6130.

46. Shen, X.; Zhao, Y.; Chen, Z.; Huang, D. Atmos Environ 2013, 68, 297–314.

247

Annex D

Figure DS1. Dependence of K_{Lin} on relative humidity at T = 296 K. The error bars represent the overall uncertainty on K_{Lin} determination. The solid line is the fit of the experimentally determined K_{Lin} equilibrium constants based on the equation: $K_{Lin} = a / (b + RH^c)$, where a, b and c are empirical parameters. The fitting is represented by the expression K_{Lin} (296 K) = 0.028 / (0.604 + $RH^{1.54}$).
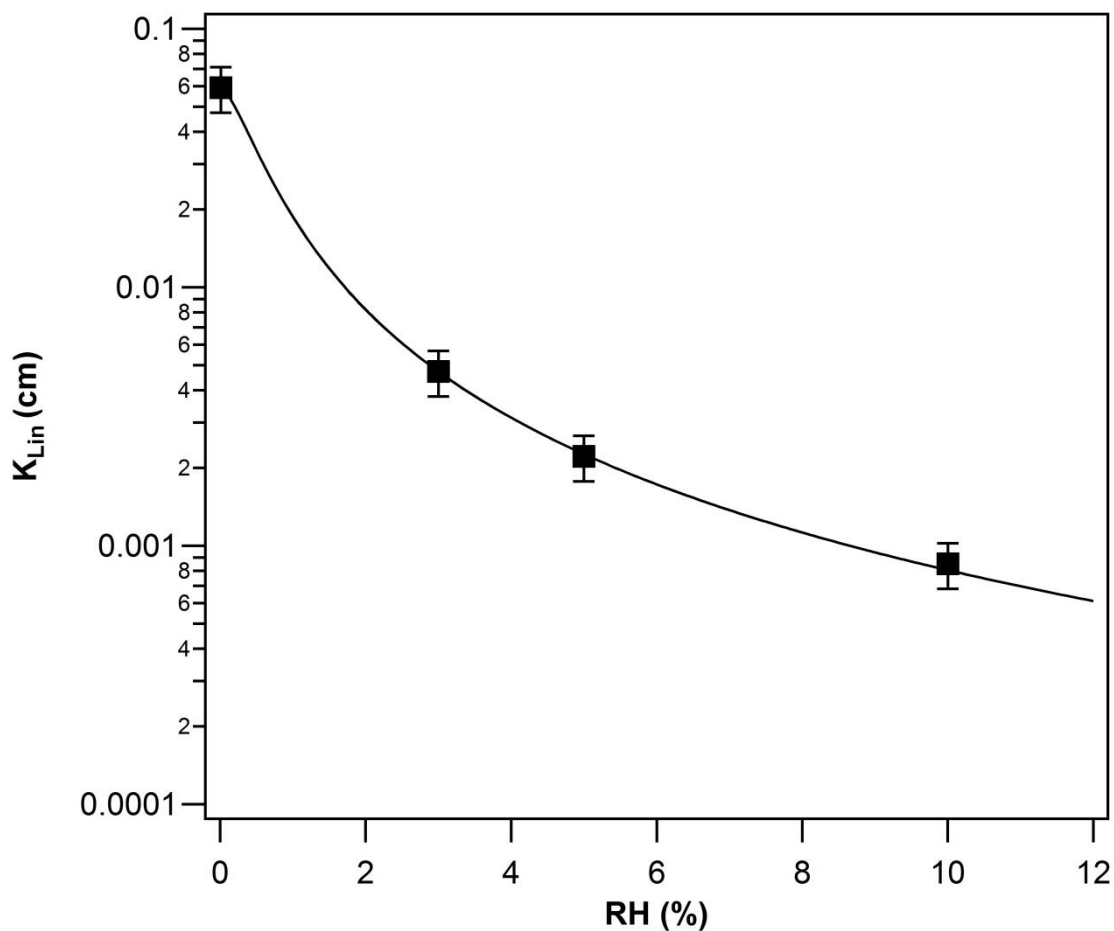
Annex E

Contents lists available at ScienceDirect

Aeolian Research

journal homepage: www.elsevier.com/locate/aeolia

CrossMark

Investigating water adsorption onto natural mineral dust particles: Linking DRIFTS experiments and BET theory

Nitesh Joshi, Manolis N. Romanias *, Veronique Riffault, Frederic Thevenet *

IMT Lille Douai, Univ. Lille, SAGE - Département Sciences de l'Atmosphère et Génie de l'Environnement, F-59000 Lille, France

ABSTRACT

The adsorption of water molecules on natural mineral dusts was investigated employing *in situ* Diffuse Reflectance Infrared Fourier Transform Spectroscopy (DRIFTS). The natural dust samples originated from North and West Africa, Saudi Arabia and Gobi desert regions. Furthermore, the hygroscopicity of commercially available Arizona Test Dusts (ATDs) and Icelandic volcanic ash were examined. N_2 sorption measurements, X-ray fluorescence and diffraction (XRF and XRD), as well as Inductively Coupled Plasma Mass Spectrometry (ICP-MS) analyses were performed to determine the physicochemical properties of the particles. The water adsorption experiments were conducted in an optical cell, at room temperature under the relative humidity (RH) range of 1.9–95%. Results were simulated using a modified three-parameter Brunauer-Emmett-Teller (BET) equation. Water monolayer (ML) was formed in the RH range of 15–25%, while additional water layers were formed at higher RH. Besides, the standard adsorption enthalpies of water onto natural mineral dust samples were determined. A thorough comparison of two commercially available ATD samples indicated that size distribution and/or porosity should play a key role in particle hygroscopicity. Regarding the natural mineral particles, Ca/Si ratios, and to a lesser extent Al/Si, Na/Si, Mg/Si ratios, were found to impact the minimum RH level required for water monolayer formation. These results suggest that the hygroscopic properties of investigated African dusts are quite similar over the whole investigated RH range. Furthermore, one of the major conclusions is that under most atmospheric relative humidity conditions, natural mineral samples are always covered with at least one layer of adsorbed water.

© 2017 Elsevier B.V. All rights reserved.

1. Introduction

According to recent estimates around 1600 Tg of mineral dust particles are released to the atmosphere each year, representing a dominant source of particulate matter at the global scale (Andreae and Rosenfeld, 2008; Satheesh and Krishna Moorthy, 2005). Although the primary sources are arid regions (e.g. Saharan and Gobi deserts contributing around 70% of global emissions), mineral dust undergoes long-range transportation to remote areas, (Engelstaedter et al., 2006; Moosmüller et al., 2009; Prospero, 1999).

The mineralogy of dust particles is complex, and depends on the primary emission sources (Fitzgerald et al., 2015; Formenti et al., 2014; Formenti et al., 2011; Journet et al., 2014; Klaver et al., 2011; Perlwitz et al., 2015a,b; Romanías et al., 2016; Scheuvens

et al., 2013; Usher et al., 2003). The most abundant elements of mineral dusts and soils are Silicon (Si) and Aluminum (Al) (Goudie and Middleton, 2006; Scheuvens et al., 2013). Si is mainly present in SiO_2 phases (e.g. quartz, cristobalite) and in various aluminosilicate minerals. Aluminosilicates such as feldspars and clays (illite, kaolinite, montmorillonite, etc.) are the major aluminum-bearing minerals (Goudie and Middleton, 2001; Goudie and Middleton, 2006; Scheuvens et al., 2013). Al is also present in the crystalline polymorphic phases of aluminum oxide Al_2O_3. Calcium (Ca) is also an important component of mineral dust mainly present in the form of calcite, calcium oxide, aragonite, and dolomite. Besides the abovementioned elements, others such as K (K-feldspar, white mica, illite), Na (albite feldspar, smectite clay minerals), Fe (in mineral oxides e.g. hematite, magnetite), Ti (TiO_2 phases of anatase and rutile) and Mg (dolomite) are also found in mineral dust and source sediments (Formenti et al., 2014; Journet et al., 2014; Klaver et al., 2011; Lafon et al., 2006; Scheuvens et al., 2011; Scheuvens et al., 2013). However, it should be noted that the mineralogical composition of airborne dust particles also depends on the size fractionation during emission and

* Corresponding authors at: IMT Lille Douai, Univ. Lille, SAGE - Département Sciences de l'Atmosphère et Génie de l'Environnement, F-59000 Lille, France.

E-mail addresses: emmanouil.romanias@mines-douai.fr (M.N. Romanias), frederic.thevenet@mines-douai.fr (F. Thevenet).

transport (Journet et al., 2014). To be able to account for these fractionation effects, Journet et al. specified the chemical composition of the finer textural classes of soils in the silt (2–63 μm) and clay (<2 μm) fractions. The silt fraction contains primary minerals such as quartz, feldspars and mica while other minerals such as clays and iron oxides are mostly found in the clay fraction (Journet et al., 2014).

The impact of mineral dust on Earth's atmosphere is manifold. Dust particles have a direct effect on the radiative budget of the atmosphere, by absorbing and scattering the radiation, thus they impact Earth's climate. On the other hand, due to their potential to interact with water vapor in the atmosphere, mineral dust can act as cloud condensation nuclei (CCN) and ice nuclei (IN) leading to cloud formation (Creamean et al., 2013; DeMott et al., 2003; Gaston et al., 2017; Levin et al., 2005; Pratt et al., 2009; Twohy et al., 2009; Wurzler et al., 2000). Beside their climatic impact, dust surfaces may provide the seedbed for specific interactions with trace gas molecules, and therefore, could play a key role in the transformation and environmental fate of many atmospheric species (Bedjanian et al., 2013; Zein et al., 2014). Recent laboratory studies have shown that the water content of aerosols significantly influences the adsorption properties, as well as the heterogeneous reactivity and photoreactivity of mineral particles (Bedjanian et al., 2013; Crowley et al., 2010; Zein et al., 2014). Water on the surface of mineral aerosol can (i) enhance its photo-reactivity by acting as a source of surface radical species (Romanias et al., 2012; Zein et al., 2014) or (ii) inhibit its adsorption efficiency by occupying the available adsorption sites (Bedjanian et al., 2013; El Zein et al., 2013; Romanias et al., 2016). Therefore, it is particularly important to determine the hygroscopic properties of natural mineral aerosols (Cwiertny et al., 2008; Dentener et al., 1996; Krueger et al., 2003; Tang et al., 2012; Usher et al., 2003). In parallel, it is challenging from a fundamental point of view to study the water sorption capacity of natural samples that originate from different regions of the planet and investigate to what extent the sample origin, and hence its physicochemical properties, could influence the corresponding hygroscopic properties.

H_2O adsorption on solid surfaces is a key issue in material and atmospheric sciences since it may impact any heterogeneous process or surface analysis of the considered material (Adolphs and Setzer, 1998). Numerous models and approximations have been developed in the literature to simulate H_2O adsorption isotherms (Adolphs, 2007; Khalfaoui et al., 2003; Ryu et al., 2001; Tang et al., 2016; van Erp and Martens, 2011). One of the primary studies that attempted to investigate the hygroscopic properties of atmospherically relevant surfaces was published by Goodman et al. (Goodman et al., 2001). The authors used transmission FTIR spectroscopy to probe H_2O adsorption on individual metal oxide surfaces (i.e. SiO_2, α-Al_2O_3, TiO_2, γ-Fe_2O_3, CaO, and MgO). The obtained results were well-simulated using a three-parameter BET equation that allowed determining the number of water layers formed as a function of relative humidity (RH). Furthermore, Gustafsson et al. have investigated the adsorption of H_2O on commercially available nominal 0–3 μm Arizona Test Dust (ATD) and on calcite ($CaCO_3$) (Gustafsson et al., 2005). Thermogravimetric analysis (TGA) experiments were performed to obtain quantitative results about H_2O monolayer (ML) formation. Based on TGA measurements the first H_2O ML on ATD is formed at ca. ∼12% RH while up to four H_2O layers are formed at ca. ∼80% RH. The hygroscopic behavior of individual metal oxides (i.e. SiO_2, Al_2O_3, Fe_2O_3, MgO and TiO_2) has also been studied employing DRIFT spectroscopy (Ma et al., 2010). H_2O adsorption followed a type-III isotherm model and the authors suggested that the three-parameter BET equation was compliant with water adsorption fitting. In addition, Hatch et al. investigated the water adsorption on clay minerals as a function of relative humidity (Hatch et al., 2012), in which the clas-

sical two-parameter BET and the Freundlich adsorption models were applied to simulate their experimental observations. One of their major conclusions was that the Freundlich adsorption model was found to fit the data well over the entire RH range, while the classical two-parameter BET failed to adequately describe adsorption phenomena at high RH conditions. The failure of classical BET equation to simulate the adsorption of water was also reported previously by Goodman et al. (Goodman et al., 2001) and other literature studies (see also Section 2.6).

Beside the abovementioned publications, several studies have been performed on natural mineral dust particles and mineral proxies probing the water uptake properties under sub- and super-saturated conditions employing either infrared spectroscopy (Hatch et al., 2014; Navea et al., 2010; Schuttlefield et al., 2007), or humidified tandem differential mobility analysis (HTDMA) (Garimella et al., 2014; Gustafsson et al., 2005; Herich et al., 2009; Koehler et al., 2009; Koehler et al., 2007; Kumar et al., 2009; Kumar et al., 2011; Sullivan et al., 2010; Vlasenko et al., 2005; Yamashita et al., 2011). A very recent review (Tang et al., 2016) summarizes the efforts carried out over the past 15 years to determine the water sorption properties of individual mineral oxides, natural and commercially-available samples.

The aim of the current study is to determine the hygroscopic properties of natural mineral dust samples originating from different arid regions on Earth. DRIFT spectroscopy was employed for the *in situ* monitoring of the adsorbed water on mineral particles. First, the experimental setup was validated by measuring and cross-checking the water adsorption behavior on pure SiO_2 that has been extensively studied in the literature (Tang et al., 2016). Then, water adsorption measurements were carried out on natural mineral dusts. Experiments were performed at room temperature, atmospheric pressure and within the relative humidity range 1.9–95%.

2. Materials and methods

2.1. Dust samples

Natural mineral dust samples were collected from various regions of the Earth in order to encompass a large diversity of hygroscopic properties (Fig. S1). African samples were collected close to the oases of Nefta (Tunisia) and Bordj (Algeria), and the city of M'Bour (Senegal), corresponding to three different regions of North and West Africa. The objective was to identify a wide range of hygroscopic properties with location points extending from the eastern part of North Africa to the west. Two other natural samples were collected from China (Gobi desert) and Saudi Arabia (Rawdat arid region), respectively. The Saharan and Rawdat dusts were soil samples manually collected with a shovel at around 20 cm depth. On the contrary Gobi dust was an aeolian sample. The hygroscopic properties were studied only for the smallest sieved size fraction of the natural dust samples (<100 μm) that can be suspended in air. In particular, a mechanical dust sifter was used to fractionate (just by weak hand-shaking) the natural mineral samples into different classes. Then, the finest fraction collected (<100 μm) was used for the experiments. Nevertheless, it should be acknowledged that sieved soil samples could have different physicochemical properties than those naturally resuspended. Besides, two commercially available ATD samples (Powder Technology Inc.) were also included. The ATD samples correspond to different collection dates and possibly to different sieving processes to obtain (a) nominal 0–3 μm ATD collected in October 2010, and (b) ISO 12103–1, A1 ultrafine ATD (3–22 μm, where ∼97% is below 11 μm) collected in June 2013. Finally, an Icelandic volcanic ash topsoil sample (<100 μm) was collected after the

eruption of the Eyjafjallajökull volcano on the 14th of April 2010 (Gislason et al., 2011). All samples were stored under ambient conditions, protected from light in amber bottles.

2.2. Physical and chemical characterization

The chemical characterization of the sample was determined employing X-ray spectroscopy and inductively coupled plasma mass spectrometry (ICP-MS) which have been widely used in the literature to determine the chemical composition of solid samples (Fultz and Howe, 2013; Hill et al., 2009; Jenkins, 1999; Jenkins and Snyder, 1996; Scott, 2016). The X-ray measurements were conducted using around 1 gram of sieved mineral dust and two complementary techniques: (i) X-ray diffraction (XRD; Bruker D2 phaser 2 theta analyzer) and (ii) X-ray fluorescence (XRF; Bruker AXS explorer S4 pioneer). Regarding the ICP-MS analysis, a few milligrams of the dust were diluted in an acidic solution (HF/HNO$_3$/HCl) and thermally pretreated at 220 °C before analysis (Alleman et al., 2010). Since the quantity required for ICP-MS analyses is in the milligram range, three sets of measurements were performed for each sample to evaluate the sample heterogeneity and the variation coefficients for the major elements never exceeded 30%.

Nitrogen adsorption measurements were performed with a home-made gas sorption analyzer, which robustness has been previously validated by comparing the specific surface area of commercially-available TiO$_2$ with that given by the supplier (Thevenet et al., 2015). Furthermore, comparing the literature values obtained for A1 ultrafine ATD (Liu et al., 2016; Wu et al., 2015; Yeşilbaş and Boily, 2016), nominal ATD (Zein et al., 2014) and volcanic ash (Gislason et al., 2011) with those of the current study showed good agreement. The specific surface area (SSA) of the collected dust samples was determined employing the BET method within 0.05 to 0.3 relative pressures, P/P$_0$. At least three adsorption measurements were conducted for each sample, and the obtained results are presented in Table S1.

2.3. Materials

H$_2$O adsorption measurements were conducted using pure N$_2$ (>99.999%, Air Liquide) as carrier gas. The relative humidity was controlled by changing the mixing ratio of dry and humid N$_2$. In particular, the N$_2$ flow was moistened after passing through a H$_2$O bubbler and was further diluted with dry N$_2$ to obtain the desired RH level. The relative humidity was recorded using a temperature and moisture meter (Testo 635-2) (see also Fig. 1). A complementary set of experiments was conducted using zero air (VOCs < 0.1 ppb, CO$_2$ < 10 ppb and CO < 80 ppb, RH < 0.01%) as a

bath gas. Prior to the adsorption experiments, each dust sample was thermally pretreated at 105 °C for at least 4 h and purged with pure N$_2$ or zero dry air to remove any pre-adsorbed species. In addition, the thermal pretreatment protocol was modified in a few experiments to examine whether the heating temperature or the duration of the pretreatment influenced adsorption measurements. No changes were observed to the H$_2$O adsorption isotherms even when the surface was pretreated at 170 °C for several hours.

2.4. Experimental setup

In situ monitoring of the dust surface has been performed in a DRIFT cell (Harrick, Praying Mantis) equipped with zinc selenide (ZnSe) windows and coupled with a Nicolet 6700 FTIR spectrometer (Romanías et al., 2016). A schematic of the experimental setup is given in Fig. 1. The dust sample (ca. 100 mg) is placed in a crucible and inserted in the DRIFT cell. Two ellipsoidal mirrors focus the infrared beam on the sample surface; the diffused radiation collected is monitored by a Mercury Cadmium Telluride (MCT) detector. The temperature of the sample is recorded using a K-type thermocouple placed on top of the sample holder, which is also equipped with a heating resistor and a liquid (water/ethanol) circulation system connected to a thermostat (Huber ministat 230) to limit possible temperature fluctuations during the experiment. DRIFT spectra are recorded using the Omnic software (version 9.2) at 100 scans per spectrum and a spectral resolution of 4 cm^{-1}. The total flow rate inside the DRIFT cell is 100 sccm.

In principle there is no linear relationship between the DRIFT band intensity or area and the surface concentration of adsorbate, since the Beer-Lambert law is not applicable. However, applying the Kubelka-Munk function to the recorded DRIFT spectra creates a linear relationship between adsorbate concentration and reflected radiation (Armaroli et al., 2004; Ma et al., 2010). This has also been validated in a recent study from our group where the adsorption of limonene and toluene was studied on natural Saharan samples (Romanías et al., 2016).

2.5. Experimental protocol

In a typical experiment, after thermal pretreatment the sample is allowed to cool down to 295 K and the background DRIFT spectrum is collected under dry N$_2$ flow. Subsequently, the humid flow of N$_2$ with the targeted level of RH is driven through the reactor and sequential DRIFT spectra are recorded to monitor H$_2$O adsorption as a function of time. Several hours are required before achieving equilibrium conditions, denoted by the stability of the characteristic infrared absorption bands of water. Specifically, we consider that water adsorption reaches an equilibrium when the
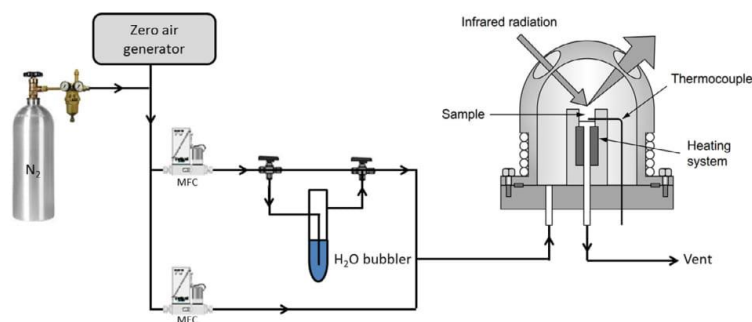

Fig. 1. Schematic of the experimental setup. MFC: Mass Flow Controllers (used to supply the optical cell with a known mixing ratio of dry and humid N$_2$).

DRIFT spectrum is constant (within 5% experimental uncertainty that corresponds to the precision of the recorded spectrum) for at least 45 min. The recorded spectra under equilibrium conditions are averaged to obtain the final spectrum for a given relative humidity that is going to be used for further calculations (see also Fig. 2). Thereafter, the RH level in the optical cell is increased and the protocol is repeated.

2.6. Data fitting methods

Several adsorption theories have been developed and used in the literature (Brunauer, Emmet and Teller – BET (Brunauer et al., 1938), Langmuir (Langmuir, 1918), Freundlich, Dubinin and Radushkevich, etc.) which deliver information either on the adsorbate monolayer formation or the specific surface area (Tang et al., 2016). Among adsorption theories, the BET isotherm is widely used to describe multilayer sorption phenomena. Furthermore, BET analysis is fundamental for the measurement of specific surface area in material characterization and is widely applied. The BET equation linearizes the curved part of the isotherm that occurs near the monolayer completion:

$$\frac{1}{V_{ads}[(P_0/P) - 1]} = \frac{c-1}{V_{mono}c}\left(\frac{P}{P_0}\right) + \frac{1}{V_{mono}c} \tag{1}$$

where V_{ads} (cm^3) is the volume of gas adsorbed at equilibrium partial pressure P (Pascal), V_{mono} (cm^3) is the volume of gas necessary

Fig. 2. DRIFT spectra of water adsorption on a) SiO$_2$, b) ultrafine ATD and c) 0–3 μm nominal ATD as a function of relative humidity at 22 °C. Each spectrum is the average of several spectra recorded under equilibrium conditions. Water adsorption reaches an equilibrium when the DRIFT spectrum is constant (within 5% experimental uncertainty that corresponds to the precision of the recorded spectrum) for at least 45 min.

to cover the surface of the adsorbent with a complete monolayer, P_0 is the saturation vapor pressure of the adsorbing gas (Pascal) at that temperature and c (dimensionless) is a temperature-dependent constant given by Eq. (2):

$$c = \exp\left(\frac{\Delta H_1^0 - \Delta H_2^0}{RT}\right) \tag{2}$$

where ΔH_1^0 and ΔH_2^0 are the standard enthalpies of adsorption of the first and subsequent layers (kJ mol^{-1}), respectively, R the gas constant (J K^{-1} mol^{-1}), and T the temperature (K). The BET equation is generally applied in the relative pressure range 0.05–0.3 but it has been evidenced that the isotherm is able to simulate experimental results up to a relative pressure of 0.6 (van Erp and Martens, 2011). Nevertheless, above that threshold and due to capillary condensation the model fails to simulate sorption data (Adolphs and Setzer, 1998; Do, 1998; Khalfaoui et al., 2003). Similarly, at lower relative pressures and due to physical phenomena (e.g. pores of molecular width, crevices between particles, lateral interactions, defects, etc.), BET assumptions are inadequate and may not satisfyingly fit experimental data (Adolphs and Setzer, 1998; van Erp and Martens, 2011). To overcome these issues, complex mathematical methods, mainly based on weighted fitting and beyond the scope of the current study, have been developed to improve the accuracy of the model (van Erp and Martens, 2011).

To simulate water adsorption on individual mineral oxides, Goodman et al. (Goodman et al., 2001) have proposed a modified three-parameter BET equation (Eq. (3)) that limits the number of layers of the sorbed gas at high RH values, and thus able to fit experimental results over the entire RH range:

$$V_{ads} = \left[\frac{V_{mono}c\left(\frac{P}{P_0}\right)}{1 - \left(\frac{P}{P_0}\right)}\right]\left[\frac{1 - (n+1)\left(\frac{P}{P_0}\right)^n + n\left(\frac{P}{P_0}\right)^{n+1}}{1 + (c-1)\left(\frac{P}{P_0}\right) - c\left(\frac{P}{P_0}\right)^{n+1}}\right] \tag{3}$$

where V_{ads}, V_{mono} and c are defined as in Eqs. (1) and (2), and n is an adjustable parameter corresponding to the maximum number of adsorbed gas layers and related to the pore size and morphological properties of the sample. Joyner et al. (Joyner et al., 1945) proposed a linear form of Eq. (3) to:

$$\frac{\Phi(n,x)}{V_{ads}} = \frac{1}{V_{mono}c} + \frac{\theta(n,x)}{V_{mono}} \tag{4}$$

where:

$$\Phi(n,x) = \frac{x[(1 - x^n) - nx^n(1 - x)]}{(1 - x)^2} \tag{5}$$

$$\theta(n,x) = \frac{x(1 - x^n)}{1 - x} \tag{6}$$

and

$$x = P/P_0 = RH \tag{7}$$

Plotting the first term of Eq. (4), $\Phi(n,x)/V_{ads}$, versus $\theta(n,x)$ and adjusting parameter n to obtain the best determination coefficient (r^2) of the linear least-square fit of the experimental data points provide the parameters V_{mono} and c from the slope and the intercept (Goodman et al., 2001; Joyner et al., 1945).

Alternatively, the results can be processed in terms of the integrated absorbance of the corresponding water vibration mode (Goodman et al., 2001; Ma et al., 2010). Therefore, V_{ads} was replaced by I_{ads}, the integrated area of the adsorbed H$_2$O stretching band (Kubelka-Munk units) at a given RH, and V_{mono} by I_{mono}, that corresponds to the integrated area for one monolayer formation (Kubelka-Munk units). Consequently, plotting $\Phi(n,x)/I_{ads}$, versus $\theta(n,x)$ provides I_m and c from the slope and the intercept (see also
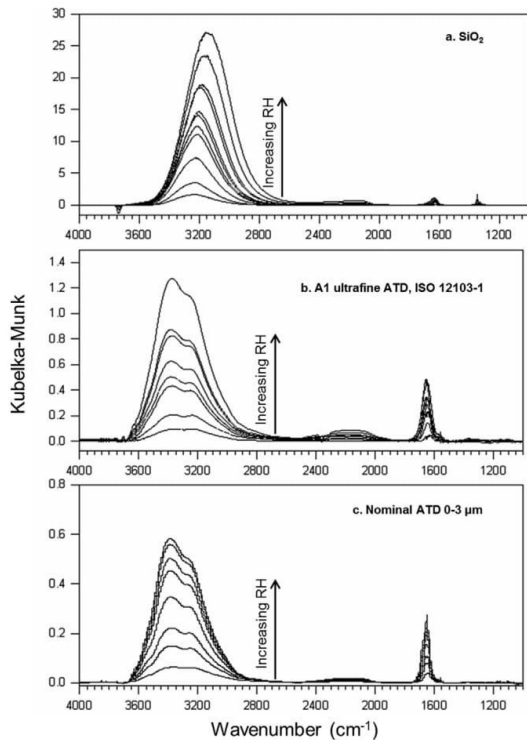
Fig. S3). Finally, the number of water layers at a given RH is derived from the ratio between the integrated areas of adsorbed H_2O stretching mode band at a given RH and for one monolayer formation, I_{ads}/I_{mono} (Goodman et al., 2001; Joyner et al., 1945; Ma et al., 2010).

3. Results and discussion

3.1. Physicochemical characterization

The relative abundances of mineral phases determined for each dust sample employing XRD are presented in Table 1. In addition the elemental bulk composition of the main elements combining X-ray spectroscopy (XRD and XRF) and ICP mass spectrometry are given in Table 2. Note that a detailed list of the concentrations ($\mu g\ g^{-1}$) of 34 major and trace elements determined with ICP-MS is also given in Table S2. For the commercially available samples the A1 ultrafine ATD was chemically characterized and results were found to be in agreement with the chemical composition provided by the supplier (Table 1). As presented in Table 2 both X-ray and ICP-MS analyses provide consistent results (besides the calcite content in Nefta sample) regardless of the technique used and the amount of dust required for each measurement (a few grams for X-ray analysis and a few mg for ICP-MS), which confirms the homogeneity of the samples.

The chemical composition of the dust samples varies significantly between sampling locations. As presented in Table 2 the relative abundance of silicon (Si) in mineral dust originating from Africa was always above 83% of the total elemental composition. In addition, the concentrations of Al, Fe, and Ca, mainly found as Al_2O_3, Fe_2O_3, and $CaCO_3$ mineral oxides respectively, are relatively low in all African samples. On the contrary, the Silica content is significantly lower for the samples originating from the Asian continent ($\leq$61%) while the calcite content was around 20%. In a recently published comprehensive review, hundreds of mineral samples around the world were used to construct a global mineralogy map for clay ($\leq$2 μm) and silt (between 2 and 63 μm) fractions (Journet et al., 2014). The authors observed a wide diversity of chemical compositions from one region to another. In addition, the elemental relative abundance was significantly different between clay and silt fractions. Nevertheless, the relative abundance of elements such as Si, Ca and Fe in the silt fraction (comparable with the <100 μm particles studied in this work) are in good agreement with those observed herein. In particular, the principal element in all samples analyzed was Si, due to the presence of quartz mineral oxide, and feldspars. In addition, the calcite content is relatively high, ca. 15%, in the regions where Rawdat and Gobi samples were collected (see also Fig. S1) and thus in excellent agreement with our measurements.

3.2. Adsorption isotherms

Adsorption isotherms of water were determined on (i) SiO_2, (ii) mineral dust samples and (iii) Icelandic volcanic ash. SiO_2 is used as a reference substrate to validate our measurements since it has been extensively studied in the literature (Tang et al., 2016). Besides, it is one of the most abundant mineral oxides in the coarse silt fraction of dust (Table 1) and always present – although as a minor component (<6%) – in the finer clay fraction (Journet et al., 2014); thus, it is interesting to assess its sorptive behavior. In the same subsection results related to commercially available (and therefore also presented as reference substrates in many studies) ATDs are presented, followed by those obtained with natural mineral dusts and Icelandic volcanic ash. Similarly to previous studies (Goodman et al., 2001; Ma et al., 2010), the proposed 3-parameter BET expression using integrated band intensities has been applied in this work to simulate the water adsorption isotherms on different natural mineral surfaces and thus to determine the number of water layers formed and to retrieve thermodynamical parameters.

3.2.1. Water adsorption on SiO_2 and commercially available Arizona test dusts

Typical DRIFT spectra of water adsorbed on (i) SiO_2, (ii) ultrafine and (iii) nominal 0–3 μm ATDs as a function of RH are presented in Fig. 2. Each spectrum is the average of several spectra recorded under equilibrium conditions as defined in the experimental protocol section. The adsorbed water absorption bands are observed at 1600–1700 cm^{-1}, 2100–2300 cm^{-1}, and 2600–3800 cm^{-1}. They are respectively attributed to water molecule bending, association, and stretching vibration modes (Goodman et al., 2001; Ma et al., 2010). The main broad band of the DRIFT spectra, located between 2600 and 3800 cm^{-1}, is a combination of O–H symmetric stretch around 3420 cm^{-1} and asymmetric stretch around 3240 cm^{-1}. In the literature this broad band has been formerly used to monitor water adsorption onto particles and to evaluate the amount of water adsorbed on the surface (Ma et al., 2010; Wang and Shadman, 2013). Therefore in the current study the integrated area of the O–H stretching region was used to construct the adsorption

Table 1
Relative abundances (in%) of mineral phases identified in each sample employing XRD analyses. For comparison purposes the mineralogical composition of ATD provided by the supplier is also given.

Mineral oxide		M'Bour	Bordj	Nefta	Rawdat	Gobi	ATD ultrafine		Volcanic ash
							This work	Supplier	
SiO_2	Quartz	95.0	88.0	82.0	61.0	55.0	76.0	68–76	3.3
	Cristobalite	–	–	–	–	–	–	–	16.3
$CaCO_3$	Calcite	1.5	1.6	11.0	21.0	17.8	–	–	–
CaO	Calcium oxide	–	–	–	–		2.5	2.0–5.0	6.1
$Ca(HPO_4)\cdot 2H_2O$	Brushite	–	–	5.0	–	–	–	–	–
$CaFeSi_2O_6$	Hedenbergite	–	–	–	–	–	–	–	9.2
$NaAlSi_2O_6\cdot H_2O$	Analcime	–	–	–	–	–	–	–	7.7
$NaAlSi_3O_8$	Albite	–	–	–	10.0	10.5	–	–	44.5
Na_2O	Sodium oxide	–	–	–	–		1.9	2.0–4.0	2.0
TiO_2	Rutile/anatase	0.3	0.2	1.5	0.2	1.0	0.3	0.5–1.0	1.0
Al_2O_3	Aluminum oxide	1.2	4.4	0.3	4.4	6.9	8.8	10–15	–
Fe_2O_3	Hematite	0.5	0.6	0.2	–		2.0	2.0–5.0	6.0
Fe_3O_4	Magnetite	–	–	–	1.3	2.6	–	–	–
MnS	Manganese Sulfide	–	1.0	–	–	–	–	–	–
MgO	Magnesium oxide	–	–	–	–	–	0.8	1.0–2.0	2.0
K_2O	Potassium oxide	–	–	–	2.0	–	2.4	2.0–5.0	–
Unaccounted fraction		1.5	4.2	None	0.1	6.2	5.3	–	1.9

Table 2
Bulk compositions (in %) of the principal elements (excluding O, C, H, N) for each sample studied combining X-ray (XRF and XRD) and ICP-MS analyses. For comparison purposes the elemental composition of Icelandic volcanic ash determined in the literature (Gislason et al., 2011) is also presented.

| Element	M'Bour	Bordj	Nefta	Rawdat	Gobi	ATD ultrafine	Volcanic ash							
	X-ray	ICP-MS	X-ray	ICP-MS	X-ray	ICP-MS	X-ray	ICP-MS	X-ray	ICP-MS	X-ray	ICP-MS	X-ray	Gislason et al. (2011)
Si	96.1	94.4	91.3	83.0	83.2	98	65.6	64	61.7	57.6	74.9	74.6	51.7	48.3
Al	1.4	1.8	5.2	5.9	0.3	0.2	6.9	6.5	10	11.0	9.8	9.5	10.4	14.1
Ca	1.3	1.3	1.4	2.8	11.3	1.0	17.4	21	15.1	16.1	3.8	4.4	11.0	7.9
Na	<0.1	0.2	<0.1	0.6	<0.1	0.2	1.8	2.7	1.92	2.5	3.0	2.5	11.6	6.8
Mg	<0.1	0.1	1	0.9	<0.1	<0.1	<0.1	1.4	2.1	2.3	1.0	1.0	2.3	3.4
Ti	0.4	0.7	0.2	0.4	2.0	<0.1	0.2	0.2	1.3	0.8	0.4	0.5	1.1	2.0
K	<0.1	0.1	<0.1	4.2	<0.1	0.1	3.4	1.9	4.0	3.5	4.2	4.0	<0.1	2.5
Fe	0.8	1.3	0.9	1.9	0.3	0.1	1.8	1.2	3.83	5.5	2.9	3.1	11.7	14.1
P	<0.1	N.D[a]	<0.1	N.D	2.7	N.D	<0.1	N.D	<0.1	N.D	<0.1	N.D	<0.1	0.3
Zn	<0.1	<0.1	<0.1	<0.1	<0.1	<0.1	<0.1	<0.1	<0.1	0.2	<0.1	<0.1	<0.1	<0.1
Mn	<0.1	<0.1	<0.1	<0.1	<0.1	<0.1	<0.1	<0.1	<0.1	0.1	<0.1	<0.1	<0.1	<0.1
Ba	<0.1	<0.1	<0.1	<0.1	<0.1	<0.1	<0.1	<0.1	<0.1	<0.1	<0.1	0.1	<0.1	N.D
Sum (%)	~100	~100	~99	~100	~99	~100	~97	~99	~100	~100	~100	~99	~100	~99
Al/Si	0.014	0.019	0.057	0.071	0.004	0.002	0.105	0.102	0.162	0.191	0.13	0.127	0.201	0.292
Ca/Si	0.013	0.014	0.015	0.033	0.140	0.010	0.265	0.328	0.245	0.280	0.051	0.059	0.213	0.164
Na/Si	$\leq$0.001	0.002	$\leq$0.001	0.007	$\leq$0.001	0.002	0.027	0.042	0.031	0.043	0.040	0.033	0.224	0.141
Mg/Si	$\leq$0.001	0.001	0.011	0.011	$\leq$0.001	$\leq$0.001	$\leq$0.001	0.022	0.034	0.040	0.013	0.013	0.044	0.070

[a] N.D: Not determined (not in the list of the 34 elements analyzed with ICP-MS).

isotherm profiles for each dust sample. It should be noted that the absorption of gas-phase water may also contribute to the 2600–3800 cm^{-1} region, hence measurements could have been affected. Nevertheless, Ma et al. (Ma et al., 2010) using an experimental setup identical to that of the current study evidenced that the contribution of gas-phase water absorption to the surface-adsorbed DRIFT spectrum is negligible. A complementary series of water adsorption measurements on SiO_2 and ATDs has been performed using zero air instead of N_2 as a bath gas and the amount of H_2O adsorbed was found to be independent on the bath gas used within the range of experimental uncertainties.

The absolute values of the integrated IR band areas that correspond to water adsorption on SiO_2 and ATDs as a function of RH are shown in Fig. S2. The obtained experimental data are fitted with Eq. (4) by adjusting the value of parameter n to optimize the correlation coefficient of the linear least-square fit and to obtain I_{mono} and the BET constant c (see also Fig. S3). Consequently, the number of water layers adsorbed is derived by dividing I_{ads} by I_{mono}.

The fitting of experimental results showed that in the case of SiO_2 the water monolayer is formed at 24% RH (Fig. 3a and Table 3). This result is in good agreement with values formerly reported by Goodman et al. (22% RH) and Ma et al. (29% RH), respectively (Goodman et al., 2001; Ma et al., 2010). In addition, at higher relative humidity, the results are in good agreement with those reported in the literature within the range of reported uncertainties (Tang et al., 2016). The estimated enthalpy of adsorption of water on SiO_2, ΔH_{ads}, was calculated to be –49.3 kJ mol^{-1}, which agrees with the literature values of Goodman et al., –50.3 kJ mol^{-1}, and Ma et al., –47.95 kJ mol^{-1} (Goodman et al., 2001; Ma et al., 2010).

Regarding ultrafine ATD the first water layer is formed at 24% RH similarly to pure SiO_2. On the contrary, on 0–3 μm nominal ATD the water monolayer is observed at 15% RH (Fig. 3b and c, and Table 3). A comparison between our measurements on 0–3 μm nominal ATD and those reported by Gustafsson et al. (Gustafsson et al., 2005) is also presented in Fig. 3c. It should be noted that Gustafsson et al. provided quantitative measurements on water adsorption employing TGA (thermogravimetric analysis) and qualitative information about the water adsorption trend on the studied sample using DRIFT spectroscopy. For comparison purposes, we used the 3-parameter BET equation to fit their DRIFT measurements. According to TGA experiments, Gustafsson et al.
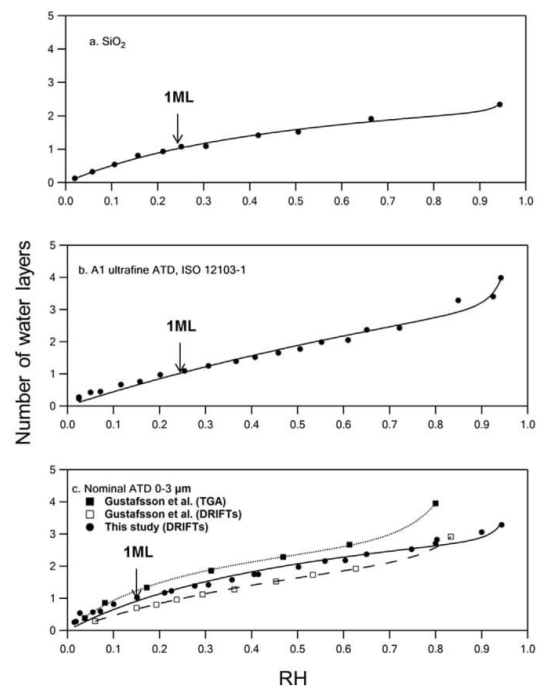
Fig. 3. Water adsorption isotherms on a) SiO_2, b) ultrafine ATD and c) 0–3 μm nominal ATD at 22 °C. The integrated area of the O–H stretching region (i.e. 2600–3800 cm^{-1}) was used to construct the adsorption isotherm profiles for each dust sample. For 0–3 μm nominal ATD, previous work by Gustaffsson et al. (Gustafsson et al., 2005) is also presented. ML: water monolayer formation.

found that the first water layer on 0–3 μm nominal ATD was formed at ca. 12% RH which is in good agreement with the value determined in the current study (15%). On the other hand, the 3-parameter BET fit of their qualitative DRIFT results indicated that the water monolayer is formed at significantly higher relative humidity levels (~26%) (Gustafsson et al., 2005). This could be

Table 3
Adsorption parameters for water uptake on SiO_2, commercially available ATDs, natural mineral dust samples and Icelandic volcanic ash.

Dust	%RH for 1 ML[a]	n	c[b]	ΔH_1^0 (kJ mol^{-1})[c]	P/P₀[d]
SiO_2	24	4	8.8	−49.3	0.020–0.94 (0.999)
ATD ultrafine	24	7	9.7	−49.6	0.025–0.94 (0.994)
ATD nominal 0–3 μm	15	5.8	55.5	−53.8	0.015–0.94 (0.999)
Rawdat	22	10	7.5	−48.9	0.020–0.94 (0.999)
Gobi	25	6	8.4	−49.2	0.024–0.88 (0.998)
M'Bour	18	13	21.8	−51.6	0.021–0.95 (0.996)
Bordj	17	10	37.6	−52.9	0.020–0.94 (0.999)
Nefta	16	21	26.2	−52.0	0.020–0.94 (0.996)
Icelandic volcanic ash	23	9	8.6	−49.3	0.019–0.94 (0.999)

[a] Percent relative humidity corresponding to the full coverage of one monolayer (ML) of adsorbed water.
[b] c is the BET constant as defined in Eq. (2).
[c] Standard enthalpy of adsorption of water.
[d] Range of relative humidity used for linear plots according to Eq. (3). The linear determination coefficient r^2 is given between brackets.

attributed to a premature recording of the DRIFT spectra since it is not clear whether they were recorded after water adsorption reaches equilibrium. Indeed if water adsorption equilibrium is not reached, then water surface coverage is underestimated for a given RH level, meaning that higher RH is required to achieve monolayer formation.

When comparing results on ultrafine and 0–3 μm nominal ATDs, it is difficult to explain the discrepancy between RH thresholds for the first water layer formation and the BET constants (higher by a factor of five for nominal ATD). Considering that the BET constant reflects the strength of the interaction between the gaseous water molecule and the dust substrate, our measurements indicate that water interacts more strongly with nominal ATD. The observed trends could be attributed to differences on either dust physical properties (porosity, particle size distributions) or chemical composition. According to the specifications provided by the supplier both samples have the same chemical composition and thus no impact on hygroscopic properties is expected. On the other hand, the size distribution of ultrafine ATD particles is between 3 and 22 μm with ∼97% lower than 11 μm, whereas nominal ATD contains particles lower than 3 μm in an unspecified proportion. Besides, the specific surface areas of both dust samples differ by a factor of 10, i.e. 6.7 and 67 m^2 g^{-1} for ultrafine and 0–3 μm nominal ATDs, respectively (Table S1). Although BET theory assumes a surface area that can have a considerable amount of uncertainty the observable differences could not be associated either to experimental uncertainties or to failure of the BET theory to describe the adsorption phenomena (Adolphs and Setzer, 1998; Do, 1998; Khalfaoui et al., 2003). Therefore, our measurements suggest that particle size distribution is a key parameter that could influence the water uptake of the samples. This effect has been recently shown using model porous oxide nanoparticles (Wang and Shadman, 2013) of two different grades, i.e. 20 and 80 nm. The authors observed that water was more efficiently adsorbed onto smaller particles, and that the rate of water desorption was significantly slower. They also determined that the activation energy for water adsorption was lower for smaller particles. The trend observed in this study for the water monolayer thresholds for both ATD samples is therefore in agreement with the literature.

3.2.2. Water adsorption on natural mineral samples and Icelandic volcanic ash

Typical DRIFT spectra of water adsorbed on natural mineral dust samples and Icelandic volcanic ash are presented in Fig. S4 and the corresponding water adsorption isotherms in Figs. 4 and 5. The relative humidity corresponding to one monolayer of adsorbed water is given in Table 3 along with those of n, c, and ΔH_1^0. Experiments were conducted over a wide relative humidity range (1.9–95%) and Eq. (3) was used to fit the experimental
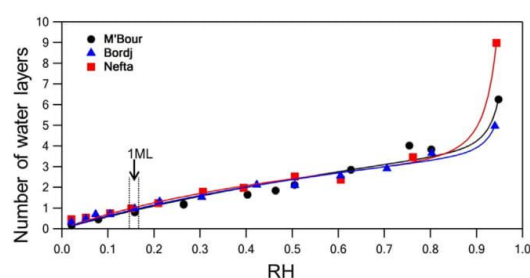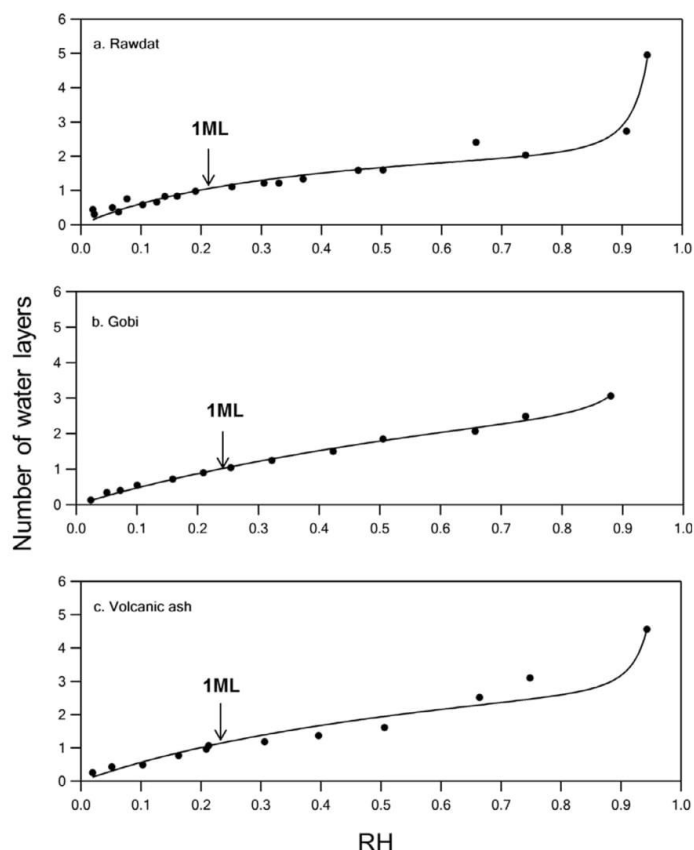

Fig. 4. Water adsorption isotherms on natural mineral dust samples originating from North Africa. The integrated area of the O–H stretching region (i.e. 2600–3800 cm^{-1}) was used to construct the adsorption isotherms profile for each dust sample. ML: water monolayer formation.

results. From a general point of view, results show that: (i) approximately one monolayer is formed between 16 and 25% RH, which is in excellent agreement with the results reported on clay minerals (15–20% RH) (Hatch et al., 2012); (ii) two water layers are present at 60% RH, and (iii) three to nine water layers at 90% RH, depending on the sample.

Comparing the water adsorption isotherms of the three samples originating from Africa, namely Bordj, Nefta and M'Bour (Fig. 4), one could note similar trends over the entire RH range. Specifically, the water monolayer formation is determined to be around 17% and the BET constants are similar for all samples. Besides, their specific surface areas (ca. 15.5 ± 1.0 m^2 g^{-1}) are almost identical (Table S1) and they show a mineral composition dominated (>82%) by quartz (SiO_2). Regarding the particle size distributions, more than 95% of the particles of the African samples ranged between 60 and 100 μm (Romanías et al., 2016). The observed similarities to the hygroscopic behavior is of significant importance considering that the dust samples originate from the Eastern (Nefta) to the Western part (M'Bour) of North Africa which globally contributes up to 62% to the annual mineral dust emissions (Engelstaedter et al., 2006). Roughly, it is possible to consider that Saharan dust particles exhibit similar hygroscopic properties; nevertheless a wider diversity of samples would be required to support that statement.

Concerning the mineral samples that originate from the Asian continent (Fig. 5a, b) the water monolayer is formed at 22% and 25% RH for Rawdat and Gobi, respectively. These values are significantly higher than those observed for African dust samples. Moreover, the BET constants of Rawdat and Gobi dusts are lower than African samples, indicating that the water interaction is weaker on Asian substrates thus increased thresholds of water monolayer

Fig. 5. Water adsorption isotherms on natural mineral dust samples originating from Asia continent (a,b) and Icelandic volcanic ash (c). The integrated area of the O–H stretching region (i.e. 2600–3800 cm^{-1}) was used to construct the adsorption isotherms profile for each dust sample. ML: water monolayer formation.

formation could be expected. Regarding Icelandic volcanic ash (Fig. 5c), the water monolayer is observed at 23% RH, and thus close to the values observed for other natural mineral dusts, in spite of large differences in chemical composition (Table 1).

Attempting to correlate the RH level for water monolayer formation with chemical composition, we compared the elemental ratios of Al/Si, Ca/Si, Na/Si and Mg/Si, for each dust sample (Table 2). We found that the Al/Si, Ca/Si, Na/Si and Mg/Si ratios of the Saharan dusts were lower than 0.08, 0.04, 0.007 and 0.011 respectively (excluding the Ca/Si ratio for Nefta determined using X-ray data). On the contrary, the corresponding ratios for Rawdat and Gobi were greater than 0.1, ca. 0.25, 0.027 and 0.022 respectively (excluding the Mg/Si ratio for Rawdat determined using X-ray data). Consequently our measurements suggest that the significant difference especially observed for the Na/Si and Ca/Si ratio, which are at least by a factor of 5 and 8 higher in Asian samples (considering the average values of X-ray and ICP measurements), could be a determining factor for water monolayer formation. The higher the Na/Si and Ca/Si ratios, the higher the RH level required to form the H$_2$O monolayer. This trend is confirmed with Icelandic volcanic ash, for which the elemental ratios were greater than those determined for Saharan samples (i.e. by a factor of 2.5, 5.2, 31 and 4 for Al/Si, Ca/Si, Na/Si and Mg/Si respectively), and the water monolayer was formed at higher RH level. Nevertheless,

more studies should be conducted using natural mineral samples to support these findings, especially considering that the observed trends for Na/Si and Mg/Si ratios encompass high uncertainty due to the extremely low relative abundances of Na and Mg in most of the natural samples (except volcanic ash).

The effect of chemical composition on water adsorption has already been discussed in the literature. In particular, Schuttlefield et al. have investigated water uptake on clay minerals (i.e. kaolinite, illite and montmorillonite) using ATR-FTIR spectroscopy coupled with Quartz Crystal Microbalance (QCM) (Schuttlefield et al., 2007). They concluded that the water content is higher for clays that can swell and that contain cations with large hydration enthalpies. The trend to the hydration enthalpies of the cations found in their study was: Fe^{3+} > Mg^{2+} > Fe^{2+} > Ca^{2+} > Li$^+$ > Na$^+$ > K$^+$, which explained very well their results but did not consider the hydration enthalpy of Aluminum, although it is the second most abundant element in their samples. For instance, the hydration enthalpy for Al^{3+} is higher than Fe^{3+}, i.e. −4665 and −4430 for Al^{3+} and Fe^{3+} respectively (Smith, 1977), consequently the observed trends could be different (by simply multiplying the relative abundance of the elements by the hydration enthalpy). In our case the hydration enthalpy of cations cannot interpret the experimental observation for water monolayer formation. However, it is important to note that both the physical properties (e.g. size distri-

bution) and chemical composition (mixture of mineral oxides and clays) of the samples used are different than the clay minerals studied by Schuttlefield et al. In addition, we have to acknowledge that the observed trends concern the RH required to form the water monolayer and not the capacity of the sample to adsorb H_2O that could be changed after the formation of several layers of water. In particular, clay minerals have the ability to adsorb significant quantity of water compared to our samples (at least by a factor of 10). Consequently, it is expected that the presence of cations should play a more important role in clays since cations may balance the charge deficiencies created from the multilayer water films formed. However, considering that water predominately interacts with the minerals through hydrogen bonds (i.e. through hydrogen bonding between lone pairs of electrons on the negative ions and the slightly positive hydrogens in water molecules) the presence of ions should play a more significant role in the case of monolayer adsorption.

Finally, using the results of the current study and those reported in the literature (Goodman et al., 2001; Ma et al., 2010), it has been attempted to correlate the BET constant, c, and the adjustable parameter, n, with the relative humidity required to form the water monolayer (% RH for 1 ML). Although the water adsorption measurements were conducted on different dust samples it was observed that the BET constant exponentially decreases with the RH threshold (Fig. 6). Since the BET constant expresses the strength of the interaction between water and the mineral substrate this behavior could be expected. On the contrary, it was not possible to derive any empirical parameterization for the parameter n versus the RH threshold or as a function of the BET constant.

4. Summary and conclusions

In the current study the chemical characterization of six mineral dusts and one Icelandic volcanic ash samples as well as the water adsorption isotherms onto these natural surfaces were investigated. The experiments were performed using a DRIFT cell and results were simulated employing a modified 3-parameter

Fig. 6. Correlation between the BET constant (c) and relative humidity that corresponds to the formation of an adsorbed water monolayer. The results obtained from the current study as well as those reported in the literature by Ma et al. (Ma et al., 2010; Ma et al., 2012)and Goodman et al. (Goodman et al., 2001) are presented. The solid line is the exponential fit through all the data points.

BET equation. Pure SiO_2 and 0–3 μm nominal ATD dust have been used to validate the relevance of the experimental technique and fitting method. The obtained results are in excellent agreement with literature data (Goodman et al., 2001; Gustafsson et al., 2005; Ma et al., 2010). Comparing the commercially available ATDs, significant differences are observed regarding their water adsorption isotherms. The water monolayer on ultrafine and nominal ATDs is respectively formed at 24% and 15% RH. Considering that both samples have similar chemical composition, the observed differences are likely related to the contrasted physical properties of the samples and in particular to the particle size distribution and porosity.

Natural mineral samples originating from Sahara exhibit similar hygroscopic properties over the entire investigated relative humidity range. The water monolayer is formed between 16% and 18% of RH. This is of significant importance since this region of the planet contributes for more than 60% to the global dust emissions. On the contrary, the water monolayer was formed at higher levels of RH for Asian samples and Icelandic volcanic ash indicating that these samples are less hydrophilic. Based on the chemical characterization performed, our results suggest that the Ca/Si ratio could be a crucial factor influencing water adsorption onto mineral particles.

Finally, one of the major conclusions of the current study is that under most ambient relative humidity conditions, natural mineral samples are always covered with at least one layer of adsorbed water. These results are of significant importance since the water uptake may considerably influence (i) the heterogeneous interaction of mineral dust with atmospheric trace gases, (ii) mineral dust lifetime, (iii) hygroscopicity and hence (iv) the particle ability to scatter and absorb solar and terrestrial radiation. In addition, these findings are expected to contribute to the improvement of the predictions of current climate models regarding dust impact on climate, since we managed to correlate the physicochemical properties of the particles with their hygroscopic behavior.

Acknowledgments

Appendix A. Supplementary data

Supplementary data associated with this article can be found, in the online version, at http://dx.doi.org/10.1016/j.aeolia.2017.06.001.

References

Adolphs, J., 2007. Excess Surface Work—A modelless way of getting surface energies and specific surface areas directly from sorption isotherms. Appl. Surf. Sci. 253, 5645–5649.
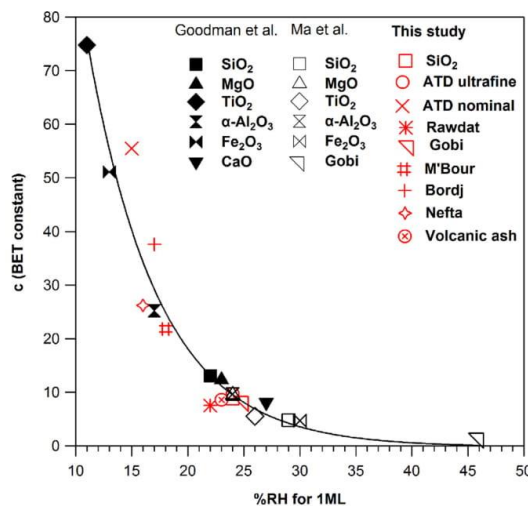
N. Joshi et al. / Aeolian Research 27 (2017) 35–45

Adolphs, J., Setzer, M.J., 1998. Description of gas adsorption isotherms on porous and dispersed systems with the Excess Surface Work model. J. Colloid Interface Sci. 207, 349–354.

Alleman, L.Y., Lamaison, L., Perdrix, E., Robache, A., Galloo, J.-C., 2010. PM10 metal concentrations and source identification using positive matrix factorization and wind sectoring in a French industrial zone. Atmos. Res. 96, 612–625.

Andreae, M.O., Rosenfeld, D., 2008. Aerosol-clouds-precipitation interactions. Part 1. The nature and sources of cloud-active aerosols. Earth Sci. Rev. 89, 13–41.

Armaroli, T., Bécue, T., Gautier, S., 2004. Diffuse reflection infrared spectroscopy (Drifts): application to the in situ analysis of catalysts. Oil Gas Sci. Technol. Rev. 59, 215–237.

Bedjanian, Y., Romanias, M.N., El Zein, A., 2013. Uptake of HO_2 radicals on arizona test dust. Atmos. Chem. Phys. 13, 6461–6471.

Brunauer, S., Emmett, P.H., Teller, E., 1938. Adsorption of gases in multimolecular layers. J. Am. Chem. Soc. 60, 309–319.

Creamean, J.M., Suski, K.J., Rosenfeld, D., Cazorla, A., DeMott, P.J., Sullivan, R.C., White, A.B., Ralph, F.M., Minnis, P., Comstock, J.M., Tomlinson, J.M., Prather, K.A., 2013. Dust and biological aerosols from the Sahara and Asia influence precipitation in the Western U.S. Science. http://dx.doi.org/10.1126/science.1227279.

Crowley, J.N., Ammann, M., Cox, R.A., Hynes, R.G., Jenkin, M.E., Mellouki, A., Rossi, M. J., Troe, J., Wallington, T.J., 2010. Evaluated kinetic and photochemical data for atmospheric chemistry: volume V - Heterogeneous reactions on solid substrates. Atmos. Chem. Phys. 10, 9059–9223.

Cwiertny, D.M., Young, M.A., Grassian, V.H., 2008. Chemistry and photochemistry of mineral dust aerosol. Annu. Rev. Phys. Chem. 59, 27–51.

DeMott, P.J., Sassen, K., Poellot, M.R., Baumgardner, D., Rogers, D.C., Brooks, S.D., Prenni, A.J., Kreidenweis, S.M., 2003. African dust aerosols as atmospheric ice nuclei. Geophys. Res. Lett. 30, 1732. 1710.1029/2003GL017410.

Dentener, F.J., Carmichael, G.R., Zhang, Y., Lelieveld, J., Crutzen, P.J., 1996. Role of mineral aerosol as a reactive surface in the global troposphere. Geophys. Res. Lett-Atmos. 101, 22869–22889.

Do, D.D., 1998. Adsorption analysis: equilibria and kinetics. Imperial College Press.

El Zein, A., Romanias, M.N., Bedjanian, Y., 2013. Kinetics and products of heterogeneous reaction of HONO with Fe_2O_3 and arizona test dust. Environ. Sci. Technol. 47, 6325–6331.

Engelstaedter, S., Tegen, I., Washington, R., 2006. North African dust emissions and transport. Earth Sci. Rev. 79, 73–100.

Fitzgerald, E., Ault, A.P., Zauscher, M.D., Mayol-Bracero, O.L., Prather, K.A., 2015. Comparison of the mixing state of long-range transported Asian and African mineral dust. Atmos. Environ. 115, 19–25.

Formenti, P., Caquineau, S., Desboeufs, K., Klaver, A., Chevaillier, S., Journet, E., Rajot, J.L., 2014. Mapping the physico-chemical properties of mineral dust in western Africa: mineralogical composition. Atmos. Chem. Phys. 14, 10663–10686.

Formenti, P., Schütz, L., Balkanski, Y., Desboeufs, K., Ebert, M., Kandler, K., Petzold, A., Scheuvens, D., Weinbruch, S., Zhang, D., 2011. Recent progress in understanding physical and chemical properties of African and Asian mineral dust. Atmos. Chem. Phys. 11, 8231–8256.

Fultz, B., Howe, J., 2013. Diffraction and the X-Ray Powder Diffractometer, Transmission Electron Microscopy and Diffractometry of Materials. Springer, Berlin Heidelberg, Berlin, Heidelberg, pp. 1–57.

Garimella, S., Huang, Y.W., Seewald, J.S., Cziczo, D.J., 2014. Cloud condensation nucleus activity comparison of dry- and wet-generated mineral dust aerosol: the significance of soluble material. Atmos. Chem. Phys. 14, 6003–6019.

Gaston, C.J., Pratt, K.A., Suski, K.J., May, N.W., Gill, T.E., Prather, K.A., 2017. Laboratory studies of the cloud droplet activation properties and corresponding chemistry of saline playa dust. Environ. Sci. Technol. 51, 1348–1356.

Gislason, S.R., Hassenkam, T., Nedel, S., Bovet, N., Eiriksdottir, E.S., Alfredsson, H.A., Hem, C.P., Balogh, Z.I., Dideriksen, K., Oskarsson, N., Sigfusson, B., Larsen, G., Stipp, S.L.S., 2011. Characterization of Eyjafjallajökull volcanic ash particles and a protocol for rapid risk assessment. Proc. Natl. Acad. Sci. 108, 7307–7312.

Goodman, A.L., Bernard, E.T., Grassian, V.H., 2001. Spectroscopic study of nitric acid and water adsorption on oxide particles: Enhanced nitric acid uptake kinetics in the presence of adsorbed water. J. Phys. Chem. A 105, 6443–6457.

Goudie, A.S., Middleton, N.J., 2001. Saharan dust storms: nature and consequences. Earth-Sci. Rev. 56, 179–204.

Goudie, A.S., Middleton, N.J., 2006. Desert dust in the global system. Springer.

Gustafsson, R.J., Orlov, A., Badger, C.L., Griffiths, P.T., Cox, R.A., Lambert, R.M., 2005. A Comprehensive evaluation of water uptake on atmospherically relevant mineral surfaces: DRIFT spectroscopy, thermogravimetric analysis and aerosol growth measurements. Atmos. Chem. Phys. 5, 3415–3421.

Hatch, C.D., Greenaway, A.L., Christie, M.J., Baltrusaitis, J., 2014. Water adsorption constrained Frenkel–Halsey–Hill adsorption activation theory: montmorillonite and illite. Atmos. Environ. 87, 26–33.

Hatch, C.D., Wiese, J.S., Crame, C.C., Harris, K.J., Kloss, H.G., Baltrusaitis, J., 2012. Water adsorption on clay minerals as a function of relative humidity: application of BET and Freundlich adsorption models. Langmuir 28, 1790–1803.

Herich, H., Tritscher, T., Wiacek, A., Gysel, M., Weingartner, E., Lohmann, U., Baltensperger, U., Cziczo, D.J., 2009. Water uptake of clay and desert dust aerosol particles at sub- and supersaturated water vapor conditions. Phys. Chem. Chem. Phys. 11, 7804–7809.

Hill, S.J., Fisher, A., Liezers, M., 2009. Plasma generation, ion sampling and focusing, Inductively coupled plasma mass spectrometry handbook. Blackwell Publishing Ltd., pp. 1–25.

Jenkins, R., 1999. X-ray Fluorescence Spectrometry. John Wiley & Sons, Inc..

Jenkins, R., Snyder, R.L., 1996. Diffraction theory, Introduction to X-ray powder diffractometry. John Wiley & Sons, Inc., Newyork, pp. 47–95.

Journet, E., Balkanski, Y., Harrison, S.P., 2014. A new data set of soil mineralogy for dust-cycle modeling. Atmos. Chem. Phys. 14, 3801–3816.

Joyner, L.G., Weinberger, E.B., Montgomery, C.W., 1945. Surface area measurements of activated carbons, silica gel and other adsorbents. J. Am. Chem. Soc. 67, 2182–2188.

Khalfaoui, M., Knani, S., Hachicha, M.A., Lamine, A.B., 2003. New theoretical expressions for the five adsorption type isotherms classified by BET based on statistical physics treatment. J. Colloid Interf. Sci. 263, 350–356.

Klaver, A., Formenti, P., Caquineau, S., Chevaillier, S., Ausset, P., Calzolai, G., Osborne, S., Johnson, B., Harrison, M., Dubovik, O., 2011. Physico-chemical and optical properties of Sahelian and Saharan mineral dust: in situ measurements during the GERBILS campaign. Q. J. R. Meteorol. Soc. 137, 1193–1210.

Koehler, K.A., Kreidenweis, S.M., DeMott, P.J., Petters, M.D., Prenni, A.J., Carrico, C.M., 2009. Hygroscopicity and cloud droplet activation of mineral dust aerosol. Geophys. Res. Lett. 36, L08805. 08810.01029/02009GL037348.

Koehler, K.A., Kreidenweis, S.M., DeMott, P.J., Prenni, A.J., Petters, M.D., 2007. Potential impact of Owens (dry) Lake dust on warm and cold cloud formation. J. Geophys. Res.-Atmos. 112, D12210. 12210.11029/12007JD008413.

Krueger, B.J., Grassian, V.H., Laskin, A., Cowin, J.P., 2003. The transformation of solid atmospheric particles into liquid droplets through heterogeneous chemistry: laboratory insights into the processing of calcium containing mineral dust aerosol in the troposphere. Geophys. Res. Lett. 30, 1148. 1110.1029/2002GL016563.

Kumar, P., Nenes, A., Sokolik, I.N., 2009. Importance of adsorption for CCN activity and hygroscopic properties of mineral dust aerosol. Geophys. Res. Lett. 36, L24804. 24810.21029/22009GL040827.

Kumar, P., Sokolik, I.N., Nenes, A., 2011. Cloud condensation nuclei activity and droplet activation kinetics of wet processed regional dust samples and minerals. Atmos. Chem. Phys. 11, 8661–8676.

Lafon, S., Sokolik, I.N., Rajot, J.L., Caquineau, S., Gaudichet, A., 2006. Characterization of iron oxides in mineral dust aerosols: implications for light absorption. Geophys. Res. Lett.-Atmos. 111. n/a-n/a.

Langmuir, I., 1918. The adsorption of gases on plane surfaces of glass, mica and platinum. J. Am. Chem. Soc. 40, 1361–1403.

Levin, Z., Teller, A., Ganor, E., Yin, Y., 2005. On the interactions of mineral dust, sea-salt particles, and clouds: a measurement and modeling study from the Mediterranean Israeli Dust Experiment campaign. Geophys. Res. Lett-Atmos. 110, D20202. 20210.21029/22005JD005810.

Liu, Q., Wang, Y., Wu, L., Jing, B., Tong, S., Wang, W., Ge, M., 2016. Temperature dependence of the heterogeneous uptake of acrylic acid on Arizona test dust. Journal of Environmental Sciences.

Ma, Q., He, H., Liu, Y., 2010. In situ DRIFTS study of hygroscopic behavior of mineral aerosol. J. Environ. Sci. 22, 555–560.

Ma, Q., Liu, Y., Liu, C., Ma, J., He, H., 2012. A case study of Asian dust storm particles: chemical composition, reactivity to SO_2 and hygroscopic properties. J. Environ. Sci. 24, 62–71.

Moosmüller, H., Chakrabarty, R.K., Arnott, W.P., 2009. Aerosol light absorption and its measurement: a review. J. Quant. Spectrosc. Radiat. Transfer 110, 844–878.

Navea, J.G., Chen, H., Huang, M., Carmichael, G.R., Grassian, V.H., 2010. A comparative evaluation of water uptake on several mineral dust sources. Environ. Chem. 7, 162–170.

Perlwitz, J.P., Pérez García-Pando, C., Miller, R.L., 2015a. Predicting the mineral composition of dust aerosols – Part 1: representing key processes. Atmos. Chem. Phys. 15, 11593–11627.

Perlwitz, J.P., Pérez García-Pando, C., Miller, R.L., 2015b. Predicting the mineral composition of dust aerosols – Part 2: model evaluation and identification of key processes with observations. Atmos. Chem. Phys. 15, 11629–11652.

Pratt, K.A., DeMott, P.J., French, J.R., Wang, Z., Westphal, D.L., Heymsfield, A.J., Twohy, C.H., Prenni, A.J., Prather, K.A., 2009. In situ detection of biological particles in cloud ice-crystals. Nat. Geosci. 2, 397–400.

Prospero, J.M., 1999. Long-range transport of mineral dust in the global atmosphere: impact of African dust on the environment of the southeastern United States. Proc. Natl. Acad. Sci. 96, 3396–3403.

Romanias, M.N., El Zein, A., Bedjanian, Y., 2012. Heterogeneous interaction of H_2O_2 with TiO_2 surface under dark and UV light irradiation conditions. J. Phys. Chem. A 116, 8191–8200.

Romanías, M.N., Ourrad, H., Thévenet, F., Riffault, V., 2016. Investigating the heterogeneous interaction of VOCs with natural atmospheric particles: adsorption of limonene and toluene on Saharan mineral dusts. J. Phys. Chem. A 120, 1197–1212.

Romanias, M.N., Zeineddine, M.N., Gaudion, V., Lun, X., Thevenet, F., Riffault, V., 2016. Heterogeneous interaction of isopropanol with natural Gobi dust. Environ. Sci. Technol. 50, 11714–11722.

Ryu, Y.K., Lee, S.J., Kim, J.W., Leef, C.-H., 2001. Adsorption equilibrium and kinetics of H_2O on zeolite 13x. Korean J. Chem. Eng 18, 525–530.

Satheesh, S.K., Krishna Moorthy, K., 2005. Radiative effects of natural aerosols: a review. Atmos. Environ. 39, 2089–2110.

Scheuvens, D., Kandler, K., KÜPper, M., Lieke, K., Zorn, S.R., Ebert, M., SchÜTz, L., Weinbruch, S., 2011. Individual-particle analysis of airborne dust samples collected over Morocco in 2006 during SAMUM 1. Tellus B 63, 512-530.

Scheuvens, D., Schütz, L., Kandler, K., Ebert, M., Weinbruch, S., 2013. Bulk composition of northern African dust and its source sediments — A compilation. Earth Sci. Rev. 116, 170–194.

Schuttlefield, J.D., Cox, D., Grassian, V.H., 2007. An investigation of water uptake on clays minerals using ATR-FTIR spectroscopy coupled with quartz crystal microbalance measurements. J. Geophys. Res.-Atmos. 112.

Scott, S.A., 2016. Basics of X-ray powder diffraction. Massachusetts Institute of Technology.

Smith, D.W., 1977. Ionic hydration enthalpies. J. Chem. Educ. 54, 540.

Sullivan, R.C., Petters, M.D., DeMott, P.J., Kreidenweis, S.M., Wex, H., Niedermeier, D., Hartmann, S., Clauss, T., Stratmann, F., Reitz, P., Schneider, J., Sierau, B., 2010. Irreversible loss of ice nucleation active sites in mineral dust particles caused by sulphuric acid condensation. Atmos. Chem. Phys. 10, 11471–11487.

Tang, M., Cziczo, D.J., Grassian, V.H., 2016. Interactions of water with mineral dust aerosol: water adsorption, hygroscopicity, cloud condensation, and ice nucleation. Chem. Rev. 116, 4205–4259.

Tang, M.J., Thieser, J., Schuster, G., Crowley, J.N., 2012. Kinetics and mechanism of the heterogeneous reaction of N_2O_5 with mineral dust particles. Phys. Chem. Chem. Phys. 14, 8551–8561.

Thevenet, F., Olivier, L., Batault, F., Sivachandiran, L., Locoge, N., 2015. Acetaldehyde adsorption on TiO_2: influence of NO_2 preliminary adsorption. Chem. Eng. J. 281, 126–133.

Twohy, C.H., Kreidenweis, S.M., Eidhammer, T., Browell, E.V., Heymsfield, A.J., Bansemer, A.R., Anderson, B.E., Chen, G., Ismail, S., DeMott, P.J., Van den Heever, S.C., 2009. Saharan dust particles nucleate droplets in eastern Atlantic clouds. Geophys. Res. Lett. 36, L01807. 01810.01029/02008GL035846.

Usher, C.R., Michel, A.E., Grassian, V.H., 2003. Reactions on mineral dust. Chem. Rev. 103, 4883–4939.

van Erp, T.S., Martens, J.A., 2011. A standardization for BET fitting of adsorption isotherms. Microporous Mesoporous Mater. 145, 188–193.

Vlasenko, A., Sjögren, S., Weingartner, E., Gäggeler, H.W., Ammann, M., 2005. Generation of submicron arizona test dust aerosol: chemical and hygroscopic properties. Aerosol Sci. Technol. 39, 452–460.

Wang, H., Shadman, F., 2013. Effect of particle size on the adsorption and desorption properties of oxide nanoparticles. AIChE J. 59, 1502–1510.

Wu, Q.Q., Huang, L.B., Liang, H., Zhao, Y., Huang, D., Chen, Z.M., 2015. Heterogeneous reaction of peroxyacetic acid and hydrogen peroxide on ambient aerosol particles under dry and humid conditions: kinetics, mechanism and implications. Atmos. Chem. Phys. 15, 6851–6866.

Wurzler, S., Reisin, T.G., Levin, Z., 2000. Modification of mineral dust particles by cloud processing and subsequent effects on drop size distributions. J. Geophys. Res.-Atmos. 105, 4501–4512.

Yamashita, K., Murakami, M., Hashimoto, A., Tajiri, T., 2011. CCN ability of Asian mineral dust particles and their effects on cloud droplet formation. J. Meteo. Soc. Japan. Ser. II 89, 581–587.

Yeşilbaş, M., Boily, J.-F., 2016. Particle size controls on water adsorption and condensation regimes at mineral surfaces. Sci. Rep. 6, 32136.

Zein, A.E., Romanias, M.N., Bedjanian, Y., 2014. Heterogeneous interaction of H_2O_2 with arizona test dust. J. Phys. Chem. A 118, 441–448.

Summary

This thesis investigates the interactions of volatile organic compounds (VOCs) with natural mineral dust samples. The VOCs used are isopropanol (IPA), isoprene (ISP) and acetic acid (AcA). Five natural mineral dust samples originating from various desert regions all over the world are used in this study.

It is evidenced that the origin, i.e. the chemical composition, of the natural dust sample plays a significant role in defining the nature of its interaction with the VOCs. In particular, an increase of uptake is observed with increasing Al/Si and Fe/Si elemental ratios. Moreover, the dust-VOC interaction is evidenced as being highly impacted by relative humidity and temperature.

Various interaction modes have been evidenced between dust and VOCs such as physisorption, chemisorption and reactive sorption depending on the chemical composition of the dust and the structure of the VOC. Depending on the interaction mode, heterogeneous processes can act as a sink of primary VOCs or even a source of secondary oxygenated VOCs in the gas phase. This work emphasizes the contribution of heterogeneous processes to the atmosphere.

Résumé

Ce travail de these vise à caractériser l'interaction entre composés organiques volatils et poussières minerales atmosphériques. Les COV sélectionnés sont l'isopropanol (IPA), l'isoprène (ISP) et l'acide acétique (AcA). Cinq échantillons naturels de poussières minerales provenant de zone désertiques situées dans plusieurs regions du globe ont été retenus.

Il a été mis en evidence que l'orgine et donc la composition chimique des poussières naturelles joue un role majeur dans la nature de leur interaction avec les COV. Plus particulièrement, les coefficients de capture tendent à croitre avec les rapports élémentaires Al/Si et Fe/Si. De plus, il est montré que l'interaction entre COV et poussières est fortement impactée par l'humidité relative et la temperature.

Plusieurs modes d'interaction entre les COV et les poussières étudiés ont été mis en evidence: physisorption, chimisorption ou adsorption réactive. Ils dependent de la composition chimique des poussières et de la structure des COV. En fonction du mode d'interaction, ces processus hétérogènes peuvent être considérés comme des puits de COV primaires voire des source de COV secondaires en phase gazeuse. Ce travail met en lumière la contribution des processus hétérogènes dans l'atmosphère.